Coherent dynamics of small molecules in rare gas crystals

Markus Gühr

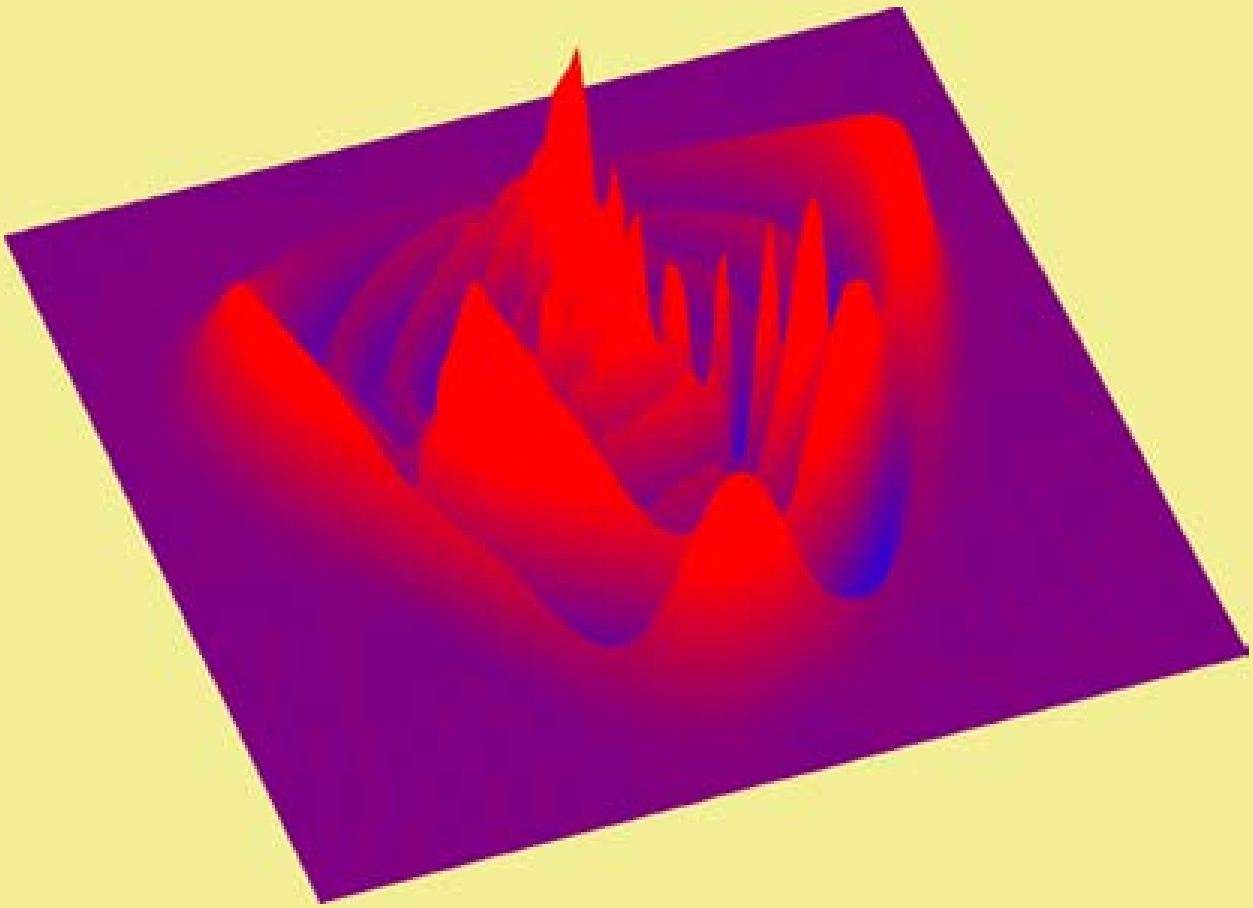

Cuvillier Verlag Göttingen

Coherent dynamics of small molecules in rare gas crystals

im
Fachbereich Physik
der
Freien Universität Berlin
eingereichte Dissertation

vorgelegt von

Markus Gühr

Januar 2005

Bibliografische Information Der Deutschen Bibliothek
Die Deutsche Bibliothek verzeichnet diese Publikation in der Deutschen Nationalbibliografie; detaillierte bibliografische Daten sind im Internet über http://dnb.ddb.de abrufbar.
1. Aufl. - Göttingen : Cuvillier, 2005
Zugl.: Berlin, Univ., Diss., 2005
ISBN 3-86537-411-5

Diese Arbeit wurde in der Zeit von Oktober 2001 bis Dezember 2004 unter der Aufsicht von Herrn Prof. Dr. N. Schwentner am Fachbereich Physik der Freien Universität Berlin durchgeführt.

Erstgutachter: Prof. Dr. N. Schwentner
Zweitgutachter: Prof. Dr. L. Wöste
Drittgutachter: Prof. Dr. T. Elsässer
Disputationstermin: 16. Februar 2005

Picture on title: Wigner function of a 1/6 revival (see Sec. 2.2.3)

© CUVILLIER VERLAG, Göttingen 2005
Nonnenstieg 8, 37075 Göttingen
Telefon: 0551-54724-0
Telefax: 0551-54724-21
www.cuvillier.de

Alle Rechte vorbehalten. Ohne ausdrückliche Genehmigung des Verlages ist es nicht gestattet, das Buch oder Teile daraus auf fotomechanischem Weg (Fotokopie, Mikrokopie) zu vervielfältigen.
1. Auflage, 2005
Gedruckt auf säurefreiem Papier

ISBN 3-86537-411-5

Kurzfassung

Die ultraschnelle Dynamik von Br_2 Molekülen in Argonkristallen (Br_2:Ar) wird mit Hilfe der Femtosekunden Anrege-Abfrage Methode zum ersten Male untersucht. In den zeitaufgelösten Spektren werden die kohärente intramolekulare Dynamik und eine kohärente Umgebungsdynamik beobachtet. Mit dem RKR Algorithmus wird die elektronische B Zustands-Potentialfläche des Br_2 konstruiert. Weiterhin wird die Energierelaxation in diesem Zustand quantifiziert. Während der ersten Kollision des Moleküls mit dem Käfig aus Edelgasatomen verliert das molekulare Schwingungswellenpaket bis zu 50 % seiner Energie. Die intramolekulare Kohärenz bleibt dennoch danach erhalten. Ebenso kann diese Kohärenz auch einen nichtadiabatischen elektronischen Übergang überleben, was am Beispiel von I_2 in Kryptonkristallen (I_2:Kr) verdeutlicht wird.

Die feste Argon-Umgebung erzeugt Dekohärenz im Molekül, dennoch können Interferenzphänomene von molekularen Schwingungswellenpaketen kontrolliert werden. Mit Hilfe eines Computerprogramms zur Wellenpaket-Propagation wird ein neues Kontrollschema, basierend auf "gechirpten" Laserpulsen, erarbeitet ("chirp" = Änderung der Lichtfrequenz mit der Zeit). Die Erzeugung des Wellenpaketes mit negativ oder positiv linear "gechirpten" Laserpulsen erlaubt eine vor- bzw. rückwärtige Zeitverschiebung der normalen Wellenpaket-Propagation.

Darauf basiert ein hier erstmals vorgestelltes Schema zur Quantifizierung des molekularen Kohärenzzerfalls (Dephasierung). Die Wellenpakete werden unter Anregung mit negativ "gechirpten" Laserpulsen zu einem Zeitpunkt $T_{\rm opt}$ räumlich fokussiert. Aus dem Modulationskontrast bestimmen wir die Vibrations-Dephasierungszeit $T^{\rm vib}_{\rm deph}$ = 3 ps im B Zustand. Diese entspricht etwa elf Schwingungsperioden von 280 fs. Die positiv "gechirpten" Pulse ziehen die molekularen Interferenzstrukturen ("revivals") bezüglich $T^{\rm vib}_{\rm deph}$ vor. Durch die kohärente Präparation von vier Schwingungszuständen mit einem positiv "gechirpten" Puls gelingt uns die Beobachtung eines 1/6 "revivals". Aus den Daten schließen wir auf eine Dephasierung der vier Niveaus in $T^4_{\rm vib} \approx 1.2$ ps. Der "chirp" verlängert den Laserpuls um einen Faktor zehn auf $\Delta\tau$ = 300 fs. Die elektronische Dephasierungzeit $T^{\rm el}_{\rm deph}$ des optischen B $\longleftarrow$ X Überganges engt die Kontrollmöglichkeit auf das Zeitintervall $\Delta\tau < T^{\rm el}_{\rm deph}$ ein. Die erfolgreiche Kontrolle erlaubt daher eine Abschätzung mit $T^{\rm el}_{\rm deph} > 300$ fs aus dem Experiment.

Eine langanhaltende, monochromatische Frequenz $f_{\rm P}$ = 2 THz wird in den molekularen Anrege-Abfrage Spektren des Br_2:Ar beobachtet. Diese entspricht der Frequenz des Zonenrand-Phonons (ZBP) im Argonkristall. Weiterhin wird eine Frequenzkomponente von $f_{\rm P}$ = 1.5 THz im Fall von I_2:Kr beobachtet, welche wiederum zum ZBP des Kryptonkristalls gehört. Weder der Absolutwert von $f_{\rm P}$ noch seine Phase hängt von der molekularen Schwingungsdynamik ab. Die Phononen werden nach dem DECP ("Displacive Excitation of Coherent Phonons") Schema beim elektronischen B $\leftarrow$ X und A $\leftarrow$ X Übergang angeregt. Eine Modellrechnung zeigt die Expansion der Elektronenhülle beim Übergang vom elektronischen Grundzustand X in den B oder A Zustand, wodurch die Edelgasatome in der Umgebung angestoßen werden. Eine Gruppe von Edelgasatomen in der (100) Ebene ist von der molekularen Schwingung entkoppelt. Die Zonenrand-Phononen haben eine verschwindend kleine Gruppengeschwindigkeit $v_{\rm g}$. Daher bleibt ihre Amplitude in der Nähe des Moleküls lokalisiert, während sich alle Phononen größerer Wellenlänge im Kristall ausbreiten. Das Zonenrand-Phonon bewirkt eine periodische Modulation der Solvatationsenergie der molekularen Ladungstransferzustände, die als Endzustände im Anrege-Abfrage Experiment benutzt werden. Dadurch wird die Detektionseffizienz des molekularen Wellenpaketes mit der ZBP Frequenz $f_{\rm P}$ moduliert.

Abstract

The molecule Br_2 embedded in solid argon is investigated for the first time on the ultrashort domain via femtosecond pump-probe spectroscopy. Coherent intramolecular vibrational wave packet dynamics and coherent host dynamics are identified in the spectra. The electronic B state potential surface is constructed from the experimental periods using the RKR algorithm, and the energy relaxation is quantified over a large range in this state. During the first molecule-cage collision, up to 50 % vibrational energy loss of the wave packet is observed; however, the intramolecular coherence is preserved in the strong interaction. Furthermore, the coherence can even survive nonadiabatic electronic transitions, as is documented for the case of I_2 in solid Kr.

Interferences in vibrational wave packets of Br_2 molecules are controlled in the presence of a solid Ar environment that provides decoherence. A control scheme based on chirped pulses is worked out with help of a numerical wave packet propagation. By applying a negatively or positively chirped excitation pulse, one can set the clock backward or forward respectively in the wave packet propagation.

Based on this mechanism, we present a general scheme to record vibrational decoherence. Wave packets are spatially focused at T_{opt} by applying negatively chirped pulses. From the focusing contrast, we determine a vibrational dephasing time on the B state of $T_{\mathrm{deph}}^{\mathrm{vib}}$ = 3 ps corresponding to about 11 vibrational periods, each of 280 fs. Positively chirped pulses advance the formation of fractional revival structures with respect to $T_{\mathrm{deph}}^{\mathrm{vib}}$. By exciting four vibrational levels with such a pulse in an experiment, we observe a 1/6 revival, indicating the vibrational coherence time $T_{\mathrm{vib}}^{4} \approx 1.2$ ps for exactly four levels. The required chirp prolongs the pulse duration by a factor of ten to $\Delta\tau$ = 300 fs. Electronic dephasing $T_{\mathrm{deph}}^{\mathrm{el}}$ of the B $\longleftarrow$ X transition restricts the revival control fidelity to parts of the pulse with $\Delta\tau < T_{\mathrm{deph}}^{\mathrm{el}}$, which allows for the determination of $T_{\mathrm{deph}}^{\mathrm{el}} > 300$ fs.

A long lasting coherent oscillation with a sharp frequency f_{P} = 2 THz is observed in Br_2:Ar pump-probe spectra. It matches exactly the Zone Boundary Phonon (ZBP) frequency of the solid Ar host. Furthermore, a frequency component with f_{P} = 1.5 THz is observed in I_2:Kr pump-probe spectra, matching the Kr crystal ZBP frequency. The value of f_{P} and its phase with respect to the pump pulse do not depend on the B or A state vibrational dynamics. The phonons originate from a Displacive Excitation of Coherent Phonons (DECP) initiated in the electronic B $\leftarrow$ X and A $\leftarrow$ X transitions. A model calculation shows that an expansion of the electronic density in going from the electronic ground state X to the B or A state kicks the Ar/Kr atoms in the Br_2/I_2 vicinity. Subsequently, a group of host atoms in the (100) plane is decoupled from the intramolecular dynamics. The ZBPs have a vanishing group velocity v_{g}, and therefore they stay in the vicinity of the chromophore, whereas phonons with longer wavelength propagate away from the molecule. The ZBP modulates the solvation energy of the terminal charge-transfer states used in the probe transition from the A and B state and thus the detection sensitivity of the intramolecular molecular wave packet.

Contents

1 Introduction **1**

2 Concepts and methods **5**
2.1 Coherence 5
2.1.1 Classical coherence 5
2.1.2 Quantum coherence 7
2.2 Dispersion and revivals in Morse oscillators. Focusing with chirped light pulses 10
2.2.1 Morse potential 10
2.2.2 Focusing of wave packets 11
2.2.3 Fractional revivals 13
2.2.4 Nomenclature for dephasing, decoherence and dispersion 18
2.3 Pump-probe spectroscopy 18
2.3.1 Pump-probe method 20
2.3.2 Vibrational energy relaxation in pump-probe spectra 24
2.3.3 Method to determine the vibrational dephasing in a Morse oscillator . . 25
2.3.4 Manipulation of fractional revival structures and their appearance in pump-probe spectra 25

3 Br_2 and I_2 in rare gas solids **31**
3.1 Gas phase properties 31
3.1.1 Physical properties 31
3.1.2 Electronic structure of halogens 32
3.1.3 Selection rules and polarization sensitive spectroscopy 34
3.1.4 Gas phase absorption spectra 36
3.2 Molecules in rare gas solids 37
3.2.1 The cage effect 37
3.2.2 Energy shifts of charge-transfer states 39
3.2.3 Absorption and excitation spectra 39
3.2.4 Literature on Br_2 in rare gas solids 42

4 Experimental setup **45**
4.1 Vacuum system and sample preparation 45
4.2 Absorption spectroscopy setup 48
4.3 Ultrashort laser pulses 49
4.3.1 Gaussian pulses 49
4.3.2 Chirping pulses 52
4.3.3 Nonlinear optics 52
4.3.4 Frequency Resolved Optical Gating (FROG) 54
4.4 Laser System 55

4.4.1 CPA system . . . 55
4.4.2 NOPA setup . . . 56
4.5 Pulse characterization . . . 57
4.6 Pump-probe and emission spectroscopy setup . . . 58

5 Spectroscopic results **61**
5.1 Absorption spectra . . . 61
5.2 Emission spectra . . . 61

6 Discussion of spectroscopic results **67**
6.1 Discussion of absorption spectra . . . 67
6.2 Discussion of emission spectra and assignment of probe windows . . . 73
6.2.1 One-photon probe transitions . . . 73
6.2.2 Two-photon probe transitions . . . 75

7 Ultrafast dynamics **79**
7.1 Intramolecular vibrational wave packets of Br_2:Ar . . . 79
7.1.1 Pump-probe spectra of the electronic A and B state . . . 79
7.1.2 Polarization sensitive pump-probe spectroscopy . . . 86
7.1.3 A and B state dynamics decomposition . . . 88
7.1.4 Wave packet focusing . . . 90
7.2 Coherent host dynamics . . . 94
7.2.1 Br_2 in solid argon . . . 94
7.2.2 I_2 in solid krypton . . . 97

8 Discussion of ultrafast dynamics **103**
8.1 Intramolecular dynamics . . . 103
8.1.1 Vibrational periods in the B state . . . 103
8.1.2 Potential construction . . . 106
8.1.3 Vibrational energy relaxation . . . 112
8.1.4 Trajectory for the first excursion of a wave packet . . . 117
8.2 Methods to determine coherences . . . 121
8.2.1 Wave packet focusing and vibrational coherence . . . 121
8.2.2 Control of fractional revivals and electronic coherence . . . 124
8.2.3 Electronic dephasing . . . 129
8.2.4 Comparison to other methods . . . 130
8.2.5 Comparison to other dephasing constants . . . 131
8.3 Coherent phonon dynamics . . . 133
8.3.1 Excitation scheme for coherent ZBP . . . 134
8.3.2 Detection scheme for coherent ZBP . . . 140
8.3.3 Comparison to alternative models . . . 144

9 Summary **147**

Bibliography **151**

Appendix **169**

List of Figures

2.1 Schemes of dephasing and dissipation 6
2.2 Vibrational and electronic dephasing 9
2.3 Dispersion and focusing of a wave packet 12
2.4 Model for quarter and half revivals 14
2.5 Wigner function of a wave packet in a Morse oscillator 16
2.6 Wigner functions of fractional revivals. 17
2.7 Revivals in R-t representation 19
2.8 Pump-probe scheme 20
2.9 Franck-Condon picture for the probe transition 23
2.10 Pump-probe spectrum for energy relaxation 24
2.11 Focusing method to determine vibrational dephasing 26
2.12 Control of fractional revival structures 27
2.13 Pump-probe spectra different R_{win} and E_{win} 28
2.14 Probe window width 29

3.1 Vibrational levels in the B state for Br_2 isotopes 32
3.2 Molecular orbitals of the electronic ground state of dihalogens. 33
3.3 Potential energy surfaces of free Br_2 33
3.4 Polarization sensitive pump-probe spectroscopy 35
3.5 Gas phase absorption spectrum of Br_2 36
3.6 Geometry of the chromophore cage 38
3.7 Configuration coordinate picture (Huan-Rhys) 39
3.8 Excitation spectrum of Br_2:Ar 41

4.1 Vacuum system 46
4.2 Absorption spectroscopy setup 48
4.3 Spectra of the high pressure Xe lamp 49
4.4 E Field and instantaneous frequency of a chirped pulse 50
4.5 FROG traces of an unchirped and a positively chirped pulse 55
4.6 NOPA setup 56
4.7 Laser, XFROG and pump-probe setup 57

5.1 Transmission and absorption spectrum of Br_2:Ar 62
5.2 Fluorescence decay of the charge-transfer states 62
5.3 Ultraviolet fluorescence bands of Br_2:Ar 63
5.4 Temperature dependence of the ultraviolet emission bands of Br_2:Ar 64
5.5 Pump-probe signals for the different ultraviolet emission bands 65

6.1 Comparison of different Br_2 absorption spectra 68
6.2 Construction of an absorption spectrum for the bromine C ⟵ X transition. . . 68

6.3 Comparison of the experimental absorbance with the projection method 69
6.4 Comparison of projection method to Franck-Condon factors 70
6.5 Spectral shift for typical laser pulses after propagating the crystal 72
6.6 Some covalent and charge-transfer states of the Br_2 molecule 75
6.7 Difference potentials to charge-transfer states for one-photon transitions 76
6.8 Probe pulse energy dependence of the UV fluorescence at 300 and 322 nm. . . 76
6.9 Difference potentials to charge-transfer states for two-photon probe transitions. 77

7.1 Long time range pump-probe spectra of Br_2 :Ar probed from 289 to 320 nm . . 80
7.2 Pump-probe spectra with λ_{probe} = 339 nm and variable λ_{pump} 81
7.3 Short time range pump-probe spectra of the Br_2:Ar B state 82
7.4 Short time range pump-probe spectra of the Br_2:Ar B state 83
7.5 Br_2:Ar pump-probe spectra with λ_{pump} = 530 nm and variable λ_{probe} 84
7.6 Pump-probe spectra of Br_2:Ar with λ_{probe} = 620 nm in a two-photon probe process 85
7.7 Polarization dependent pump-probe spectra for Br_2:Ar 86
7.8 Polarization dependent pump-probe spectra for I_2 :Kr 87
7.9 Pump-probe spectra with λ_{pump} = 600 nm, λ_{probe} = 570 nm 88
7.10 Polarization dependent pump-probe spectra for λ_{probe} = 620 nm 89
7.11 Pump-probe spectra with λ_{pump} =580 nm and λ_{probe} = 600 nm 90
7.12 Pump-probe spectra of Br_2:Ar and reconstructed A,B state dynamics 91
7.13 SFG FROG and FODM of negatively chirped pulse 92
7.14 Pump-probe spectra excited with different chirped pulses 93
7.15 Pump-probe spectra for different excitation chirps 95
7.16 Pump-probe spectrum of Br_2:Ar with λ_{pump} = 520 nm and λ_{probe} = 348 nm . . 96
7.17 Pump-probe spectra of Br_2:Ar with λ_{probe} = 348 nm and λ_{pump} varied from 500 to 530 nm. 96
7.18 Normalized pump-probe spectra of Br_2:Ar probing the B or the A state 97
7.19 Fourier spectrum of the λ_{pump} = 520 nm, λ_{probe} = 348 nm transient of Br_2:Ar . . 98
7.20 Pump-probe spectra of I_2:Kr under different excitation conditions 98
7.21 Pump-probe spectra of I_2:Kr with λ_{pump} =520 nm and λ_{probe} varied 99
7.22 Pump-probe spectra of I_2:Kr for fixed λ_{probe} = 520 nm and λ_{pump}varied 100
7.23 Fourier spectrum of an I_2:Kr pump-probe spectrum 101

8.1 Br_2:Ar pump-probe spectra for $\lambda_{\mathrm{pump}} = 570$ nm and variable λ_{probe} 104
8.2 Illustration of the window effect 105
8.3 Squared vibrational frequencies in the Br_2:Ar B state 107
8.4 Pump-probe spectrum and scheme of Br_2:Ar excited at 510 nm 109
8.5 RKR potential of Br_2:Ar 110
8.6 Free Br_2 molecule included Br-Ar interaction 111
8.7 Br_2:Ar pump-probe spectra with $\lambda_{\mathrm{probe}} = 345$ nm pulses and λ_{pump} varied . . . 113
8.8 Apparent periods T of Br_2:Ar as a function of the period number 114
8.9 Vibrational energy relaxation rates for Br_2:Ar B state 115
8.10 Energy relaxation for different dihalogens in rare gas solids 116
8.11 Trajectory for a wave packet with λ_{pump} = 530 nm in Br_2:Ar 117
8.12 Ultrafast nonadiabatic transition in I_2:Kr 119
8.13 Focusing times T_{opt} as a function of chirp 121
8.14 Comparison of experimental pump-probe spectra to simulations 122
8.15 Simulated Wigner plots and of Br_2 with negative chirp excitations 123
8.16 Pump pulse spectral shape and pump-probe spectrum with revivals 125

8.17 Simulated revival pattern of Br_2 in a pump-probe spectrum for different chirps . 126
8.18 Spectra of a 1/6 revival excited by a positively chirped pump pulse 127
8.19 Spatial interference patterns of a advanced 1/6 revival 128
8.20 Population of vibrational levels by a positively chirped pulse 129
8.21 Phonon dispersion relations of solid argon and krypton and coherent host peaks 134
8.22 Cage geometry of I_2:Kr. Interaction of I_2 with Kr and Br_2 with Ar 138
8.23 Variation of phonon contribution upon changing λ_{probe} 141
8.24 Phonon detection mechanism 142

List of Tables

3.1 Physical constants of I_2 and Br_2. 31
3.2 Spectroscopic data for the free Br_2 molecule. 34
3.3 Emission bands of Br_2:Ar 42

5.1 Ultraviolet emission bands (1-3) of Br_2:Ar 63

6.1 Population of the vibrational levels 1 and 2 for the Br_2 X state at 20 and 300 K . 67
6.2 Spectroscopic data for Br_2:Ar and gas phase 71
6.3 Calculated UV emission bands of Br_2:Ar 74

8.1 B state periods T as a function of energy 106
8.2 Morse fits for Br_2:Ar vibrational frequencies. 107
8.3 $R_{\mathrm{win}}(\lambda_{\mathrm{probe}})$ for different λ_{probe} 118
8.4 Time constants used in this thesis 130
8.5 Morse parameters for I-Kr and Br-Ar 136

Abbreviations

CARS - Coherent anti-Stokes Raman scattering
CT - Charge-Transfer
DECP - Displacive Excitation of Phonons
DIM - Diatomics In Molecules
FC - Franck-Condon
fcc - face centered cubic
FODM - First Order Delay Marginal
FROG - Frequency Resolved Optical Gating
fs - femtosecond $(10^{-15}s)$
FWHM - Full Width at Half Maximum
LIF - Laser Induced Fluorescence
nm - nanometer $(10^{-9}m)$
NOPA - Noncollinear Optical Parametric Amplifier
OMA - Optical Multichannel Analyzer
ps - picosecond $(10^{-12}s)$
RGS - Rare Gas Solids
RKR - Rydberg-Klein-Rees
SFG - Sum Frequency Generation
SHG - Second Harmonic Generation
ZBP - Zone Boundary Phonon

Chapter 1

Introduction

The typical time for chemical bond cleavage and reformation is situated in the range of a few femtoseconds to some picoseconds, dictated by the motion of molecular fragments on their potential energy surfaces. Besides analysis of chemical reactions using ultrashort laser pulse spectroscopy [1–3], the possibility to control the reaction arose [4]. In most of these schemes, a *coherence* in the reacting system is a precondition in achieving the goal, and therefore the term "coherent control" has been applied.

By *coherence*, a well defined phase relation among quantum mechanical wave functions is meant. For molecular systems, the wave functions are divided into electronic, vibrational and rotational parts. The coherent superposition of corresponding eigenstates is called an electronic, vibrational or rotational *wave packet* [5].

Coherently coupled eigenstates can show interference patterns. In the optical double slit experiment, the interference pattern can only be observed if the relative phase of the field emerging from the two slits is stable. In an analogous way, one can construct an interference pattern of two quantum states with fixed relative phases. The optical analogy for the interference of more than two eigenstates is a multiple slit or grating experiment. Due to these formal similarities, the field of coherent quantum phenomena is often called "quantum optics" [6]. Coherent control schemes exploit the interference patterns of wave functions to control the output of a reaction. For example, the "Tannor-Rice" method [7,8] uses the interference of intramolecular vibrational wave functions to achieve a control goal.

The decay of coherence is called *decoherence* or *dephasing*.[1] It is induced by the coupling of the coherent system to an environment which provides statistical fluctuations on the phases of eigenstates. This leads to attenuated interferences among the eigenstates.

Dephasing, used here synonymously with decoherence, destroys the premise of coherent control. For an application, the dephasing times of the molecule involved have to be taken into account. In case of free molecules in the vacuum, the electronic, vibrational, and rotational dephasing times are much longer than the timescales of chemical reactions. Molecules solvated in a liquid or solid environment show considerably shorter dephasing times in the range of femto- to picoseconds. The trend in coherent control of chemical reactions moves in the direction of multidimensional systems in solution, often with biological relevance. Besides dephasing and dissipation of energy, the *dispersion* of wave packets is a crucial process. Wave packets on *anharmonic* potentials (which all relevant molecular potentials are) undergo a broadening, however without a loss of phase memory.

This study aims at establishing a basic model for multidimensional systems like organic dyes or biomolecules in solution, and to isolate dissipation, dephasing and dispersion processes. The insight gained in the model can clarify the preconditions for the observation of coherences in complex systems.

[1] The terminology will be specified in section 2.2.4.

Rare Gas Solids (RGS) present conceptually simple hosts. They have a large ionization energy which allows for using high intensity laser pulses. The rare gas atoms are spherical because of their closed electronic shells and they form face centered cubic (fcc) crystals at low temperature [9]. The phonon dispersion relations and optical properties of the crystals are well studied [10–12]. The rare gas atoms are chemically inert, thus one can use adapted gas phase potentials for the molecular dopants.

The molecule in RGS system, studied in this thesis, is chosen under the constraint of an ultrafast dissipation and dephasing, since this is generally the case for large molecules in solutions. In RGS, excited electronic states of halogens undergo such fast processes because their vibrational level spacing is close to the Debye frequency. A variety of halogens has been studied before in RGS.

The molecule can be described as a one dimensional vibronic quantum system, if its rotation is blocked in the RGS. The ClF molecule is sitting on a single-substitutional site in RGS [13–19] and undergoes ultrafast angular randomization after excitation [20] and is therefore not appropriate. First experiments on Cl_2, sitting on a double-substitutional site in RGS, indicate it to be a suitable system under the above mentioned constraints. However, the anharmonicity and resulting dispersion on the electronic B state of Cl_2 are so large that only a few vibrational periods of the wave packet can be observed in experiments. The anharmonicity of I_2 molecules is much lower. The electronic B state of I_2 in RGS shows rich vibrational wave packet structure. An enormous amount of pump-probe spectroscopy has been done by Apkarian and coworkers [21–24] and the Schwentner group [20, 25–28]. The Coherent Raman Antistokes Scattering (CARS) however indicates a limited electronic coherence $T^{\mathrm{el}}_{\mathrm{deph}}$ time of less than 100 fs in the B $\longleftarrow$ X transition [29–34]. Some of the control methods conducted here will need an electronic coherence time of several hundred femtoseconds and therefore, the B state of the I_2:RGS system cannot be used. However, coherent phonon dynamics and an example of coherent spin-flip will be presented for the I_2:Kr system. The electronic ground state X of I_2 in RGS is not of interest for this study, since the CARS spectra indicate a vibrational dephasing time of several hundred picoseconds, much too long in comparison to complex systems.

Combining the preconditions, we conclude that Br_2 in solid Ar should fulfill all requirements. Excitation spectra of the B $\longleftarrow$ X transition indicate an electronic dephasing of some hundred femtoseconds. The anharmonicity of the B state is in a convenient range that allows for the observation of a few vibrational wave packet periods without major broadening due to dispersion. From the experiments we found that the vibrational dephasing in the electronic B state is in the picosecond domain. Throughout the thesis, the methods and concepts are primarily conducted on the system Br_2 in solid argon.

The ultrafast dynamics of Br_2 has only been studied in two experiments for the free molecule case [35, 36]. Results on ultrafast dynamics of Br_2 in condensed media have not been documented; this thesis presents the first ones. The potential energy surfaces of free Br_2 are documented in literature [37–52]. The electronic potential surfaces can be approximated by Morse potentials very well [53]. The covalent states of Br_2:RGS were studied in absorption and emission spectroscopy [54–66]. The spectra of the charge-transfer states, needed to establish a pump-probe scheme, have been measured by us and are presented in chapters 5 and 6.

To detect the ultrafast vibrational dynamics of the molecule in its environment, the femtosecond pump-probe spectroscopy is applied. By use of a first femtosecond laser pulse (pump), a coherent superposition of vibrational eigenstates (vibrational wave packet) in an excited electronic state (described by a Morse potential) is created. The interference of the vibrational wave functions is interrogated with a second time delayed fs laser pulse (probe).

The wave packet disperses on the Morse oscillator potential of Br_2, since it spans over a

finite range in energy, all of which give rise to different oscillation periods. However, due to the discrete structure of the vibrational levels, the wave packet will revive after some time T_{rev} (determined by the anharmonicity) and regain its narrow shape. The phenomenon is known under the term revival [67–75]. If the vibrational dephasing time $T_{\mathrm{deph}}^{\mathrm{vib}}$ of the molecule in the RGS is larger than the revival time, the decay of coherence among the vibrational eigenstates can be deduced from the pump-probe spectra directly as a decay of revival features [76–78]. If the vibrational dephasing time is shorter than the revival time but larger than the oscillation period T, a new scheme, which is presented in this thesis and a supplementary article [79] has to be applied. The dispersion reduces the modulation contrast on the same timescale as dephasing does. However, dispersion can be suppressed at a distinct time T_{opt} in the evolution by excitation with a negatively chirped pulse (see section 2.2.2). The method has been used before to demonstrate the possibility of vibrational wave packet focusing [80–83]. The scheme will be systematically applied in this thesis to suppress dispersion at a given time T_{opt} and deduce the vibrational dephasing from a background at T_{opt} in the experimental pump-probe spectra (see sections 2.3.3 and 8.2.1).

Apart from full revivals of the vibrational wave packets in Morse oscillators, fractional revivals arise that cause multiples of the fundamental oscillation frequency in the pump-probe spectrum. Using the fractional revivals, information about coherence of a distinct group of vibrational levels can be deduced. Here, the measured vibrational dephasing time $T_{\mathrm{deph}}^{\mathrm{vib}}$ is too short to observe fractional revivals directly. Therefore, a novel scheme to control the fractional revivals of a vibrational wave packet based on chirped excitation pulses is worked out (see section 2.3.4). The revival features are shifted towards the time-zero by a positively chirped excitation pulse. A 1/6 revival, exhibiting the threefold vibrational period, is observed on the B state of Br_2 in solid Ar. From this experiment, a coherence time of four vibrational levels is estimated in section 8.2.2.

The positively chirped excitation pulses used to advance the revival structures in time are actually longer than one oscillation period of the molecule in its excited electronic state. The vibrational wave packet portions created by the first part of the pulse will interfere with the later created parts of the wave packet. Therefore, the electronic coherence between ground and excited state is involved in the coherent preparation of the wave packet (see section 8.2.3). From the pulse duration an electronic coherence time for the B $\longleftarrow$ X transition of Br_2 in solid Ar is estimated.

The coherent vibrational dynamics is used to deduce a detailed picture of the molecule-host interaction. We are able to construct an effective intramolecular B state potential for Br_2 in solid Ar in section 8.1.2. Furthermore, the vibrational energy relaxation of wave packets on the electronic B state is determined (section 8.1.3) and a representative trajectory of a vibrational wave packet is shown (section 8.1.4). For the case of I_2:Kr, the vibrational coherence even survives vibrational energy losses of 1 eV connected to a spin-flip transition to another electronic state (section 8.1.4).

It will turn out that the interaction of the vibrating molecule with the matrix is not necessarily statistical. In contrast, collisions of the molecule with the matrix can lead to the creation of coherent wave packets built from vibrational levels not populated before the collision.

Coherent motions are found even for host atoms, showing up in the pump-probe spectra of the molecular guest. The conflictive issues of the specific mode, together with its excitation and probe mechanism were discussed in [24,29,30,32,84–86]. We attribute the coherent host motion to a Zone Boundary Phonon (ZBP) of the rare gas crystal. To support assignment, spectra of I_2:Kr (also measured by the author) are presented alongside the spectra of Br_2:Ar, both showing the coherent ZBP signature. The excitation of the coherent host phonon is achieved via the

expansion of the molecular electronic cloud during the A ⟵ X or B ⟵ X transition. This scheme is very similar to the model of Displacive Excitation of Coherent Phonons (DECP) [87–95] and will be presented in section 8.3.1. Many different phonon modes are excited, but only the ZBP having a vanishing group velocity stay at the excited molecule. They change the local density in the vicinity of the chromophore and thereby change the solvation energy of the molecular charge-transfer states [86, 96, 97], which in turn modulates the probe transition efficiency (see section 8.3.2).

Several theory groups treat the halogen in RGS systems extensively and their efforts have, to a large extent, motivated our experiments. Classical and quantum mechanical simulations mostly based on the DIM (Diatomics In Molecules) [98–103] approach give a detailed picture of the dynamical processes of molecular guests in a RGS host. Besides calculations on small molecules F_2, HCl, and Cl_2 in rare gases [104–108], simulations of the heavier I_2 molecules in rare gas environments exist [109–116]. Up to now, no simulations of the Br_2 in RGS have been published. Due to the results presented in this thesis, a collaborative effort within the Sfb 450[2] with the groups of Prof. Manz and Prof. Gerber aims to perform such calculations.

This thesis is organized as follows:

Chapter 2 introduces the basic ideas of coherence, dephasing, dispersion and fractional revivals. Furthermore, the ultrafast pump-probe spectroscopy and the methods used to determine vibrational and electronic dephasing times are explained.

The potential energy surfaces of the free Br_2 molecule and the general effects of the RGS on the spectroscopic molecular properties are presented in chapter 3. The experimental setup is described in chapter 4, together with a summary of ultrashort (chirped) laser pulses. The chapters 5, 6 on absorption and emission spectroscopy provide the information needed to conduct fs pump-probe spectroscopy on the system Br_2:Ar.

Chapter 7 presents the first results on Br_2:Ar dynamics, where one- and two-photon probe processes are used to detect vibrational wave packet dynamics. The rotation of the molecule is proved to be frozen. Furthermore, the coherent host motion in Br_2:Ar and I_2:Kr is illustrated.

The vibrational wave packet dynamics is used to determine an effective molecule-matrix potential for the electronic B state of Br_2 in solid Ar in chapter 8.1. Furthermore, the vibrational energy relaxation and an experimental trajectory are calculated in this section. The results on vibrational and electronic dephasing in Br_2:Ar are discussed in chapter 8.2. This chapter ends with the discussion of the coherent zone boundary phonon in I_2:Kr and Br_2:Ar (chapter 8.3).

[2]The collaborative research center SFB 450 is also financing and supporting this experimental work.

Chapter 2

Concepts and methods

Part 2.1 of this chapter will introduce the concepts of coherence, which is a central issue in this thesis. This will be followed by a presentation of dispersion, wave packet focusing and fractional revivals in section 2.2. The pump-probe method and the wave packet control schemes are presented in the final section 2.3 of this chapter.

2.1 Coherence

This section will provide the definition of coherence needed throughout the thesis. It is necessary to have the ideas of coherence in mind to follow the sections to come.

It is reasonable to start from the classical idea of coherence, defined for an ensemble of trajectories in phase space. For convenience, the dephasing and dissipation processes will be explained using a harmonic oscillator potential. The step from classical coherence to quantum coherence is made with the help of the density operator. Since the harmonic approximation is not sufficiently accurate for diatomic molecular electronic potentials, the Morse potential and the propagation of classical trajectories and quantum mechanical wave packets on it will be discussed afterwards. This will lead to the definition of dispersion and fractional revivals of a vibrational wave packet.

2.1.1 Classical coherence

The electronic state of a diatomic molecule is presented in the harmonic approximation. The molecules are elongated from the equilibrium distance (for example in an optical transition) and an oscillatory motion of the molecular ensemble sets in. The classical molecular ensemble shall have a finite width in the spatial distribution, inducing also a finite width in the momentum distribution. The ensemble is represented in phase space. One dimension describes the elongation q of the oscillators, the other dimension the momentum p. The distribution of oscillators is represented as a grey shaded area in phase space as shown in Fig. 2.1.

The molecules are considered as oscillating freely in Fig. 2.1a. The q and p axis of phase space shall be scaled such that q^2 represents the potential energy and p^2 the kinetic energy. For that case the total energy is given by $r^2 = q^2 + p^2$, where r is the distance to phase space origin. Since the energy of each oscillator is conserved, the value of r is not changed in the propagation. Apart from this, the angle α which the ensemble spans from the phase space origin is also not changed in the course of time. The propagation is said to be completely coherent in the case described in Fig. 2.1a.

Next, statistical elastic collisions with an environment are introduced. The molecular oscillators will not lose any vibrational energy in the collision, but the phase of an individual oscillator is changed by a small random value. The molecular oscillator will jump to another position in phase space, nevertheless keeping the same energy (*i.e.* r^2). The change of the molecular ensemble in this *dephasing* process is shown in Fig. 2.1b. The angle α gets broader in the

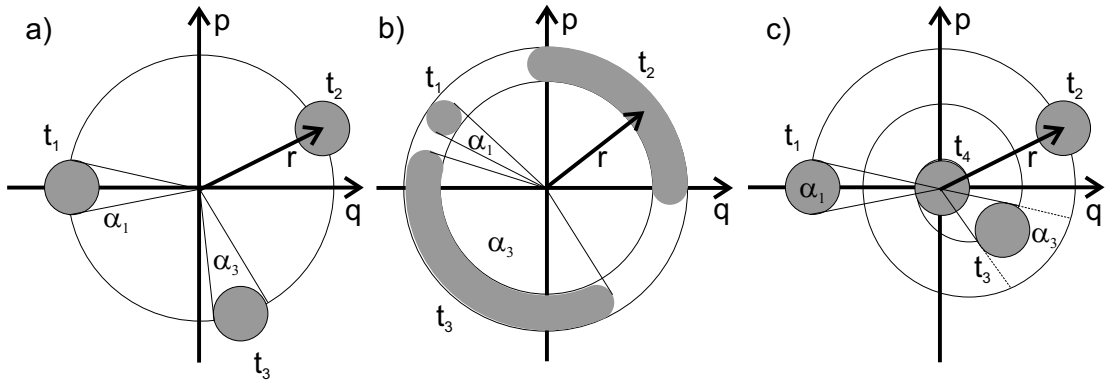

Figure 2.1: a) An ensemble of free classical harmonic oscillators in phase space position (q, p)(position,momentum) is shown as the grey area. No dephasing or dissipation occurs and the angle α under which the ensemble is seen from the origin of phase space does not change in the course of time (t_1< t_2<t_3). The radius r being proportional to the average energy is also constant in time. b) Case of pure dephasing. The molecules suffer statistical elastic collisions with an environment. The phase of a single molecular oscillator is changed by a small random value in a collision. The angle α for the ensemble average grows with propagation time (α_1 < α_3). c) Dissipative case. The molecules suffer inelastic collisions with a bath. The absolute width of the ensemble shall not be changed (no pure dephasing). The mean energy decreases as a function of time and the ensemble spirals to the potential minimum in the origin of the phase space plot. Furthermore, α increases with time, indicating the connection of dissipation and dephasing (form Ref. [73]).

course of time, with $\alpha_3 > \alpha_1$ for ($t_3 > t_1$). With increasing time, the molecular oscillator ensemble will fill the complete iso energetic ring depicted in Fig. 2.1b with a corresponding angle $\alpha = 2\pi$. Such an ensemble would be called completely incoherent or completely "*dephased*". Each molecule would still fulfill a harmonic oscillation, but its phase cannot be predicted, since the elastic collisions occur statistically. The same effect would occur, if the oscillation frequency would be slightly different for the groups of molecules. For example, some molecules can be heavier than others, as is the case for different molecular isotopes. Such a broadening of the angle α due to a splitting of the ensemble in groups with different oscillatory properties will be called in general *inhomogeneous*, while broadening effects being the same for every member will be generally called *homogenous*.

Apart from elastic collisions, inelastic collisions also occur in the investigation. The effect is called *dissipation*, or in the special case described in this thesis vibrational energy relaxation, and is illustrated in Fig. 2.1c. The molecular ensemble loses energy and spirals towards the center of phase space. The molecular ensemble propagates to smaller distances in r but keeps the width in q and p, since the phase of an individual oscillator is not changed. Connected with the loss of energy is the broadening of the angle α. Therefore, dephasing is directly connected to dissipation and cannot be avoided. When the vibrational ensemble has relaxed to the center of phase space, α is equal to 2π. To distinguish the dephasing induced by dissipation (Fig. 2.1c) from the dephasing described in Fig. 2.1b, the latter is often called *pure dephasing*.

The classical coherence introduced above can indeed be used to describe many experiments. Apkarian and coworkers, for example, have used classical trajectories for a calculation of pump-probe experiments [22–24]. However, the interference phenomena cannot be simulated in the classical approach. The quantum coherence is therefore introduced in the next section. The picture developed for a completely classical ensemble of molecules deserves to introduce the

term of quantum coherence here.

2.1.2 Quantum coherence

The nth eigenfunction $|\phi_n\rangle$ in a potential shall belong to energy eigenvalue E_n. A wave packet $|\Psi(t)\rangle$ can be written as a superposition of energy eigenfunctions :

$$|\Psi(t)\rangle = \sum_n c_n e^{-i\frac{E_n}{\hbar}t}|\phi_n\rangle, \tag{2.1}$$

where c_n are the excitation coefficients. The $|\phi_n\rangle$ can be vibrational, rotational or electronic eigenfunctions of the molecule.

In order to define the quantum coherence properly, one has to consider the density operator ρ:

$$\rho = \sum_i p_i |\Psi_i\rangle\langle\Psi_i|. \tag{2.2}$$

$|\Psi_i\rangle$ is a wave function or wave packet. The p_i are the statistical probabilities of finding the system in the state $|\Psi_i\rangle$. They have to fulfill the condition:

$$\sum_i p_i = 1.$$

The state is called *pure*, if there is one i for which p_i = 1 and all the other p_j = 0 ($i \neq j$). In any other case, the state is said to be *mixed*. Let $\rho(x', x)$ be the density operator in the position representation of $|\Psi(t)\rangle$, which is a wave packet according to Eq. (2.1). Then:

$$\begin{aligned}
\rho(x', x) &= \langle x'|\Psi(t)\rangle\langle(t)\Psi|x\rangle \\
&= \sum_{m,n}\langle x'|\phi_m\rangle\langle\phi_m|\Psi(t)\rangle\langle(t)\Psi|\phi_n\rangle\langle\phi_n|x\rangle \\
&= \sum_{m,n}\phi_m(x')(c_m\mathrm{e}^{-\frac{\mathrm{i}}{\hbar}\mathrm{E_m t}})(\mathrm{c_n^*e}^{+\frac{\mathrm{i}}{\hbar}\mathrm{E_n t}})\phi_\mathrm{n}^*(\mathrm{x}) \\
&= \sum_{m,n}\phi_m(x')\rho_{mn}\phi_n^*(x),
\end{aligned} \tag{2.3}$$

with $\rho_{mn} = c_m c_n^* e^{-\frac{i}{\hbar}(E_m - E_n)t}$ being the density operator (matrix) in the energy representation. A simple example to illustrate ρ_{mn} shall be given in a two-state system:

$$\rho_{mn} = \begin{pmatrix} |c_1|^2 & c_1 c_2^* e^{-\frac{i}{\hbar}(E_1 - E_2)t} \\ c_1^* c_2 e^{-\frac{i}{\hbar}(E_2 - E_1)t} & |c_2|^2 \end{pmatrix} \tag{2.4}$$

The diagonal elements of the density matrix are called populations. The off-diagonal elements are called quantum *coherences*. In contrast to the diagonal elements, they are complex and oscillate in time with a frequency corresponding to the energy difference.

These coherences are crucial for the development of interference patterns between the different eigenfunctions, as shall be explained for a system consisting of two vibrational eigenfunctions $\phi_0(R)$ and $\phi_1(R)$ with energies $E_0 = \frac{1}{2}\omega_e$ and $E_1 = \frac{3}{2}\omega_e$. The wave packet is written as: $\Psi(R,t) = c_0\mathrm{e}^{-\mathrm{i}\omega_\mathrm{e}(0+\frac{1}{2})\mathrm{t}}\phi_0(\mathrm{R}) + \mathrm{c_1 e}^{-\mathrm{i}\omega_\mathrm{e}(1+\frac{1}{2})\mathrm{t}}\phi_1(\mathrm{R})$. One obtains the probability density: $|\Psi(R,t)|^2 = |c_0|^2|\phi_0(R)|^2 + |c_1|^2|\phi_1(R)|^2 + 2Re(c_0^* c_1 \phi_0^*(R)\phi_1(R)e^{-i/(E_1 - E_0)t/\hbar})$. The interference term in the last equation is is based on the real part of the coherence of the density

operator. If this coherence vanishes, only the incoherent superposition given by the first two terms (populations) in the last equation remain and any time-dependent behavior of the wave packet is cancelled.

If the entity

$$Tr(\rho\rho) = 1. \tag{2.5}$$

is fulfilled, the system is called *coherent*. A pure state is coherent *per se*. A mixed state of n pure states will be called *partially coherent*, if $1 > Tr(\rho\rho) > 1/n$. A state is called *incoherent* if $Tr(\rho\rho)$ =1/n.

The question of how to describe the dephasing and dissipation processes in quantum mechanics arises. The Liouville-von Neuman equation gives the propagation of ρ by:

$$i\hbar\frac{\partial\rho}{\partial t} = [H, \rho] + \Gamma\rho, \tag{2.6}$$

where Γ is a tensor describing the dissipation and dephasing. Without Γ, the equation is equal to the Schrödinger equation. Descriptions of Γ were given for example by Redfield [117, 118] or Lindblad [119, 120]. In contrast to these studies, the processes here are treated empirically.

The density operator in phase space is discussed and compared to the classical density shown in Fig. 2.1. This "phase space approach" is taken from D. Tannor [73, 121, 122]. For that reason, the Wigner transformation of the density operator has to be defined. The Wigner function $f_W(q, p)$ is a very natural way to describe the density operator. For a pure state it is given as:

$$f_W(q,p) = \frac{1}{2\pi\hbar}\int_{-\infty}^{\infty} e^{\frac{i}{\hbar}p(x-x')}\langle x'|\rho|x\rangle ds = \frac{1}{2\pi\hbar}\int_{-\infty}^{\infty} e^{\frac{i}{\hbar}p(x-x')}\langle x'|\Psi\rangle\langle\Psi|x\rangle ds, \tag{2.7}$$

where $x = q + s/2$ and $x' = q - s/2$. Thus $f_W(q, p)$ is the Fourier transform of $\langle x'|\Psi\rangle\langle\Psi|x\rangle$ = $\Psi(x')\Psi^*(x)$ along the difference coordinate $s = x - x'$. When interpreting q as a position (for example the internuclear distance R in case of a molecular vibrational wave packet), the corresponding interpretation of p would be momentum. The projections of the Wigner functions on q or p show the absolute square of the wave packet on the respective coordinate. Nevertheless, $f_W(q, p)$ itself might become negative. This is in contradiction to its assignment as an analogue to classical phase space probability distribution, which is discussed in the literature [73].

The phase space representation of a vibrational wave packet on a harmonic potential[1] can be compared to Fig. 2.1. In order to achieve an increasing angle α as in Fig. 2.1b, a rate constant T_2^* has to be introduced and the coherences (off diagonal elements) of the density matrix in energy representation have to be multiplied by a factor $\mathrm{e}^{-\mathrm{t}/(|\mathrm{n}-\mathrm{m}|\mathrm{T}_2^*)}$, where n describes the row and m the column of the density matrix [73]. The populations (diagonal elements) stay untouched. The nomenclature for the rate constants is adapted from the Bloch equations in NMR spectroscopy [123]. Here they are defined for a multi-state system instead of only a two level system as in NMR.

The populations of the density matrix will decay if *dissipation* (or in the special case of the molecular potential, *vibrational energy relaxation*) occurs. In order to produce the phase space propagation in Fig. 2.1c with the Wigner transformation of a density operator, a time constant T_1 has to be introduced. It acts on the populations by the decay term $\mathrm{e}^{-\mathrm{t}/\mathrm{T}_1}$ and on the coherence by the decay $\mathrm{e}^{-\mathrm{t}/2\mathrm{T}_1}$ [73]. In a mixed case of pure dephasing and dissipation, a new dephasing time T_2 can be defined in a two-level system with the dissipation T_1 and pure dephasing T_2^*:[2]

$$\frac{1}{T_2} = \frac{1}{2T_1} + \frac{1}{T_2^*}. \tag{2.8}$$

[1] The evolution on an anharmonic oscillator will be the topic of the next section.

[2] T_1 will be used throughout this thesis for dissipation, whereas T_2 will be substituted by T_{deph}.

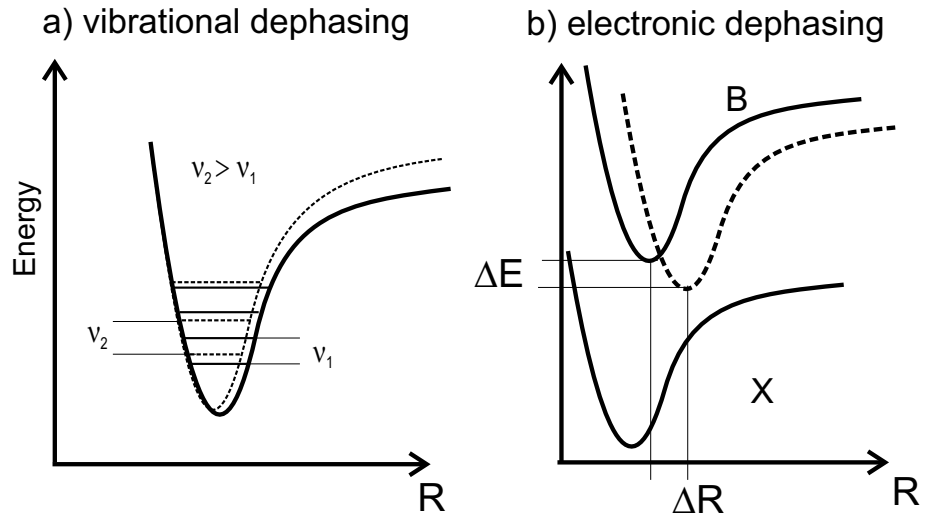

Figure 2.2: a) Scheme for vibrational dephasing. The effective molecular electronic potential $V(R)$ changes due to molecule solvent coordinate changes. The cage is tightening in this example (dashed line). This shifts the vibrational spacing from ν_1 to ν_2. b) Scheme for electronic dephasing. The transition energy from one electronic state X to another state B is changed by ΔE and/or ΔR.

The Born-Oppenheimer approximation is inherent in the separation of electronic and vibrational degrees of freedom and thus in the separation of dephasing processes. The motion of the electrons is fast compared to the nuclear motion in a molecule and therefore the electronic wave function can be calculated for a fixed set of nuclear parameters. This leads to the calculation of electronic potentials $V(R)$, having defined vibrational and rotational wave functions. The coherences of the density operator have the form $c_n c_m^* \mathrm{e}^{-\frac{\mathrm{i}}{\hbar}(\mathrm{E_n}-\mathrm{E_m})\mathrm{t}}$. States n and m can be vibrational levels on one electronic surface $V(R)$ of the molecule. If the coherence term vanishes, the process is called *vibrational* dephasing. In the same manner, state n can be a vibrational state on the electronic ground state, whereas state m is a vibrational level on an excited electronic state of a molecule. In that case, the loss of coherence is called *electronic* dephasing.

Figure 2.2 presents possible origins of vibrational and electronic dephasing. In panel a), the vibrational dephasing is sketched (the picture is adapted from Ref. [78]). The solid curve represents the molecular potential as it is deformed in some solvent. The vibrational eigenstates of the potential shall have an energy spacing of ν_1. If a relative motion between molecule and solvent atoms occurs, this potential energy surface will be disturbed (dashed line). As sketched here, the effective intramolecular potential gets steeper and the vibrational spacing ν_2 bigger than ν_1. This leads to a disturbance (dephasing) in the coherence of the vibrational levels n and m, since the energy difference[3] $(E_n - E_m)$ between the vibrational levels n and m shows up in the coherence $c_n c_m^* \mathrm{e}^{-\frac{\mathrm{i}}{\hbar}(\mathrm{E_n}-\mathrm{E_m})\mathrm{t}}$. Thus, the wave packet will lose coherence and interference of vibrational levels will decay. As a consequence, the probability density loses its localization in phase space according to the classical dephasing in Fig. 2.1b. The effect can also be formulated in semi classical terms: the wave packet propagates in a dynamical potential. The dynamics of the effective potential is statistical in an ensemble. A wave packet of a *single* molecule does not dephase at all. In an *ensemble* or time-averaged experiment the averaged wave packet structure will "smear out". The calculation in Ref. [78] is done in exactly that way: a quantum wave packet is propagated on a dynamical potential that is calculated by classical interaction with the environment. The final result is averaged over many wave packet propagations.

In case of the electronic dephasing (Fig. 2.2b), the relative energy or/and equilibrium poten-

[3] Between two neighboring levels, the difference is called ν in Fig. 2.2.

tial distance of two effective electronic surfaces of the molecule in the solvent (denoted by X and B) changes; however, without an alternation of the potential energy surface shape. This is again induced by relative molecule-solvent motions. The energy difference between two levels, one of which is on ground and the other one on the excited state, is changed. The interference (due to the coupling by a light pulse) is changed and the interference term vanishes analog to vibrational dephasing. The deformations on the upper state surface shown in Fig. 2.2a also destroys electronic coherence, since the upper vibrational levels are shifted. In contrast, the shift ΔR and/or ΔE does induce electronic dephasing but *no* vibrational dephasing, since the relative energies of the vibrational levels in the excited electronic state are not changed.

2.2 Dispersion and revivals in Morse oscillators. Focusing with chirped light pulses

The connection of quantum and classical mechanics is given by the Ehrenfest theorem. It allows for prediction of the expectation values of general conjugate coordinates q and p, which are usually position and momentum:

$$\begin{aligned} \frac{d\langle q\rangle}{dt} &= \frac{\langle p\rangle}{m}, \\ \frac{d\langle p\rangle}{dt} &= \langle -\frac{dV}{dq}\rangle \doteq -\frac{dV(\langle q\rangle)}{d\langle q\rangle}. \end{aligned} \tag{2.9}$$

These are formally very similar to the classical equations of motion. It can be shown, that the relation with a dot over the equality holds true for linear and quadratic potentials $V(q)$. For a harmonic (quadratic) potential, the width in momentum and coordinate of a wave packet at a fixed position q or p does not change with time [6, 73].

In case of anharmonic oscillators, a broadening of the wave packet (dispersion) in phase space occurs even for free molecules with perfect coherence. One of the most prominent examples for dispersion is the broadening of a wave packet on a constant potential (see standard quantum mechanics textbooks like Refs. [124, 125]). Another prominent example is the Morse potential. Because of its special quantum structure, the dispersion is reversible and so called "revivals" occur (section 2.2.3).

2.2.1 Morse potential

The Morse potential is a standard way to parameterize a molecular potential of a diatomic [53, 126]. A Morse potential V as a function of the internuclear distance R is given as:

$$V(R) = D_e(1 - e^{-\alpha(R-R_e)})^2, \tag{2.10}$$

with

$$\alpha = \sqrt{\frac{\mu}{2D_e}}\omega_e \tag{2.11}$$

$$D_e = \frac{\hbar\omega_e}{4x_e}, \tag{2.12}$$

where D_e is the dissociation energy, R_e the equilibrium distance, ω_e the harmonic eigenfrequency and x_e the anharmonicity.

The classical frequency ν of a trajectory started with energy E in a Morse oscillator is given as:

$$\nu(E) = \frac{\omega_e}{2\pi}\sqrt{1 - \frac{E}{D_e}}. \tag{2.13}$$

Considering this expression, it is immediately clear, that an ensemble of classical trajectories representing a "classical wave packet" will disperse. The trajectories in the ensemble having a high vibrational energy E ("blue" ones) have a lower oscillation frequency than the low energy ("red") parts. Therefore, the trajectories excited in the red are at later time located at another internuclear distance than the trajectories excited in the blue part of the oscillator. Fig. 2.3 gives a pictorial interpretation of the dispersion with the help of quantum mechanics. In panel a), the frequency-time distribution of an unchirped excitation pulse is shown. The pulse starts all the components of the wave packet at the same time. As depicted in Fig. 2.3b, the vibrational spacing ν is much larger in the low energy range of the Morse oscillator than in the high energy range. Therefore, parts of the wave packet excited at low energies will oscillate faster than those excited at high energies (as in the classical trajectory analogue). Once more, this leads to the spreading of the wave packet due to different oscillation periods as a function of vibrational energy in the Morse oscillator. The quantization is not needed in the calculation of dispersion. Even in pure quantum calculations, the time domain of dispersion is often called the classical domain [68]. The dispersion time T_{disp}, that is the time until the wave packet has completely lost its initial localization, fulfills the following equation (see appendix Eq. (14)):

$$T_{\mathrm{disp}} = \frac{\nu}{\omega_e x_e \Delta E}, \tag{2.14}$$

where ΔE is the full spectral width of the wave packet and ν the central vibrational frequency.[4] In case of no anharmonicity $\omega_e x_e = 0$ (harmonic oscillator) no dispersion occurs and thus T_{disp} goes to infinity. The bigger the anharmonicity, the faster the wave packet broadens due to dispersion. The $1/\Delta E$ proportionality in Eq. (2.14) can be explained via the extremes: in case of a monochromatic excitation, all trajectories have absolutely the same energy and will not show any broadening due to dispersion. In a broadband excitation, the oscillation frequency difference between the upper (blue) and lower (red) trajectories scales with the width of the excitation source and the dispersion time decreases. It is nevertheless possible to compensate for the dispersion by special excitation pulses.

2.2.2 Focusing of wave packets

A compensation scheme is depicted in Fig. 2.3. As shown in the last section, the red components of a wave packet or classical ensemble oscillate faster than the blue ones. Now one starts the slower oscillating blue components earlier than the red ones (see Fig. 2.3d) by a specially tailored laser pulse shown in Fig. 2.3c. The instantaneous optical frequency of the pulse is described by a linear function in time. The blue components arrive at the molecule earlier than the red ones. Such a pulse is negatively linear chirped (section 4.3.2). The red components will have caught up with the blue components after a time T_{opt}, which will be called the *focusing time*.

A detailed classical analysis in the appendix (Eq. (23)) leads to an expression for the focusing time T_{opt}:

$$T_{\mathrm{opt}} = -\frac{\beta' \nu^2}{4\pi\omega_e x_e}, \tag{2.15}$$

where $\beta' = \frac{\beta(\nu)}{c}$ is the chirp parameter in units of fs cm, ν is the oscillation frequency at the wave packets center in cm^{-1} and $\omega_e x_e$ the respective molecular constants of the Morse oscillator (see Eq. (2.11)). The chirp parameter will be introduced properly in section 4.3.2. The

[4] For reasons of convenience, all units shall be given in cm^{-1}.

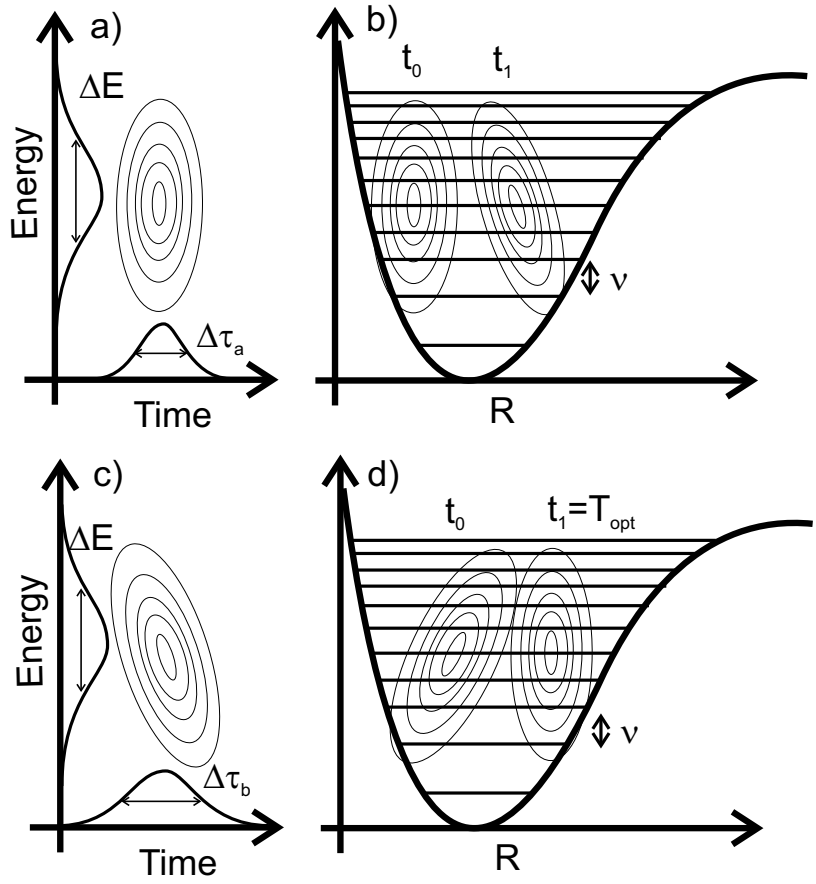

Figure 2.3: Dispersion and focusing of a wave packet. The wave packets are shown when propagating in direction from left to right. a) Equal intensity line plot of a light pulse frequency-time distribution for an unchirped laser pulse. b) Wave packet travelling from left to right at time t_0 (at excitation) and at some later time t_1. At t_0, all parts of the wave packet are located at the same internuclear distance, whereas the dispersion has caused a tilt in the wave packet distribution at time t_1. c) A negatively chirped pulse in the equal intensity line plot. The blue components arrive earlier at the molecule than the red ones. d) Wave packet excited with the pulse from c) at t_0 . The slowly oscillating high energy components of the vibrational wave packet are excited earlier than the faster oscillating low energy components. At T_{opt}, the low energy components will have caught up with the high energy components that were excited earlier. The wave packet is perfectly localized (focused).

larger the chirp parameter, the stronger is the tilt of the laser pulse frequency-time distribution in Fig. 2.3c.[5]

The focusing scheme was theoretically worked out in Refs. [82, 127] and applied successfully to free I_2 molecules [80] and to I_2 in solid Kr [83], however with a small contrast in the latter case due to the small anharmonicity of the system. One aim of this thesis is to use the focusing of a vibrational wave packet to disentangle dispersion (the reversible broadening of a wave packet in a Morse oscillator) and dephasing. The method will be presented in section 2.3.3.

The dispersion was described classically here, but it once more occurs in a quantum description of the Morse oscillator. It will turn out, that the broadening due to dispersion is reversible and a revival of the wave packet occurs. Besides, not only revivals of the fundamental oscillatory frequency appear, but also high harmonics of the fundamental frequency show up.

2.2.3 Fractional revivals

The phenomenon of fractional revivals, explored theoretically in Refs. [67–75] relies on the distinct spacing of quantum levels (which is often referred to as *first quantization*).

The quantum energy of levels in a Morse oscillator can be written as:

$$E_n = \hbar\omega_e(n+\frac{1}{2}) - \hbar\omega_e x_e(n+\frac{1}{2})^2, \tag{2.16}$$

The standard literature often uses another formula for the energy in an anharmonic oscillator given by: $E_n = \hbar\omega_e(n - x_e n^2)$ [70, 71]. This predicts the correct revival times, however the oscillation periods T of the wave packet are wrong neglecting the zero point energy terms.

In agreement with Refs. [70, 71] the *autocorrelation function* $P(t)$ of a vibrational wave packet is used to explain the revival phenomenon in simple terms. It is given by:

$$\begin{aligned} P(t) &= \langle\Psi(R,t)|\Psi(R,t=0)\rangle \\ &= \sum_n |c_n|^2 \exp(-i\frac{E_n}{\hbar}t), \end{aligned} \tag{2.17}$$

when using Eq. (2.1) in its R representation. The absolute square of the autocorrelation function is the *survival function* $S(t)$, which mimics a pump-probe spectrum when one probes the wave packet at the inner turning point, since it was initially created there as $\Psi(R, t=0)$. When using the autocorrelation function as given in 2.17, the survival function $S(t)$ is given as:

$$S(t) = |P(t)|^2 = \sum_{m,n} |c_m|^2|c_n|^2 \exp(i\frac{E_m - E_n}{\hbar}t), \tag{2.18}$$

with the populations and coherences of the density operator included here. First of all, a two-state system will be discussed. The state j and $j+1$ shall be populated with weights $|c_j|^2$ and $|c_{j+1}|^2$. The autocorrelation function (2.17) reads like:

$$P(t) = |c_j|^2 \exp(-i\frac{E_j}{\hbar}t) + |c_{j+1}|^2 \exp(-i\frac{E_{j+1}}{\hbar}t).$$

Therefore, the survival function is given as:

$$S(t) = |c_j|^4 + |c_{j+1}|^4 + 2|c_j|^2|c_{j+1}|^2 \cos(\frac{E_{j+1} - E_j}{\hbar}t).$$

[5] A short example shall be given here: A laser pulse has a chirp of $\beta' = -1.78$ fs cm. The molecular vibration ν at an excitation energy of 570 nm in the Br_2 B state is 118 cm^{-1} and $\omega_e x_e = 1.6361$ cm^{-1}. This leads to a T_{opt} of 1.2 ps.

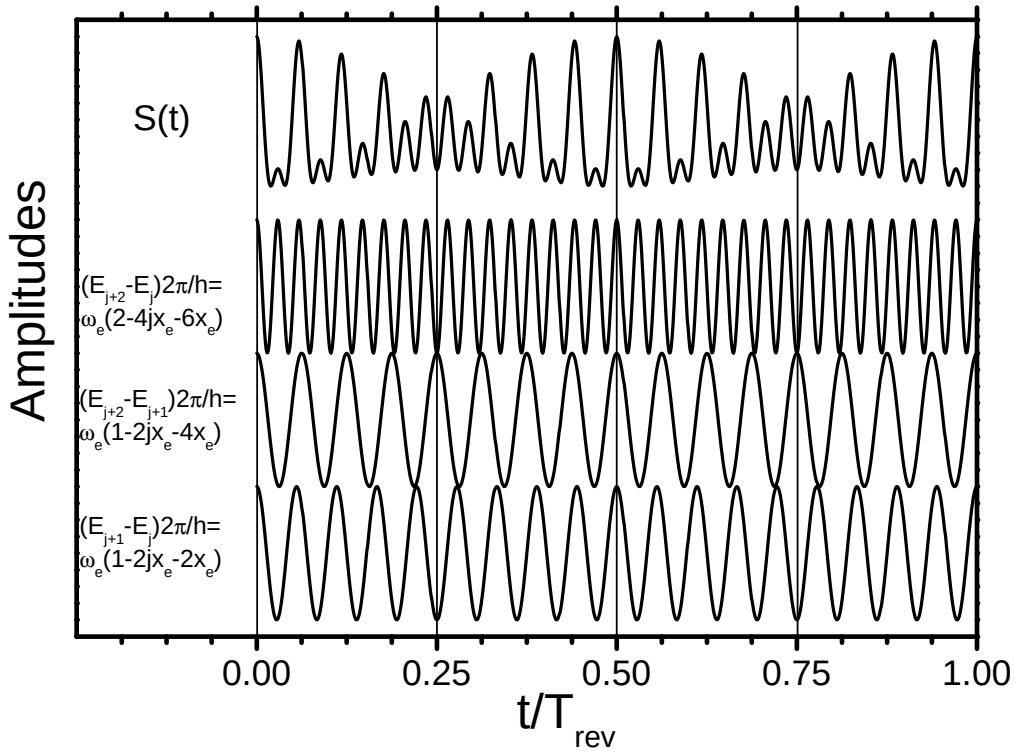

Figure 2.4: Model for quarter and half revivals. See text for details.

The energy difference using Eq. (2.16) is given as:

$$E_{j+1} - E_j = \hbar\omega_e(1 - 2x_e - 2x_e j). \tag{2.19}$$

Thus, the signal consists of a single cosine modulation that cannot be distinguished from a harmonic oscillator with angular frequency $\frac{E_{j+1}-E_j}{\hbar}$. The information about the anharmonicity is missing, since only one energy difference between two states is taken into account. The main feature of an anharmonic oscillator is the changing energy difference as a function of j.

Therefore, at least a three state system has to be considered to explain survival functions of a Morse oscillator. An additional level $j+2$ is added. The survival function looks like:

$$\begin{aligned} S(t) &= |c_j|^4 + |c_{j+1}|^4 + |c_{j+2}|^4 + 2|c_j|^2|c_{j+1}|^2\cos(\frac{E_{j+1}-E_j}{\hbar}t) + \\ & \quad 2|c_{j+1}|^2|c_{j+2}|^2\cos(\frac{E_{j+2}-E_{j+1}}{\hbar}t) + 2|c_j|^2|c_{j+2}|^2\cos(\frac{E_{j+2}-E_j}{\hbar}t). \end{aligned}$$

The angular frequencies $(E_{j+1} - E_j)/\hbar = \omega_e(1 - 2jx_e - 2x_e)$ and $(E_{j+2} - E_{j+1})/\hbar = \omega_e(1 - 2jx_e - 4x_e)$ (lower two curves in Fig. 2.4), that are quite close to each other and in addition a "doubled" angular frequency[6] at $(E_{j+2} - E_{j+1})/\hbar$ appears. The close lying components will produce a beat pattern, that has to be analyzed. A node in the beating occurs, when the two arguments in the cosine functions have a shift of $\pi(2n+1), n = 0 \cdots \infty$. The condition reads: $((E_{j+1} - E_j)/\hbar)t_{\min} = ((E_{j+2} - E_{j+1})/\hbar)t_{\min} + \pi(2n+1)$. Using Eq. (2.19), the calculation

[6] It is a bit less than the doubled of the first frequency because of the anharmonicity.

leads to:

$$t_{\min} = T_{\rm rev}\frac{2n+1}{4}, \tag{2.20}$$

introducing the so called *revival time* $T_{\rm rev}$

$$T_{\rm rev} = \frac{2\pi}{\omega_e x_e}. \tag{2.21}$$

At $t_{\min} = T_{\rm rev}/4$ and $3T_{\rm rev}/4$ described by Eq. (2.20), the doubled frequency $(E_{j+2}-E_{j+1})\hbar$ can be effectively probed in $S(t)$ as shown in Fig. 2.4 because the cosine contributions with frequencies $(E_{j+1} - E_j)/\hbar$ and $(E_{j+2} - E_{j+1})/\hbar$ cancel each other. At $T_{\rm rev}/2$, a pattern of regular vibrational period can be observed. This is due to the fact, that the two frequencies producing a node at $t_{\min}$ generate an antinode at $2t_{\min}$. This pattern is called half revival. The peaks occur at a position where one should classically observe minima, as can be seen at $S(t)$ in Fig. 2.4, when marking every second peak from the beginning. A simulated pump-probe spectrum is shown in Fig. 2.12a with the fractional revivals marked.

To observe a so called 1/6 revival, which will be relevant in the experiments, one needs to take *four* levels into account. Otherwise the threefold vibrational frequency associated to the 1/6 revival cannot be observed. At t=$T_{\rm rev}$/6, $T_{\rm rev}$/3, 2$T_{\rm rev}$/3 and 5$T_{\rm rev}$/6, one third of the classical oscillation period will be observed in $S(t)$. This already provides a method to determine coherences among distinct vibrational levels (applied in section 8.2.2). If one observes for example the 1/6 revival in a pump-probe spectrum, at least four vibrational levels are coupled coherently. In agreement with the coherence definition in section 2.1, it indicates that the off-diagonal element $(j, j+3)$ of the density matrix being $c_j c^*_{j+3} \mathrm{e}^{-\frac{\mathrm{i}}{\hbar}(\mathrm{E_{j+3}-E_j})\mathrm{t}}$ has not yet dephased.

In a general theory [6, 67, 73], one expands E_n in a Taylor series around $E_{\bar{n}}$: $E_n = E_{\bar{n}} + \frac{\partial E}{\partial \bar{n}}(n-\bar{n}) + \frac{1}{2}\frac{\partial^2 E}{\partial \bar{n}^2}(n-\bar{n})^2$, neglecting the higher order terms and using the relation 2.16 for the anharmonic oscillator energies. Setting $k = (n - \bar{n})$, one can write the wave packet as:

$$\Psi(R,t) = \sum_k |c_k|^2 \exp(-2\pi i(k\frac{t}{T} + k^2\frac{t}{T_{\rm rev}})), \tag{2.22}$$

with $T = 1/\nu_{cl} = h(\frac{dE}{dn})^{-1}$, the local oscillation period and $T_{\rm rev} = 2h(\frac{d^2E}{dn^2})^{-1} = \frac{2}{h}(\nu_{cl}\frac{d\nu_{cl}}{dE})^{-1}$ the revival time.

When t/$T_{\rm rev}$= m/n, where m/n is a fraction of two mutually prime integers, the differences in the phases of the eigenfunctions are stationary. In this case, the wave packet can be represented as:

$$\Psi(R,t) = \sum_{s=0}^{l-1} a_s \Psi_{\rm cl}(R, t + \frac{s}{l}T), \tag{2.23}$$

where

$$\Psi_{\rm cl}(r,l) = \sum_{k=-\infty}^{\infty} c_k \phi_k(R) \exp(-2\pi i k\frac{t}{T}). \tag{2.24}$$

The parameter $l = n/2$ in the case where n is divisible by 4 or otherwise $l = n$. The open question in Eq. (2.23) is, how many of the coefficients a_s are zero? It can be shown, that r replicas of the $\Psi_{\rm cl}$ exist, with

$$\begin{aligned} r &= l \text{ if n} \bmod 4 \neq 2 \\ r &= \frac{l}{2} \text{ if n} \bmod 4 = 2. \end{aligned} \tag{2.25}$$

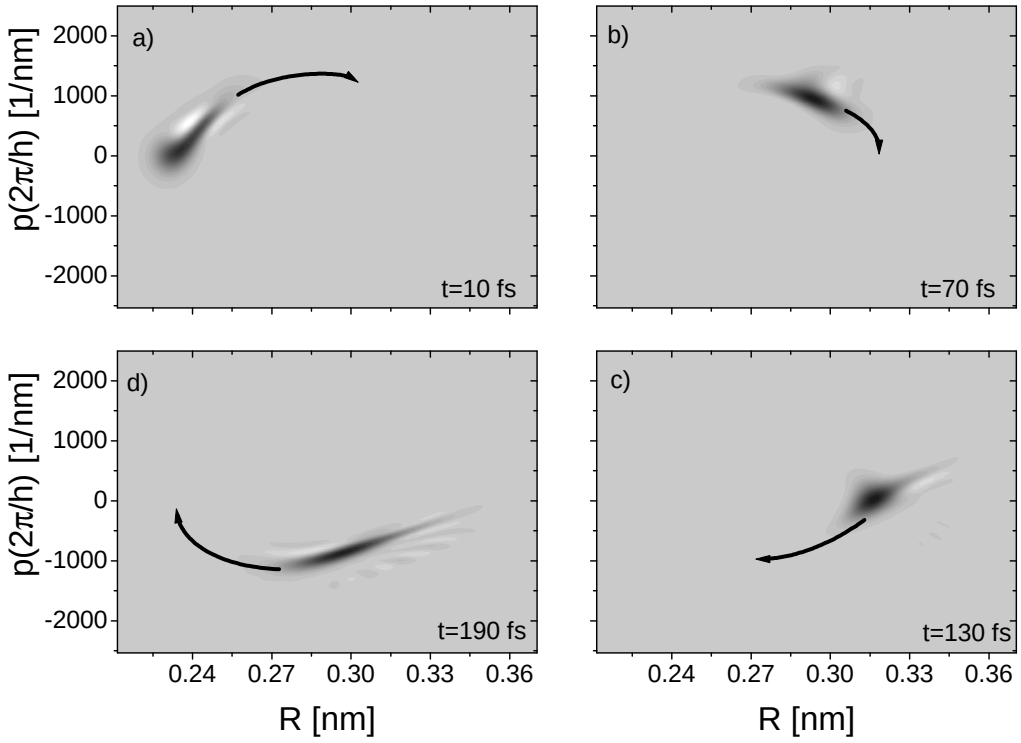

Figure 2.5: Wigner function of a wave packet in a Morse oscillator. The potential parameters are adapted from the free Br_2 molecule [53]. Shown is the vibrational wave packet a) shortly after excitation, b) on the way to the outer turning point, and c) at the outer turning point 130 fs after creation on the potential. In d), the dispersive broadening can be observed.

With the values of the electronically excited B state of Br_2, $\omega_e = 167.6$ cm^{-1} and $x_e = 9.7610^{-3}$ [53] the revival time is T_{rev} = 21.08 ps. Fractional revivals can be observed in all kinds of anharmonic potentials (*e.g.* vibrational [35, 69–74, 128, 129], rotational [130–133] and Rydberg [134] revivals.). The Morse oscillator is conceptually very easy due to its vanishing higher order anharmonicity.

The Wigner transformation to phase space introduced in Eq. (2.7) provides an ideal tool to visualize the properties of fractional revivals. Wigner functions can be calculated from the propagated wave function in the program described in the appendix and using the definition in Eq. (2.7). The Wigner function of a wave packet in a harmonic potential without dissipation would travel in a circle on isoenergetic rings in phase space, as demonstrated in Fig. 2.1a. In an anharmonic oscillator, it travels on egg-shapes isoenergetic surfaces (see Fig. 2.5). The Fig. 2.5 shows also how the wave packet disperses even in the first oscillation period. The wave packet in the quantum mechanical calculation splits in sub-structures after a distinct time, which are mathematically described by Eqs. (2.23) and (2.24). The revival structure can be perfectly observed in the Wigner representation, as Fig. 2.6 shows.

The calculation for this Fig. 2.6 uses the same molecular parameters as for Fig. 2.5. In Fig. 2.6a, the almost undispersed wave packet is shown at the outer turning point of the anharmonic potential (the B state of Br_2 is chosen here). In Fig. 2.6b, the Wigner function at $T_{\mathrm{rev}}/8$ is shown. One observes four sub-wave packets (A,B,C,D) that interfere with each other. The sub-structures are visible better in c) and d), where the 1/6 and 1/4 revival are shown. Especially

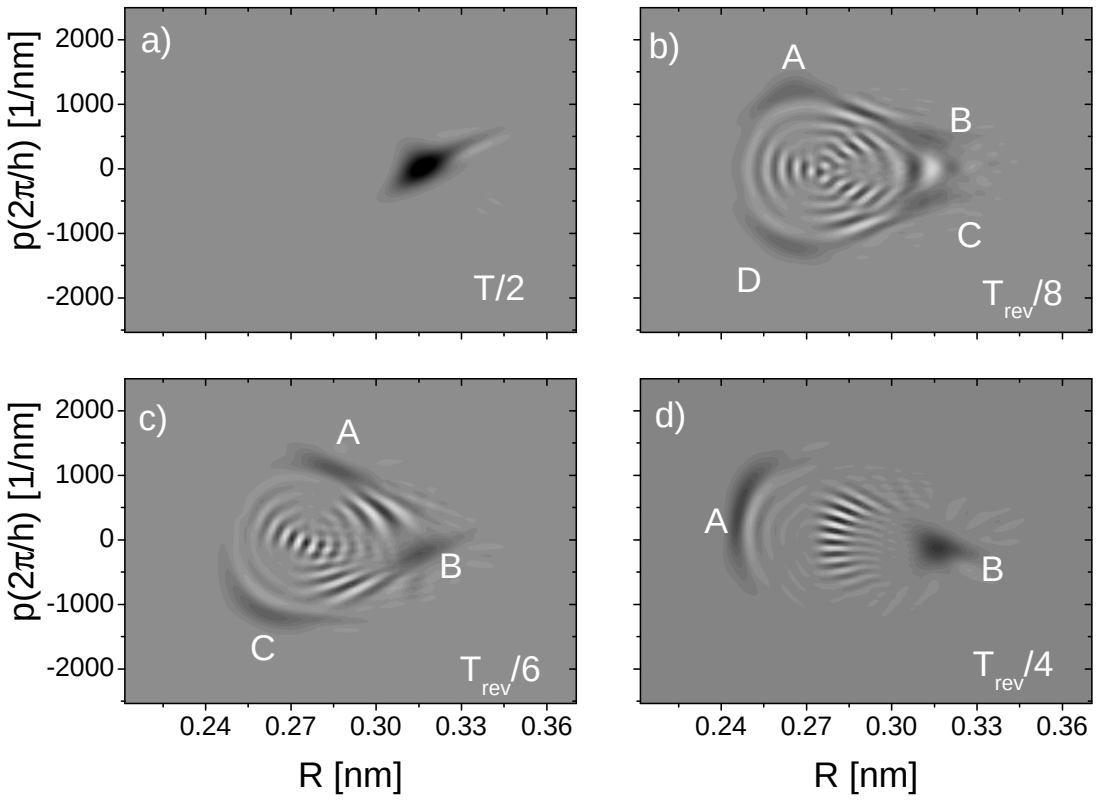

Figure 2.6: Wigner functions of fractional revivals, positive values are plotted dark, negative values light. a) Shows the wave packet $T/2$ = 130 fs after excitation. The wave packet shows no interference structure. In the course of time, the packet broadens and splits into sub wave packets according to Eqs. (2.23) and (2.24) that travel on isoenergetic lines. b) At $T_{\rm rev}/8$, the splitting into four wave packets with interferences among them is shown. The wave packet maxima are denoted A,B,C and D. c) At $T_{\rm rev}/6$, the splitting into three wave packets A,B and C with interferences can be observed. d) Two substructures A,B which interfere pattern in the middle can be observed at the quarter revival occurring at $T_{\rm rev}/4$.

in Fig. 2.6d, the doubling of the frequency for the 1/4 revival is easy to understand: two wave packets exist, that travel on isoenergetic lines in phase space. The interference structure in the middle shows their coherence.

To allow for a comparison with experiments, the Wigner functions shown in Fig. 2.6 have been projected onto the internuclear coordinate R (usually called q in phase space). This results in the squared wave packet on the R coordinate. Fig. 2.7 shows the probability distribution as a function of internuclear distance R and time t. In Fig. 2.7a, the first excursions of the wave packet are shown. No spatial interference structure is visible on the first outward motion of the vibrational wave packet, since the wave packet does not yet "know" about the bound character of the Morse potential. The argument uses a picture of wave packets developed by E. Heller [135–138]. The appearance of spatial interference structures is indicative for a quantum system. If one would simulate the dynamics with classical trajectories, these interferences would be missing. This is a further indication for a *coherent quantum system* besides the fractional revival structures.

The 1/8, 1/6 and 1/4 revival structures appear in Fig. 2.7b, c, and d respectively. Recording the wave packets probability at a fixed internuclear distance R, one observes high harmonics of the fundamental period. However, the exact frequency pattern depends strongly on the choice of R, since the spatial nodal structures modify the frequency pattern. This was the topic of a recent study by V. Engel and coworkers [74] and will be exemplified on a 1/4 revival in section 2.3.4. The possibility to detect the wave packet probability as a function of R and t will be explored in section 2.3.1.

2.2.4 Nomenclature for dephasing, decoherence and dispersion

The word "dephasing" is used in different contexts depending on the scientific community. In the quantum optics and revival literature, dephasing is often used for processes, in which phase information is not irreversibly lost but rather the discrete quantum system shows a broadening of the wave packet due to the propagation on an anharmonic potential (see for example [6, 69–71]). In other references, dephasing appears for the irreversible loss of phase information due to the interaction with a statistical bath [73, 121, 122].

In this work, the term dispersion will be used for the broadening of a wave packet due to propagation effects on anharmonic potentials with no phase information loss. The term dephasing is used to describe the irreversible loss of phase information or coherence throughout. The term decoherence is used as a synonym for dephasing.

2.3 Pump-probe spectroscopy

The femtosecond pump-probe method allows one to study ultrafast processes on electronically excited states of molecules. It was applied to many systems in pure gas phase (see for example the references from the Zewail group on ICN [139–142], NaI [143–145] and I_2 [146]). Furthermore this method has been applied to molecules (specially to iodine) in buffer gases [76, 147, 148], liquids [23, 149, 150] and solids like rare gas crystals [21–25, 81, 83, 86] or zeolite [151–154].

Here, a pump-probe scheme detecting the Laser Induced Fluorescence (LIF) of an excited electronic state versus the pump-probe delay Δt is applied. Apart from recording a fluorescence, one can also use the excited state absorption as a signature of the wave packet. The setup is exactly the same. Instead of recording the LIF one records the absorption of the probe pulse as a function of time [155, 156]. In the gas phase, one might probe to ionic states and use the ions instead of the LIF [157].

Furthermore, the pump-probe spectroscopy performed here is sensitive to *vibrational* coherence only, since the probe pulse interrogates the absolute square of a *vibrational* wave packet

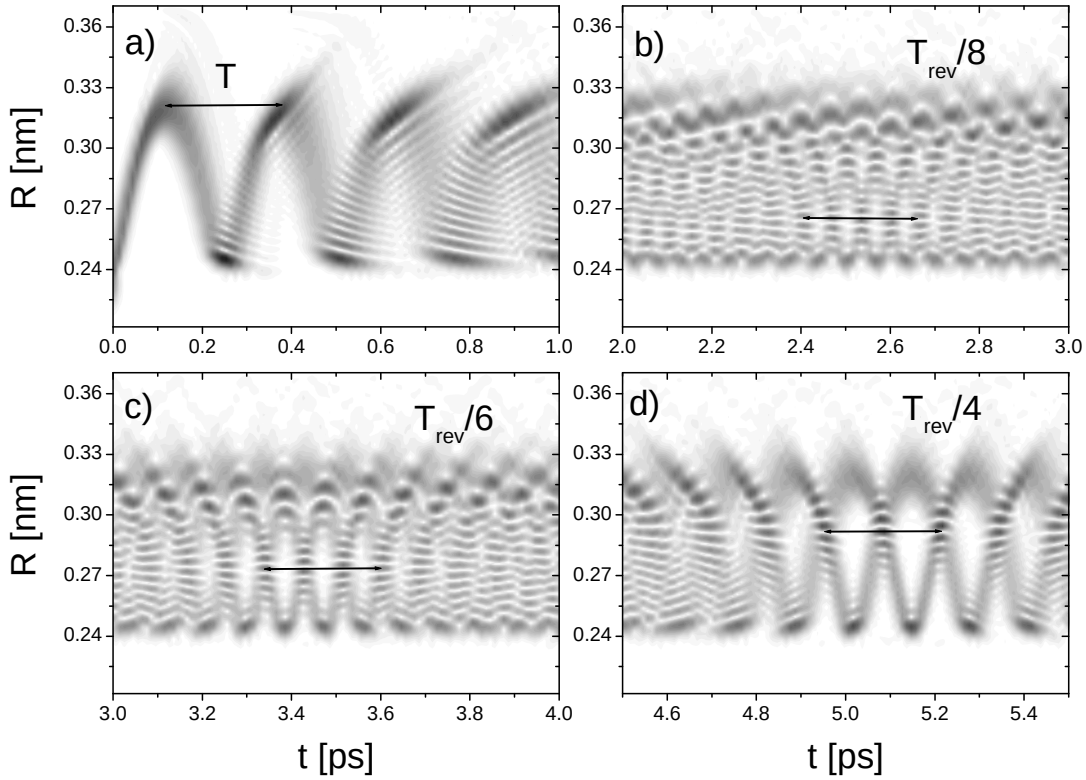

Figure 2.7: Fractional revivals of the Br_2 B state. Shown is the absolute square of the wave packet as a function of R and t. a) The beginning of the wave packet propagation. b) The 1/8 revival, c) the 1/6 revival d) the 1/4 revival observing.

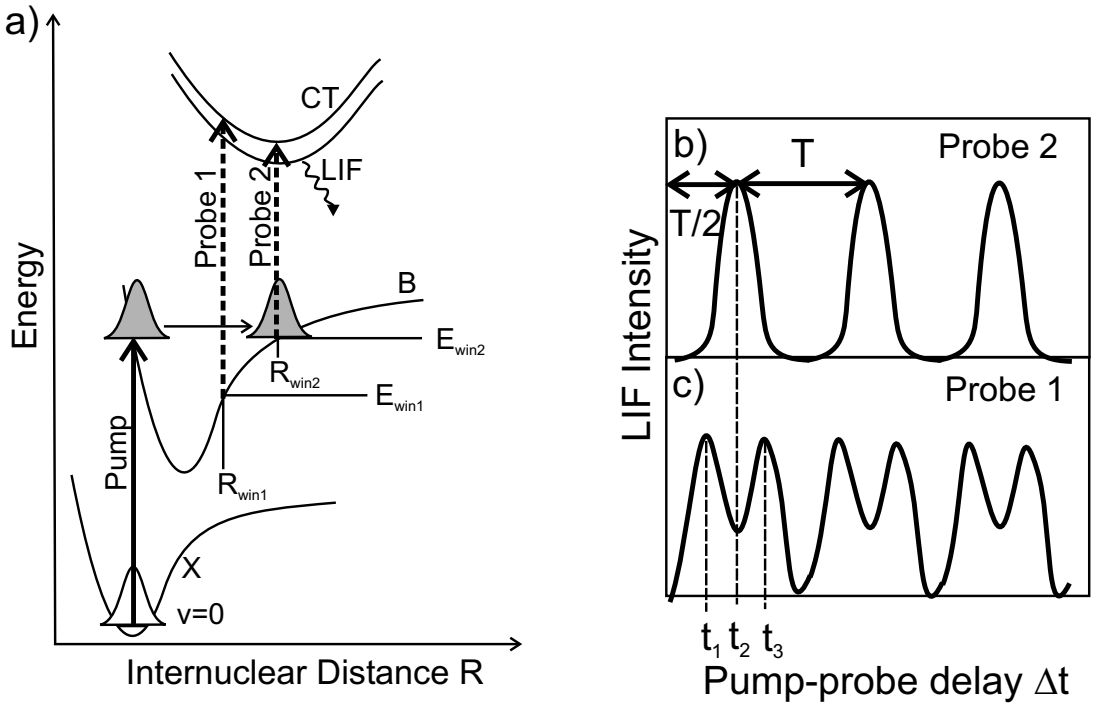

Figure 2.8: a) Pump-probe scheme. The pump pulse transfers population from the electronic ground state $v = 0$ level (higher v not populated see text) to the excited electronic B state (or any other covalent state) and excites several vibrational levels coherently. The created wave packet evolves in the potential as described in section 2.2. The fs probe pulse transfers parts of the wave packet to a Charge-Transfer state (CT) after a time delay of Δt. The population on the charge-transfer states relaxes to the lowest of the CT manifold and fluoresces (LIF). The fluorescence is detected as a function of the pump-probe delay Δt. Two different probe conditions are shown: Probe pulse 2 interrogates the wave packet at the outer turning point, whereas probe pulse 1 has a higher quantum energy and probes the wave packet closer to the potential minimum (see text). b) Pump-probe spectrum for Probe 2: The distance of the maxima in the pump-probe spectrum reflects the oscillation period of the wave packet. c) Pump-probe spectrum for Probe 1, the maxima of b) split into two maxima (explanation see text).

on an excited covalent state. This is in gross opposition to ultrafast schemes using *electronic* coherences like CARS [158] or PLPP [159, 160]. In case of long pump pulses, the electronic coherence is involved here (section 8.2.3).

2.3.1 Pump-probe method

Two ultrafast laser pulses are needed to perform the pump-probe spectroscopy. A first pump pulse excites a superposition of vibrational eigenstates on an electronic potential, thereby triggering a wave packet motion on the internuclear coordinate R (exemplified on the B state here). A second time delayed probe pulse interrogates this dynamics. Its transition is fixed to a certain value in the internuclear coordinate R_{win} and only if the wave packet has reached this R_{win} in its propagation, a probe signal is generated.

At temperatures used in the experiments described here (typically around 20 K), most of the molecular population is located on the ground vibrational level.[7] An ultrashort pump pulse induces an optical transition between the electronic ground state $v = 0$ level and an excited

[7] Applying Boltzmann statistics to the vibrational levels of the electronic ground state of I_2 with ω_e = 214 cm^{-1} leads to about 10^{-7} in $v = 1$ compared to the $v = 0$ population at 20 K. In Br_2 the population in the higher levels is even less because of the bigger ω_e of 325 cm^{-1}.

electronic state surface (B state in Fig. 2.8). Since the ultrashort pump-probe pulse is spectrally broad, a coherent vibrational wave packet is created on the excited electronic state. The wave packet propagates as described in the previous section 2.2 (see Fig. 2.8).

The propagating wave packet is interrogated by a second time delayed ultrashort pulse called the probe pulse. Here, the probe pulse induces a transition from the electronic B state to a Charge-Transfer (CT) state. The internuclear distance at which the probe pulse can catch the wave packet and propagate it to the CT state is called R_{win}, and will be determined shortly. If the wave packet has reached R_{win} in its propagation and the probe pulse acts on the molecule at the same time, the wave packet will be propagated to the CT state. The fluorescence (LIF) of the lowest CT state can be detected by a photomultiplier. If the probe pulse acts on the molecule at a distinct time and the wave packet is not located at the probe window R_{win}, the wave packet will not be excited to the charge-transfer state and thus no Laser Induced Fluorescence (LIF) will occur.

The actual value for R_{win} follows from the difference potential $\Delta V(R)$ of the B and CT states and the probe wavelength λ_{probe}. The condition is first formulated for the classical outer turning point R_{win2} of the vibrational wave packet (Probe 2 in Fig. 2.8a). What is the right probe wavelength λ_{probe} to induce the transition? At the outer turning point, the expectation value of the wave packets momentum is equal to zero. Momentum has to be conserved in the probe transition. Therefore, the wave packet created by the probe pulse on the CT state has to be excited with zero momentum. It can only have a zero momentum when excited with no excess kinetic energy in the CT state. This is the case when the quantum energy of the probe pulse hν_{probe}=hc/λ_{probe} matches the potential energy difference between the B and CT states at the outer turning point of the wave packet:

$$\frac{hc}{\lambda_{\mathrm{probe}}} = \Delta V(R_{\mathrm{win}}) \tag{2.26}$$

The pump-probe spectrum recorded at R_{win2} is shown in Fig. 2.8b. At zero delay (Δt = 0) between pump and probe pulse, no wave packet has arrived at R_{win2}, therefore no population is transferred to the CT state and no LIF is created. If the delay between the pump and probe pulse Δt is equal to half a vibrational period ($T/2$), the wave packet is located at the probe position. A maximal amount of population is transferred to the CT state and a maximum in the pump-probe spectrum occurs. Furthermore, a maximum can be found at a delay which is one vibrational period T longer, since the wave packet is once again located at the outer turning point at that time. One can read the vibrational period T from the distance of the maxima in the pump-probe spectrum. This fact will be used to construct a potential energy surface in section 8.1.2. The wave packet is excited at different vibrational energies and is always probed at the outer turning point by changing λ_{probe}. From the different vibrational periods $T(E)$ as a function of excitation energy E, a potential energy curve can be constructed with the RKR algorithm [161–163]. It is important to note that only the position of the maxima in the pump-probe spectra will be analyzed. The general shape of the peaks will not be taken into account for potential construction.

Now, the vibrational wave packet should not be probed at the outer turning point but closer to the potential minimum as depicted by the arrow Probe 1 (dashed) at R_{win1} in Fig. 2.8a. At this internuclear distance, the wave packet carries a non vanishing momentum and kinetic energy expectation value $\langle E_{\mathrm{kin}} \rangle$. The momentum has to be conserved in the probe transition as in the first case. Thus, the wave packet excited in the CT state during the probe transition at R_{win1} should have the same amount of kinetic energy $\langle E_{\mathrm{kin}} \rangle$ as a wave packet in the B state. The energy conservation requires: $\langle E_{\mathrm{kin}} \rangle + hc/\lambda_{\mathrm{probe}} = \Delta V(R_{\mathrm{win1}}) + \langle E_{\mathrm{kin}} \rangle$. After subtracting

$\langle E_{\mathrm{kin}} \rangle$ from both sides, the condition reads as Eq. (2.26). Therefore, the arrow Probe 1 is drawn from one potential surface to the other without including the kinetic energies. In the situation depicted in Fig. 2.8a, the probe wavelength has to be shortened when going from R_{win2} to R_{win1}.

The pump-probe spectrum recorded at R_{win1} shown in Fig. 2.8c looks more complicated than that at R_{win2}, nevertheless the same vibrational wave packet is assumed. The wave packet first passes the distance R_{win1}. This should happen at a time t_1. The signal at R_{win1} decreases again. At R_{win2}, the wave packet maximum is reached at a later time t_2. The wave packet then changes direction at the outer turning point and passes R_{win1} for a second time in this oscillation period at time t_3. The phenomenon of a peak splitting when probing between inner and outer turning point is called *vibrational splitting*. The time difference of maxima in Fig. 2.8c does not reflect the oscillation period in the potential.

The B state potential energy at R_{win} is called E_{win} as shown in Fig. 2.8a. The wave packet is said to be *probed at resonance*, if E_{win} is located at the central energy of the vibrational wave packet. The wave packet is probed at the outer turning point in case of probe resonance and T can be used to determine the potential (section 8.1.2). For Br_2:Ar, the molecular Br_2 electronic potentials are deformed and thus R_{win} and E_{win} are not accurately known. The resonance condition can however be determined with help of a systematic variation of λ_{pump} or λ_{probe} in pump-probe spectra. One keeps λ_{probe} constant and thus fixes R_{win} and E_{win}. Now the wave packet is successively excited with decreasing vibrational energy by reducing $h\nu_{\mathrm{pump}}$. The vibrational splitting visible for $h\nu_{\mathrm{pump}} > E_{\mathrm{win}}$ vanishes for $h\nu_{\mathrm{pump}} = E_{\mathrm{win}}$.

The time integrated pump-probe signal strength at R_{win1} and R_{win2} was compared in a classical study [164]. The wave packet travels through window R_{win1} with a high kinetic energy E_{kin} and thus with a high velocity v. The interaction with the probe pulse is short. In contrast, it stays at R_{win2} (the outer turning point) for a long time, allowing for a long interaction with the probe pulse. Thus, the time integrated signal probed at R_{win2} is larger than the spectrum probed at R_{win1}. This results in a strength of the probe transition scaling with the inverse velocity $1/v$ or $1/\sqrt{E_{\mathrm{kin}}}$ of the wave packet, where v and E_{kin} are determined at R_{win} [164]. The resulting shape of the curve is shown in Fig. 2.9b.

A quantum mechanical interpretation of Eq. (2.26) and the shape of the probe transition intensity is sketched in Fig. 2.9. The classical probe condition Eq. (2.26) requires conservation of momentum. This is substituted by the Franck-Condon principle in the quantum formulation. A vibrational wave packet in the B state is centered at the level v_1'' (see Fig. 2.9a). It is probed at the outer turning point. The wave functions building up the packet are strongly peaked close to the potential limb. The probe transition obeys the Franck-Condon principle and the biggest overlap with the CT vibrational eigenfunctions has to be determined. The overlap is maximal, for eigenfunctions being peaked in the same range, as shown for the level v_1' on the CT state. The example shows, that the probe transition occurs from the potential edge on the B state to the CT state potential edge at R_{win} with transition energy $h\nu_{\mathrm{probe}} = \Delta V(R_{\mathrm{win}})$. This is in agreement with the classical formulation, since the momentum of the wave packet created on the CT state by the probe pulse is zero (and thus conserved). The intensity of the probe transition is given by all the Franck-Condon factors of the transitions $v' \longleftarrow v''$ being possible within the spectral width of the given probe pulse. It has a maximum at E_{win}, as as shown in Fig. 2.9b and decays below due to the vanishing Franck-Condon overlap.

The $1/v$ characteristics above E_{win} are not explicitly calculated here, but is illustrated in the following text. The wave packet is excited at higher energy in the B state centered around level v_2''. The wave packet is probed with the same pulse as in the situation above. The maximal overlap of vibrational wave functions is now achieved to level v_2' on the CT state. The window (dashed arrow in Fig. 2.9a) has the same R_{win} as above, since the upper vibrational

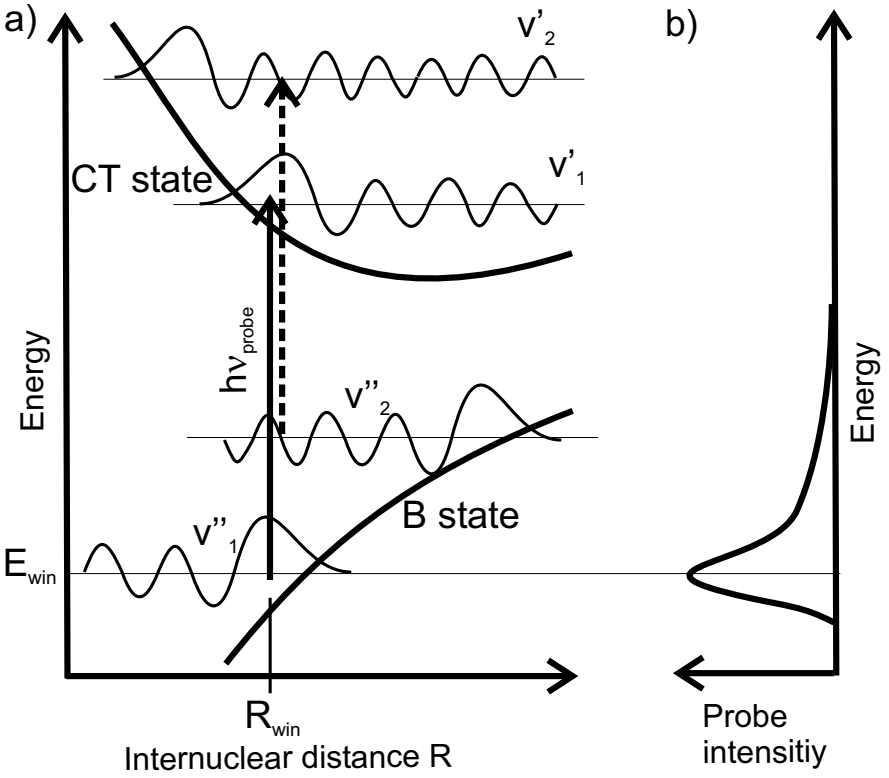

Figure 2.9: Franck-Condon picture for the probe transition. a) The solid arrow gives the probe transition for a wave packet at the outer turning point. For better visibility, only one eigenfunction v_1'' in the wave packet is shown. The Franck-Condon overlap is maximal for transitions to levels around v_1' on the CT state. The probe window is marked by R_{win} and E_{win} The dashed arrow gives the transition with the same probe pulse energy as before $h\nu_{\mathrm{probe}}$, however, the wave packet is excited above E_{win}. The wave function overlap to the CT state is still maximal at R_{win}, since there, the spatial oscillation period is the same for the levels coupled by the probe pulse. This is exemplified for the levels v_2'' and v_2'. b) The solid curve sketches the probe intensity. It mimics the Franck-Condon factors of the vibrational levels on the B and CT states coupled by a probe laser pulse of finite spectral width.

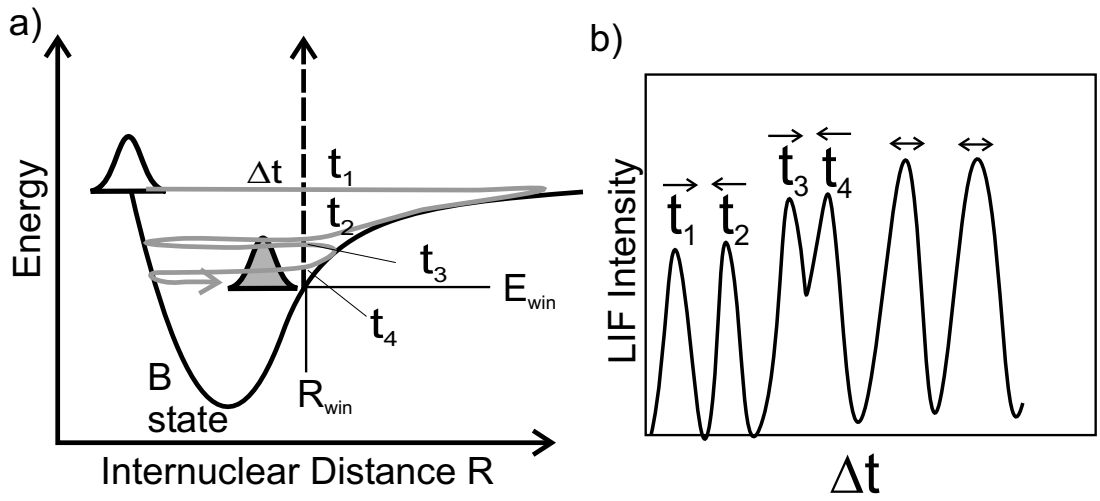

Figure 2.10: a) The vibrational wave packet is excited above the probe window energy E_{win}. It propagates to the outer turning point crosses R_{win} at t_1 and collides with the environment (matrix) there. It returns to the inner turning point with lowered energy and crosses R_{win} once more at t_2. Even in the second vibrational excursion, the wave packet's central energy is located above E_{win}, it crosses R_{win} at t_3 and t_4. After the second collision with the environment, the wave packet's central energy is located at E_{win}. b) Pump-probe spectrum of the dynamics depicted in a). The vibrational splitting during the first and second period vanishes in the third period due to vibrational energy relaxation. The arrows give the direction of the wave packet motion when detected at R_{win}

functions v' show the same spatial oscillation period as the lower one v'' in this range. Thereby, the Franck-Condon overlap is maximized. The spatial frequency corresponds to the kinetic energy and the quantum condition reduces once more to the classical momentum or to kinetic energy conservation. The probe transition intensity, is however smaller than the intensity at E_{win} (Fig. 2.9b). An exact calculation of the probe intensity curve sketched in Fig. 2.9b would require the Franck-Condon factors of the B and CT potential surfaces. Since the exact shape of the involved molecular electronic states in the matrix is not known, the calculation is skipped. The qualitative trend however is well established [86, 97, 164] and will be used in section 8.3.2 to explain the probe scheme of coherent phonons.

2.3.2 Vibrational energy relaxation in pump-probe spectra

The vibrational energy dissipation or relaxation of a vibrational wave packet due to the molecule-host interaction, that has been explained in section 2.1, can be quantified using the methodology explained above as shown in Fig. 2.10. The wave packet is initially excited above the probe window energy E_{win} (see Fig. 2.10a). After passing the probe window R_{win} at time t_1, it strongly interacts with the matrix, creates phonons, and thereby loses vibrational energy. The passage at time t_1 results in a first peak in the pump-probe spectrum shown in Fig. 2.10b. On the way from the cage region to the inner turning point, it is once again probed at t_2. The splitting t_2 - t_1 can be rather long. In the new oscillation of the vibrational wave packet another splitting of outward and inward motion occurs, since the total energy of the wave packet is still located above E_{win}. However, due to the energy loss in the first oscillation, the splitting t_4 - t_3 is smaller than t_2 - t_1. Finally, during the third excursion, the wave packets total energy has reached E_{win}. In the example presented here, the wave packet has lost its excess vibrational energy above E_{win} after two oscillation periods. The wave packet's initial energy and E_{win} are known, and the number of oscillations needed to relax to E_{win} are determined from the pump-probe spectrum. Thus, the

energy relaxation (dissipated energy per time) can be quantified. Furthermore the wave packet periods T get shorter when the wave packet relaxes to lower energies, due to the anharmonicity of the molecular state. The energy relaxation will be quantified with this scheme in section 8.1.3.

2.3.3 Method to determine the vibrational dephasing in a Morse oscillator

Dispersion and dephasing have the same apparent effect on the pump-probe spectra. In both cases, the wave packet dynamics are smeared out after some time. If the vibrational dephasing is too fast to see any fractional revivals, it will be impossible to disentangle dispersive effects from vibrational dephasing in a conventional pump-probe spectrum.

As introduced in section 2.2.2, the dispersion of a wave packet can be compensated at the focusing time T_{opt} by exciting the vibrational wave packet on the Morse oscillator by a negatively chirped pulse. The wave packet will reach its narrowest width with best modulation contrast at T_{opt}. The width at T_{opt} corresponds exactly to the initial width at Δt = 0 of a wave packet excited by an unchirped pulse.

Fig. 2.11a illustrates the probe process in phase space for no dephasing. The probe window is located at the outer turning point indicated by the dashed area. The vibrational wave packet is focused at T_{opt}. In a), it is located at the inner turning point. This position corresponds to a minimum in the pump-probe spectrum shown in b). No dephasing occurs and therefore, the vibrational wave packet can be focused perfectly to the width dictated by the excitation laser pulse. The minima in the pump-probe spectra in b) around $\Delta t = T_{\mathrm{opt}}$ will have no background. The case of finite vibrational dephasing is shown in Fig. 2.11c). The dephased parts of the initial wave packet do not focus, since the correct phase of the eigenstates (or in a classical picture the undisturbed position of a trajectory in phase space) is required for focusing. Even if the coherent vibrational wave packet is located at the inner turning point, a remaining population is probed at the outer turning point. Thus, the minima of the pump-probe spectrum in d) will show a background at $\Delta t = T_{\mathrm{opt}}$.

The variation of T_{opt} by the pump pulse chirp will allow for a systematic determination of the dephased background as a function of time and therefore to determine the vibrational dephasing time $T_{\mathrm{deph}}^{\mathrm{vib}}$ of the vibrational wave packet (see section 8.2.1).

2.3.4 Manipulation of fractional revival structures and their appearance in pump-probe spectra

Fig. 2.12a shows a pump-probe spectrum calculated for a vibrational wave packet on the electronic B state of a free Br_2 molecule (dispersion and no dissipation/dephasing). The 1/6 revival at T_{rev}/6, 1/4 revival at T_{rev}/4 and 1/2 revival at T_{rev}/2 are marked. The threefold, twofold, and fundamental vibrational frequencies occur in the respective time range. By excitation with a negatively chirped probe pulse, the vibrational wave packet is focused at T_{opt}. The time zero of Fig 2.12a is now located at the positive focusing time T_{opt}, determined by the laser chirp and molecular anharmonicity. Therefore, the fractional revival structures will be advanced in time to T_{rev}/q+T_{opt}, where q denotes the order of the revival. The case of a positively chirped pump pulse is shown in the simulation in Fig. 2.12c. Again, one can calculate T_{opt} (Eq. (2.15)), which will be negative, since the chirp β' is positive. The time zero of Fig. 2.12a is shifted to "negative" times in the pump-probe spectrum shown in c). The revival structures are advanced accordingly in time to T_{rev}/q+T_{opt}, where T_{opt} is the *negative* focusing time.

One can think about this scheme in terms of compensation and addition of molecular dispersion by laser pulse dispersion (chirp). The *positive dispersion* of the wave packet on a molecular state can be compensated by a *negatively dispersed* laser pulse with negative chirp, which leads to focusing. In the same way, parts of the *positive dispersion* can also be transferred into the

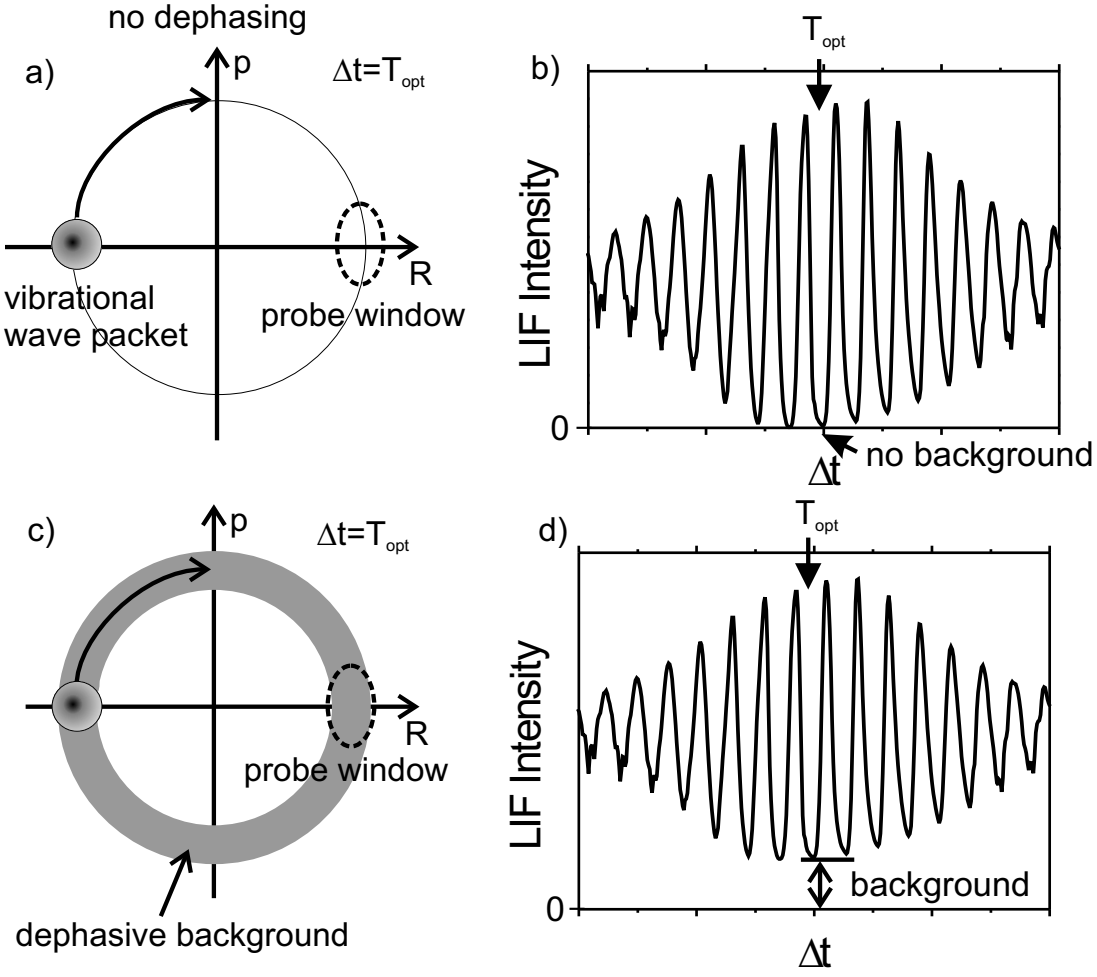

Figure 2.11: Focusing method to determine vibrational dephasing. a) Case of no dephasing (free molecule). The probe window at the outer turning point (usually used in our experiments) in phase space is depicted by the dashed circle. The vibrational wave packet on the Morse oscillator has propagated and focused at the inner turning point. No molecular population is detected in the probe window. Thus the minima of the vibrational modulations in the pump-probe spectrum b) will show zero background. c) Dephasing case. The vibrational wave packet is focused at the inner turning point. Dephased parts of the initial wave packet, spread over an isoenergetic area (no dissipation), cannot be focused. Thus, the background in the minima indicates the amount of population being dephased. d) Pump-probe spectrum with dephasing. Due to the dephased background in phase space, the LIF intensity is not modulated to zero at the minima, but some background remains. The background rises with larger T_{opt}, according to the general theory from section 2.1.

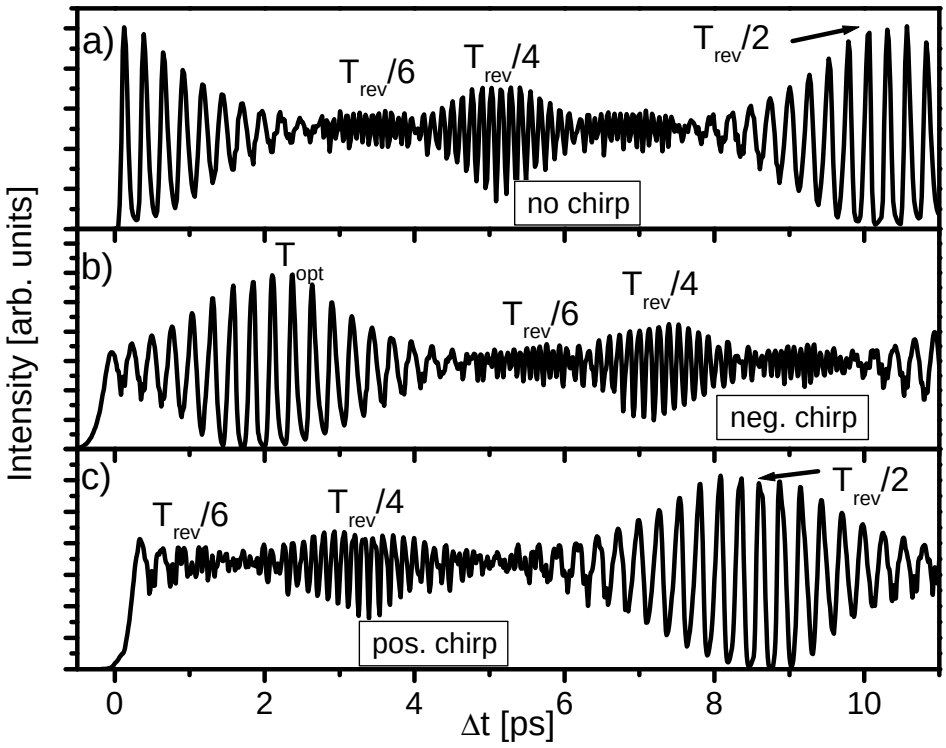

Figure 2.12: Control of fractional revival structures. Simulations for different pump conditions in a Morse oscillator. a) Excitation via an unchirped pump pulse. The vibrational wave packet is probed at the outer turning point. The 1/6, 1/4 and 1/2 revivals are marked. b) Excitation with a negative chirp. The wave packet is focused at T_{opt} and the revival features are shifted by T_{opt} to larger times . c) Excitation with a positive chirp. The fractional revival features are advanced in time by a "negative focusing time T_{opt}". The "focus" of the wave packet would be in the range of negative pump-probe delays Δt.

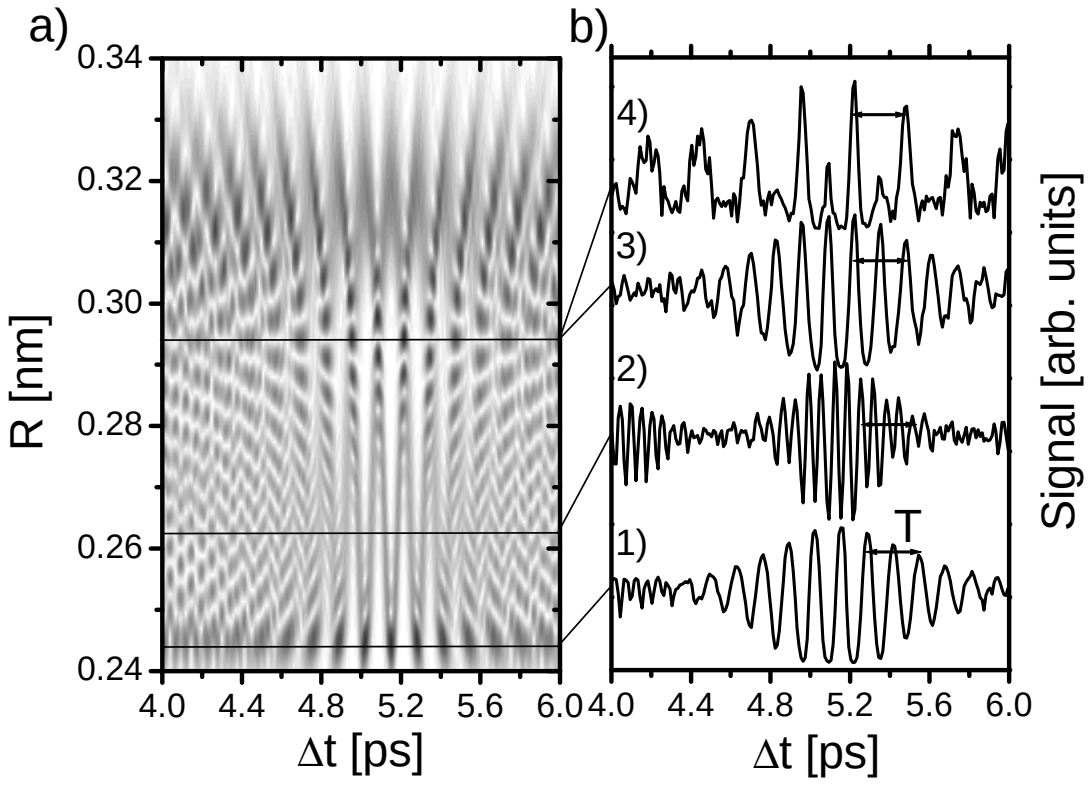

Figure 2.13: a) Density plot showing the absolute square of the wave packet as a function of time. The time interval from 4 to 6 ps includes the 1/4 revival for the free Br_2 B state, also shown in 2.7d). b) Simulated pump-probe spectra generated by integrating the signal over R with a Gaussian window of 0.011 nm FWHM for 1) to 3) and for 0.0011 nm FWHM for 4). The center of the probe window R_{win} is given as the line in a) connected to the spectra.

laser pulse (by positive chirping) and the molecular wave packet starts with a dispersion corresponding to some later time in the normal propagation.

The positive chirp excitation scheme will be used in this thesis to reach a pump-probe spectrum of the 1/6 revival. It occurs after 3.5 ps for the unchirped case, and it will turn out, that the vibrational coherence of the wave packet is lost at that time. Therefore the fractional revivals have to be advanced by an appropriately chirped pulse. Due to the pump pulse elongation, the electronic coherence is involved, as demonstrated in section 8.2.3.

Figure. 2.13a shows a density plot of the wave packet's absolute square. The time interval near the 1/4 revival appearing about 5.2 ps after the wave packet excitation is shown. The spectra in part b) are probed at different internuclear distances, indicated by the solid lines in Fig. 2.13a. The wave packet propagation is described in the appendix. To generate a pump-probe spectrum, distinct R_{win} is chosen (indicated by one solid line in 2.13a), and the wave packet absolute square in Fig. 2.13a is integrated within a Gaussian window in R direction. The Gaussian window has a Full Width at Half Maximum (FWHM) of 0.011 nm for spectra 1) to 3) in Fig. 2.13. The pump-probe spectrum 1) in Fig. 2.13b is probed at the inner turning point. A temporal structure showing $T/2$ appears. The solid arrow in all spectra indicates the full vibrational period T. Changing the R_{win} towards the potential minimum leads to the pump-probe spectrum 2). A dominant period of 1/4 T occurs for this particular R_{win}. Usually, this

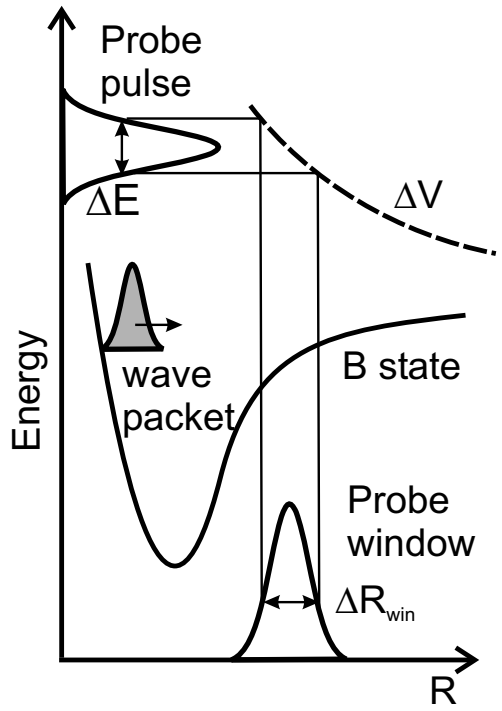

Figure 2.14: Sketch illustrating the probe window width ΔR_{win}. The B state potential and the difference potential ΔV (dashed line) to a charge-transfer state are shown. The pulse spectral envelope (on the energy axis) is reflected at the difference potential resulting in the probe window on the R axis. The probe pulse spectral width transforms to the spatial width of the probe window ΔR_{win} on the internuclear coordinate R.

period is observed at 1/8 revival (section 2.2.3) when probing at the inner or outer turning point. This indicates the importance of the right R_{win} to attribute the correct revival structure. But not only R_{win}, but also the width of the probe window ΔR_{win} is important, as is shown in pump-probe spectra 3) and 4) of Fig. 2.13b. The R_{win} now lies in a region of rich spatial interference structures in Fig 2.13a. The width is chosen to be ΔR_{win} = 0.011 nm as before in spectrum 3) and the half vibrational period occurs around 5.2 ps time delay. If the value of ΔR_{win} is reduced by a factor of ten, the full vibrational period dominates the pump-probe spectrum, as shown in spectrum 4). In this case, the width is small enough to reflect the spatial interference structures in the pump-probe spectrum. The effect has also been described in Ref. [74] and states the importance of both R_{win} and ΔR_{win}. In particular, the spatial interference phenomena will occur in section 8.2.2 in connection with the revival control by positive chirps.

The probe window width is determined by the spectral width of the probe pulse and the difference potential $\Delta V(R)$. This is illustrated in Fig. 2.14. There, the B state is probed to a charge-transfer state. The difference potential ΔV between the two potentials is shown as a dashed line. The probe spectral envelope is reflected to the R coordinate at the dashed line. This results in the probe window as a function of R. In case of a locally linear difference potential with slope dΔV/dR, the probe window width ΔR_{win} is connected to the probe pulse spectral width ΔE by:

$$\Delta R_{\text{win}} = \Delta E(\frac{d\Delta V}{dR})^{-1}. \tag{2.27}$$

The slope of the difference potential cannot be influenced, thus the spectral width ΔE of the probe pulse has to be changed in order to change ΔR_{win}. However, when ΔE is minimized, the duration of the probe pulse increases, which leads to a vanishing structure in the pump-probe spectrum. This effect is not included in the simulated pump-probe spectra. If the temporal resolution dictated by the probe pulse is much better than the peak structure in the simulated spectrum (which is always the case in this thesis), the time broadening can be neglected. If this is not the case, the simulated pump-probe spectra should be folded with the temporal width of the probe pulse to deliver the right pump-probe spectrum.

Chapter 3

Br_2 and I_2 in rare gas solids

This chapter introduces the potential energy curves and literature for the free Br_2 molecule in 3.1. The I_2 is not treated to a large extent, since most of the later chapters will refer to the Br_2 case only. The relevant aspects of molecule doped rare gas crystals are presented in a general way in section 3.2. Finally, the existent literature on Br_2 in rare gas solids will be reviewed.

3.1 Gas phase properties

In this work, the halogen molecules Br_2 and I_2 have been isolated in rare gas matrices like Ar and Kr crystals. In order to understand the spectroscopy and the ultrafast (coherent) processes, it is necessary to introduce the gas phase potential energy surfaces. Later on, the effect of the solid environment will be introduced.

3.1.1 Physical properties

The physical properties of I_2 and Br_2 are given in Tab. 3.1. The data are from Ref. [165] and [166] . Iodine appears as grey crystals under room temperature having a relatively low vapor pressure. It is toxic and corrosive but does not corrode stainless steel. Bromine is a red-brown liquid under room temperature having a relatively high vapor pressure. It is highly toxic and corrodes even stainless steel [167]. Therefore, it is usually handled in glass vessels.

Table 3.1: Physical constants of I_2 and Br_2.

	Melting point	Boiling point	Vapor pressure	Density
I_2	114°C	185°C (1atm)	0.41 hPa (25°C)	4.93 g/cm^3
Br_2	-7.2°C	58.8°C (1 atm)	220 hPa (25°C)	3.12 g/cm^3

The iodine atom has only one stable isotope, namely the $^{127}_{53}$I, whereas the bromine atom has two stable isotopes $^{79}_{35}$Br and $^{81}_{35}$Br, with a 50 % natural abundance of each. Therefore, three different species of dibromides exist: ^{79}Br^{79}Br, ^{79}Br^{81}Br and ^{81}Br^{81}Br, with ratios 1:2:1. This leads to a splitting of vibrational and rotational eigenstates, since the molecular constants $\omega_e = \sqrt{k/\mu}$ and $B = \hbar^2/2\Theta$ change with mass, where k is the spring constant, μ the reduced mass and Θ the moment of inertia. This phenomenon is demonstrated in Fig. 3.1, where the vibrational eigenstates for the isotopes in the electronic B state of Br_2 are given. Isotope effects on ω_e in Br_2 are on the order of 1%. Spectrally, the isotope shift accumulates, as seen in Fig. 3.1, where the sticks of different isotopes merge at a vibrational quantum number of v = 36.

Br_2, with isotopes in natural abundance, was used for experiments described in this work. However, isotope pure Br_2 can be produced for example by using isotope pure BrNa as an educt in the oxidation with CrO_3 [49].

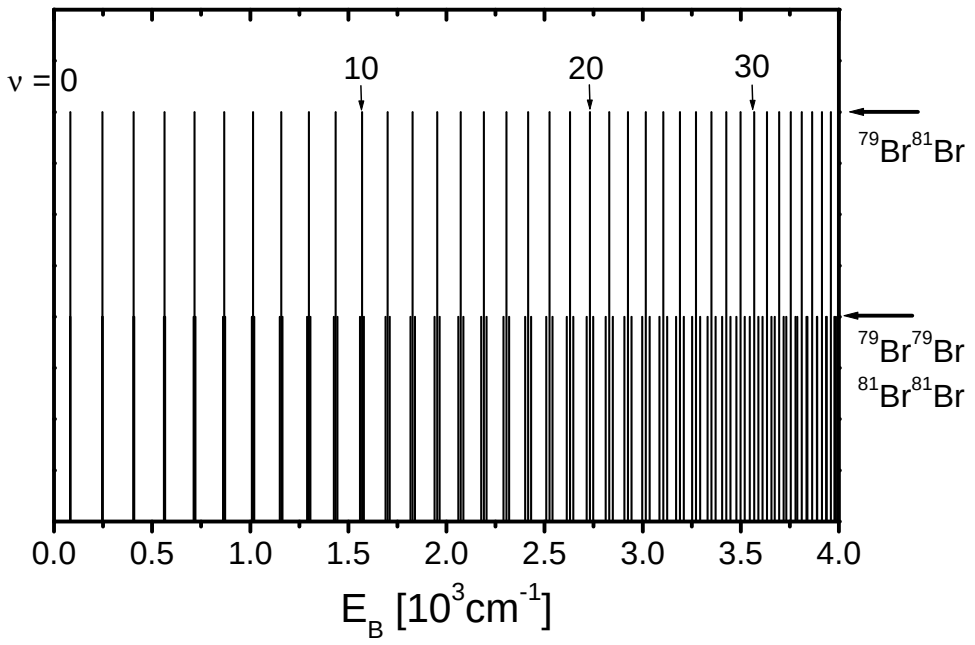

Figure 3.1: Vibrational levels in the B state for the three dibromide species as a stick diagram. The longest sticks indicate the energy of the most abundant $^{79}Br^{81}Br$, the other isotopes are given as sticks to the right and left.

3.1.2 Electronic structure of halogens

The halogen atoms are short one electron and one proton of a rare gas. The electronic configuration of a bromine atom is [Ar] $3d^{10}\,4s^2\,4p^5$, and that of an iodine atom is [Kr] $4d^{10}\,5s^2\,5p^5$, where [Ar] and [Kr] denote the structure of the core electrons. The combination of the atomic electrons in the molecular orbitals of a diiodide and dibromide are shown in Fig. 3.2.

The electronic ground state of all dihalogens is $^1\Sigma_{0g}$, where the upper index 1 denotes the multiplicity of the spin (S=0), Σ is the value of the angular momentum Λ, the index 0 gives the value for the combined angular momentum Ω and g is the parity (gerade)[1]. In the molecular orbital nomenclature the electronic configuration is given as $\sigma_g^2\pi_u^4\pi_g^4\sigma_u^0$ or shortly (2440). As indicated by the dashed arrow in Fig. 3.2, the next higher lying excited states are (2431) states. The following combinations of quantum numbers exist: $^1\Pi_1$, $^3\Pi_{0,1,2}$. The triplet states with $\Omega = 0, 1, 2$ are named B, A, A' respectively. The B state splits into two according to a plane of symmetry. The 0^+ state is called B, the 0^- state is called B'. An overview of halogen spectra based on I_2 is given in Ref. [168].

Spectroscopic information on free Br_2

Since the spectroscopy part of this thesis focuses mainly on the case of bromine in solid argon, the electronic potential energy curves of free Br_2 shall be introduced here briefly. A collection of the spectroscopic literature on free I_2 is found in Ref. [26].

The known electronic potential energy curves are shown in Fig. 3.3. Information on the $^3\Pi_{0,1,2u}$ states can be gained by absorption spectroscopy. Coxon measured absorption spectra in the "extreme red" indicating the $A^3\Pi_1 \longleftarrow X\ ^1\Sigma_0$ transition [42] and in the visible region identifying the $B^3\Pi_0 \longleftarrow X\ ^1\Sigma_0$ transition [41]. Further research was performed on B state

[1] For general nomenclature of molecular angular momenta and Hund's coupling cases see Ref. [126].

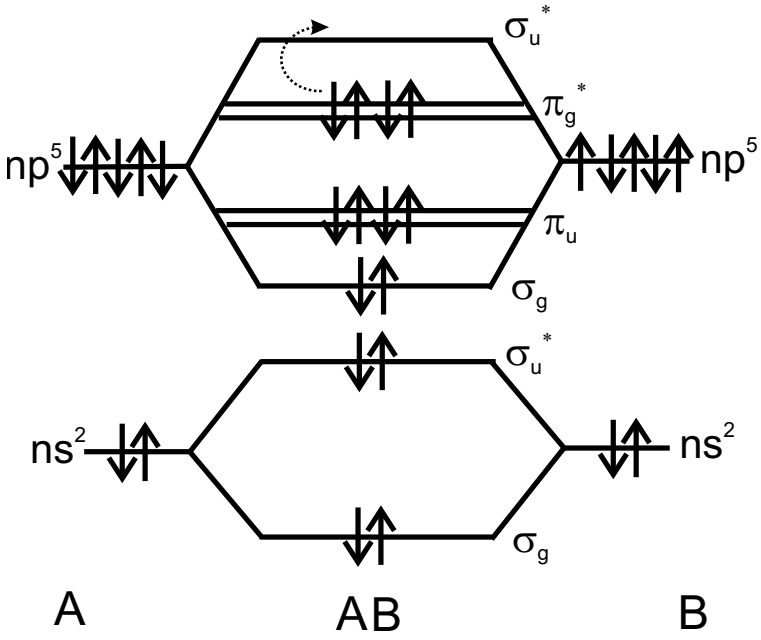

Figure 3.2: Molecular orbitals of the electronic ground state of dihalogens. The separate atom nomenclature of atoms A and B is given on each side. The transition from the ground state X (2440) to the covalent $^{1,3}\Pi$ states (2431) is indicated by the dashed arrow (nomenclature see text). n is the main quantum number of the system.

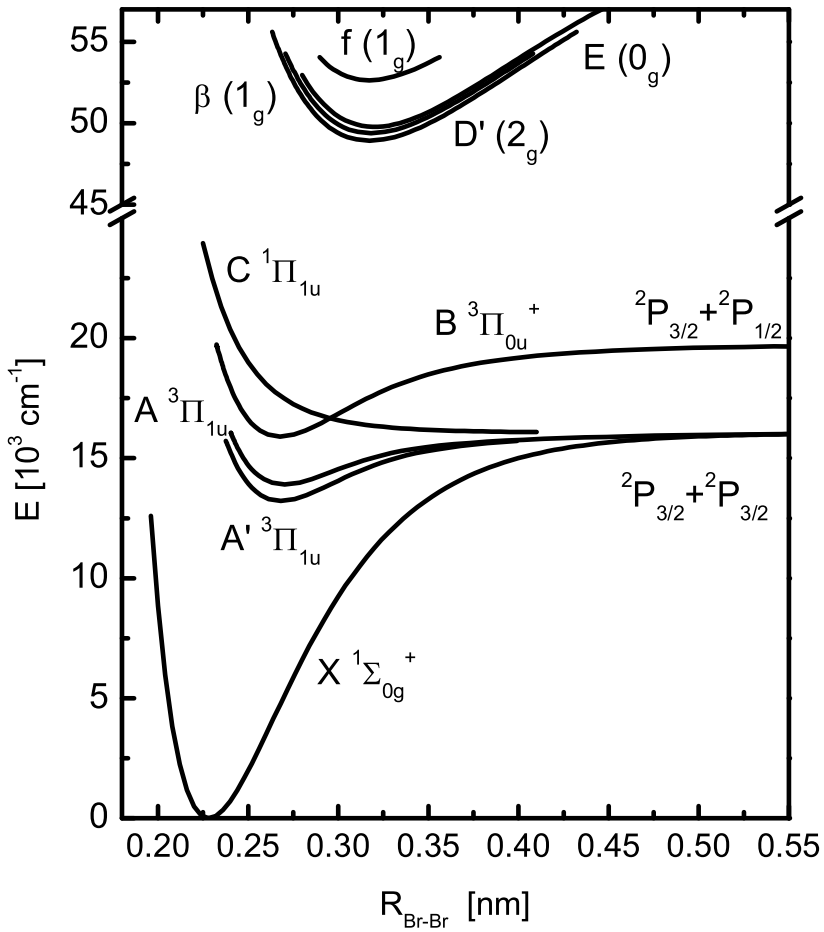

Figure 3.3: Potential energy surfaces of Br_2 in the gas phase. The covalent states X, A', A and C have the dissociation limit leading to two $^2P_{3/2}$ atoms. The B state dissociates into one $^2P_{3/2}$ and one $^2P_{1/2}$ atom. The covalent state nomenclature is given according to Hund's case (a) and (b), the charge-transfer state (states D' to f) nomenclature follows case (c) (see Ref. [126]).

Table 3.2: Spectroscopic data for the free Br_2 molecule. The expansion of the potential anharmonicity is only shown up to the first term $\omega_e x_e$. States X, A', A, B, C are covalent, D', β, E and f are charge-transfer states.

State	Isotope	T_e [cm^{-1}]	ω_e [cm^{-1}]	$\omega_e x_e$ [cm^{-1}]	r_e [nm]	Ref.
X	79,81	0	323.3069	1.0641	0.228107	[43]
A'	79,79	13223	165.172		0.25	[49]
A	79,81	13918	155.5	2.83	0.27	[42]
B	79,81	15902.47	166.5688	1.6159	0.26776	[43]
D'	79,81	48934	150.86		0.317	[49]
β		49398			0.319	[52]
E	79,79	49779.06	150.46		0.32	[50]
f	79,79	52641.554	153.8654	0.42863	0.318	[50]

absorption spectra by Yee and coworkers [43], using the Rydberg-Klein-Rees (RKR) algorithm [161–163] for potential construction. The electronic ground state originates from that study too. A set of spectroscopic data on bound states is given in Tab. 3.2.

Further information about the $^3\Pi_{0,1,2}$ states and charge-transfer states is contained in fluorescence spectra observed in discharge processes. The E $\longrightarrow$ B transition was documented by Tellinghuisen and coworkers [50] apart from the D' $\longrightarrow$ A' transition [49]. The $\beta 1_g$ state was subject of a recent study [52]. Information on the f1_g charge-transfer state was extracted from optical-optical double resonance spectroscopy [169]. The charge-transfer state data are also collected in Tab. 3.2.

The B state lifetime (in the μs range) is reduced by a population loss due to predissociation into the C state [40, 45, 46, 48]. The C($^1\Pi$) state of Br_2 was calculated from predissociation data by Heaven [51] based on a theoretical method developed by Child [170]. The potential energy curve $U(R)$ is repulsive and can be approximated by $U(R) = 1.59410^7/R^{9.384} + D_e(X)$, where the values for U are given in wavenumbers, R in 10^{-10} m and D_e(X) is the dissociation energy of the X state.

3.1.3 Selection rules and polarization sensitive spectroscopy

A detailed survey on molecular selection rules is given in Ref. [126]. In homonuclear molecules, there is a non vanishing electric dipole transition only if the light field couples states of different parity:

$$g \longleftrightarrow u. \tag{3.1}$$

A state with g (gerade) parity is totally symmetric with respect to the inversion center, whereas it is antisymmetric when having u (ungerade) parity.

For the heavy molecules Br_2 and I_2 the spin selection rule is weakened. This rule will be weakened furthermore for a molecule embedded in a matrix. The quantum number Ω (defined in Hund's case c) can only change by:

$$\Delta\Omega = 0, \pm 1, \tag{3.2}$$

where transition with $\Delta\Omega = 0$ are stronger than those with $\Delta\Omega = \pm 1$.

The Ω selection rules lead to the method of photoselection, that is described in Refs. [171, 172]. In case of $\Delta\Omega = 0$, the molecular axis parallel to the transition dipole μ is preferred. Thus the transition matrix element $|\langle i|\mu\mathbf{E}(t)|f\rangle|^2$ selects a $\cos^2\theta$ distribution of molecules in the excited state f, when using linear polarized light (see Fig. 3.4 first column upper picture). The angle θ is defined between the molecular axis and the electric field direction. In contrast,

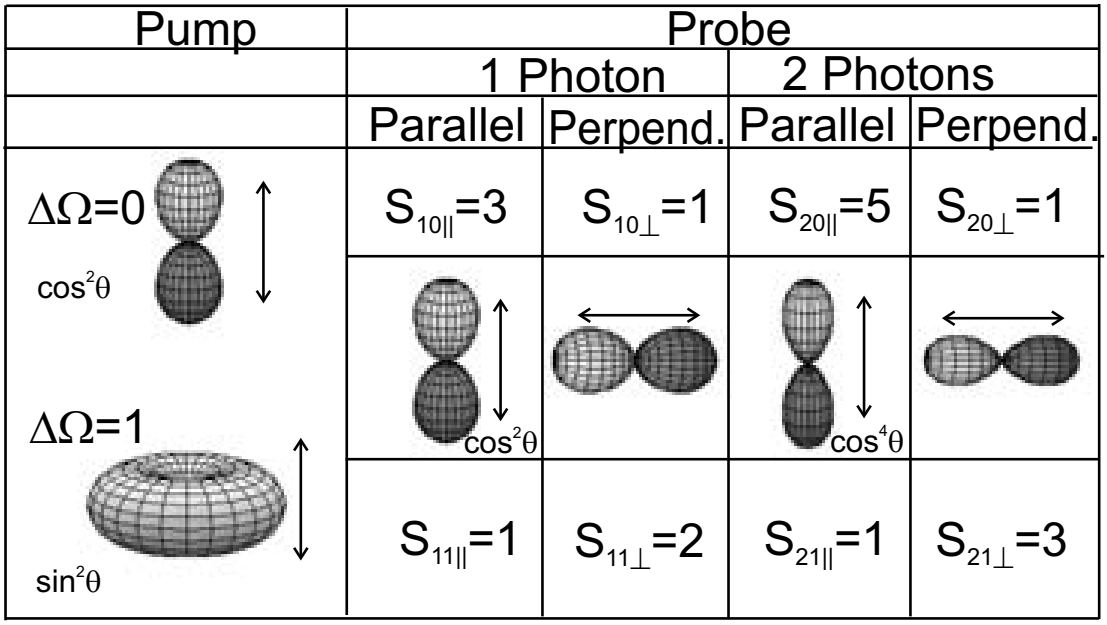

Figure 3.4: Polarization sensitive pump-probe spectroscopy. The linearly polarized pump pulse (E Field direction given by double side arrows), creates molecular distributions given on the left side. For the probe process a one or two-photon transition is used. Given are the relative signal intensities S_{abc} where a denotes the number of photons involved in the probe transition, b denotes the $\Delta\Omega$ of the pump process and c the relative orientation of the pump and probe polarization.

for a $\Delta\Omega = \pm 1$ transition, the transition dipole is perpendicular to the molecular axis and a $\sin^2\theta$ distribution will be selected according to Fig. 3.4. When inducing a transition from a covalent to a charge-transfer state, the $\Delta\Omega = 0$ rule holds, since the field has to be parallel to the nuclear axis to separate the charge. Pump-probe spectroscopy is performed in this thesis. The pump pulse selects an angular distribution of molecules. The probed signal depends on the orientation of this distribution with respect to the pump pulse polarization.

Figure 3.4 summarizes the relative transition intensities S when pumping and probing with linear polarized light. Depending on the number of photons involved in the probe step, one calculates these ratios for probing with parallel or perpendicular polarization with respect to the pump polarization. This requires a calculation of the overlap integrals of the corresponding distributions. An example shall be given: The B state was populated from the ground state X in a $\Delta\Omega$ = 0 transition. The molecular ensemble follows a $cos^2\theta$ distribution. The probe pulse couples the covalent B to the charge-transfer state E, thus since $\Delta\Omega$ = 0, it probes the B state molecules with a $\cos^2\theta$ sensitivity (in a one-photon transition) or with a $\cos^4\theta$ sensitivity (in a two-photon transition) aligned parallel to the probe polarization. The lobes of the B ensemble and the probe sensitivity are overlapped to get a value that is proportional to the angular probe efficiency. The ratio in a one-photon probe process, performed parallel or perpendicular to the pump polarization, is $S_{10||}/S_{10\perp}$= 3/1 in case of the B state. That means parallel probing is three times more effective than perpendicular probing on the B state for a one-photon probe transition. In case of a two-photon probe transition the ratio is 5/1. For two-photon transitions, the contrast is higher, since the spatial characteristics of the probe process is sharper ($\cos^4\theta$ distribution).

By introducing a time delay between pump and probe pulse, one can test the randomization (or depolarization) of the molecular axes (section 7.1.2). In case of gas phase molecules, this process proceeds on the rotational timescale of the molecule. In the condensed phase, the

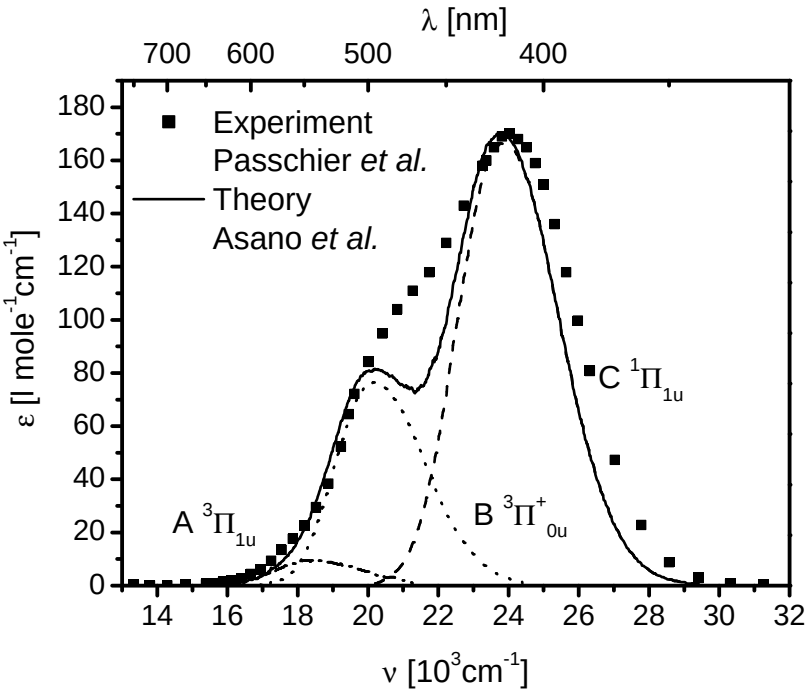

Figure 3.5: Gas phase absorption spectra of Br_2. The solid squares represent the experimental values measured at 25°C [39]. The solid theoretical curve represents the superposition of the continuous absorption of C (dashed), B (dotted) and A (dash dotted) state and is taken from Ref. [173]. It was calculated for 0 K.

molecular axis might be fixed by the crystal atoms in the vicinity [20]. In addition to this, one can also introduce polarizers through which excited state fluorescence is detected [171].

If two states with different Ω quantum number are excited from the ground state X and probed in an experiment, one can employ a scheme to separate the individual contributions (see section 7.1.3). This can be accomplished only for non-depolarizing molecules. The rotational stiffness of the the molecules in RGS will be shown in section 7.1.2.

3.1.4 Gas phase absorption spectra

The absorption spectrum of Br_2 plays a crucial role in the course of this work. Absorption spectroscopy on bromine dates back to the beginning of the last century [37]. Full experimental gas phase absorption spectra of Br_2 are published in Refs. [38, 39]. A temperature dependence from 25°C to 440°C is measured in Ref. [39] and successfully fitted by a general law given in Ref. [174]. Seery and coworkers [38] measured the VIS and UV absorption spectra of several halogens and interhalogens. They are mostly unstructured since only small fractions of the B and A state are bound as can be seen in the potential diagram in Fig. 3.3. The most recent attempt to theoretically explain the absorption spectrum is presented in Ref. [173]. The results of this reference are shown in Fig. 3.5.

For I_2 gas phase absorption, we refer to literature [38] and especially to articles by Tellinghuisen [49, 175, 176], with the decomposition of the electronic absorption spectrum into three contributions (B", B and A state).

3.2 Molecules in rare gas solids

Crystals doped with molecules or atoms are widely applied in the field of solid state lasers. Familiar examples are Ti:Sa, Nd:YAG and Nd:YLF. Thus, doped crystals have been studied extensively and the atomic and molecular processes are treated in detail in Refs. [177, 178]. Rare Gas Solids (RGS) are very special hosts for impurities. The RGS are chemically inert[2], they form simple fcc structures [9] and their interaction is only mediated by Van der Waals forces.[3] Due to the conceptual simplicity, they are treatable in theory on a very high level.

RGS can be doped by many different atoms and molecules [183]. In this work, Kr and Ar crystals were doped with the halogens Br_2 and I_2, respectively. These impurities are embedded in the RGS in double-substitutional[4] sites (see Fig. 3.6) because of two reasons: The Van der Waals radius of the halogen atom is almost that of the rare gas and the typical molecular internuclear distances are in the range of the nearest neighbor distances of the RGS.

The fcc structure of a molecule doped RGS is shown in Fig. 3.6a. It is exemplified for I_2 in Kr, but looks the same for Br_2 in Ar. The molecule sits on a double-substitutional site and its axis (dashed line) is aligned along the <110> direction. The atoms are grey coded to express the third dimension (black: nearest to reader, dark grey: further away, light grey: far away). In Fig. 3.6b and c, cuts in the (100) and (111) plane are shown with the Van der Waals radii of the atoms. Most of the 18 closest Kr atoms (as well as the Ar atoms in the Br_2:Ar system) are classified according to their position with respect to the dopant.[5] Atom 3 is the so called "head-on" atom sitting in the elongation of the molecular axis. One finds this group of crystal atoms in the (100) and (111) plane. The head-on atom is the direct collision partner of the chromophore in a vibrational motion. It will play an important role for energy relaxation (see section 8.1.3) and the effective potential (see section 8.1.2). The "cap-window" atoms 4 in the (111) plane will also participate in those processes. In order to reach the "head-on" atom, the atomic fragment of the solute has to penetrate a rectangular window formed by the "cap-window" atoms. The "belt" atoms in the (111) plane numbered 5 can enter the space between the iodine atoms of the molecule in case of a large molecular elongation. The effect has been simulated in [84] and found in experiments on I_2:Kr [13, 25, 28]. For the case of Br_2:Ar, the effect will be discussed in section 8.1.3. Atoms numbered 1 in the (100) plane will play an important role in the coherent host dynamics. Therefore, they are called a "coherent" phonon atoms, treated in section 8.3.1.

3.2.1 The cage effect

The tight packing of the molecule in the crystal derived from the the Van der Waals radii suggests a stabilization with respect to molecular dissociation. Even if the molecules are optically excited above the dissociation limit in a molecular electronic state, permanent dissociation will be hindered. This phenomenon is known as the "cage effect" and has been introduced in the seminal work of Franck and Rabinowitch [184–186]. The cage effect has been observed in dense rare gas environments [76, 77, 148, 187], in liquids [188], and in solids [183]. Its influence on the dynamics is a central topic of this thesis.

Clearly, the potential energy surface of the molecule in the host is multidimensional since all nearest-neighbor molecule-host coordinates can contribute to the dynamics. One can project the multidimensional surface on the intranuclear coordinate of the molecule. This leads to a bend

[2] Some very prominent exceptions exist. Solid xenon is relatively reactive because of its size, but even in molecule doped solid Kr and Ar new molecules containing the rare gas atoms have been found [179, 180].

[3] Three body forces play a crucial role for the formation of the fcc lattice in RGS. With pair potentials only, the hcp structure would be favored [181, 182].

[4] That means they replace two rare gas nearest neighbor atoms. This has been experimentally verified by Raman Spectroscopy [54].

[5] The numbering is done in agreement with Ref. [86].

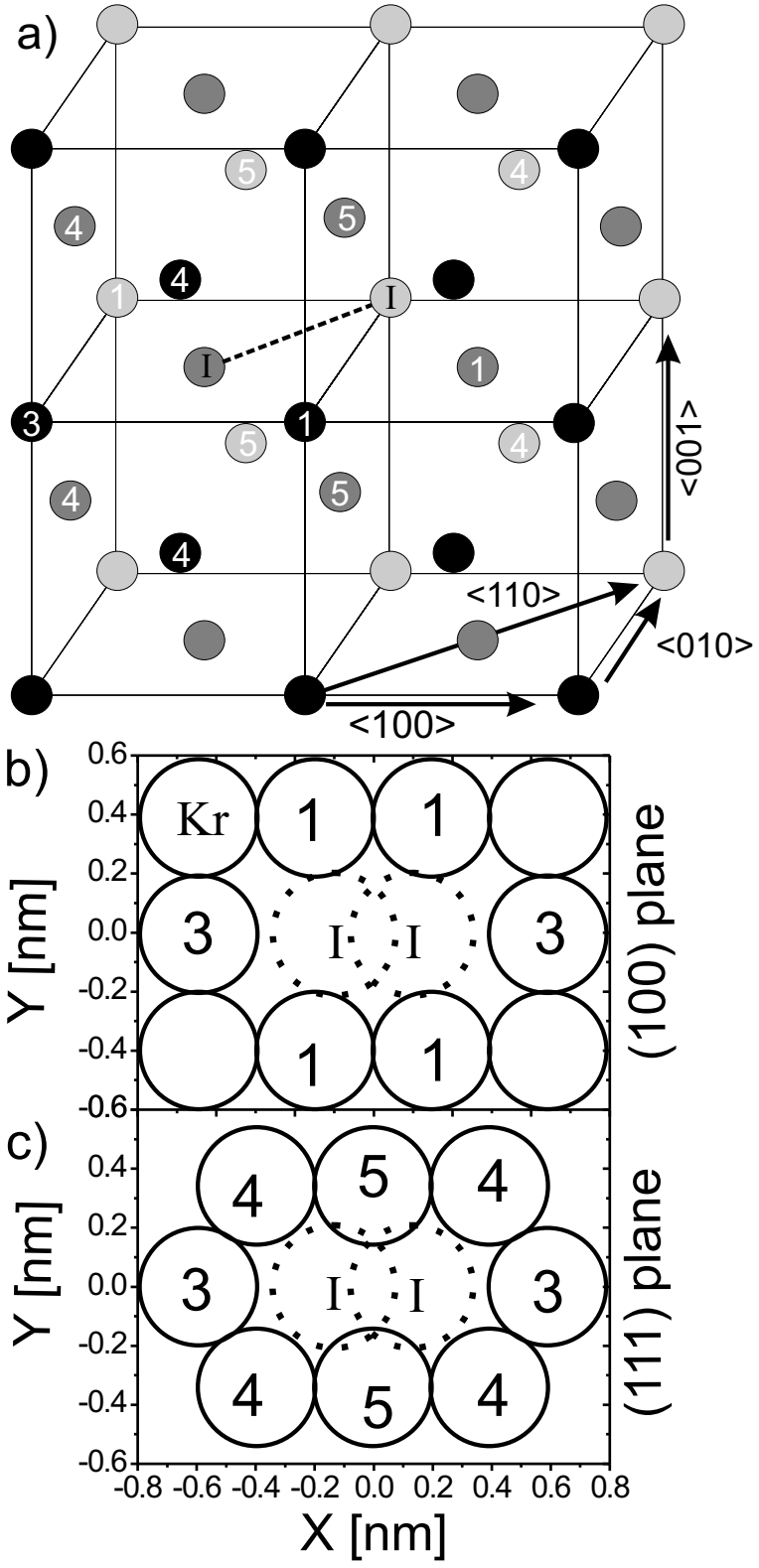

Figure 3.6: Geometry of the chromophore in the fcc cage, exemplified for I_2 in solid Kr. The situation for Br_2 in solid Ar is analogous, and only the axis numbering in b) and c) has to be rescaled. a) The molecule I_2 sits in a double-substitutional site in the fcc Kr crystal. The internuclear axis (dashed line) is aligned along the <110> direction. The atoms closest to the reader are marked black, the ones sitting further away are dark grey and those sitting far away are marked light grey. The numbers are defined in b), c) and the text. b) Cut in (100) plane containing the I_2. Kr atom 3: "head-on" atom, 1:"coherent phonon" atom. c) (111) plane (hexagonal symmetry): Kr atom 4: "cap-window" atom, 5: "belt" atom. The radii in b) and c) are the Van der Waals radii for the I-Kr and Kr-Kr interaction.

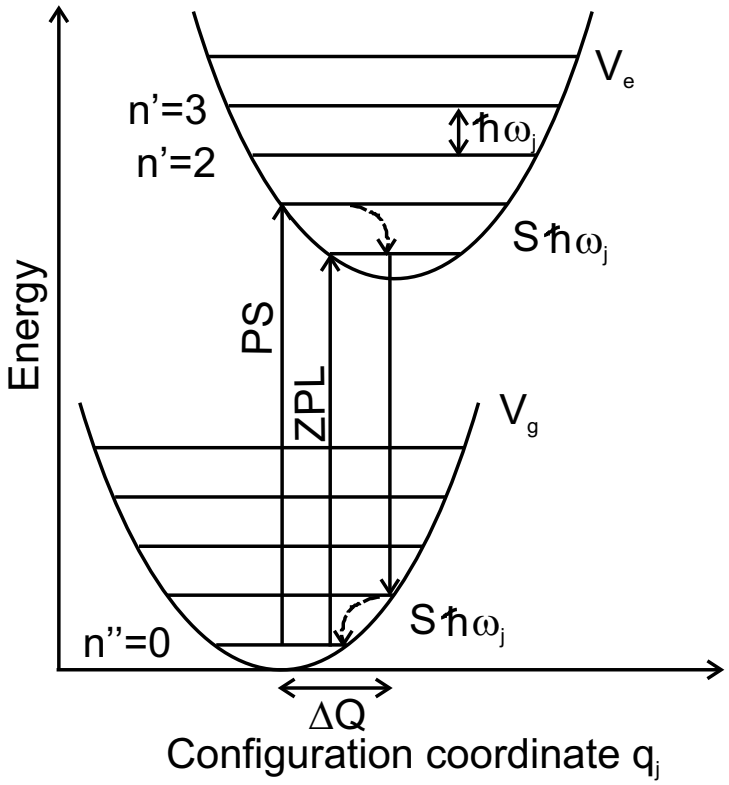

Figure 3.7: Configuration coordinate picture. One coordinate of q_j of the crystal is picked out. The interaction of the molecule with the phonon mode j is described by a harmonic potential V_g in the molecular ground state and V_e in the molecular excited state. The e and g denote different vibrational states either in the same electronic state of the molecule or in different electronic states. The shift ΔQ of the equilibrium coordinate in V_g and V_e is related to the Huan-Rhys coupling constant S. n' and n'' correspond to the phonon number of the mode j. The solid arrows indicate the Zero Phonon Line (ZPL) and the Phonon Sideband (PS). See text for details.

up of the molecular electronic potentials near the dissociation limit. The term "geometrical shift" has been established for corrections of molecular potentials due to the influence of the host atoms.

Besides the effect on the shape of the effective potential energy curves, the cage strongly influences the coupling between different molecular electronic states. This has been extensively treated in theory for the I_2-Ar system [189–192], in which the influence of only one argon atom in the vicinity is considered. Therefore the term "one atom cage effect" has been established.

3.2.2 Energy shifts of charge-transfer states

In addition to a geometrical shift, the Charge-Transfer (CT) states experience a strong inductive shift, leading to a large solvation energy. As the name implies, the CT states have a very large electric dipole moment μ. The host RGS is a polarizable medium. Thus, upon polarizing the host, the energy of the molecular CT state is lowered. A simple model (Onsager model [193]) allows to estimate the energy shift ΔE of the dipole μ sitting in a spherical cavity with diameter d in a polarizable host with the dielectric constant ϵ:

$$\Delta E = \frac{1}{4\pi\epsilon_0}\frac{\mu^2}{d^3}\frac{8(\epsilon-1)}{2\epsilon+1}. \tag{3.3}$$

Eq. (3.3) has been described in Refs. [96, 193]. The dipole moment μ of the covalent molecular states is quite small resulting in a small inductive shift [194]. However, for the CT states ΔE may reach several thousand wavenumbers as it was documented for I_2 in different RGS [27, 96]. References for the CT shift in RGS for the case of Br_2 are not available, and indeed they are spectroscopically measured in this thesis for the first time (chapters 5 and 6).

3.2.3 Absorption and excitation spectra

When an impurity molecule is embedded in a crystal, any molecular excitation (here vibrational and electronic) can couple to the crystal phonons. This results in special features in absorption,

excitation and emission spectra. Intuitive models for the underlying physics were discussed in 1950 by Huang and Rhys [195] and they are still widely used. The faster molecular coordinates are first separated from the slower solvent coordinates in the sense of a Born-Oppenheimer Approximation (BOA). The authors of Ref. [195] treat the interaction potential of the ground molecular state with a phonon mode j of the matrix as a harmonic potential in the crystal coordinate q_j: $V_g = \frac{1}{2}M\omega_j^2 q_j^2$. An excited molecular state (vibronic in the same electronic state or even in another electronic state) is described by another potential V_e of this type. In the linear approximation, only the equilibrium distance in the configuration coordinate q_j of the oscillator changes by a value ΔQ: $V_e = E_e + \frac{1}{2}M\omega_j^2(q_j + \Delta Q)^2$. In a quadratic approximation, also the curvature of the excited state potential would change. The linear approximation is depicted in Fig. 3.7. The absorption and emission of radiation in the configuration coordinate model follows the Franck-Condon arguments [177]. Lets first treat the absorption: at low temperatures, all population is in the ground state $n'' = 0$ of the V_g surface, which means no phonon is excited in that mode.[6] The Franck-Condon integral to the excited states n' is calculated. The spectral trace of the $n' = 0 \longleftrightarrow n'' = 0$ transition is the so called Zero Phonon Line (ZPL). No phonon is created in this case. If the two surfaces V_g and V_e are not displaced (ΔQ = 0), it would be the most intense one. In the case of a non-vanishing displacement as shown in Fig. 3.7, transitions with $n' - n'' \neq 0$ are favored. Those give rise to a Phonon Sideband (PS) in the spectrum. The equivalent phonon modes can be densely spaced (many relevant coordinates q_j) and the PS is broad. In the example given here, a one-photon transition is favored.[7] To describe the intensities in a quantitative fashion, the Huan-Rhys coupling constant S is introduced: $S = \frac{1}{2}M\omega_j^2\Delta Q^2/(\hbar\omega_j)$. It is the number of the most intense phonon line in absorption (or emission). In Fig. 3.7, S corresponds to one. The larger the displacement ΔQ gets, the larger is the coupling constant. The intensity of the n-phonon line I_n(corresponding to the creation of n phonons) is given by a Poisson statistics when calculating the Frank-Condon factors of wave functions on V_g with V_e [177, 197]:

$$I_n = e^{-S}S^n/n!. \tag{3.4}$$

Before radiative decay occurs, which is observed in the emission spectra, a Stokes shift due to dissipation of the phonons to the crystal will be induced. From Fig. 3.7 a Stokes shift of $2S\hbar\omega_j$ in the mode j follows.

The excitation spectrum of Br_2:Ar was recorded by V. Bondybey and coworkers. It is shown in Fig. 3.8. The spectrum was recorded monitoring the B state emission intensity of Br_2 in solid argon (see 3.3) while changing the excitation wavelength λ_{exc} continuously. The excitation light was generated in a dye laser. One has to keep in mind, that the spectrum was not normalized with respect to the laser intensity. Thus, the envelope of the excitation spectrum is determined by the molecular absorption multiplied by the dye laser spectral distribution. Unfortunately, the normalization cannot be carried out now, since the laser spectral intensity was not published.[8] The lines for different isotopes in the B state emission could be separated. The excitation spectrum in Fig. 3.8 was recorded on a $^{79}Br^{81}Br$ isotope line. The ZPL and PS of the intramolecular vibrational progression are resolved in the whole spectral range shown in Fig. 3.8. The lowest observed vibration with the the ZPL at 15946 cm^{-1} was assigned to $v' = 3$. This was however

[6] For very low frequency phonons, this temperature must be very deep to reach the condition.

[7] A very interesting analogy between ZPL and the Mössbauer line in gamma spectroscopy appears [177, 196]. As in the case of the Mössbauer line, no phonon is created for the ZPL. The excitation mechanism of the environment in the Mössbauer case is the big atom recoil when absorbing/emitting a gamma photon, whereas in the ZPL case it is the potential change due to the molecular excitation.

[8] An request for the laser spectral intensity curve remained unanswered by the author of Ref. [55].

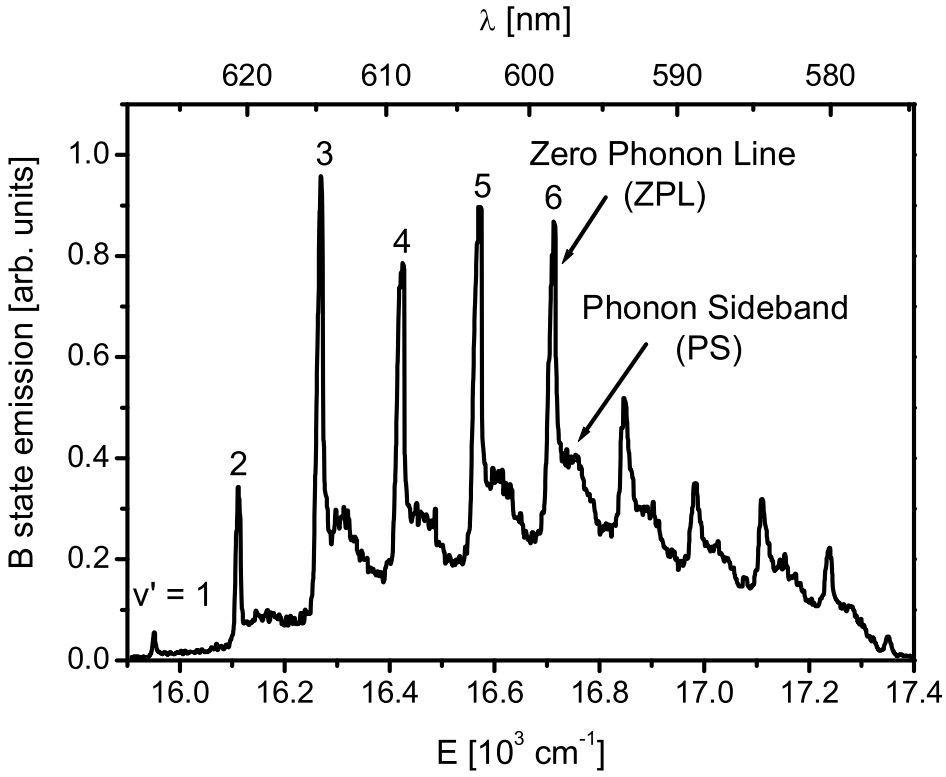

Figure 3.8: Excitation spectrum of Br_2:Ar from Ref. [55]. The sample temperature was 5 K. The B fluorescence was collected/selected for the $^{79}Br^{81}Br$ isotope. The excitation spectrum shows rather sharp Zero Phonon Lines (ZPL) and broad spectral features called Phonon Sidebands (PS).

Table 3.3: Emission bands with lifetimes and spectral range for Br_2:Ar. All transitions terminate in the electronic ground state $X^1\Sigma_{0g}$. The A* state in Ref. [66] is not closer specified.

Emitter	Lifetime [μs]	Spectral range [μm]	Ref.
$B^3\Pi_{0u}$	(8.0 ± 0.5)	0.7 – 1.1	[60]
	7.3	0.75 – 0.9	[55]
	(6.57 ± 0.05)	0.8 – 1.1	[66]
$A^3\Pi_{1u}$	(67 ± 4)	1–2	[60]
A*	(61 ± 1)	1 – 1.7	[66]
A	(107 ± 7)	1 – 1.7	[66]
A'$^3\Pi_{2u}$	$11\ 10^3$	1.1 – 1.35	[63]
A'	$(11 \pm 1)10^3$	1 – 2	[60]
A'	$(44.2 \pm 3)10^3$	1 – 1.7	[66]

strongly doubted by Langen and coworkers in [66]. The counting was changed by -2, thus the line at 15946 cm^{-1} was assigned to $v' = 1$.

The origin of the rising background in the excitation spectrum is not clear. It may either be due to a mixing to the electronic A state or result from a superposition of phonon sidebands.

Besides the description of absorption and emission spectroscopy, the configuration coordinate model can also be applied on nonradiative transitions like vibrational energy relaxation and electronic vibrational relaxation [197]. In case of vibrational relaxation, the two levels g and e belong to two vibrational eigenstates of a molecule being associated to the same electronic state. The upper levels n' in e shall be populated, while the n'' levels in g should not be. The transitions from n' to n'' are again dominated by the Franck-Condon Factors. If all levels n' have decayed to the $n' = 0$ level, Eq. (3.4) can be applied. Based on this, a rate for vibrational energy relaxation can be determined for special cases [197].

3.2.4 Literature on Br_2 in rare gas solids

Absorption studies of Br_2 in solid argon have been performed for the first time by Andrews [57]. His results will be compared to the absorption spectra of this work in section 6.1. Furthermore, absorption spectroscopy in the UV was used to determine the Br_2 cluster concentration in Ar crystals. A signal feature at 300 nm was found to depend on the Br_2 to argon mixing ratio. Thus, the absorption was attributed to clusters, however without giving any information on the states responsible for absorption. The monomer content of Br_2 in an Ar crystal was estimated to be 95 % for Br_2 / Ar mixtures of 1/500.

Most information on the chromophore matrix system was gained by the use of emission spectroscopy. Emission bands with different wavelength and decay times have been reported for various matrices (Ar, Kr and Xe). Emission always occurs from the $v' = 0$ level of the excited state. This manifests the effective vibrational energy relaxation of Br_2 in RGS. A collection of emissions attributed to transitions from different covalent states to the ground state is given for an Ar matrix in Tab. 3.3. Of all references in Tab. 3.3, Langen and coworkers [66] have the best spectral resolution and can distinguish A, A' and another state A* (non specified by authors [66]). Data for the potential energy curves can be deduced from the emission spectra, which will be presented in Tab. 6.2 in the discussion of the spectroscopic results.

The B state emission intensity was much weaker than expected. This gave rise to the idea that the matrix-induced-predissociation of the B state is much stronger than that of the free molecule. This idea is shortly reviewed in the following. The absorption of the different electronic states of Br_2 in RGS was observed to be approximately equal to the free Br_2 transition

strength distribution among the A, B and C states (Fig. 3.5), however, showing line-broadening due to the molecule-host interaction mentioned in the previous section. The B state emission was observed for the first time by Bondybey and coworkers [55]. The polarization ratio and the spectral region of the emission were indicative for a B $\longrightarrow$ X transition.[9] The C $^1\Pi$ state does not seem to feed population into the B state, since the excitation spectrum follows the B absorption envelope when recording the B fluorescence [55]. This fact was taken as an evidence for a complete decoupling of the B and the C state [63]. However, this assumption might be wrong. It was only stated in [55] that C does not feed into B when excited in the maximal FC range of C, which lies high above the B-C crossing energy. In that case, the Landau-Zener mechanism would indeed propose a rather small population loss of C into B or vice versa [27, 198]. Nevertheless, near the crossing of the C and B state (see Fig. 3.3), the population transfer from B to C might be rather effective.

Flynn and coworkers measured the emission from the B, A, and A' states in solid Ar [60] as given in Tab. 3.3. With an approximation for the transition matrix elements, they conclude that the A state contains 25 times more population than the B state, although the absorption of the A state is only 20 % of the B state absorption at the excitation wavelength used. The authors explain this by a population transfer from the B to the A state. This can either happen via the crossing with the C state (since the C state effectively couples to the A state [60]) or a direct predissociation from B to high vibrational (matrix bound) levels in the A or A' state.

The idea of a B population transfer to the A and A' state is doubted in all articles published afterwards. Heaven and coworkers argued, that the excitation spectrum of Br_2:Ar follows the C and A absorptions when monitoring the A, A' fluorescence [63]. Furthermore, they conducted a study using a 532 nm laser with linear polarization and analyzing the polarization of the A state emission. All results seem to be consistent with an exclusive A excitation, however the polarization parameters seem to be affected by a strongly scattering matrix [64]. The authors in Ref. [64] indeed propose a population loss of the B state to explain the low population observed in B emission. However, the B population should not show up in the A, A' states but recombine to the electronic ground state or another state invisible in emission spectroscopy. Our study does not further resolve the problem but future investigations aim on a detailed picture of the Br_2 predissociation.

[9] The B emission does not occur for Cl_2 in solid Ar because of a large Franck-Condon (FC) overlap of B state with A state wave functions. In Br_2, the FC overlap is much smaller because of a larger spin orbit splitting.

Chapter 4

Experimental setup

The rare gas crystals can only exist at very low temperatures. Therefore, a vacuum system (in parts made of glass) and cryostat had to be set up, described in section 4.1. Furthermore the absorption, emission and pump-probe experiments are described in the chapter. Since the wave packet control schemes are based on chirped pulses, the theory of ultrashort laser pulses and their chirping is introduced in section 4.3.

4.1 Vacuum system and sample preparation

Briefly, the halogen and the rare gas are mixed in a vessel and afterwards sprayed on a cooled substrate in the cryostat. On this substrate, the gas mixture freezes and a polycrystalline film of the halogen-rare gas mixture grows. The vacuum system, used in all experiments documented in this thesis work, is divided into three parts (see Fig. 4.1). Parts a) (iodine mixing system) and b) (bromine mixing system) in Fig. 4.1 are used to mix the halogens I_2/Br_2 with krypton/argon, part c) represents the cryostat chamber. The grey shaded parts in Fig. 4.1 consist of stainless steel, whereas the transparent parts consist of glass (if not stated otherwise).

First, the I_2:Kr mixing apparatus is described. The apparatus consists of a stainless steel reservoir of about 0.5 liter volume. Connected to this are iodine reservoir, krypton bottle and a turbo pump. Before preparing the gas mixture, the mixing vessel is pumped by the turbo pump and reaches a typical pressure in the range of 10^{-7} mbar (measured by the ionization gauge). The iodine is placed in a glass vessel and connected via a KF flange to a metal valve (all metal valves are stainless steel NUPRO valves). The iodine (Sigma Aldrich, 99.999% purity) has a vapor pressure of 0.41 hPa or 0.41 mbar (see table 3.1). Before mixing I_2 with krypton, the prepump is directly connected to the iodine vessel without being connected to the mixing vessel (a combination of valves allows for that). Air which might have leaked into the iodine vessel is removed in this way. Afterwards the walls of the mixing vessel are carefully passivated with I_2, to assure a constant I_2 partial pressure during the crystal growth. The composition of the mixture is controlled in the following way: the mixing volume is filled with the vapor pressure of I_2 according to baratron I. Afterwards, the volume is filled with 1000 times more krypton pressure, which assures a ratio in I_2:Kr of 1:1000. Baratron I is limited to pressures up to 10 mbars, therefore a coarse manometer records the high Kr pressure. Krypton (Linde, 99.999% purity) from a high pressure gas vessel is used with a pressure reducer. The mixture prepared in this way is transferred to the cryostat chamber (Fig. 4.1c) in a steel tube and sprayed on the substrate as will be described below.

In the beginning, we tried to prepare the bromine-rare gas mixture in the stainless steel vessel used for I_2 before. The vessel for the iodine experiment was backed and evacuated to about 10^{-8} mbar. Nevertheless, we could not succeed to grow a crystal containing bromine. The bromine is more reactive than iodine and therefore removes all iodine bound to the walls. Thus, the rare gas crystals were doped with iodine instead of bromine. In contrast to other

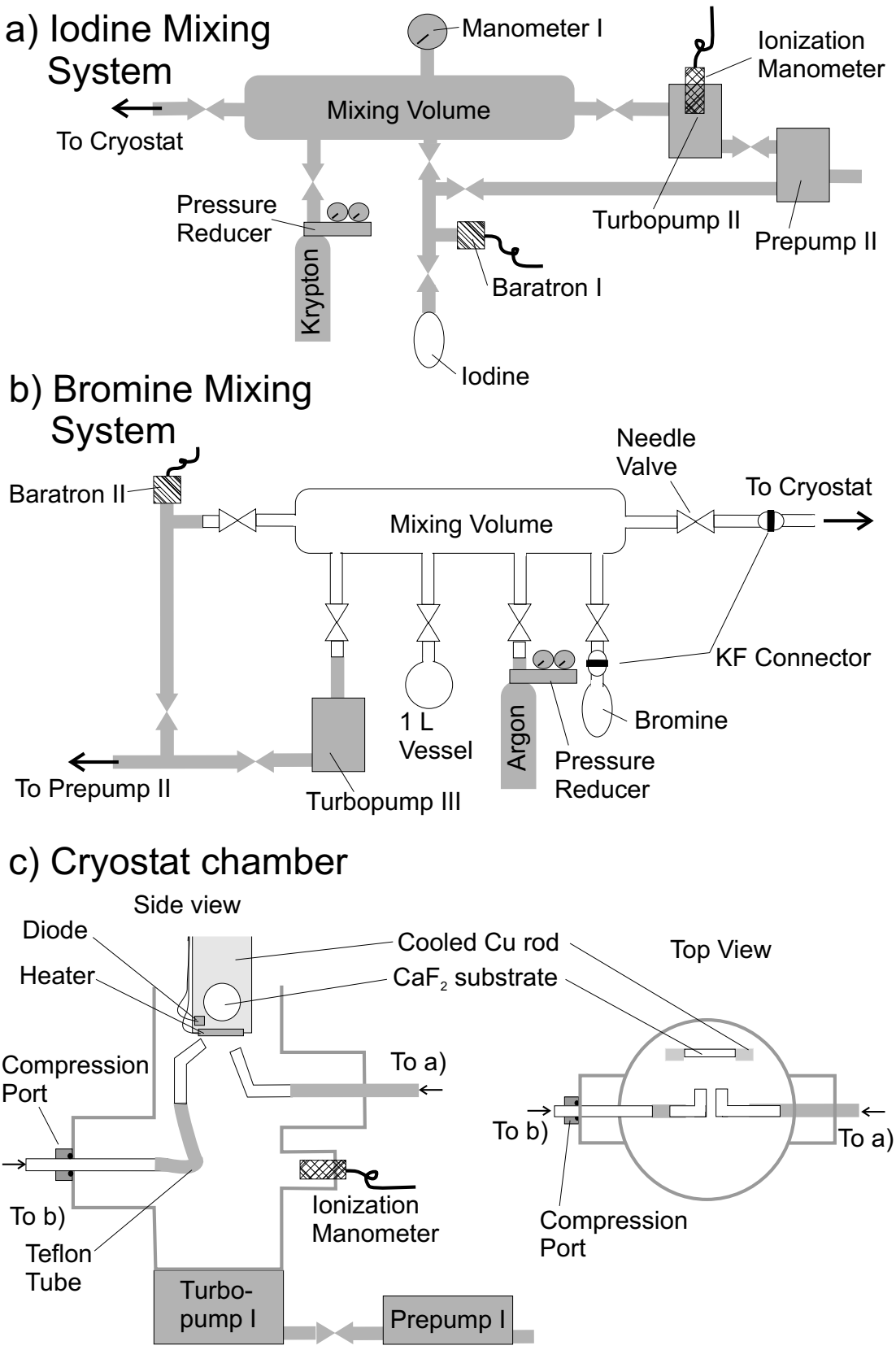

Figure 4.1: The vacuum system consists of a) the I_2:Kr mixing apparatus, b) the Br_2:Ar mixing apparatus and c) the cryostat vessel. Glassware is marked by thin black lines and stainless steel components are shaded. Details see text.

halogens, the bromine reacts with stainless steel as documented in Ref. [167] and destroys the vessel as well as the sealing. Thus a mixing apparatus made from glass, teflon and viton (all being inert concerning bromine) had to be constructed. The setup is shown in Fig. 4.1b. A central mixing volume of about one liter is connected to a bromine reservoir, an argon vessel, another reservoir of one liter volume and pumping facilities. The pressure monitoring is not trivial, because most pressure measuring devices contain some metal parts. The baratron II (pressure limit 1 bar) is completely set up in a metal housing. To avoid a longer contact with the bromine mixture, baratron II can be separated from the central vessel with a glass valve and connected to the prepump, to remove bromine that probably sticks to the metal. The metal glass contact is always set up with KF flange connectors. The seals in this case are made of teflon and viton. Before preparing the bromine:argon mixture, the bromine is frozen in its vessel by liquid nitrogen, heated a bit, and pumped by the turbo pump to remove all air inside (the temperature rises and the eventually frozen air evaporates). The turbo pump is disconnected and the bromine turns to liquid. Those freeze-thaw cycles are repeated several times. Since Br_2 has a vapor pressure of 200 mbars at room temperature, it cannot be cleaned without freezing.

The glass mixing vessel can be evacuated to a pressure of about 10^{-7} mbar. The mixing process requires more steps as in the case of iodine. To achieve a Br_2:Ar ratio of 1:500, first a ratio of 1:40 is mixed. Some premix is pumped away and the rest is again diluted by Ar gas until the 1:500 ratio is reached. During the addition of argon to the bromine gas in the mixing vessel, a condensation of bromine at the glass walls can be observed. This is due to the rapid increase of pressure. After a few minutes, the condensated drops have vanished and the bromine is perfectly mixed with argon.

The mixture is introduced in the cryostat by glass and teflon transfer lines only to avoid any metal contact before the mixed gas reaches the cooled substrate. The glass tube coming from outside the cryostat is prolonged by a teflon tube inside, that ends again in a bent glass tube which faces the cooled substrate. The glass tube is sealed to the cryostat walls made of stainless steel via a compressed viton ring (see Fig. 4.1c).

In the case of iodine, the gas is transferred inside the cryostat by metal tubes and only the final few centimeters are made from glass. The whole iodine mixing system is made form steel and no strong iodine-steel reaction was observed.

The cryostat chamber (Fig. 4.1c) consists of a Ultra High Vacuum (UHV) stainless steel vessel evacuated by the turbo pump I. A closed cycle refrigerator or alternatively a liquid He flow cryostat cools a CaF_2 substrate of one mm thickness via a copper rod. A heater and a temperature diode (Lakeshore) are connected to the copper rod to control and measure the actual temperature.

In case of the closed cycle He refrigerator a temperature of about 17 K can be reached at the substrate, whereas 5 K can be achieved when operating the apparatus with the liquid He flow cryostat. The cooling acts as a cryopump and produces a pressure of 10^{-9} mbar together with the turbo pump. If only the turbo pump is active, the pressure is one order of magnitude higher.

Cryostat and copper rod are placed on a UHV manipulator and thus their position can be controlled. The manipulator allows for placing the cryocrystals in the laser beams, that cross the cryostat chamber about ten cm above the glass tube endings. For crystal preparation, the substrate is positioned 5 cm in front of the glass tube ends. The valves connecting the mixing vessel and the cryostat are opened and the gas mixture flows on the substrate. In a systematic study, the optimal gas flow parameters for best crystal growth were searched using the pressure in the cryostat measured by the ionization gauge as an indicator. For a close cycle refrigerator, the best crystals are grown at a pressure of $1 \cdot 10^{-5}$ mbar. In case of the liquid He flow cryostat, a different pressure of $6 \cdot 10^{-5}$ mbar was figured out to be optimal. The difference originates from

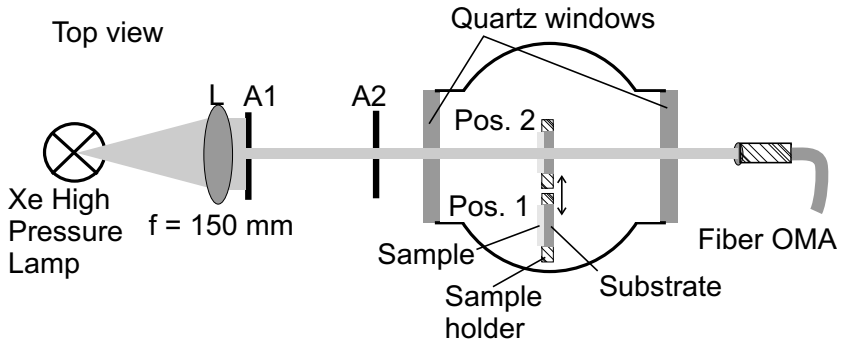

Figure 4.2: Setup for absorption spectroscopy. The Xe high pressure lamp delivers a light continuum in the visible and UV spectral range. The quartz lens L (f = 150 mm) forms a parallel beam. The sample holder with substrate and sample can be positioned outside (Pos. 1) and inside (Pos. 2) the beam. The transmitted spectra are analyzed via a fiber OMA. Apertures A1 and A2 define the beam.

the changed cryo-pumping properties of the substrate holders. Since the gas not only freezes on the substrate but also on the cold holder, the amount of gas not freezing and thus being detected by the ionization gauge is different from the cycle refrigerator situation. In case of the closed cycle refrigerator, the crystal grows with a rate of approximately 90 μm per hour, which was confirmed before by interferometry with a HeNe laser [83]. The crystals are crack free at the end of the growing process and develop some cracks in the course of time, most probably due to temperature fluctuations and strain. In case of the I_2 doped Kr, the cryocrystals are purple (as gas phase I_2), whereas the color of Br_2 doped Ar crystals is brown-orange (as Br_2 gas).

4.2 Absorption spectroscopy setup

The setup used for absorption spectroscopy is shown in Fig. 4.2. A structured continuum of radiation in the visible and ultraviolet light range is produced by a high pressure Xe lamp (ORIEL) operated at 300 W electrical power. The spectrum of the Xe lamp is shown in Fig. 4.3. The solid spectrum is monitored via the visible light (VIS) channel of the Optical Multichannel Analyzer (OMA), whereas the dashed spectrum is monitored via the ultraviolet (UV) channel of the same instrument. The gratings and detectors are different in those channels, resulting in a different spectral sensitivity depicted in Fig. 4.3 (the OMA will be described more detailed in section 4.5). As can be seen in the spectra, absorption measurements are possible in the range from 12000 to 40000 cm^{-1}, since the spectrum is smooth and intense in this interval.

To perform the absorption spectroscopy, the light beam from the Xe lamp is aligned through the vacuum chamber as shown in Fig. 4.2. A f = 150 mm lens (L) is used in combination with apertures A1 and A2 to create a narrow beam of about 3 mm diameter that traverses the cryostat with its two quartz windows and enters the fiber connected to the OMA. Inside the chamber, the sample holder with substrate and sample can be positioned in the beam. For that purpose, the UHV manipulator is used (as already mentioned in the previous section). The quartz windows (see Fig. 4.2) are located higher in the cryostat than the glass tubes for gas deposition. Thus, the sample has to be driven upwards until it is positioned in the beam. This corresponds to position 2 (Pos. 2) as indicated in Fig. 4.2. If this is assured, the sample is horizontally (sidewards as indicated by the arrow) driven out of the beam to position 1 (Pos. 1). A reference spectrum $I_0(\lambda)$ is recorded while all ambient light is carefully avoided. Afterwards, the sample is positioned in the beam (Pos. 1) and once more, the transmitted spectrum $I(\lambda)$ is recorded. From the two spectra, the absorption of the sample can be reconstructed. One might argue, that the absorption of the sample *and* the substrate is measured, and indeed, this is in principle true. However, the substrate consists of CaF_2 which is completely transparent in

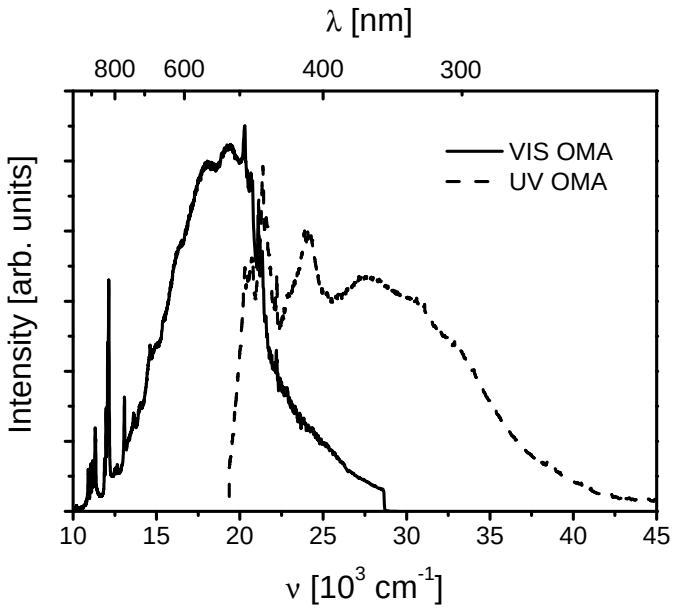

Figure 4.3: Spectra of the high pressure Xe lamp monitored via the visible (solid line) or ultraviolet (dashed line) channel of the OMA. The beampath is as described in Fig. 4.2. The channels of the OMA have different spectral sensitivity.

the whole visible-ultraviolet range until its first absorption band in the vacuum UV at 130 nm occurs.

Absorption is governed by the so called Lambert-Beer law that connects $I_0(\lambda)$ and $I(\lambda)$:

$$I(\lambda) = I_0(\lambda)\mathrm{e}^{-\mu(\lambda)\mathrm{x}}, \tag{4.1}$$

with x being the sample thickness and $\mu(\lambda)$ being the extinction coefficient. Usually, the absorbance A (in unit optical density o. D.) is plotted as a measure for absorption (as will be done in chapter 5.1). The absorbance A is defined as the decadic logarithm of the ratio $I_0(\lambda)/I(\lambda)$. Thus it is connected to μx via:

$$A = \log(\frac{I_0}{I}) = \ln\frac{(\frac{I_0}{I})}{\ln(10)} = \frac{\mu x}{\ln(10)}. \tag{4.2}$$

Besides real absorption by the halogen:rare gas sample, also scattering at the sample occurs, that increases with decreasing wavelength.

4.3 Ultrashort laser pulses

This section will provide information about properties of ultrashort laser pulses. However, only methods used in the following chapters will be covered. For a detailed description of ultrafast optics, the reader is referred to Refs. [199, 200].

Since the pulse is short in time, a Fourier transformation delivers some finite spectral width in the frequency or energy distribution of the pulse spectrum. A light pulse is called Fourier transform limited if its duration is given by a Fourier transformation of its frequency distribution. One can retard some spectral components of the pulse versus others. This is generally called chirp (see Fig. 4.4). This quantity will be a central topic in the following experiments.

4.3.1 Gaussian pulses

A light pulse consists of a magnetic and an electric field fulfilling the wave equation, the magnetic is much smaller than the electric part. The component of the electric field in a distinct

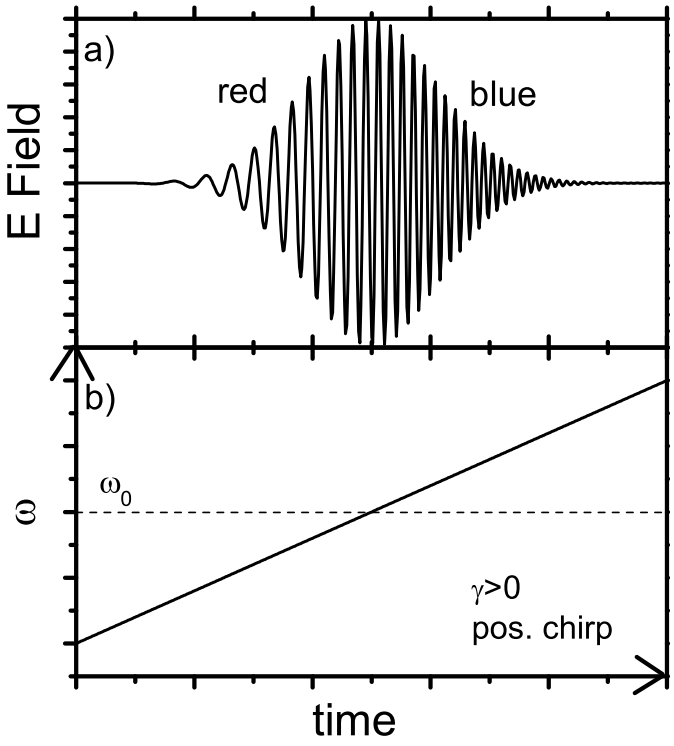

Figure 4.4: a) Electric field $E(t)$ of a chirped pulse. At early times (left side) the oscillation of the field proceeds slowly increasing its frequency when going to later times (right side). b) The instantaneous frequency $\omega(t)$ is plotted as a function of time. The slope is positive, corresponding to a positive chirp. The dashed line marks ω_0, the carrier angular frequency.

direction is called $E(t)$. For a Gaussian light pulse, $E(t)$ is given by:

$$E(t) = Re(E_0 \mathrm{e}^{-\frac{\mathrm{t}^2}{2\tau^2}} \mathrm{e}^{-\mathrm{i}\Phi(\mathrm{t})}) \,, \tag{4.3}$$

where $\mathrm{e}^{-\frac{\mathrm{t}^2}{2\tau^2}}$ is the Gaussian envelope, τ the duration and $\Phi(t)$ is the phase of the pulse. The phase of the pulse can be expanded in time:

$$\Phi(t) = a + \omega_0 t + \frac{\gamma}{2} t^2 + ... \tag{4.4}$$

The higher order phases are not manipulated here and are thus not further treated. The angular frequency of the pulse is given by the time derivation of the phase:

$$\omega(t) = \frac{\partial \Phi}{\partial t} = \omega_0 + \gamma t + ... \,, \tag{4.5}$$

ω_0 is the carrier angular frequency, γ will be called the linear chirp parameter. It corresponds to a quadratic phase in time and changes the instantaneous angular frequency $\omega(t)$! Fig. 4.4a shows the electric field E as a function of time for a positively chirped pulse. The direction of time is defined on a fixed point of space passed by the laser pulse. The pulse front passes the point at early times, whereas the pulse center and back parts pass the point at later times. At early times (left side), the oscillation period is long, becoming shorter at later times (right side in Fig. 4.4a). The frequency change according to definition 4.5 is given in Fig. 4.4b. The $\omega(t)$ increases linearly with time for this linear positive chirp.

A transformation of the field to the angular frequency domain ($\varepsilon(\omega)$) will prove to be advantageous for many applications. From now on, the electric field will be given in its complex

representation, keeping in mind that only the real part is of physical importance. Fourier transformations (FT) can be done like follows:

$$\begin{array}{rcl} E(t) & = & E_0 \mathrm{e}^{-\frac{\mathrm{t}^2}{2\tau^2}} \mathrm{e}^{-\mathrm{i}\omega_0 \mathrm{t} - \mathrm{i}\frac{\gamma}{2}\mathrm{t}^2} \\ FT \downarrow & & \uparrow FT^{-1} \\ \varepsilon(\omega) & = & \varepsilon_0 \mathrm{e}^{-\frac{(\omega-\omega_0)^2}{2\eta^2}} \mathrm{e}^{-\mathrm{i}\frac{\beta}{2}(\omega-\omega_0)^2} \ . \end{array} \tag{4.6}$$

The linear chirp in the time domain γ leads to a quadratic phase β in the angular frequency domain. Explicitly performing the transformation leads to the relations between the parameters:

$$\gamma = \beta \frac{\eta^2}{\tau^2} \tag{4.7}$$

$$\tau = \frac{1}{\eta}\sqrt{1+\beta^2\eta^4}. \tag{4.8}$$

Since one usually measures intensities instead of fields in the time and frequency domain, we need to connect full at width half maximum of the intensity observables $\Delta\tau$ respectively $\Delta\eta$ to field parameters τ (temporal width) and η (spectral width) described above: $\Delta\tau = 2\sqrt{\ln 2}\tau$ and $\Delta\eta = 2\sqrt{\ln 2}\eta$. In case of unchirped pulses (γ = 0 and β = 0), Eq. (4.8) leads to: $\Delta\eta\Delta\tau = 4\ln 2$. When measuring in the frequency domain, the width $\Delta\nu$ is given as $\Delta\nu = \frac{\Delta\eta}{2\pi}$. The last relation leads to:

$$\Delta\nu\Delta\tau = \frac{4\ln 2}{2\pi} \approx 0.441, \tag{4.9}$$

which is the well known Fourier limit for the chosen Gaussian pulses.[1] For other pulse shapes, this relation has different numerical values (see Table 2.1. in [199]). When calculating in the frequency domain (instead of the angular frequency domain), $\beta(\omega)$ has to be changed to $\beta(\nu)$. As can be seen in Eq. (4.8), the relation has to be: $\beta(\nu) = 4\pi^2\beta(\omega)$, since the term $\beta^2\eta^4$ has to be dimensionless.

Using relation 4.8 one can calculate the chirp of a pulse from the duration τ of the pulse when its Fourier transformed duration τ_0=$\frac{1}{\eta}$ is known:

$$\beta = \pm\frac{\tau_0}{2}\sqrt{\tau^2 - \tau_0^2}. \tag{4.10}$$

The chirp parameter β has the unit fs^2. Another chirp parameter $\beta'(\nu)$ will be introduced. It is defined as:

$$\beta'(\nu) = \frac{\beta(\nu)}{c}, \tag{4.11}$$

where c is the velocity of light. The unit of β' is usually given in fs cm. Therefore, the chirp parameter $\beta(\nu)$ with unit fs^2 is transformed into the unit cm^2. Afterwards, this value is divided by c in the right units cm/fs. The parameter $\beta'(\nu)$ has a helpful interpretation: in a Wigner plot of the pulse, where the quantum energy is plotted versus time, the parameter $1/\beta'(\nu)$ gives the rate at which the instantaneous pulse quantum energy changes with time.

[1] Example: A pulse centered at λ = 540 nm shall have a spectral width of $\Delta\lambda$ = 12.3 nm. Since $\Delta\nu = \frac{c}{\lambda^2}\Delta\lambda$, $\Delta\nu$ = 12.6 THz . This leads to a transform limited length of $\Delta\tau$ = 35 fs. The corresponding field parameters are: τ = 21 fs and ν = 7.56 THz.

4.3.2 Chirping pulses

Depending on the sign of the chirp parameter γ one speaks about a linear positive or negative chirp. In case of the positive chirp, the red components advance the blue ones in time according to Eq. (4.5) (see Fig. 4.4) and vice versa for a negative chirp.

It is relatively easy to impose a positive chirp on pulses. In normal dispersive media, the red light components of a laser pulse have a higher group velocity v_{g} than the blue ones. Therefore, after passing a material of a given thickness, the pulse has accumulated a positive chirp. After passing material of thickness x, the field of an originally unchirped pulse is given in the angular frequency domain by:

$$\varepsilon(\omega, x) = \mathrm{e}^{-\frac{(\omega-\omega_0)^2}{2\eta^2}} \mathrm{e}^{-\mathrm{ik}(\omega)\mathrm{x}}. \tag{4.12}$$

Expanding $k(\omega)$ to second order $k(\omega) = k(\omega_0)+k'(\omega-\omega_0)+\frac{1}{2}k''(\omega-\omega_0)^2+...$ with $k' = (\frac{dk}{d\omega})_{\omega_0}$ and $k'' = (\frac{d^2k}{d\omega^2})_{\omega_0}$ leads to the following form of Eq. (4.12):

$$\varepsilon(\omega, x) = \exp[-ik(\omega_0)x - ik'x(\omega-\omega_0) - (\frac{1}{2\eta^2} + i\frac{1}{2}k''x)(\omega-\omega_0)^2]. \tag{4.13}$$

Thus, the quadratic phase or linear chirp is given by:

$$\beta = \frac{d^2\Phi(\omega)}{d\omega^2} = k''x. \tag{4.14}$$

$k''(\omega) = (\frac{d^2k}{d\omega^2})$ is often called Group Velocity Dispersion (GVD). It is a material constant and can be calculated using the Sellmeier formula or by public computer programs [201, 202].[2]

A negative chirp can be accomplished by a grating [203] or prism compressors [204–206]. Since in the experiments, only prism compressors were used, grating compressors will not be discussed here. A prism compressors consists of two prisms. The first one disperses the beam, the second is placed at a variable distance in the dispersed spectrum. An end mirror retro reflects the beam back. The chirp can be calculated with Eq. (4.14) using the distance between the prisms as x. The GVD is given as [204–206]:

$$k''(\omega) = -\frac{8\omega_0}{c}(\frac{dn}{d\omega})^2_{\omega_0}. \tag{4.15}$$

The GVD does not only depend on the material constant n but also on the light angular frequency ω_0.[3]

4.3.3 Nonlinear optics

This section is included here for two reasons: first of all, nonlinear optics is used to generate ultrashort laser pulses and to manipulate their characteristics. Second, nonlinear optical components are used to determine the pulse parameters in optical correlation experiments. Even the fastest electronics with a time resolution of about 100 ps are to slow to characterize pulses in the femtosecond regime.

[2] An example of pulse lengthening using a piece of quartz shall be given. A transform limited pulse centered around 540 nm and having a width of $\Delta\lambda$ = 12.3 nm (ν = 7.56 THz) travels trough 1 cm of quartz. The GVD k"(ω) = 645 fs^2/cm. Therefore, the chirp $\beta(\nu) = 4\pi$ 645 fs^2 = 2554 fs^2. This leads to a pulse lengthening from τ = 21 fs transform limit to 37.2 fs due to the positive chirp (see Eq. (4.8)).

[3] An example of pulse lengthening using a quartz prism compressor. A transform limited pulse centered around 540 nm and having a width of 12.3 nm (ν = 7.56 THz) travels trough the compressor of length x = 55 cm. The GVD k"(ω) = -11.727 fs^2/cm. Therefore, the chirp $\beta(\nu)$ = -4π^2 -645 fs^2 = -2554 fs^2. This leads to a pulse lengthening from τ = 21 fs transform limit to 37.2 fs due to the negative chirp. By this negative chirp one can compensate the dispersion of 1 cm quartz material.

The electrical component of a laser field $\mathbf{E}(t)$ (bold letters describe a vector) induces a time dependent polarization $\mathbf{P}(t)$ in some material:

$$\mathbf{P}(t) = \varepsilon_0(\chi^{(1)}\mathbf{E}(t) + [\chi^{(2)}\mathbf{E}(t)]\mathbf{E}(t) + [[\chi^{(3)}\mathbf{E}(t)]\mathbf{E}(t)]\mathbf{E}(t) + ...), \tag{4.16}$$

where $\chi^{(n)}$ is the n-order susceptibility of the material[4], which is in general a tensor. In linear optics, Eq. (4.16) ends after the first order in the electric field. The second order i component of the vector **P**(t) in Eq. (4.16) reads as:

$$(\mathbf{P}^{(2)})_i = \varepsilon_0([\chi^{(2)}\mathbf{E}(t)]\mathbf{E}(t))_i = \varepsilon_0 \sum_j \sum_k \chi^{(2)}_{ijk} E_j E_k. \tag{4.17}$$

The second order susceptibility $\chi^{(2)}$ is used for Second Harmonic Generation (SHG) in NOPA (Noncollinear Optical Parametric Amplifier) devices explained in section 4.4.2 and for Sum Frequency Generation (SFG) in cross-correlations. The third order susceptibility $\chi^{(3)}$ is used for white light generation in the NOPA and in correlation experiments.

Sum frequency generation

The electric field moving in one distinct direction shall be given as a superposition of two components with angular frequencies ω_1 and ω_2: $E(t) = A\cos\omega_1 t + B\cos\omega_2$t. Inserting the formula in Eq. (4.17) and introducing the effective susceptibility d for the given direction of the field, one ends up with:

$$P^{(2)} = \frac{1}{2}\varepsilon_0 d((A^2+B^2)+A^2\cos 2\omega_1 t+B^2\cos 2\omega_2 t+2AB\cos(\omega_1+\omega_2)t+2AB\cos(\omega_1-\omega_2)t)$$

Besides a dc term, also second harmonic frequencies $2\omega_1$, $2\omega_2$, the sum frequency $\omega_1+\omega_2$ and the difference frequency $\omega_1-\omega_2$ occur. Thus light of different color is generated by the second order interaction in the nonlinear material.

In the photon picture, a photon with energy $W_1 = \hbar\omega_1$ and one with $W_2 = \hbar\omega_2$ would be combined to form a new SFG photon with $W_{SFG} = \hbar(\omega_1+\omega_2)$. In such a way, total energy is conserved. The same type of arguments can be applied for difference frequency and second harmonic generation.

Apart form the energy, the wave vectors have to be conserved, too. This shall be explained for the case of SFG. The requirement of momentum conservation for SFG $\mathbf{p}_{SFG}$= $\mathbf{p}_1$+$\mathbf{p}_2$ with $\mathbf{p} = \hbar\mathbf{k} = \frac{\hbar n}{\lambda}\frac{\mathbf{k}}{k}$ gives a condition for the refractive index n: $n_{SFG} = \frac{\lambda_2 n_1+\lambda_1 n_2}{\lambda_1+\lambda_2}$. For the special case of SHG, the equation reads $n_{SHG} = n_1$, the index of refraction for the second harmonic n_{SHG} should be the same as the index of refraction for the fundamental n_1. This cannot be achieved in isotropic media because of dispersion. Therefore, birefringent crystals are used where for example the fundamental has an ordinary, the second harmonic has an extraordinary polarization resulting in different refraction indices. The angle of the optical axis is tuned to fulfill the index matching condition.

A SFG signal of two independent ultrashort laser pulses can only be generated, if the pulses interact in a nonlinear crystal, meaning they have an overlap in space and time in the crystal. One can delay one pulse versus the other and measure the *cross-correlation* time τ_{cc} in SFG:

$$\Delta\tau_{\mathrm{cc}}^2 = \Delta\tau_1^2 + \Delta\tau_2^2, \tag{4.18}$$

[4]Higher order susceptibilities of some pm/V are much smaller than $\chi^{(1)}$. Therefore, one needs a high field strength to observe nonlinear phenomena. A 100 fs pulse of 10 μJ energy provides an intensity of 3 10^{17} Wm^{-2}, when focused to a spot of radius 10μm. This corresponds to a field strength of 1.5 10^{-2} V/pm or 0.03 a.u.. Having such fields, nonlinear phenomena become observable. The high field strength can only be achieved with (pulsed) laser technology.

where $\Delta\tau_1$ and $\Delta\tau_2$ are the pulse durations. Therefore one can determine the duration of a pulse if the duration of the correlated pulse is known. In case of a correlation of two identical pulses, the cross-correlation turns into an *autocorrelation* with time constant τ_{ac} and Eq. (4.18) transforms into: $\Delta\tau_{ac}^2 = 2\Delta\tau^2$.

4.3.4 Frequency Resolved Optical Gating (FROG)

To obtain information about the complete phase and amplitude of a pulsed electric field, one applies an all optical correlation technique called Frequency Resolved Optical Gating. Here, the focus is on the SFG FROG or XFROG: two different pulses are overlapped in a nonlinear crystal with large $\chi^{(2)}$ to generate the sum frequency of both pulses. The pulse to be analyzed is associated to the field E_r. Another pulse (called gate pulse) with field E_g is successively delayed by a time τ. The sum frequency intensity I_{FROG} is spectrally resolved for a variable τ. The FROG trace is given as:

$$I_{\mathrm{FROG}}(\tau,\omega) = |\int_{-\infty}^{+\infty} E_r(t)E_g(t-\tau)\exp(i\omega t)dt|^2, \tag{4.19}$$

where

$$E_r(t) = E_{0r}\exp(-\frac{t^2}{2\tau_r^2} - i\frac{\gamma}{2}t^2 - i\omega_r t),$$

is the chirped pulse to be analyzed and

$$E_g(t-\tau) = E_{0g}\exp(-\frac{(t-\tau)^2}{2\tau_g^2} - i\omega_g t),$$

is the gate pulse that is assumed to be unchirped.

From the FROG trace, one can derive $E_r(t)$ by application of a so called "phase retrieval algorithm" [207].

A linear chirp parameter γ can be determined more easily from the "First Order Marginal" (FOM).

The First Order Spectral Marginal (FOSM) $T(\nu)$ is defined as:

$$T(\nu) = \frac{\int \tau I_{\mathrm{FROG}}(\nu,\tau)d\tau}{\int I_{\mathrm{FROG}}(\nu,\tau)d\tau}. \tag{4.20}$$

$T(\nu)$ gives the intensity maximum in every time profile versus frequency (see Fig. 7.13). In the same manner, a First Order Delay Marginal (FODM) $N(\tau)$ is defined, that gives the intensity maximum in every spectral profile versus time:

$$N(\tau) = \frac{\int \nu I_{\mathrm{FROG}}(\nu,\tau)d\nu}{\int I_{\mathrm{FROG}}(\nu,\tau)d\nu}. \tag{4.21}$$

$T(\nu)$ and $N(\tau)$ can be extracted from experimental FROG traces. There is a close connection between the FODM and the linear chirp β of a pulse. The relation is derived in the appendix (Eq. (6)) and corresponds to:

$$N(t) = \frac{\beta\eta^2}{2\pi\tau_{\mathrm{cc}}^2}t. \tag{4.22}$$

A similar relation holds for $T(\nu)$ and β [208].

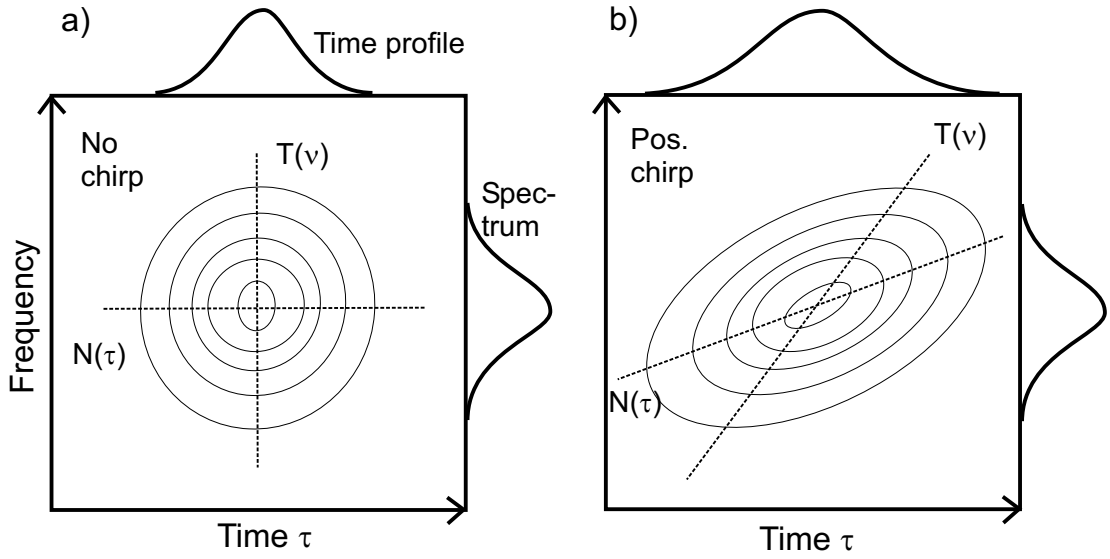

Figure 4.5: Frog traces of an unchirped pulse a) and a pulse having a positive linear chirp b). The First Order Marginals (FOM) as a function of time $N(t)$ and frequency $T(\nu)$ are given by the dashed lines. The FROG traces can be "sliced" in frequency spectra for different times τ. The spectral maxima for a variable time form the FODM $N(\tau)$. In an analogue manner, the FROG trace can be "sliced" in time transients for different frequencies ν. The time maxima versus ν form the FOSM T(ν).

4.4 Laser System

The laser system is designed to achieve ultrashort pulses in a spectral range from the near infrared at 775 nm through the whole visible range into the ultraviolet at approximately 240 nm. Such a high tunability can only be achieved when using optical parametric amplification. Thus, the laser system consists of a commercial fs Chirped Pulse Amplifier (CPA) that pumps four Noncollinear Optical Parametric Amplifiers (NOPAs) that can be tuned from about 700 nm to 480 nm. Furthermore, they can be frequency doubled to cover the UV spectral range from 350 to 240 nm. A gap from 480 to 350 nm remains, that can be closed partly by the frequency doubled CPA fundamental at 387.5 nm. The different parts of the laser system are briefly described below. For a rather general overview of ultrafast laser technology, the reader is referred to Refs. [199, 200, 209].

4.4.1 CPA system

The laser system pumping the NOPAs is a commercially available Clark-MXR CPA 2001. It consists of a fiber oscillator, stretcher, the CPA cavity and a compressor.

The ultrashort pulses are generated in the fiber oscillator [210]. An Er doped quartz fiber is pumped by commercial telecommunication diodes at 980 nm. The Er emits around 1550 nm. The dispersion in the fiber in combination with a prism compressor allows for passive mode locking yielding a pulse length of 130 fs and repetition rates in the MHz regime. The pulses are frequency doubled in a periodically poled SHG crystal to 775 nm.

The frequency doubled pulses are stretched in time to some ps in order to protect the optics and amplified in a regenerative amplifier. This consists of a cavity with a Ti:Sa crystal that is pumped by the second harmonic (532 nm) of a 1 kHz Q-switched Nd:YAG laser. Afterwards, the pulse is picked out of the cavity by a polarizer-Pockels cell setup. It is recompressed to about 160 fs. The final pulse has an energy of about 700 μJ, a central wavelength of 775 nm and the beam is linearly polarized, parallel to the laser table surface.

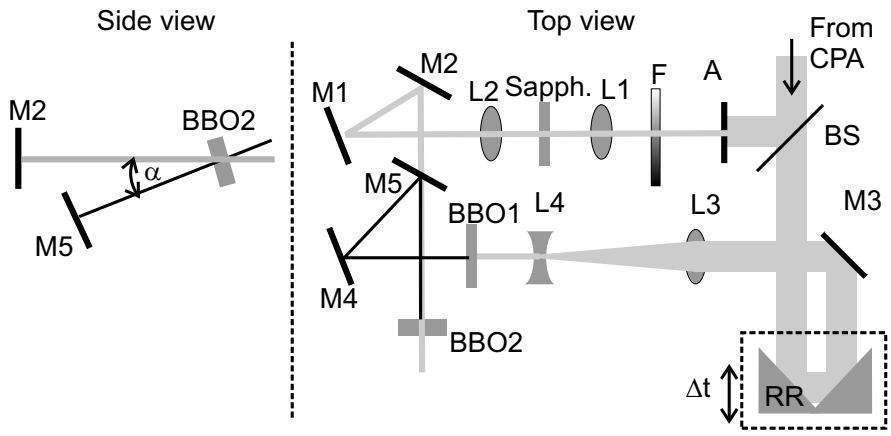

Figure 4.6: NOPA setup used to generate visible light pulses with sub 30 fs duration. Components are described in the text.

4.4.2 NOPA setup

The setup of our homebuild Noncollinear Optical Parametric Amplifier is shown in Fig. 4.6. The design is adopted from the NOPAs build by Riedle and coworkers [211, 212] and improved with respect to efficiency. It consists of three parts: the white light generation, the second harmonic generation and the amplification of the white light. In the amplification process, the photon from the SHG stage is split into two photons in a nonlinear crystal. One is a visible photon (called signal), stimulated by seeding with the white light, and the other is an IR photon (called idler). The pulse duration of our NOPAs signal output is in the sub 30 fs range. Shorter pulses are possible for example by avoiding dispersive optics in the NOPA [213, 214], but not of advantage for the experiments presented here. Our NOPA pulses have a typical energy of 4-10 μJ depending on the wavelength range. Their spectral profile is approximately Gaussian.

About 150 μJ of the fundamental are used for the operation of one NOPA. Circa 4 % of this are needed for the white light generation. The reflected part of the beam at beam splitter BS in Fig. 4.6 is attenuated by a aperture A and a variable grey filter F. It is then focused by lens L1 (f = 20 mm) in a sapphire crystal (thickness = 1 mm) and a white light continuum is generated.[5] The beam is collected by lens L2 and transferred to crystal BBO2 by aluminum coated mirrors M1 and M2.

The 96 % of the 150 μJ which pass the beam splitter BS are guided to a retroreflector RR, mounted on a hand movable micrometer delay stage. The beam is then directed to a telescope by mirror M3. All mirrors up to here are dielectric with maximum reflection at 775 nm. The beam diameter is narrowed in the telescope, consisting of lenses L3 and L4. Afterwards, the pulses are frequency doubled to 387.5 nm wavelength in BBO1.[6] The pulses are transferred to mirrors M4 and M5 (dielectric coated for 387.5 nm). M4 has a vertical tilt, such that the beam height at M5 is below the original optical plane. From M5 it is sent upwards to BBO2, thereby forming the noncollinear angle α with the white light beam (see side view in Fig. 4.6). Finally the SHG pulses are overlapped with the white light pulses in BBO2 at the standard height of the beam.[7]

[5] The white light generation is mainly based on the third order susceptibility $\chi^{(3)}$ of a nonlinear material and its resulting nonlinear index of refraction $n(I) = n_0 + n_2 I(t)$, where n_0 is the linear index of refraction and n_2 the intensity dependent part. Since the phase is a function of n, the frequency changes in time with the time dependent $I(t)$ [199, 200].

[6] BBO is the acronym for a nonlinear birefringent crystal Beta-Barium Borate β-BaB_2O_4 [215].

[7] In Optical Parametric Amplifiers (OPAs) the noncollinear angle is zero.

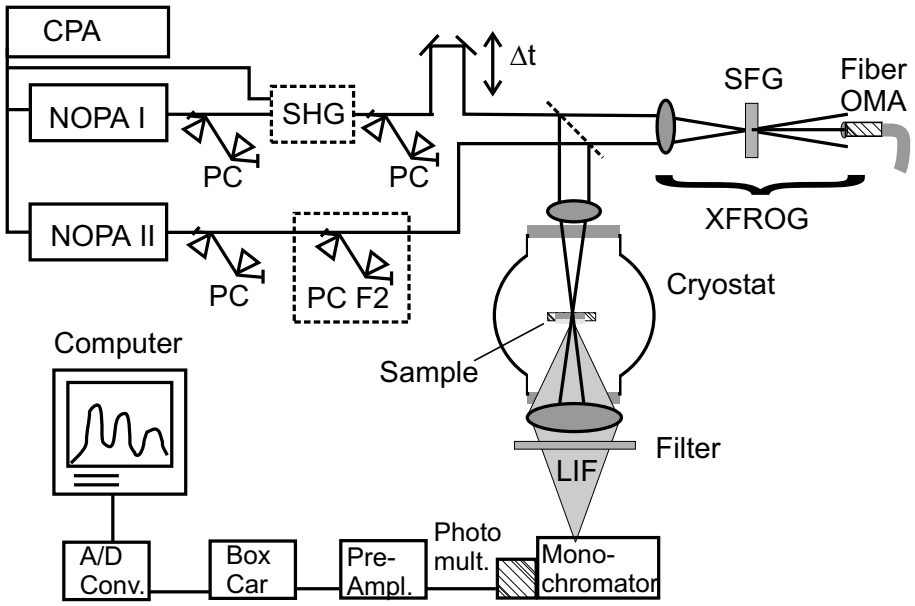

Figure 4.7: Setup for laser system including XFROG and Fluorescence detection for pump-probe spectroscopy. Explanation see text.

For amplification of the white light in BBO2, the white light and SHG pulses have to overlap in BBO2 in space and time. The time overlap can be controlled by the delay of the retroreflector RR. Since the white light is positively chirped, changing the time delay results in an overlap of SHG with different spectral regions of the white light pulse. When the SHG pulse catches the early part of the white light pulse, only the red components are amplified. The blue components are amplified by adjusting the delay to the later part of the white light pulse. In addition to the time overlap, the phase matching angle of the BBO2 has to be tuned according to the color. This reflects the momentum conservation of the photons as described in section 4.3.3. In case of the NOPA for special angle α, the phase matching angle varies only slightly with wavelength [214]. Therefore, a wide spectral range of the white light can be amplified in the signal beam.

To compensate the accumulated positive dispersion from the material in the NOPA and to precompensate for all the lenses and vacuum windows of the cryostat chamber, the pulses pass a prism compressor as described theoretically in section 4.3.2. Examples for precompensating material dispersion have been given there. For achieving the strong negative chirps used in the focusing experiments (section 7.1.4), a strongly dispersive compressor had to be set up. The prisms were made of F2, a highly dispersive glass material. With a 21 cm prism-prism distance chirps β' of more than -2 fs cm were reached. To reach the same amount of negative chirp by the lower dispersive quartz prisms, the quartz compressor has to be a factor of ten longer for visible laser pulses. This large elongation was avoided.

4.5 Pulse characterization

Two pulses (usually from NOPA I and NOPA II) are used for pump-probe spectroscopy. One pump pulse in the visible is required to prepare a vibrational wave packet on covalent states of Br_2 or I_2. Furthermore, a probe pulse is needed according to section 2.3.1, that transfers parts of the wave packet to the CT states. In the system I_2:Kr, a visible pulse can be used to probe the B state wave packet. The doubled CPA fundamental can be used to interrogate an A state wave packet. In the case of Br_2:Ar, one has to generate ultraviolet pulses to transfer a B or A state wave packet to the CT states throughout. Alternatively, a two-photon transition from covalent to CT states can be induced by visible pulses. For visible excitation, the NOPA pulses

are directly used (see Fig. 4.7). To achieve ultraviolet probe pulses, a NOPA can be frequency doubled in a simple type I SHG process [199,200] (see SHG after NOPA in Fig. 4.7). The Prism Compressors (PC) of the NOPA output which is frequency-doubled are adjusted to deliver the highest doubling efficiency. After the SHG generation (typically with 20 % efficiency), the UV pulses pass PCs to precompensate the positive dispersion of the optical elements that follow in the beam path. The generated pulses have to be characterized in the frequency and time domain.

The spectral profile of NOPA pulse is recorded by the OMA. Therefore, a reflection of the pulse on a white surface is monitored. For the frequency doubled NOPA pulses, the beam is directed on a scattering disc, sitting in front of the fibers connected to the OMA. The OMA (commercial by Avantes) consists of two sets of gratings, placed behind a 10 μm entrance slit. One grating, having 600 lines/mm, is specified for 350-850 nm (VIS channel); the other one, having 1200 lines/mm, is specified for 200-400 nm (UV channel). The spectrum is recorded by a 2048 pixel CCD line and digitalized by a 12 bit A/D converter.

The duration of the laser pulses is usually determined by a standard SHG autocorrelator (commercial by APE). The autocorrelator is equipped with thin SHG crystals and one can determine pulse widths in the sub-20-fs range.

Home built cross-correlation setups are used to determine pulse lengths and chirp parameters. One such setup is the so called SFG FROG or XFROG. The principle is described in section 4.3.4. The visible pump pulse coming from NOPA II can be characterized with help of the CPA fundamental or another visible pulse coming from NOPA I (often called gate pulse). The time delay Δt of the two pulses is controlled by a mechanical delay stage. The correlation is performed in the following way: the two pulses are focused and overlapped in a thin BBO crystal (thickness 100 μm SFG in Fig. 4.7). The sum frequency signal is generated, if the two pulses arrive at the crystal at the same time and the phase matching angle of the crystal is correct. It is analyzed by the OMA, as can be seen in Fig. 4.7. The spectrum of the sum frequency is now recorded as a function of the time delay Δt between the two pulses. An example illustrates the mechanism: the pulse from NOPA II is positively chirped and the gate pulse is unchirped. The FROG trace, that means the two dimensional plot of the sum frequency spectra versus the time delay, will show a clear feature: When the gate pulse overlaps with the front part of the chirped pulse, the sum frequency signal is in the red, while it is in the blue at later delays. The FROG spectrum is tilted with respect to time and frequency axis (Fig. 7.13). This is used in Eq. (4.22) to determine the chirp from the FODM.

UV pulses cannot be characterized by a XFROG setup, since the sum frequency photon energy with visible light would exceed the transmission range of any nonlinear crystal. Thus another correlation setup, the so called Polarization Gating (PG) FROG has to be used. It is based on the polarization rotation of a pulse in a Kerr medium gated by another very intensive gate pulse [216].

4.6 Pump-probe and emission spectroscopy setup

The pump and probe pulses are overlapped in space and time in the substrate located in the cryostat chamber.[8] The spatial overlap is controlled via the scattered light from the doped rare gas film. The temporal overlap is searched with help of the real pump-probe signal, that means the emission from the CT states. This Laser Induced Fluorescence (LIF in Fig. 4.7) is emitted into the full spatial angle 4π. Some of it is collected by a f = 120 mm quartz lens outside the chamber and focused on the entrance slit of a monochromator. The detection is

[8] It is worth mentioning, that from the CPA to the experiment, the pulses have travelled approximately 12 m. Still, the pulses have to overlap with fs accuracy (beampath accuracy in the μm range).

collinear with the laser beam direction. Therefore, appropriate filters[9] in combination with a 1/4 m single monochromator (ORIEL CORNERSTONE) are used to block the laser pulses. To reduce scattered light from the probe pulse in case of difficult filtering, a 1/4 m double monochromator (B&W) is used.

A photomultiplier (PM) sensitive in the UV and visible spectral range is attached to the monochromator. The signal of this device is preamplified (FEMTO 1000x) and gated in a boxcar integrator. The boxcar has a window of defined width, during which it integrates the signal. The laser pulses have a repetition rate of one kHz. The charge-transfer fluorescence has a decay in the nanosecond range. Thus, the PM and electronic noise generated in front of the boxcar is strongly reduced with a gate window in the ns range. The integrated signal is digitalized in an analog to digital converter (A/D conv.) and recorded by a computer.

When recording a pump-probe spectrum, an average over several thousand shots is performed for each time delay Δt, to improve the signal to noise ratio.

To record the spectral distribution in an emission spectrum, the time delay Δt between pump and probe pulse is kept fixed. The monochromator transmission wavelength is scanned slowly, while monitoring the boxcar signal with a calibrated x-y recorder. The filters in front of the monochromator entrance slit have to be selected carefully, not to block fluorescence light in the scanning range of the experiment.

[9] If the wavelength of the ultraviolet probe pulse is shorter than the fluorescence to be observed, it is very easy to block the pulse by an edge filter. If it is the other way around, blocking the pulse becomes difficult, if not sometimes impossible.

Chapter 5

Spectroscopic results

The spectroscopic results will be presented in chapter 5 and discussed in chapter 6. They provide useful information for fs pump-probe experiments. The absorption from the electronic ground state X determines the wavelength of the pump pulses to be used. The absorption from the excited covalent states to the charge-transfer states determines the wavelength of the probe pulses. Finally, the emission of the charge-transfer states specifies the detection range of the laser induced fluorescence. The emission and absorption spectra of I_2 in krypton crystals are well understood [26, 96] and shall not be presented here.

5.1 Absorption spectra

The absorption spectra of the Br_2:Ar samples were taken as described in section 4.2. The spectrum of the lamp $I_0(\lambda)$ is smooth in the range to be measured as seen in Fig. 4.3. An example is shown in Fig. 5.1a. The dilution ratio was 1:500 Br_2:Ar, as in all measurements and the sample was deposited for about two hours. A transmission spectrum of the sample-substrate combination is shown in Fig. 5.1a. The spectrum covers the range from 16000 to 42000 cm^{-1}. This could only be achieved by combining the spectra taken by the VIS and UV channel of the OMA. Fig. 5.1b shows the decadic logarithm of the ratio I_0/I (solid line). A background due to scattering of the sample and reflection of surfaces is approximated by a linear function (dashed line). The estimated background is subtracted form the solid line in b) and the resulting graph is plotted in Fig. 5.1c. The CaF_2 substrate is transparent throughout the spectral range shown and the curve in c) reflects the absorbance of the Br_2:Ar sample. The spectrum consists of bands in the visible and ultraviolet range between 16000 and 28000 cm^{-1}, which will be attributed to the electronic transitions to covalent states in the discussion. Furthermore, a strong ultraviolet absorption sets in at 40000 cm^{-1}, which was attributed to Br_2 cluster absorption [57, 62].

5.2 Emission spectra

Emission spectra of Br_2:Ar in the ultraviolet range were recorded upon excitation with visible and ultraviolet NOPA pulses. To attribute the different bands in the ultraviolet, fs pump-probe spectra will be shown. The fluorescence lifetime was determined for these bands and lies in the nanosecond range. The amplified photomultiplier signal is shown in Fig 5.2. Besides a rise which indicates the photomultiplier and electronics response times, a decay on the order of 100 ns can be determined.

The sample of Br_2:Ar was excited by two focused ultrashort laser pulses, one being centered at 498 nm (coming out of a NOPA), the other one centered at 267 nm (the second harmonic of a NOPA). The spectral distribution of the induced fluorescence is shown as the solid line in Fig. 5.3a. The sample temperature was about 20 K. Two bands labelled 1 (broad at 29450 cm^{-1} or 340 nm) and 2 (narrow at 31080 cm^{-1} or 322 nm) were found. The bands appeared only for excitation with both pulses. Furthermore, the time order was important: the visible pulse had to

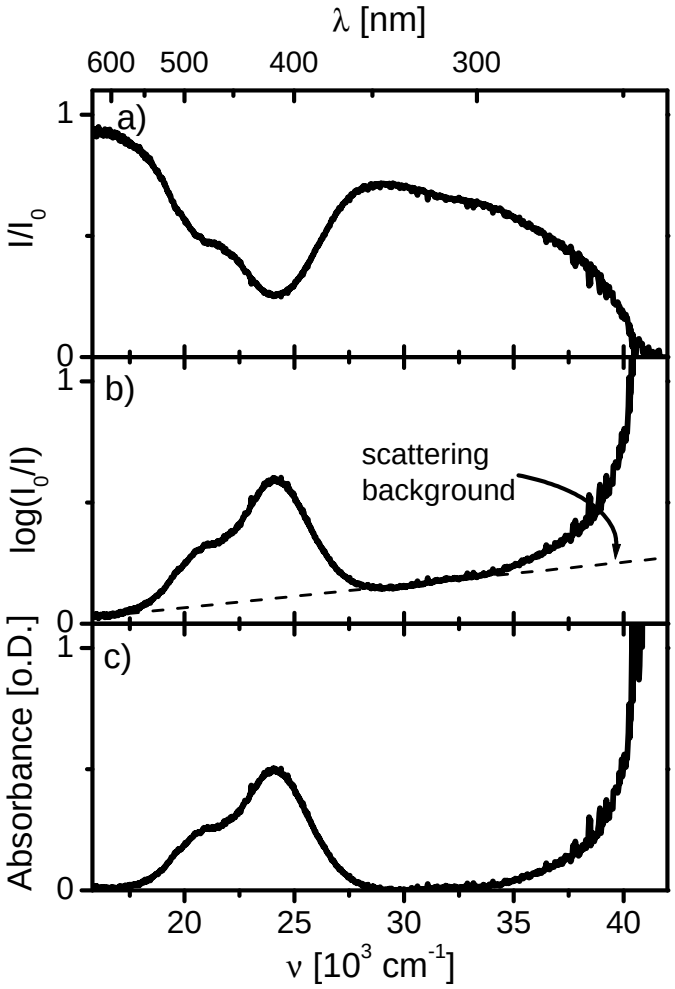

Figure 5.1: a) The transmission I/I_0 of the substrate with the Br_2:Ar crystal is shown versus wavelength or quantum energy. b) $\log(I_0/I)$ (solid line) and background due to scattering (dashed line) are displayed. c) The spectrum of b) after background subtraction corresponds to the the absorbance of the system Br_2:Ar.

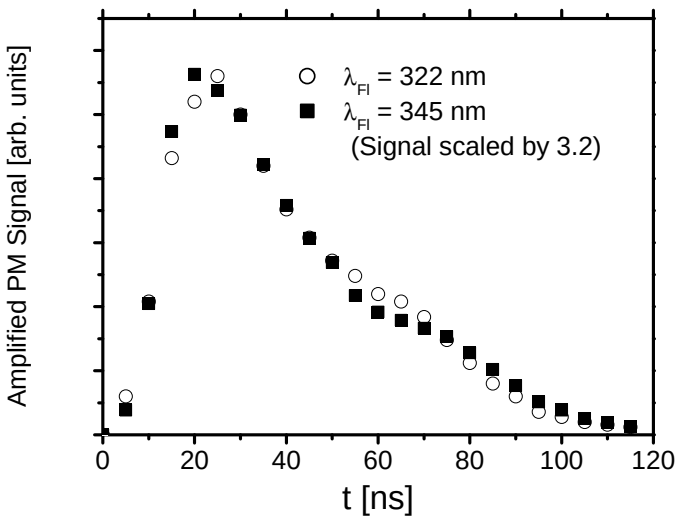

Figure 5.2: Amplified photomultiplier signal time course for detecting the fluorescence of on band 2 at 322 nm wavelength (solid squares) and on band 1 at 345 nm at 345 nm wavelength (open circles). The Br_2:Ar sample (T = 20K) was excited in a three photon process with pulses centered at 500 nm.

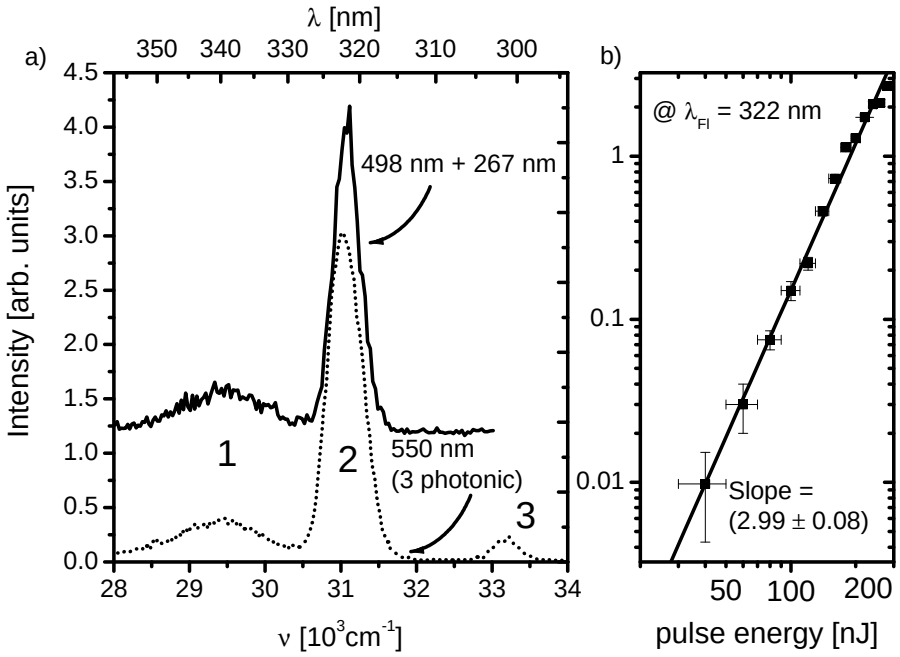

Figure 5.3: a) Ultraviolet fluorescence bands of Br_2:Ar. Solid line: The fluorescence induced by adjacent pulses of 498 nm and 267 nm central wavelength. A background was added to distinguish it from the other data. Dotted line: Fluorescence induced by a single 550 nm pulse. The power dependence of the latter fluorescence at 322 nm is presented in b): The slope in the double logarithmic graph indicates a three photon transition.

excite the sample before the ultraviolet pulse. Tab. reftab:uvbands summarizes the experimental findings for emission bands in the ultraviolet range for different excitation conditions.

Besides an excitation with two separate pulses (for example 498 and 267 nm), one visible pulse alone can also induce ultraviolet emission when it is tightly focused. The corresponding bands are shown as the dashed line in Fig. 5.3a. Bands 1 (at 29350 cm^{-1}) and 2 (at 31060 cm^{-1}) are similar to the combined excitation and a new band labelled 3 (at 33180 cm^{-1} or 300 nm) shows up in the high energy part of the spectrum. A multiphoton excitation process is required. An analysis of the fluorescence versus the pulse energy for fixed focusing conditions is shown in in Fig. 5.3b. The slope of the line in the double logarithmic graph has a value clearly indicating a three photon transition.

These fluorescence bands have been observed for a variety of excitation wavelength combinations and the power dependence indicates one-photon (1 phot.) and two-photon (2 phot.) contributions as given in Tab. 5.1. For example, a first excitation pulse between 490 and 610 nm induces a one-photon transition while for the following pulse situated between 540 and 640 nm

Table 5.1: Ultraviolet emission bands (1-3) of Br_2:Ar with band centers (first number) and widths (FWHM in brackets) in cm^{-1}.

Excit. [nm] (n photons)	1 [cm^{-1}]	2 [cm^{-1}]	3 [cm^{-1}]
498 (1 phot.) + 267 (1 phot.)	29450 (1360)	31080 (420)	-
550 (3 phot.)	29350 (1500)	31060 (530)	33180 (450)
535 nm (1 phot.) + 630 nm (2 phot.)	29380(1400)	31100 (560)	33190 (528)

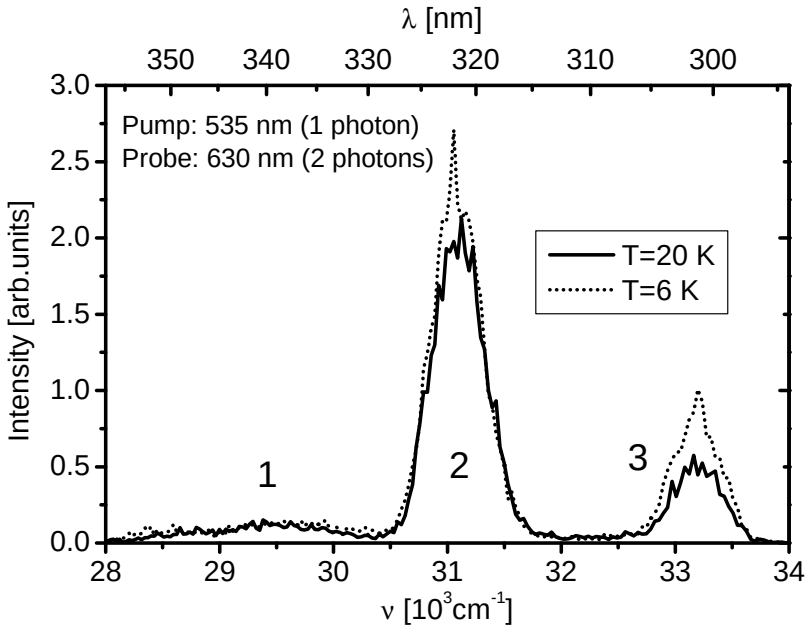

Figure 5.4: Temperature dependence of the ultraviolet emission bands of Br_2:Ar. The 535 nm pulse induces a one-photon transition, whereas the 630 nm pulse gives rise to a two-photon transition. The temperature increase leads to a quenching of fluorescence being the same for bands 1 and 2 and larger for band 3. The sub-structures on the bands are statistical and could not be reproduced in other experiments.

a two-photon transition signature is observed. Typical emission spectra for these excitation conditions (535 nm (1p) + 630 nm (2p)) are displayed in Fig. 5.4 for two different sample temperatures.

This figure stresses another remarkable aspect of the band intensity: it decreases with increasing sample temperature. The effect is rather small on bands 1 and 2, with an increase by a factor 1.3 when decreasing the temperature from 20 K to 6 K. On band 3, the intensity increases by a factor of 2 for the same temperature change.

The ultrafast dynamics detected via the different fluorescence bands will be presented in the next sections. It is however necessary to take this aspect into account when assigning the bands to certain transitions of the molecule. Some time resolved pump-probe spectra are shown in Fig. 5.5. The sample was excited to a covalent state via a one-photon transition (540 nm central wavelength) and the excited state dynamics was probed by two photons from a 620 nm pulse. The dynamics time courses with 322 and 340 nm fluorescence wavelength are identical (Fig. 5.5c, e and d, f). Recording the fluorescence at 300 nm (Fig. 5.5a and b), a shortening of the decay in Fig. 5.5a compared to Fig. 5.5c and e is observed. Nevertheless, the oscillations in Fig. 5.5b, d and f emerging from vibrational wave packet dynamics are the same for all fluorescence bands.

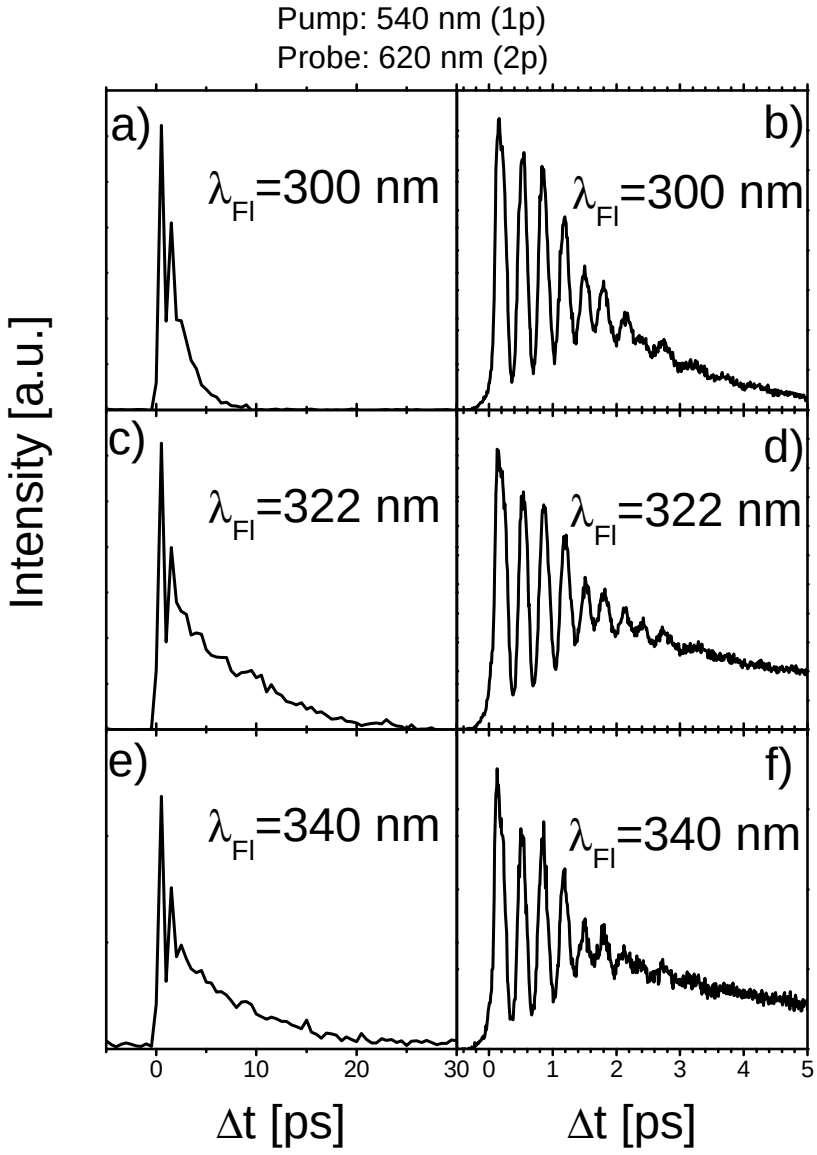

Figure 5.5: Pump-probe signals for the different ultraviolet emission bands. A large time range with picosecond signal decay is shown in the left panel, whereas the wave packet dynamics is resolved on the right panel spectra. The step width of 500 fs is large in the left long time range, which washes out the oscillatory behavior visible in the right panels with 20 fs step width.

Chapter 6

Discussion of spectroscopic results

6.1 Discussion of absorption spectra

The experimental absorption spectrum from Fig. 5.1c with subtracted scattering background is reproduced in the range of covalent transitions as the solid line in Fig. 6.1. As mentioned above, the Br_2 to Ar ratio in the premixed gas was 1:500 and the temperature of the sample was kept at 20 K. This spectrum is compared to the free Br_2 absorption spectrum at 300 K published in Ref. [39], shown as solid squares in Fig. 6.1. The maximum at 24100 cm^{-1} and the shoulder at 23000 cm^{-1} coincide. Only the blue and red wings of the gas phase absorption seem to extend further than in the solid phase. One explanation for this behavior rests on the different temperatures. Vibrational levels $v'' = 1$ and $v'' = 2$ in the electronic ground state X are populated in case of a measurement at 300 K; whereas at 20 K, essentially only the $v'' = 0$ level is populated (see Tab. 6.1). The vibrational wavefunctions of $v'' = 1, 2$ are more expanded in the internuclear coordinate compared to $v'' = 0$ leading to broader absorptions.

Our absorption spectrum is also compared to data taken by L. Andrews on similar samples at 17 K [57] in Fig. 6.1, however at a larger Br_2 concentration of 1:200. A scattering background was also removed in this case.

The spectral position of the maximum at 24100 cm^{-1} (415 nm) coincides in both spectra. The differences in the red part with a strong shoulder and a more extensive wing in the spectrum with 1:200 dilution may be due to the clustering in this higher concentrated sample. The background in Andrews data [57] is also larger than the background measured in the course of this work.

In order to create a theoretical absorption spectrum, the projection (or reflection) method was applied for the states A, B and C separately. Finally the covalent state absorbances were added up to yield a theoretical absorption spectrum. The relative strength of the individual theoretical covalent absorbances was optimized for a good agreement with the experimental curve.

The projection method shall be briefly described. It works very well for unstructured absorption spectra in the case of transitions to a continuum or highly excited, densely spaced vibrational states of an anharmonic oscillator [217]. In principle, one has to calculate the Franck-

Table 6.1: Population N_1 and N_2 of the vibrational levels $v'' = 1$ and 2 in units of the population of $v'' = 0$ (N_0) for the Br_2 X state at 20 and 300 K. Boltzmann statistics in the harmonic limit with a value for ω_e = 325 cm^{-1} (79,79 isotope [43]) is used.

T [K]	N_1	N_2
20	$7 \cdot 10^{-11}\ N_0$	$5 \cdot 10^{-11}\ N_0$
300	0.21 N_0	0.04 N_0

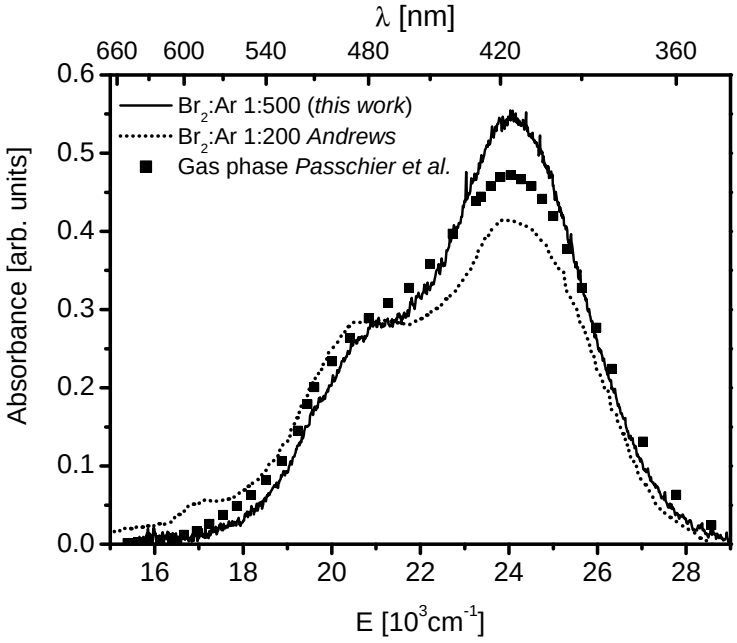

Figure 6.1: Comparison of the different Br_2:Ar absorption spectra with gas phase spectrum. Solid line: this work with a dilution of 1:500. Dotted line: spectrum using a sample of 1:200 dilution, measured by Andrews [57]. The solid squares give the scaled gas phase absorption from Passchier *et al.* [39].

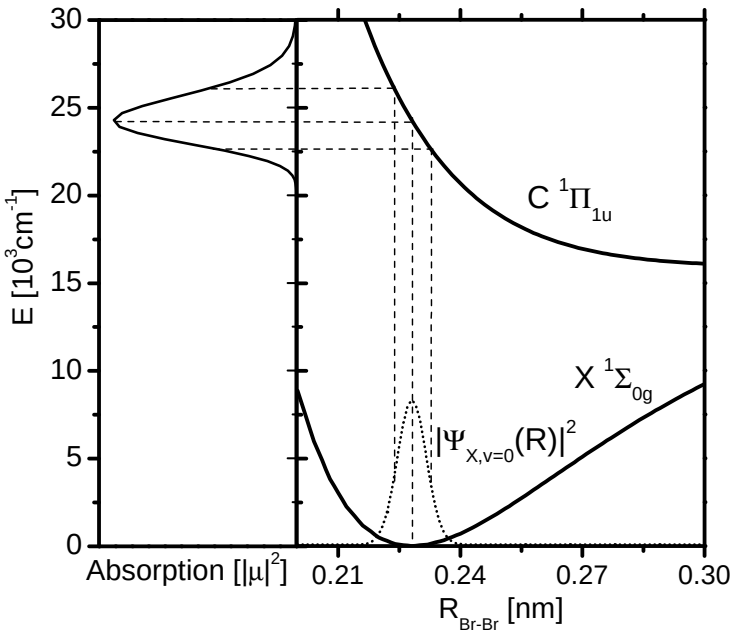

Figure 6.2: Construction of an absorption spectrum for the bromine C $\longleftarrow$ X transition. The ground state X, $v = 0$ population (79,81 isotope) is projected on the C state. This yields the absorption spectrum without including the transition dipole μ (Condon approximation for constant transition dipole). A finite curvature in the excited state results in a asymmetry of the absorption.

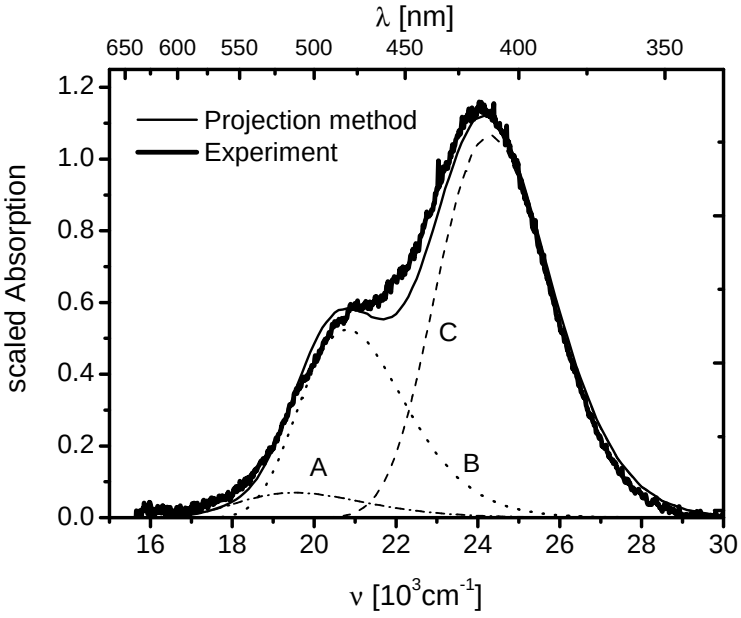

Figure 6.3: Comparison of the experimental absorbance (thick solid line) with the projection method absorbance (thin solid line). The A (dash dotted), B (dotted), and C (dashed) states are taken into account.

Condon factors to construct an absorption spectrum $\sigma_{abs}(\nu)$. In case of a dissociative state, the eigenstates form a continuum and the corresponding wave functions are strongly peaked at the limb of the potential energy surface. Thus, the electronic absorption spectrum can be simulated by projecting the absolute square of the ground state wave function $|\Psi_X(R)|^2$ on the repulsive limb of the excited electronic state and multiplication with the square of the electronic transition $|\mu_{X-B}(R)|^2$ dipole

$$\sigma_{abs}(\nu) = |\Psi_X(R)|^2 |\frac{dV(R)}{dR}|^{-1} |\mu_{X-B}(R)|^2, \tag{6.1}$$

with an excited state potential V(R). The projection method is illustrated in Fig. 6.2 for the C ⟵ X transition. The ground state probability is projected on the C state yielding a smooth absorption spectrum. The wider the electronic ground state population extends in R, the broader are the wings of the absorption spectrum in Fig. 6.2. This confirms the trend of a wider absorption spectrum at high temperatures, mentioned in the comparison with the gas phase absorption at 300 K.

To perform this calculation of absorbances of the covalent states A, B and C, one needs the ground state and excited state data. The gas phase values were chosen as a first attempt. For the A and B states, gas phase data given in [52] and [43] were taken. For the C ($^1\Pi$) state, the potential of Ref. [47] was used. This reference also contains explicit expressions for the transition dipole elements of the B←X and C←X transitions. The transition dipole to the A state was set constant ("Condon approximation"), since no reference on its R dependence could be found.

The results of the projection method for different states are shown in Fig. 6.3. The C state (dashed line), B state (dotted line) and A state (dash dotted line) absorbances are added up to yield the theoretical absorption spectrum shown as the thin solid line in Fig. 6.3. The relative absorbance strength among the three transitions was scaled until their sum agreed with the experimental spectrum for Br_2 in solid argon (thick solid line in Fig. 6.3). The ratio of the absorbance maxima for the C, B, and A state are 1 : 0.48 : 0.067. This can be compared with theoretical results from *ab initio* calculations in [173], shown in Fig. 3.5. The respective ratio

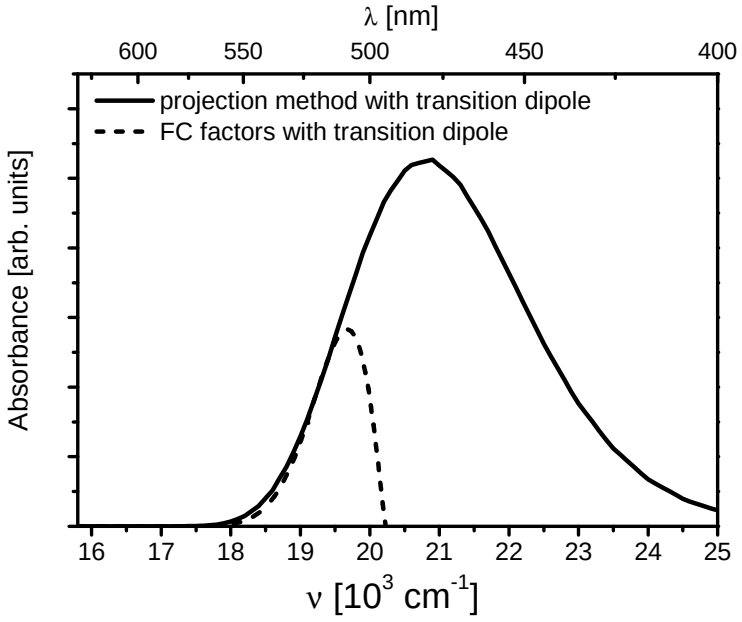

Figure 6.4: Comparison of projection method to Franck-Condon factors. The solid line is calculated by the projection method including the squared transition dipole from [47]. The dashed curve shows the Franck-Condon factors also multiplied by the squared transition dipole from [47].

was 1 : 0.46 : 0.057. Thus only a small variation in the relative state absorptions comparing Ref. [173] to our results are found.

The A state absorbance between 16000 cm^{-1}(625 nm) and 18500 cm^{-1}(540 nm) is much higher than the corresponding B state absorbance in this range. The maximum and the shoulder of the experimental absorption spectrum are reproduced quite well by the projection method (see Fig. 6.3). The transition to the relevant B and C state terminate on the repulsive limb above the gas phase dissociation limit and the projection method should work well. From the agreement of the matrix spectrum with the simulated one, based on gas phase potentials, we conclude that the molecule-matrix interaction does not shift the potentials in the energy range close to the maxima of the absorption spectrum. For the A state, such a statement cannot be deduced from the absorption spectrum.

The projection or reflection method does not work very well for low vibrational levels in a bound electronic state. A relevant example is the absorption to the B state of Br_2. The Franck-Condon (FC) factors for the B $\longleftarrow$ X transition were calculated by integrating Morse oscillator wavefunctions. The parameters for the potential were adopted from Langen *et al.* [66]. The wavefunctions were calculated by polynomials with a limited accuracy. From about 19400 cm^{-1} to higher energies, the FC factors cannot be considered as useful because of numerical errors. The FC factors were multiplied by the squared transition dipole strength from Ref. [47], which depends on the excitation energy. The resulting spectrum is the dashed line in Fig. 6.4. The B state absorption was also calculated by the projection method with the same squared transition dipole and is shown as the solid line in Fig. 6.4. The spectra are scaled to read a coincidence in a interval around 19200 cm^{-1}. In this way, the FC factors yield a smaller absorption below 19000 cm^{-1} compared with the projection method. The projection method is not reliable any more for these deep excitation energies in the B well. Therefore, the absorption calculated with FC factors will be used in this range.

Table 6.2 contains spectral information on the covalent states A', A and B in gas phase as well as in an Ar matrix taken from the literature. Throughout all states, a general redshift of the T_e value from the gas phase to the matrix can be found. However, only low vibrational states in

Table 6.2: Spectroscopic data for different electronic states of Br_2 in solid Ar and gas phase with T_e (minimal potential energy), ω_e (vibrational frequency), and $\omega_e x_e$ (anharmonicity).

State	Isotope	System	T_e [cm^{-1}]	ω_e [cm^{-1}]	$\omega_e x_e$ [cm^{-1}]	Ref.
$X^1\Sigma_{0g}$	79,79	gas	0	325.3213	1.07742	[43]
	79,79	matrix	0	318.65	0.820	[66]
	81,81	gas	0	321.2798	1.0508	[43]
	81,81	matrix	0	317.0	1.04	[55]
	81,81	matrix	0	314.91	0.858	[66]
$B^3\Pi_{0u}$	79.79	gas	15902.47	167.6066	1.63608	[43]
	79,79	matrix	15415.0	169.5	1.59	[55]
	79,79	matrix	15701.2 (emission)			[66]
	79,79	matrix	15722 (absorption)	167.14	1.588	[66]
	81,81	gas	15902.47	165.5244	1.5957	[43]
	81,81	matrix	15705.9			[66]
$A^3\Pi_{1u}$	79,79	gas	13905	153.8	2.78	[42]
	79,79	matrix	13650			[60]
	79,79	matrix	13650			[66]
	79,79	matrix	13665.4 (A*)			[66]
	81,81	gas	13905	151.9	2.71	[42]
	81,81	matrix	13650			[60]
	81,81	matrix	13699.9			[66]
	81,81	matrix	13663.0 (A*)			[66]
$A'^3\Pi_{2u}$	79.79	gas	13220	165.172	2.504	[49]
	79,79	matrix	12966			[63]
	79,79	matrix	12974.7			[66]
	81,81	gas	13220			[49]
	81,81	matrix	12966			[63]
	81,81	matrix	12976.5			[66]

the covalent electronic states were addressed in literature. Thus, our result of no potential shift in the range of the absorption maxima remains untouched. The shift for the B state is supposed to be 487 cm^{-1} according to Bondybey [55]. Langen proposes a smaller shift of 180.5 cm^{-1} in absorption and 201.3 cm^{-1} in emission [66]. Since the $v' = 0 \longrightarrow v'' = 0$ cannot be observed in emission, the assignment of the potential minimum energy T_e has to rely on other facts like the isotope splitting. Langen *et al.* doubt the assignment in [55] and propose a new one, leading to the shift of T_e (minimal potential energy) in [66] and Tab. 6.2, which we follow throughout this work. The different redshift in absorption and emission can be explained by a cage rearrangement due to a different Br-Ar interaction in the molecular B state compared to the ground state Br-Ar potential (see section 8.3.1 for a model calculation on that). The spectral parameters in Tab. 6.2 are taken from Morse potentials. Those are precise only near the potential minimum of the excited electronic states.

An excitation spectrum for the Br_2:Ar system was measured by V. Bondybey and coworkers. The spectrum is reproduced in Fig. 3.8 and shows sharp spectral features known as ZPL, which could not be observed in absorption spectra performed in this work. The spectra remained unstructured even for cooling the Br_2:Ar sample down to 5 K by a liquid He flow cryostat. The sample preparation in Ref. [55] and this work was the same. Thus, a stronger inhomogeneous broadening of our Br_2:Ar samples compared to those of Ref. [55] is unlikely. Even the fact,

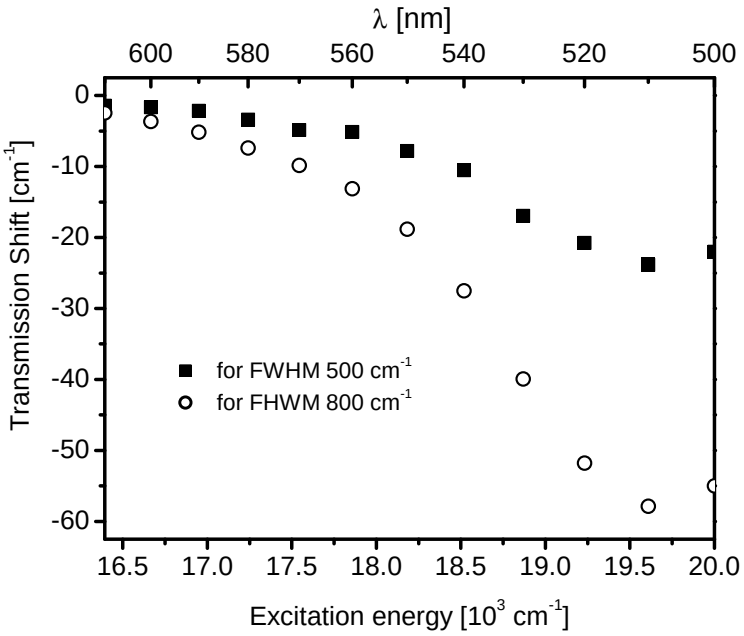

Figure 6.5: Spectral maximum shift for typical laser pulses after propagating through half the crystal. The mean energy before passing the sample is given on the x axis. The shift of the pulse spectral maximum in wavenumbers is given on the y axis for a width of 500 cm^{-1}(solid squares) and 800 cm^{-1} (open circles).

that all isotopes should be visible in absorption spectra, could not hide the ZPLs as explained in context with Fig. 3.1. The origin for the vanishing ZPL is the strong absorption background due to the A state in the range of interest (16000–17500 cm^{-1}). From the decomposition of the absorbance in the projection method and by use of the FC factors for the B state (Fig. 6.3), it follows that the B state absorption is about three orders of magnitude smaller than the A state absorption in this spectral domain. The excitation spectroscopy in [55] is free of this A state background. Thus, a much better signal to noise ratio would be required in the absorption spectra to observe the B state vibrational structure.

Considering the intensity distribution in the vibrational progression shown in Fig. 3.8, a yet unresolved problem occurs: the FC factors (see Fig. 6.4) increase exponentially throughout the spectral range shown in Fig. 3.8. Indeed, for $v' = 1, 2, 3$ (according to Langens nomenclature [66]), the signal rises. From $v' = 4$ to higher levels, only small intensity variations appear in the ZPL. Even if also the phonon sideband is taken into account, only a mild rise is obtained. A real quantitative analysis is not possible, since the spectrum in Fig. 3.8 is not normalized on the excitation laser intensity. Nevertheless, from $v' = 4$ on, the intensity distribution is unusual. A crossing of another electronic state with the B state leading to predissociation above $v' = 3$ or 4 could present an explanation. Above the crossing, predissociation can remove population from the B state, thereby reducing its $v' = 0$ emission intensity, while the population remains unaffected when excited below the electronic state crossing. A study comparing predissociation and vibrational energy relaxation was performed for I_2 in solid Kr [26, 27].

To create wave packets, several vibrational levels are coherently coupled by spectrally broad pulses. The increase of total absorption with photon energy leads to a stronger absorption on the blue side which could lead to a spectral red shift in the propagation through the sample. The effect was estimated with the absorption spectrum (Fig. 6.1). The shift is less than 20 cm^{-1} for typical pulses of 500 cm^{-1} FWHM and less than 60 cm^{-1} for very broad pulses of 800 cm^{-1} FWHM. The shift is shown in Fig. 6.5 and corresponds to less than 1.5 nm at 510 nm central wavelength and is not relevant for the further discussion.

6.2 Discussion of emission spectra and assignment of probe windows

A method to determine R_{win} from the probe wavelength λ_{probe} was worked out in section 2.3.1. For the probe window, we derived the condition (see Eq. (2.26)) $\Delta V(R_{\mathrm{win}}) = hc/\lambda_{\mathrm{probe}}$, with $\Delta V(R)$ being the difference potential between the covalent and the CT state involved in the probe transition. For the free Br_2 molecule, the difference potentials are known from high resolution spectroscopy (see Fig. 3.3). In case of Br_2:Ar, the charge-transfer (CT) states are stronger redshifted than the covalent states (Tab. 6.2) as explained in section 3.2. The redshift observed in emission spectra from CT to covalent states will be used to determine the difference potentials for the resulting probe transitions.

6.2.1 One-photon probe transitions

The lower covalent states A, B, and C are excited by visible light from the electronic ground state, as shown by absorption spectroscopy (Fig. 6.3). A following UV pulse can excite the transient population to CT states within the lifetime of the covalent states (see Tab. 3.3). The C state is dissociative in the free molecule case and decays into lower lying states like A, A' and X. The absorption from the covalent state to the CT states has to fulfill the selection rule $\Delta\Omega$ = 0 (section 3.1.3). The transitions from B, A, and A' to the lowest CT states correspond to E $\longleftarrow$ B, $\beta \longleftarrow$ A and D' $\longleftarrow$ A' [111, 112]. Within the CT tier, a strong mixing is expected leading to a competition between radiative decay and nonradiative transitions to lower states.

The upper spectrum in Fig. 5.3a (solid line) was recorded with a visible pulse exciting the covalent manifold and a subsequent ultraviolet pulse (both one-photon transitions) inducing a transition to CT states. The lowest group of CT states has its energetic minimum at 48934 cm^{-1} (at R_e = 0.317 nm) in the gas phase [49] (see Tab. 3.2), the second at 52641 cm^{-1} (at R_e = 0.318 nm) [169]. The combined photon energy of 498 and 267 nm laser pulses is 57530 cm^{-1}. This energy is sufficient to reach the CT manifolds. The fluorescence of the lowest lying charge-transfer state D'(2_g) to the covalent A'(2_u) state is located between 280 and 295 nm for free Br_2 molecules [49]. In the condensed phase, a redshift of the fluorescence is expected according to the inductive and geometrical shifts explained in section 3.2.

The emission of the CT states to the covalent states is usually strong from the lowest lying charge-transfer state D'(2_g), as can be learnt from I_2 in matrices [26, 27, 96]. Energy relaxation funnels the population down to the lowest lying D' state. Hence, the strong emission at band 2 is attributed to the D'$\rightarrow$A' fluorescence from the lowest vibrational level of the D' state, since the selection rule $\Delta\Omega$ = 0 is fulfilled in that transition.

Taking the free Br_2 molecular potentials into account, an emission from the $v' = 0$ level of the D' state to the A' state would lead to a band centered around 34380 cm^{-1}. Comparing it to the experimental transition energy for Br_2:Ar of 31080 cm^{-1}, leads to a redshift of 3300 cm^{-1}. This emission redshift might be either due to a *blueshift* of the lower A' state or to a redshift of the D' state energy. The first choice is ruled out, according to the *redshifts* at internuclear distances close to the minima of the CT states (collected in Tab. 6.2). The emission redshift of the covalent states are one order of magnitude lower than the charge-transfer emission redshifts. In conclusion, the shift of 3300 cm^{-1} will be fully attributed to a redshift of the CT state D' (Fig. 6.6). All other CT states lying in that first manifold are shifted by the same amount. The shift is reasonable compared to other molecules in condensed rare gases, *e.g.* about 5000 cm^{-1} for I_2 in solid Kr [27, 96], about 3000 cm^{-1} for I_2 in solid Ar [96] and 10000 cm^{-1} for ClF in solid Ar [14].

Besides the transition energy, one can compare the expected bandwidth from the redshifted potentials to those observed in the experimental spectrum (Fig. 5.3a). In order to calculate the width, one applies the projection method used for absorption spectroscopy before (section

6.1). The excited state $v' = 0$ population distribution is projected on a lower lying state to determine the theoretical emission bandwidth. With ω_e = 150 cm^{-1} = $2.83 \cdot 10^{13}$ rad/s for the CT states [53], the FWHM of the CT $v' = 0$ population is given as $\Delta x = \sqrt{(4 \ln 2\hbar)/(\mu\omega_e)}$ = 0.0124 nm. Taking Δx and projecting it from the D' state to the A' state, an emission bandwidth of 350 cm^{-1} is calculated, which is close to the experimental value of (500 $\pm$ 100) cm^{-1}. Thus, the result again confirms the assignment of band 2 to the D'→A' transition. Fig. 6.6 shows the redshifts of the CT states compared to the gas phase value.

Table 6.3 collects emission energies calculated from gas phase CT states with a redshift of 3300 cm^{-1} together with the bandwidth.

Table 6.3: Calculated UV emission bands of Br_2:Ar with a redshift of 3330 cm^{-1} relative to the free molecule and assignment to bands in Fig. 5.3a.

Transition	$\Delta\Omega$	center [cm^{-1}]	width [cm^{-1}]	band
D'→A'	0	31080	350	2
D'→A	1	30738	270	1
E→B	0	28955	430	1
$\beta \rightarrow$ A	0	31174	260	2

Band 2 in Fig. 5.3a could have additional contributions from a close lying $\beta \rightarrow$ A transition. However, most of it should originate from the lowest lying D' state.

The photon energy of band 1 is consistent with the transitions D' $\longrightarrow$ A and E $\longrightarrow$ B according to Tab. 6.3. Among the transitions, those obeying $\Delta\Omega$ = 0 are most likely. None of the transitions has the experimentally observed width of 1400 cm^{-1}, but a superposition of several transitions mimics a broader width. Apart from the documented molecular covalent states, several non documented repulsive (but cage-bound in our case) states exist. This can be deduced from the states published for I_2 [168] and the similarity of halogen molecules considering the number and character of electronic states. They have potential curves similar to the C($^1\Pi$) state. They cross the B state and have the same gas phase dissociation limit as the ground state. Emissions from the CT states to those undocumented manifold is very likely to contribute to band 1 in addition to those collected in Tab. 6.3.

The dynamics observed on band 1 and 2 are similar and therefore they should belong to the same probe transition. This is consistent with the fact that all the CT states D', β and E belong to the same tier and mix effectively. To derive the difference potential $\Delta V(R)$ for a probe transition, the free molecule shape of the potential energy curves is assumed. The selection rule $\Delta\Omega$ = 0 and the 3300 cm^{-1} shift for the CT states are considered. The difference potentials taken into account in Fig. 6.7a are E-B (solid curve in Fig. 6.7)a)), β-A (dashed curve in Fig. 6.7)a)) and 0_g-B (dotted curve in Fig. 6.7)a)). The last transition will be discussed in connection with the two-photon probe transitions in the next section.

The scheme in Fig. 6.7a gives valuable information about possible probe wavelengths. A wavelength limit for λ_{probe} < 350 nm is obvious since the CT states have to be in reach from the covalent states.[1] The A state can be probed to β for λ_{probe} < 322 nm (see dashed curve in Fig. 6.7a). Separation of A and B state dynamics can be achieved by selecting a special λ_{probe}. When λ_{probe} is chosen between 350 and 322 nm, the B state will be probed exclusively, since the probe quantum energy hc/λ_{probe} is not large enough to induce the $\beta \longleftarrow$ A transition.

The difference potentials can also be used to determine the probe window parameter R_{win}, *i.e.* the internuclear location of the probe window, and E_{win} the covalent state energy at R_{win} (see

[1] Indeed, it will be shown in Fig. 7.4, that probe transitions with λ_{probe} = 354 nm are possible. This is due to the fact of a finite spectral width and the influence of the coherent host motion that will be discussed in section 8.3

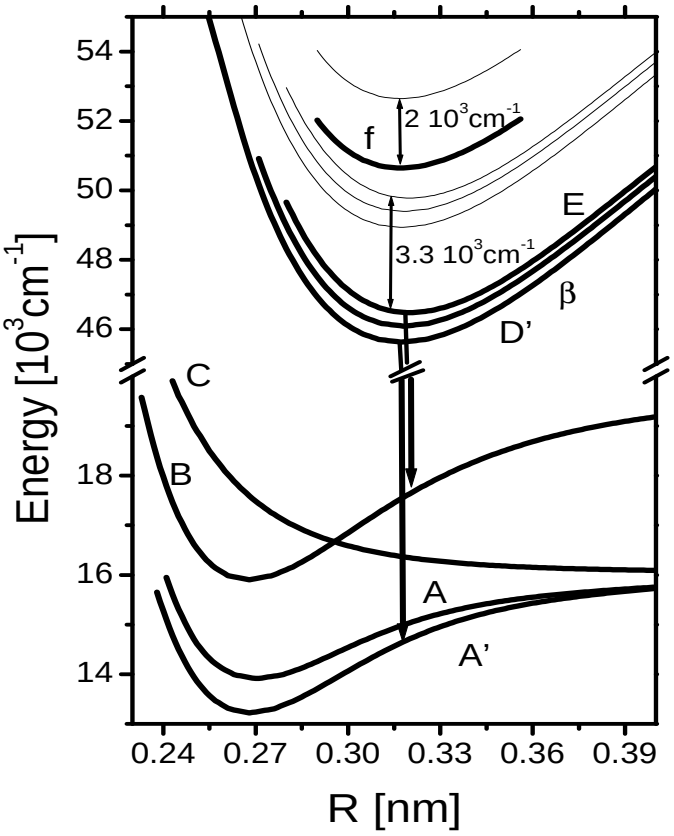

Figure 6.6: Covalent and charge-transfer states of the Br_2 molecule. The thin lines represent some charge-transfer states of the free molecule, the thick lines are reshifted states in the RGS. The matrix induces a redshift in emission of 3300 cm^{-1} for the lower charge-transfer states and 2000 cm^{-1} for the second tier.

section 2.3.1). The B ⟵ E probe transition is chosen as an example: For $\lambda_{\rm probe}$ = 350 nm the B-E difference potential is resonant with ΔV at $R_{\rm win}$ = 0.334 nm (see solid curve in Fig. 6.7a). The B state has a potential energy of 18087 cm^{-1} = $E_{\rm win}$ at this given $R_{\rm win}$.

6.2.2 Two-photon probe transitions

The reason to postulate a two-photon probe step is given by the dotted curve in Fig. 5.3a. A fs laser pulse at 550 nm induces three ultraviolet fluorescence bands, two of them already known from visible pump and UV probe. The power dependence in the inset of Fig. 5.3a clearly demonstrates the three photon character of this transition. One photon is needed to excite the covalent states (A,B,C) from the ground state. The remaining two photons induce a probe step to the first and second charge-transfer manifold. The sequence is broken up in Fig. 6.8, using a 535 nm centered pulse for pumping and a 620 nm centered pulse for probing. The probe pulse power dependence in Fig. 6.8 is second order, confirming the two-photon probe process.

The fluorescence bands at 345 (band 1) and 322 nm (band 2) are the same as in the one-photon case. Therefore, the first ionic manifold is definitely fluorescing and the assignment of the emission from the previous subsection must be applied here. Nevertheless, the CT states to be excited are most likely different. A one-photon transition couples the ungerade (u) valence states to gerade (g) CT states, *e.g.* B($^3\Pi_{0u}$) to E(0_g). A two-photon transition has to couple states of equal parity. Thus a E ← B transition is forbidden for two photons, if the matrix does not weaken this rule. Up to now, no indications for a weakening exist. Therefore, CT states of ungerade parity are excited in the two-photon probe step. Unfortunately, those states are not known from free Br_2 molecular spectroscopy. From analogy with I_2 (a case in which potentials for ungerade charge-transfer states are documented), a solution is constructed: The D(0_u) state likely for a D ← B probe transition, is substituted by the E state, because they are quite close in

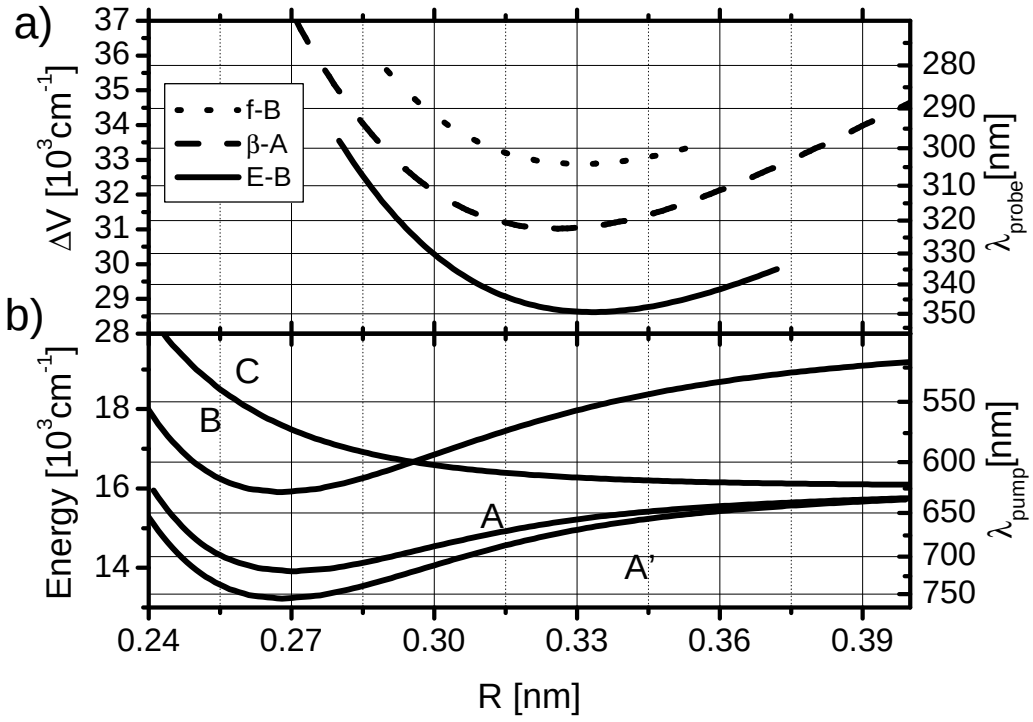

Figure 6.7: b) Covalent potential curves of Br_2 and a) difference potentials to appropriate charge-transfer states. For the selection of the difference potentials, the selection rule $\Delta\Omega = 0$ is obeyed and the E-B, β-A and f-B potential curves are shown in a).

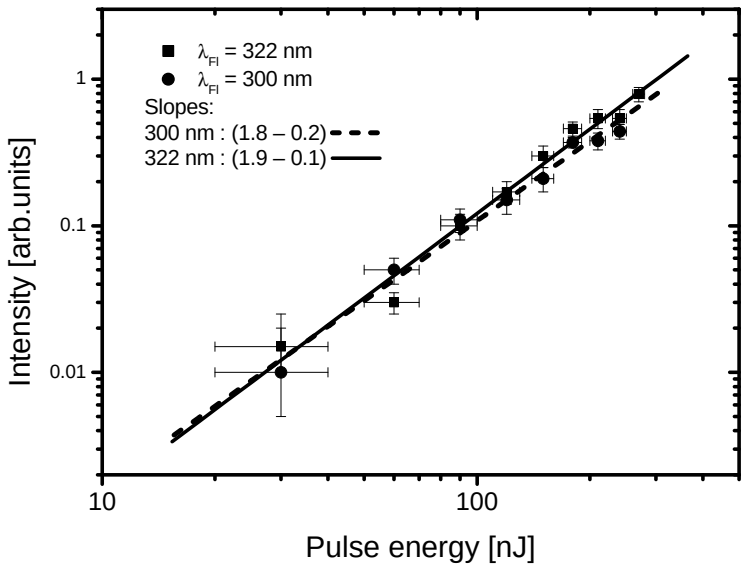

Figure 6.8: Probe pulse energy dependence of the UV fluorescence at 300 and 322 nm. The slopes of about two in the double logarithmic plot clearly indicate a two-photon probe process. The pump pulse was centered at λ_{pump} = 535 nm, the probe pulse at λ_{probe} = 620 nm.

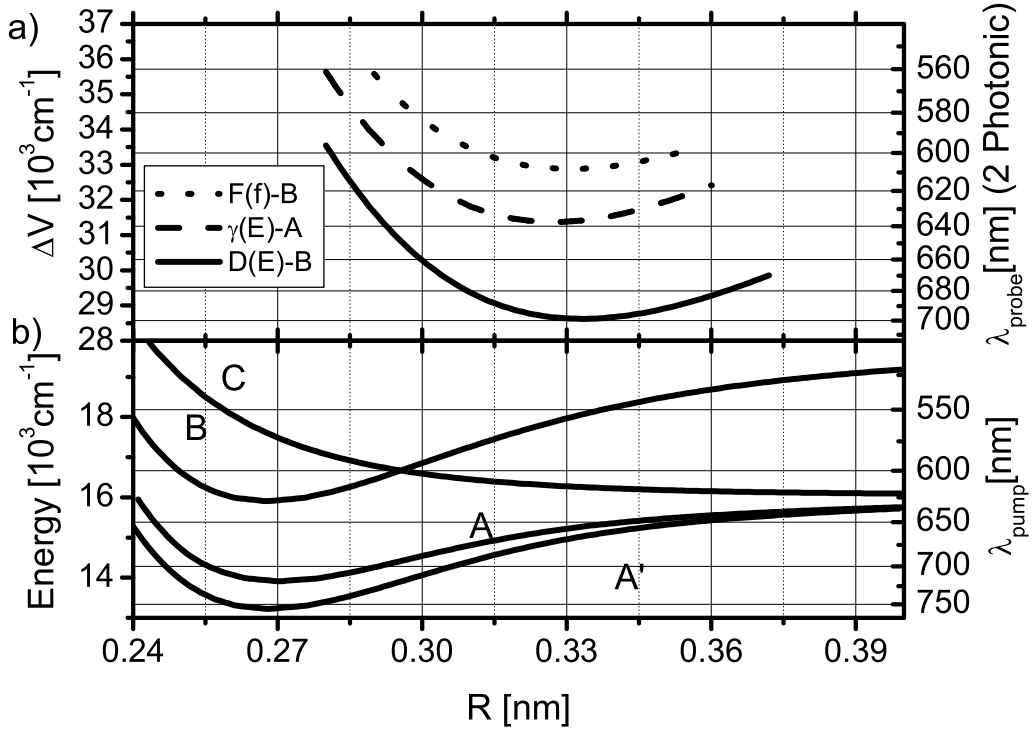

Figure 6.9: Covalent potential curves of Br_2 (b) and difference potentials to appropriate charge-transfer states (a) for two-photon probe transitions. For the selection of the difference potentials, the $\Delta\Omega$ = 0 and u-u transition rules were chosen. Thus, the D-B, γ-A and F-B potential curves are shown in (a). Since for the D and γ states no potential data are available in case of Br_2, they were substituted by the E(0_g) state. However, this induced an uncertainty of about 500 cm^{-1} in the absolute value of the potential difference.

the case of I_2 [112]. In analogy, the $\gamma(1_u)$ state (appropriate for probing the A state) will also be substituted by the E state. The corresponding difference potentials are shown in Fig. 6.9.

The derivation of the parameters R_{win} and E_{win} for the two-photon transition is similar to the recipe presented for Fig. 6.7. The ungerade D and γ states, populated in the probe step, relax in a non-radiative way to the states with gerade parity, which in turn decay under radiation emission to the covalent states.

The fluorescence band 3 at 300 nm in the dotted spectrum of Fig. 5.3a and Fig. 5.4 has to be assigned. Its energy is 3100 cm^{-1} above band 2, that has been assigned to a D'→A' transition. The energy difference indicates an emission from the second charge-transfer tier, with a 0_g state being the lowest in energy. Furthermore, the pump and probe pulse quantum energies used in the experiments are sufficient to populate this second CT tier. To confirm the interpretation, the time resolved spectra on different fluorescence bands (Fig. 5.5) are compared. Fig. 5.5 shows pump-probe spectra probing the dynamics induced by a pump pulse with λ_{pump} = 540 nm. The probe pulse is centered at λ_{probe} = 620 nm, however it is very broad and extends at the "blue" end to a wavelength of 600 nm within its FWHM. The decays in the spectra originate from energy relaxation out of the probe windows. The decay of the 300 nm fluorescence (5.5a) is much faster than the decay at 322 nm (5.5e)) and 345 nm (5.5c)). According to section 2.3.2, the probe window leading to the fluorescence at 300 nm must be located above the windows

leading to bands 1 and 2 on the covalent surfaces. The only possibility to have such a transition is a two-photon probe process to the second charge-transfer (CT) tier.

The redshift of the second CT manifold is estimated from the emission spectrum. The emission at band 3 is centered at 33180 cm^{-1}. The lowest state in this tier is of 0_g symmetry [112]. We assume an emission from the 0_g to the B($^3\Pi_{0u}$) state. To determine the redshift, the T_e of the 0_g state of free Br_2 should be known, which is not the case. Therefore, the 0_g potential minimum is set to be equal to the documented f(1_g) value, which is accurate within approximately 200 cm^{-1} [112]. Comparing the calculated free Br_2 emission from the lowest state of the second CT tier to the experimental value of band 3 leads to a redshift of 2000 cm^{-1} as shown in Fig. 6.6. The second tier is shifted downwards using the same arguments as in the one-photon probe transitions. A state of the second CT manifold with right parity and Ω has to be found to explain the ultrafast features in Fig. 5.5 f). The dynamics clearly emerges from a B state wave packet (it has the right vibrational period). Thus, the state to be probed is B($^3\Pi_{0u}$). The upper state in the two-photon probe transition has to be of 0_u symmetry. Such a state is not documented experimentally but due to the similarity to I_2, a F(0_u) state is appropriate. It is very close to the f(1_g) state [112]. Therefore, the 2000 cm^{-1} redshifted $f(1_g)$ state is used in the calculation of the difference potential F-B, shown as the dotted line in Fig. 6.9a. The difference potential excludes a probe to the F state with λ_{probe} > 610 nm. In experiments, this transition has been induced with pulses centered at 620 nm, extending to the in the wavelength range of 600 to 610 nm.

The vibrational wave packet dynamics on all emission bands in Fig. 5.5b, d and f are similar and correspond to a wave packet dynamics that is probed close to its turning point in the B state, as will be shown in the next two chapters. The dynamics also appears on the bands originating from the first charge-transfer manifold. Thus, some population from the second CT tier must undergo a non-radiative transition to the first manifold and contribute to the fluorescence there. The temperature induced quenching of band 3, which originates from the higher lying second tier, is more efficient than that of band 2, emitted from the lower first CT manifold (see Fig. 5.4). This observation is consistent with an enforced non-radiative relaxation from the second to the first CT tier.

Chapter 7

Ultrafast dynamics

The chapter presents the first wave packet dynamics ever measured for Br_2 in a solid, which is an argon crystal here. Based on the results of the last chapter, a separation of vibrational wave packets on the A and B state can be achieved by choosing distinct combinations of λ_{pump} and λ_{probe}. Furthermore, a separation based on polarization dependent pump-probe spectra is demonstrated in section 7.1.3. The focusing of vibrational wave packets is presented in section 7.1.4. Despite the intramolecular coherent dynamics, the coherent host dynamics will be presented in section 7.2. In addition to Br_2:Ar results, spectra for I_2:Kr will be shown.

7.1 Intramolecular vibrational wave packets of Br_2:Ar

7.1.1 Pump-probe spectra of the electronic A and B state

The A and B states of Br_2 are excited simultaneously by laser pulses in the range of 490 to 600 nm. In order to learn something about the dynamics of a distinct state, one has to separate the dynamics excited on both states. In principle, there are two possibilities: First, the dynamics can be recorded with different relative polarizations of pump and probe pulse. A scheme to separate the dynamics with different $\Delta\Omega$ will be presented in section 7.1.3. Second, one can choose λ_{probe} in such a way, that one state is predominantly probed. The separation by a clever probe wavelength is accomplished in two different ways. The λ_{probe} is so long, that only the B state is interrogated in accordance with Figs. 6.7 and 6.9. This scheme can be used to follow the B state dynamics exclusively (see Figs. 7.3 and 7.4). In order to isolate the A state contribution, another technique has to be applied. A wave packet central energy below E_{win} on the B surface is chosen. In this case, the A state wave packet dynamics dominates the pump-probe spectra.

In the following, the pump-probe dynamics for one-photon (UV probe pules) and two-photon probe transitions (visible probe pulses) will be presented. Situations, where essentially only one state is probed will be explained carefully.

Probing with ultraviolet pulses

Figure 7.1 shows the picosecond kinetics of the Br_2 molecule. The envelope consists of a rise and a decay. The shape displays the molecular population sliding through the probe window (as sketched in Fig. 2.9b) driven by vibrational energy relaxation.

All wavelengths λ_{probe} used for Fig. 7.1 probe the B as well as the A state according to the difference potentials in Fig. 6.7a.

The λ_{probe} of 289 nm reaches very low vibrational levels in the B and A state. Therefore, its rise and decay have rather long time constants compared to λ_{probe} = 310 to 320 nm. At these longer wavelength, higher vibrational levels are probed and thus energy relaxation funnels the population faster out of the window. The dynamics visible on a shorter timescale provides more information about the state addressed by the probe window.

In addition, if λ_{probe}> 325 nm only B state wave packet dynamics is visible (see Fig. 6.7a).

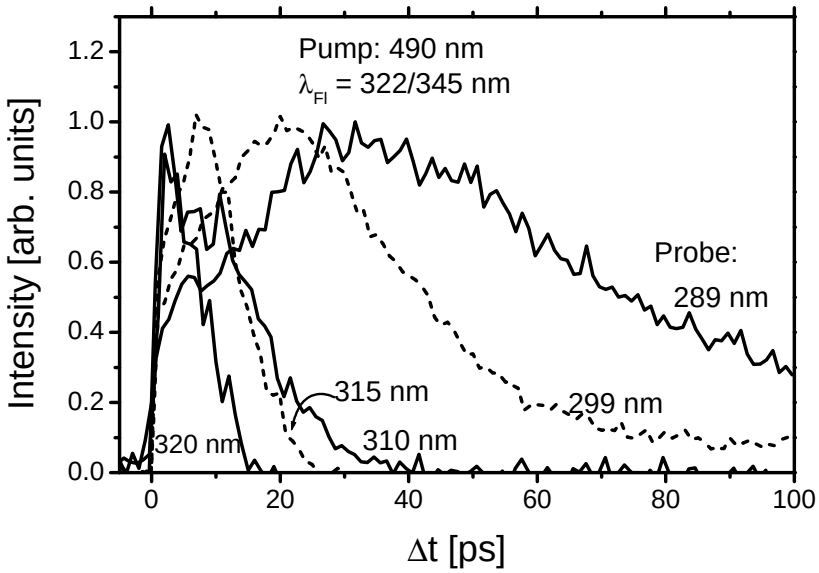

Figure 7.1: Long time range pump-probe spectra of Br_2:Ar pumped at 490 nm and probed by one photon from 289 to 320 nm. For λ_{probe} = 320, 315 and 310 nm λ_{Fl} = 345 nm, for the other λ_{probe} the λ_{Fl} = 320 nm. The decays get shorter with longer probe wavelength indicating higher probe window energies E_{win} with increasing λ_{probe}. Oscillations at short times are washed out due to the large delay step width of 0.5 ps.

Figures 7.3 and 7.4 show pump-probe spectra for the B state of Br_2 in solid Ar upon a systematic change of pump and probe wavelengths. The spectra with λ_{probe} = 339 to 345 nm (Fig. 7.3) can be understood well in terms of intermolecular vibrational wave packet motion. They show systematic trends in:

- The splitting of the first peak.
- A variation in vibrational periods depending on λ_{pump} and λ_{probe}.
- The overall picosecond decay.

For all probe wavelengths, a double structure (*vibrational splitting* according to Fig. 2.10) is observed in the first oscillation when pumping high in the B state potential well. The structure vanishes as the λ_{pump} increases and thus the vibrational energy of the wave packet decreases.

Figure 7.2 shows the first two picoseconds of a group of pump-probe spectra taken at a λ_{probe} = 339 nm. The spectra pumped with long wavelengths 570 and 580 nm display a simple single oscillatory period of the vibrational wave packet in the B state. When exciting with $\lambda_{\mathrm{pump}} \leq$ 560 nm, the earliest vibrational features split, as marked by the dashed lines denoted 1 and 2. The splitting is getting longer with decreasing wavelength *i.e.* with increasing vibrational energy in the B potential well. Even the second peak in the 570 nm pumped spectrum splits in maxima 3 and 4. The time delay between 3 and 4 being smaller than the delay between 1 and 2 for a fixed λ_{pump}. The dependence of the 3-4 splitting on excitation energy is analogous to the 1-2 case. The spectrum, in which the splitting first vanishes for a systematic increase of λ_{pump} with fixed λ_{probe} is called a resonantly probed spectrum. The vibrational splitting is caused by wave packet energy lying above E_{win} as described in section 2.3.2.

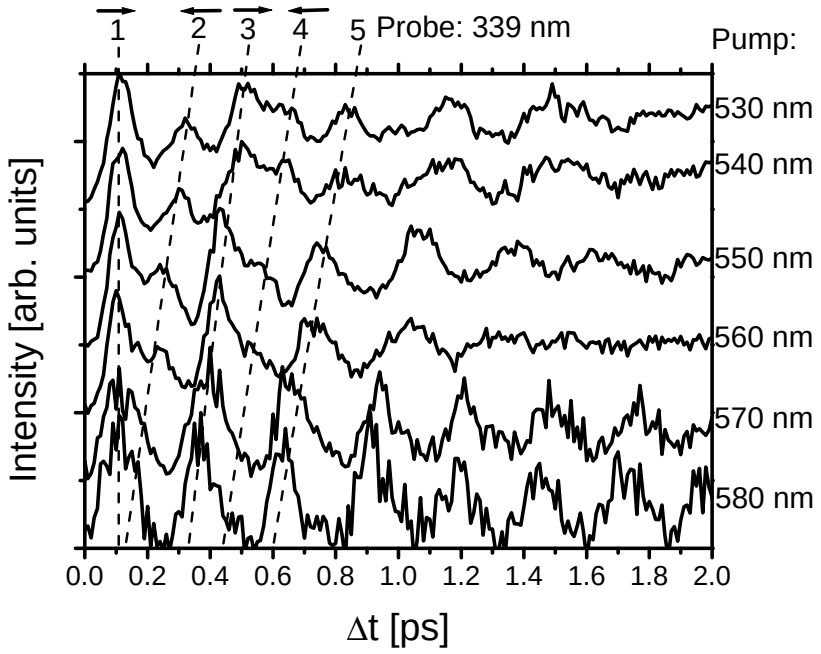

Figure 7.2: Pump-probe spectra with λ_{probe} = 339 nm detected at λ_{Fl} = 322 nm. The pump wavelength was varied between 530 and 580 nm. The dashed lines denote systematic trends in vibrational features (see text). The arrows give the direction of the vibrational wave packet according to Fig. 2.10.

A second feature observed in all pump-probe spectra is the *lengthening of the vibrational wave packet period* when exciting with shorter λ_{pump} *i.e.* with more vibrational energy. The phenomenon is quite obvious in Fig. 7.2. A vibrational period in this figure can be defined as the delay from peak 1 to peak 3. Peak 2 is attributed to the returning (travelling from large internuclear distances to smaller ones) wave packet, whereas peaks 1 and 3 are the outgoing (from small to large internuclear distances) wave packets (Fig. 2.10). The line denoted by 3 is tilted with respect to line 1 in Fig. 7.2. This indicates the lengthening of the vibrational periods as one excites at higher vibrational energies. The first vibration in the λ_{pump} = 580 nm spectrum has an oscillation period of 265 fs, whereas it has a period of 400 fs in the case of λ_{pump} = 530 nm. The lengthening follows from the anharmonicity of the B state Morse oscillator (see section 2.2).

Pump-probe transients for fixed λ_{pump} = 530 nm are presented in Fig. 7.5. The values for λ_{probe} are varied between 339 and 357 nm. For λ_{probe} = 339 nm, the vibrational wave packet lies above the corresponding probe energy E_{win}. It passes the window twice per period as indicated by the dashed lines denoted 1 and 2. The arrows indicate the direction in which the wave packet moves. As λ_{probe} becomes larger, the probe energy E_{win} moves closer to the initial excitation energy of the wave packet. Thus the vibrational splitting between 1 and 2 (and 3 and 4 for the second vibrational period) is reduced. Finally, at λ_{probe} = 348 nm, the splitting has vanished. This indicates the resonance condition in the pump-probe process (see section 2.3.1). Going to even longer probe wavelengths and thus to even higher E_{win} leads to a decrease of the overall signal, but a vibrational splitting should not be observed any more. The difference potentials in Fig. 6.7a predict the loss of the signal for probe wavelengths larger than 350 nm. However, from λ_{probe} = 351 nm to 357 nm signals with different vibrational dynamics and new splitting appear as indicated by the two solid lines. It will be attributed to the host dynamics in

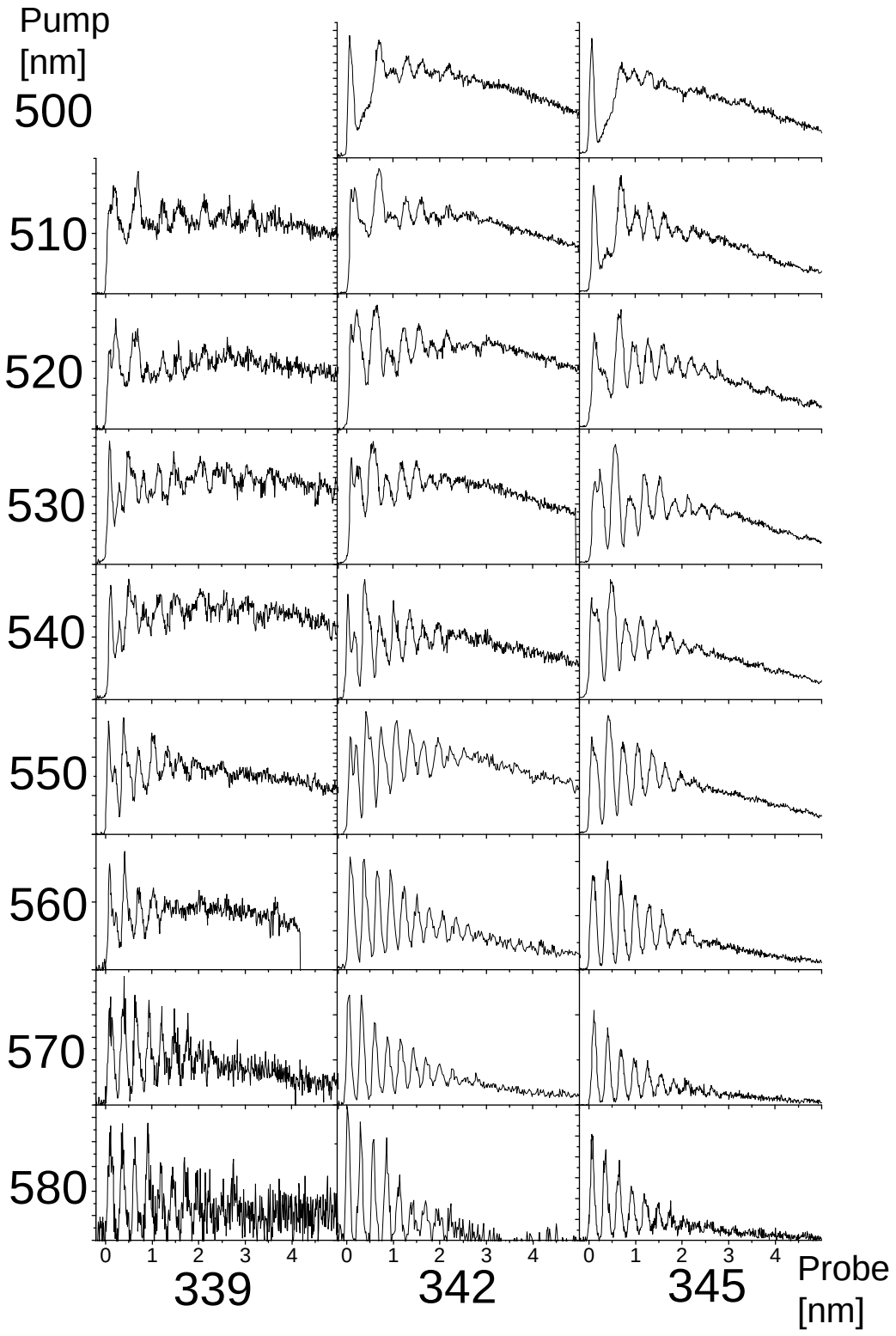

Figure 7.3: Pump-probe spectra for the B state of Br_2:Ar for pump wavelengths from 500 to 580 nm and probe wavelengths 339, 342 and 345 nm, λ_{Fl} = 322 nm

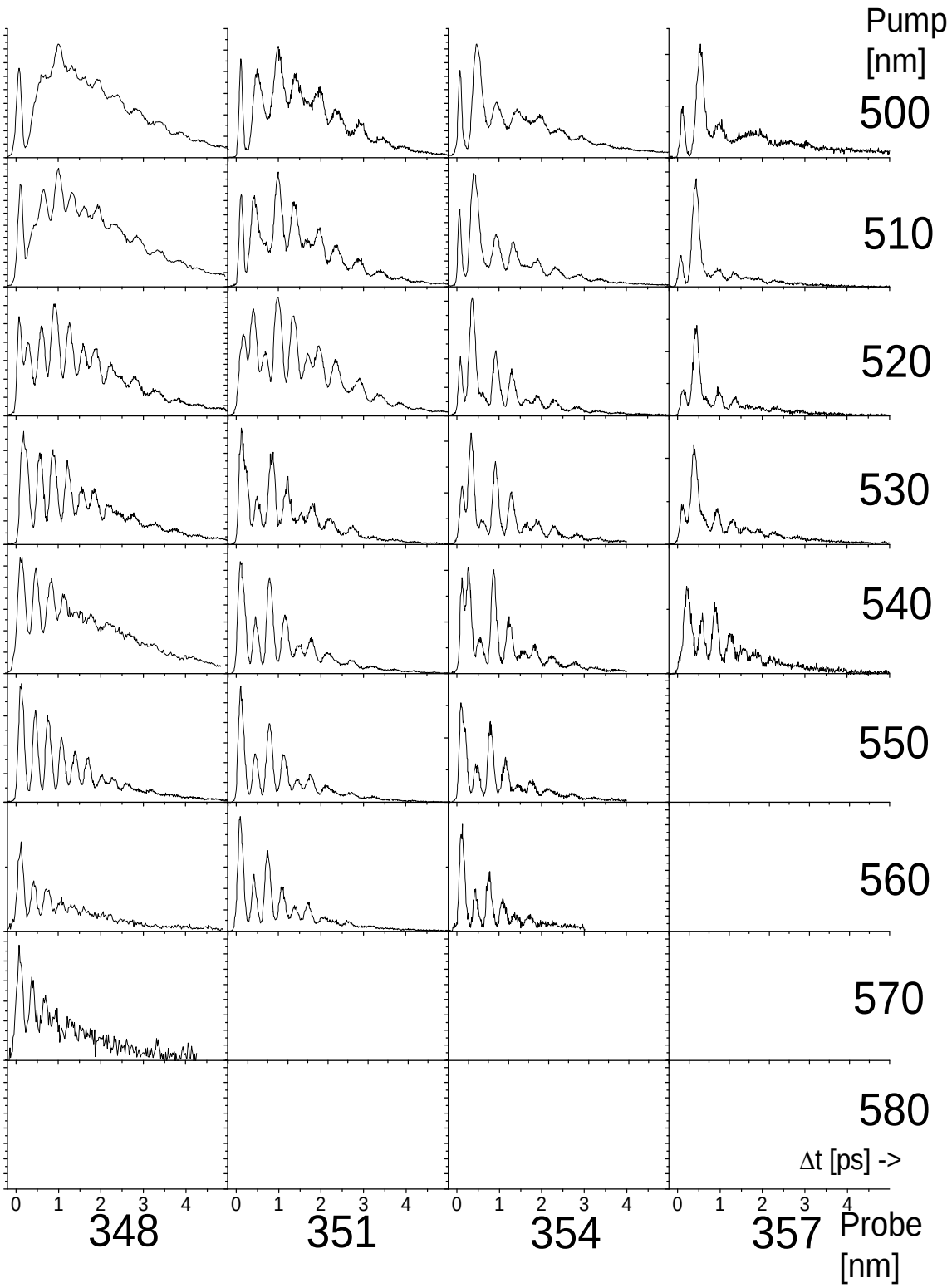

Figure 7.4: Pump-probe spectra for the B state of Br_2:Ar for pump wavelengths from 500 to 580 nm and probe wavelengths of 348, 351, 354 and 357 nm, λ_{Fl} = 322 nm

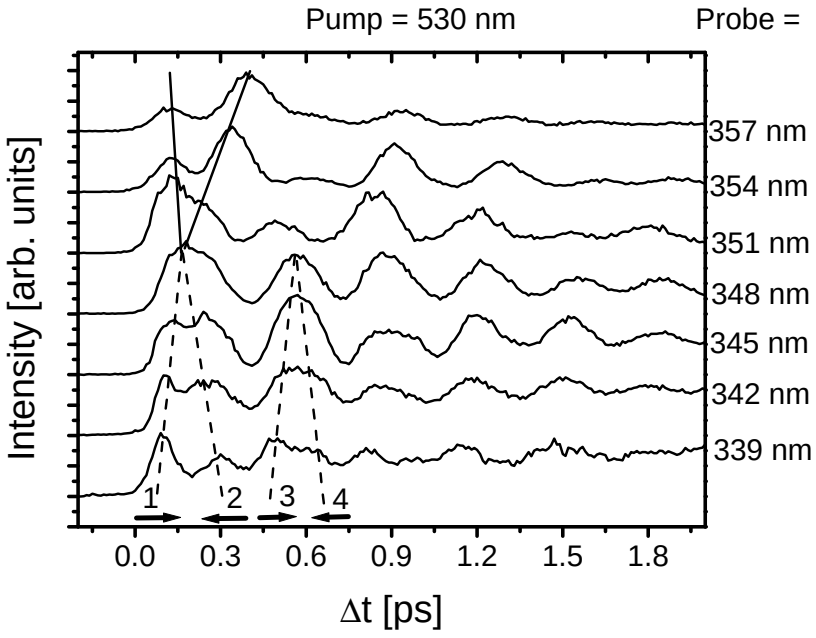

Figure 7.5: Br_2:Ar pump probe spectra with λ_{pump} = 530 nm and λ_{probe} changed from 339 nm to 357 nm. The fluorescence is recorded at λ_{Fl} = 322 nm. The dashed lines indicate the vibrational splitting. The solid lines indicate a host induced splitting.

section 8.3. As a consequence, the resonance condition, with E_{win} equal to the central energy of the vibrational wave packet cannot be identified by the vanishing of the vibrational splitting for pump wavelengths longer than 530 nm. This will be of importance for the construction of the Br_2:Ar RKR potential in section 8.1.2.

Finally, the *picosecond decay* shall be described. For a fixed λ_{pump} the decay gets faster when increasing λ_{probe}. For example at a pump wavelength of 510 nm, no decay is visible in Fig. 7.3 when probing by 339 nm. In contrast to this, at λ_{probe} = 357 nm the spectrum pumped at 510 nm decays very quickly in less than 2 ps (see Fig. 7.4). For a fixed λ_{probe}, the decay is also a function of λ_{pump}. As λ_{pump} gets bigger, the decay is faster for a fixed λ_{probe}. This can be illustrated in case of the λ_{probe} = 342 nm series. At 500 nm excitation, only a slight decay is visible in the 5 ps time interval shown in Fig. 7.3. At λ_{pump} = 580 nm the spectrum has a short decay time of about 3 ps.

Probing with visible pulses

The discussion of the emission spectra delivered two probe windows according to two different probe transitions: The first is the fluorescence at 300 nm (band 3 in Fig. 5.3a) originating from a probe window to the second charge-transfer manifold, whereas the second group of windows corresponds to bands 1 and 2 from the first charge-transfer state manifold.

The ultrafast spectra observed on band 3 when probing by visible pulses in a two-photon process are presented in Fig. 7.6. The probe wavelength is 620 nm throughout the series. The excitation λ_{pump} was varied from 500 to 580 nm in 10 nm steps. The measurements show a B state wave packet dynamics. When excited above the free molecule dissociation limit (at about 507 nm), the intermolecular vibrational wave packet is hardly visible after 1 ps. Furthermore, the separation of the first and the second peak is very large. This splitting reduces as the excitation energy in the B well is reduced. In analogy to the splitting described in Fig. 7.2, at a well

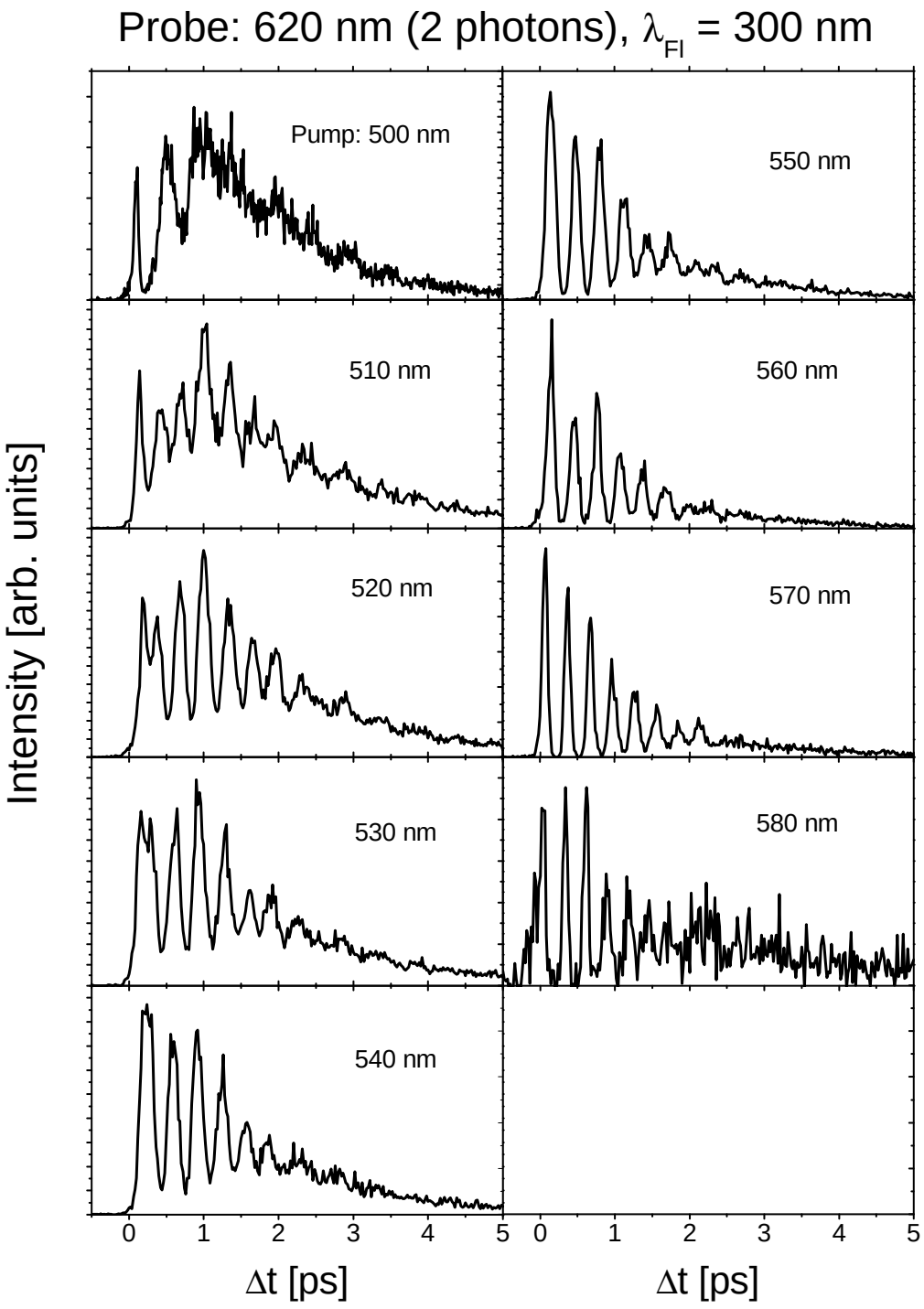

Figure 7.6: Pump-probe spectra of Br_2:Ar with λ_{probe} = 620 nm in a two-photon probe process. The fluorescence is detected at λ_{Fl} = 300 nm. The pump wavelength is varied between 500 and 580 nm. The spectra show only B state vibrational wave packet dynamics.

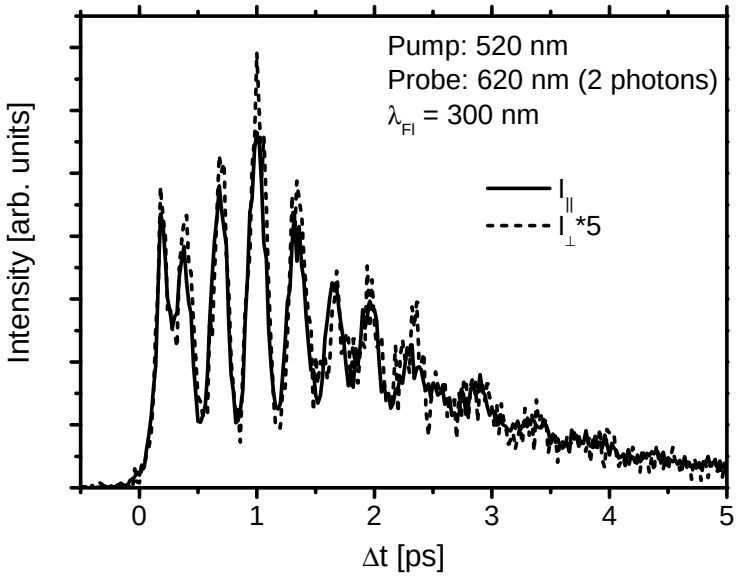

Figure 7.7: Pump-probe spectra of Br_2 under different relative polarization of pump and probe pulse. Solid line: pulses have parallel polarization ($I_{||}$). Dashed line: pulses have perpendicular polarization ($I_{\perp}$). The intensity of the latter signal is scaled up by a factor 5.

defined λ_{pump} the splitting vanishes here at λ_{pump} = 540 nm. It follows, that the probe resonance for λ_{probe} = 620 nm is fulfilled for a λ_{pump} = 540 nm. In this respect, the spectra detected on band 3 probed by two photons of 620 nm are equivalent to the spectra detected on bands 1 and 2 probed at 348 nm in a one-photon transition, since for λ_{probe} = 348 nm the probe resonance condition is also fulfilled for 540 nm excitation wavelength.

7.1.2 Polarization sensitive pump-probe spectroscopy

The laser pulses used in the experiments described below are always linearly polarized. Figure 7.7 shows two pump-probe spectra of the Br_2 molecule in a solid Ar host for parallel (solid line) and perpendicular (dashed line) polarization of pump and probe pulse. The pump pulse at 520 nm excites the electronic B state in a one photon transition with $\Delta\Omega = 0$, creating a $\cos^2\theta$ molecular angular distribution (Fig. 3.4). The two-photon probe step excites the CT state in a $\Delta\Omega = 0$ transition. The angular probe characteristics is given by a $\cos^4\theta$ distribution. Figure 3.4 gives the ratio for probing with parallel ($S_{20||}$) to probing with perpendicular polarization ($S_{20\perp}$) as $S_{20||}/S_{20\perp} = 5/1$. This value is however reached only if the molecule does not change its alignment in the time interval Δt between pump and probe pulse. The perpendicular probed spectrum (dashed) in Fig. 7.7 is scaled by the theoretical factor of 5 and agrees with the parallel probed spectrum in the whole time range. This indicates a fixed molecular alignment on the picosecond time scale. The same holds true for the I_2 molecule in solid Kr. The probe step is however a one-photon transition and the theoretical value for fixed molecular alignment of $S_{10||}/S_{10\perp} = 3/1$ (Fig. 3.4) has to be applied. Figure 7.8 shows the parallel probed spectrum (solid line) and the perpendicular probed spectrum (dashed line) which is scaled up by the theoretical factor of 3.

The agreement of the spectra shows the persistent molecular alignment on the picosecond time scale. Therefore, all peaks in the pump-probe spectra are due to *vibrational* wave packet motion only. The molecule can be described as a *one dimensional* quantum system in a condensed environment.

For the case of I_2:Kr, the CT fluorescence was polarization analyzed yielding the mathematical ratio for non-rotating molecules on a *nanosecond* timescale.

Probing only *one* covalent state results in pump-probe spectra that deviate only by a mul-

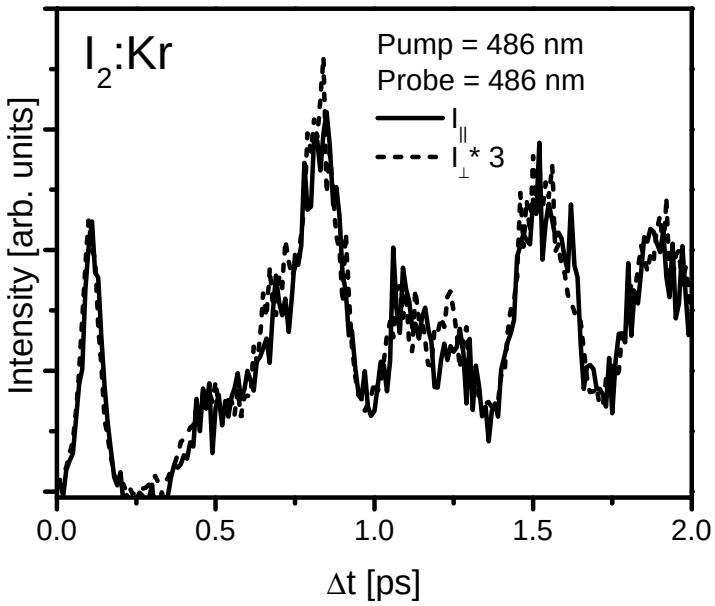

Figure 7.8: Polarization dependent pump-probe spectra for I_2:Kr. The molecules were pumped above their gas phase dissociation limit. The solid line gives the spectrum with pump polarization being parallel to the probe polarization ($I_{||}$). The dashed line is taken with pump polarization perpendicular to probe polarization ($I_{\perp}$).

tiplicative factor (Fig. 7.7,Fig. 7.8) for different polarizations. Probing states with different quantum number Ω yields generally different structures in the polarization dependent spectra. An example is shown in Fig. 7.9. A λ_{probe} in Br_2:Ar of 570 nm gives the opportunity to observe A state vibrational dynamics besides B state dynamics at a $\lambda_{\mathrm{Fl}} = 300$ nm. The pump pulse used for Fig. 7.9 excites the Br_2 B state in a $\Delta\Omega = 0$ and the A state in a $\Delta\Omega = 1$ transition from the ground state X. Parallel probing prefers the detection of the B state, since the ratio of B state probing to A state probing (uncorrected for the relative absorbtion of the states) is $S_{20||}/S_{21||} = 5/1$ (Fig. 3.4, the second index in S is the $\Delta\Omega$ of the pump transition: 0 is B state, 1 is A state). Perpendicular probing prefers the A state detection since $S_{20\perp}/S_{21\perp} = 1/3$.

The two maxima marked by the arrows in Fig. 7.9 clearly originate from the B state vibrational wave packet, since they are favored in the parallel probe case. The other signatures are a mixture of B and A state wave packet dynamics.

Next, results for emission bands 1 and 2 shall be described. The bands are equivalent, thus pump-probe spectra recorded at a λ_{Fl} of 322 nm (band 2) are presented exclusively. Fig. 7.10 shows a set of pump-probe spectra with λ_{probe} = 620 nm. The pump wavelength is varied between 500 and 580 nm in 10 nm steps and spectra for perpendicular and parallel relative polarization of pump and probe pulse are shown. The group of spectra with λ_{pump} varying from 500 to 540 nm show no polarization dependence in the dynamics which is essentially that of the B state. Indeed, in the discussion of the spectroscopic results, a population transfer from the second to the first charge-transfer manifold was proved. Thus, the B state dynamics observed here is analogous to the one observed at λ_{Fl} = 300 nm in Fig. 7.6. The splitting of the first peak vanishes at λ_{pump} = 540 nm when going to lower excitation energies in B. At the fluorescence wavelength of 300 nm, parallel and perpendicular probed spectra are the same despite an overall scaling factor. The dynamics recorded at 322 nm (band 2) behaves differently. For λ_{pump} = 500 to 520 nm, the spectra are almost equal. A difference in the parallel and perpendicular spectra can be clearly recognized from λ_{pump} = 530 to 580 nm. At 530 nm excitation wavelength, the second peak is smaller in the perpendicular spectrum compared to the parallel one. Therefore, it is attributed to B state wave packet dynamics, as in the case of Fig 7.9. The trend continues

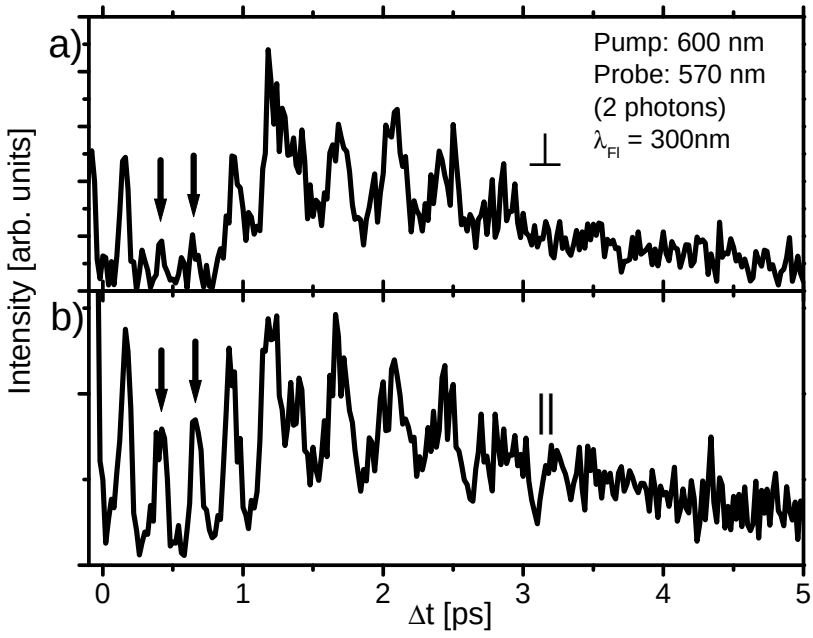

Figure 7.9: Pump-probe spectra of Br_2:Ar with λ_{pump} = 600 nm, λ_{probe} = 570 nm in a two-photon probe process. The fluorescence was detected at 300 nm. The spectrum probed with perpendicular polarizations (a)clearly shows an A vibrational dynamics. The B state vibrational wave packet produces a maxima at 400 and 650 fs, being best visible in the parallel case (b).

for longer excitation wavelength. The A state is always excited above its gas phase dissociation limit at 620 nm and thus the A state vibrational wave packet shows a very long first passage outwards to the cage atoms. This means a lack of signal for delays of 200 to about 800 fs.

The B state dynamics vanishes from λ_{pump} = 530 nm on. At λ_{pump} = 550 to 580 nm, the A state dynamics signal grows in the spectra. It is enhanced for perpendicular relative polarization, according to the $\Delta\Omega$ = 1 selection rule for the A state. The most pronounced case is the perpendicular spectrum with λ_{pump} = 580 nm. The B state signature at 400 fs has vanished completely. The remaining dynamics is that of the A state wave packet only. However, the probe window acts on the A and B state surface, as described in Fig. 6.9. The B state wave packet is excited below E_{win} and is therefore not probed efficiently.

When probing deeper in the B state, the amount of B population probed to the second charge-transfer manifold is increased. Thus, even at λ_{pump} = 580 nm, the B state dynamics signal can be increased when using a probe wavelength of 600 nm, as Fig. 7.11 shows.

7.1.3 A and B state dynamics decomposition

Based on the theoretical considerations in Fig. 3.4 and the fact, that the molecules do not change their alignment, a separation of A and B dynamics can be executed. The decomposition of wave packet dynamics can yield valuable information on the molecular dynamics in cases where wave packet spectroscopy on isolated states is not possible. No such attempts for the case of ultrafast spectroscopy are documented in literature to the authors best knowledge.

For the case of a one-photon pump excitation and two-photon probing, the decomposition formula shall be deduced. The index of $I_{0,1}$ gives the $\Delta\Omega$ in the excitation or pump step, the σ denotes the absorption of the probe pulse from the excited states to the charge-transfer states.

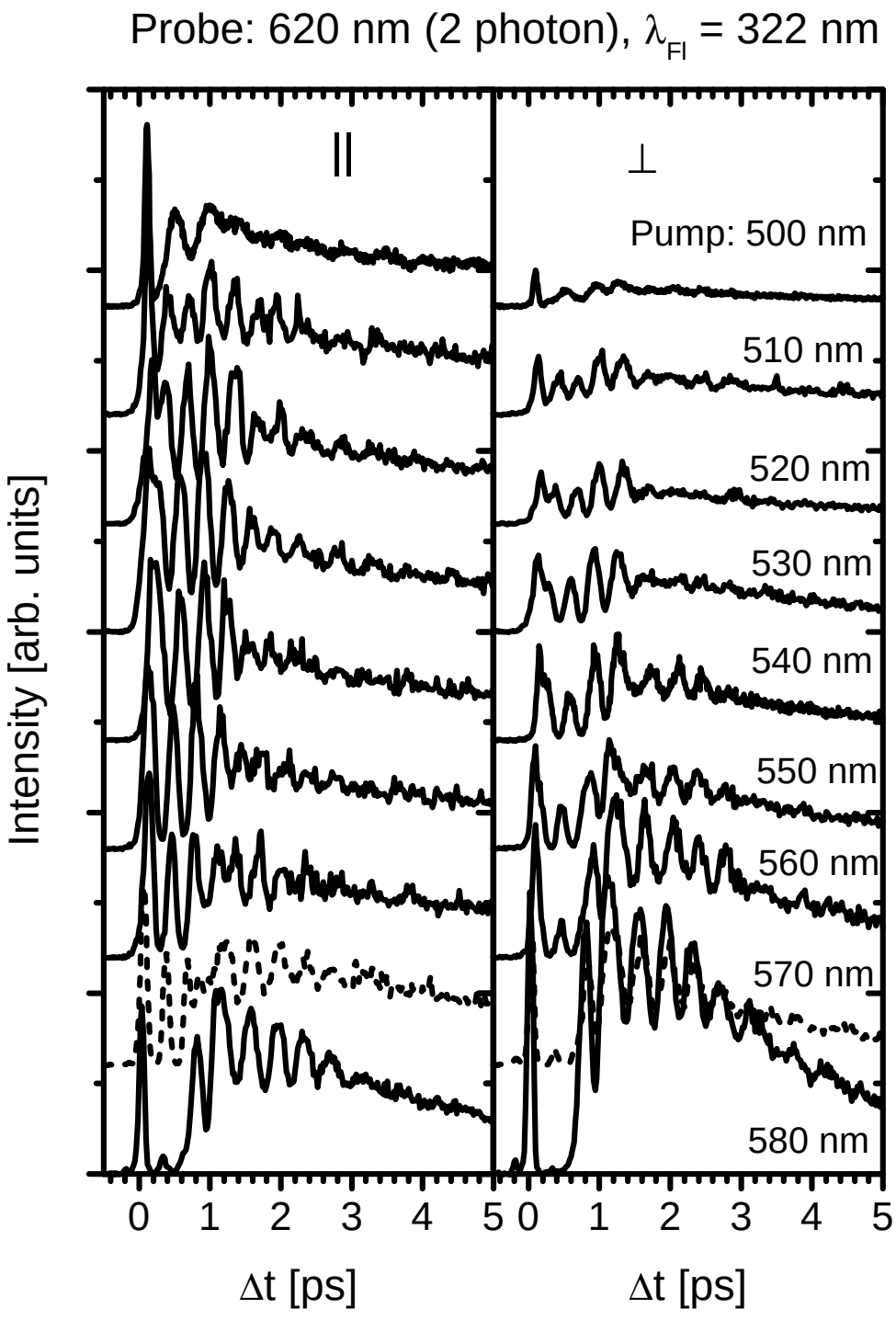

Figure 7.10: Pump-probe spectra of Br_2:Ar for λ_{probe} = 620 nm (2 photon) and parallel or perpendicular relative polarization of pump and probe pulse. A shift from B state dominated wave packet dynamics (at λ_{pump} = 500 to 540 nm) to A state dominated wave packet dynamics (at λ_{pump} = 560 to 580 nm) can be observed. The relative intensity of parallel and perpendicular probed spectra with the same λ_{pump} is maintained in the figure.

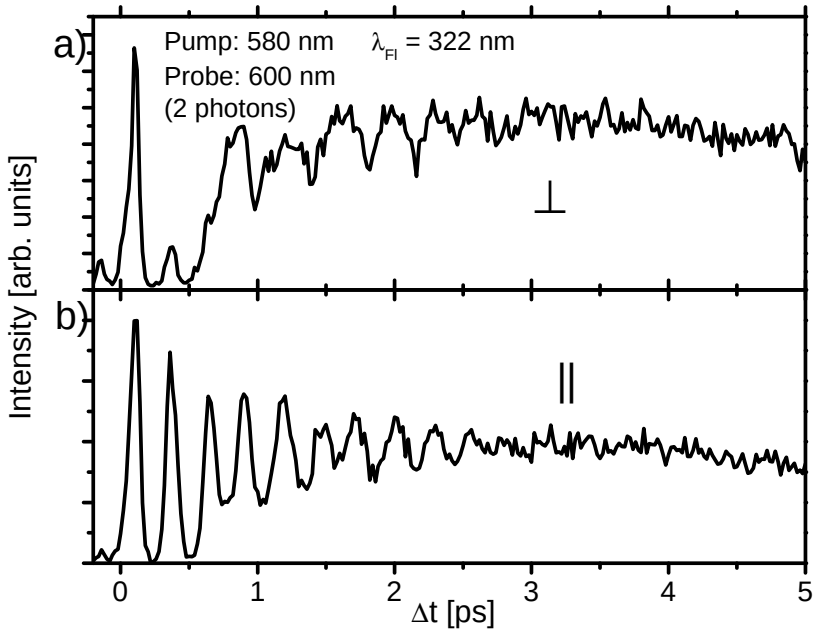

Figure 7.11: Pump-probe spectra of Br_2:Ar with λ_{pump} =580 nm and λ_{probe} = 600 nm (two-photon). The perpendicular polarization case (a) shows A and B state dynamics whereas the parallel case (b) shows a well modulated B state wave packet dynamics.

When the probe polarization is parallel to the pump polarization, the signal $I_{||}$ is given as:

$$I_{||} = S_{20||}\sigma_0 I_0 + S_{21||}\sigma_1 I_1, \tag{7.1}$$

with $S_{20||} = 5$ and $S_{21||} = 1$. For perpendicular probing, it is given as:

$$I_{\perp} = S_{20\perp}\sigma_0 I_0 + S_{21\perp}\sigma_1 I_1, \tag{7.2}$$

with $S_{20\perp} = 1$ and $S_{21\perp} = 3$. The factors used in the decomposition are taken from Fig. 3.4. The system of equations 7.1 and 7.2 can be solved for I_0 and I_1 leading to:

$$\begin{aligned} I_0 &= \frac{1}{14\sigma_0}(3I_{||} - I_{\perp}), \\ I_1 &= \frac{1}{14\sigma_1}(5I_{\perp} - I_{||}). \end{aligned} \tag{7.3}$$

Thus, when measuring $I_{\perp}$ and $I_{||}$ in an experiment, the contributions of the B state (I_0) and the A or C state (I_1) can be derived from those spectra.

As can be seen in Fig. 7.12, the dynamics are separated and typical features of A and B state dynamics show up. The C state is not excited at λ_{pump} = 560 nm. Comparing the B state signal I_0 in Fig. 7.12b with the fluorescence selected B state signal at 300 nm (Fig. 7.12c) shows a remarkable difference. The long lasting background on a picosecond timescale in Fig. 7.12b is absent in c). Thus, another probe window deeper in some state (B or A) is involved here at λ_{Fl}=322 and 345 nm.

7.1.4 Wave packet focusing

Section 2.3.3 presented a scheme to determine the vibrational dephasing of molecular wave packets on Morse potentials with chirped pulses. The experiments with chirped pulses were

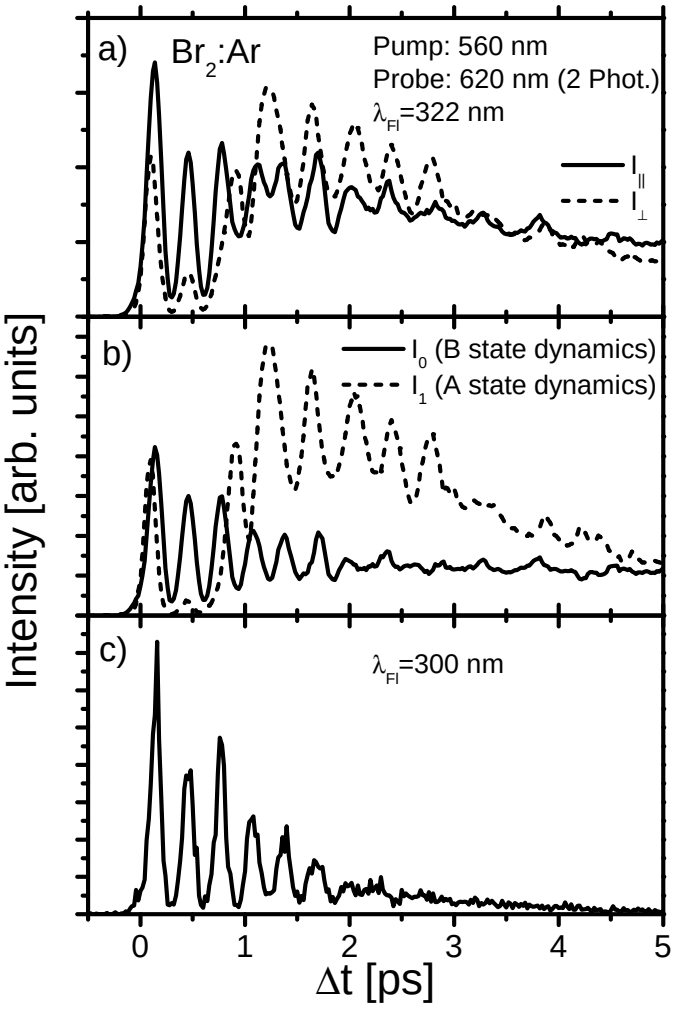

Figure 7.12: a) Pump-probe spectra of Br_2:Ar pumped at 560 nm and probed at 620 nm via a two-photon transition. The fluorescence is recorded at 322 nm. b) the two signals from a) are subtracted with right scaling factors to get the separate state dynamics. c) Fluorescence recorded at 300 nm, that shows only B state dynamics.

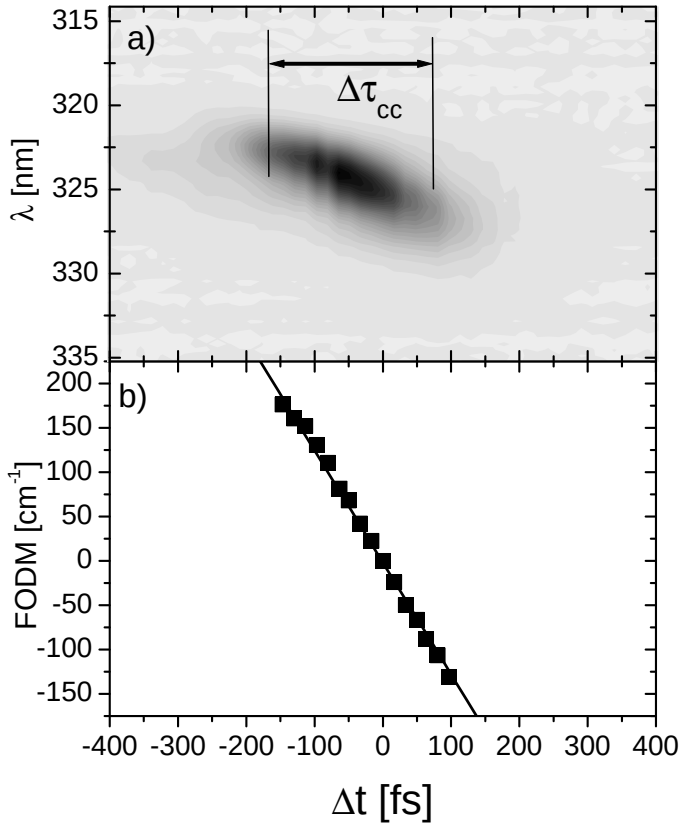

Figure 7.13: a) SFG FROG trace of a negatively chirped pulse centered at pulse at 560 nm using a gate pulse centered at 775 nm. b) The First Order Delay Marginal (FODM) is used to determine the linear chirp parameter β.

performed at different excitation energies in the B state of Br_2 in Ar crystals. In order to negatively chirp the excitation pulse (pump pulse), a F2 (highly dispersive glass) prism compressor (section 4.3.2) section was set up. By introducing glass material of one prism into the beam, a compensation of the negative chirp introduced by the compressor could be achieved (zero dispersion compressor). The large amount of F2 in the beam gives rise to a small nonlinear chirp besides the strong linear chirps possible with this compressor. The nonlinear chirps vanish when removing material out of the beam to create linear negatively chirped pulses. The width of the pulses carrying the most nonlinear chirp (at zero linear chirp) is however short enough to modulate pump-probe spectra down to zero signal (see first minimum in Fig. 7.15a). Overcompensating the negative chirp leads to positively chirped pulses.

The pulses were characterized in a SFG FROG (section 4.3.4). The fundamental of the chirped pulse amplifier at 775 nm was used as a gate pulse. Figure 7.13a shows the SFG FROG trace when overlapping the 560 nm pump pulse later used in the experiment with the 775 nm fundamental, that is unchirped. The tilt in the FROG trace is an immediate indication for the chirp on the 560 nm centered pulse. Since the blue tail of the pulse is detected at negative times and the red wing at positive times, the pulse has a negative chirp (compare Fig. 4.4). The slope of the FODM in Fig. 7.13b is $N'(t) = -1.26$ fs cm . From a projection of the chirp trace on the time axis, a cross-correlation time of $\Delta\tau_{\rm cc} = 244$ fs can be deduced, assuming Gaussian pulses. The spectral width of the pulse was independently measured in a spectrometer to be $\Delta\eta$ =460 cm^{-1}. Using formula 4.22 leads to $\beta' = (N'\Delta\tau_{\rm cc}^2 2\pi)/(\Delta\eta^2 c)$ = -2.26 fs cm. The duration $\Delta\tau_{\rm p}$ of the 560 nm laser pulse can be calculated to be $\Delta\tau_{\rm p} = \sqrt{\Delta\tau_{\rm cc}^2 - \Delta\tau_{\rm gate}^2}$= 175 fs using $\Delta\tau_{\rm gate}$ = 170 fs in addition. Eq. (4.10) presents an alternative to determine the chirp parameter β' from the pulse duration. It delivers the $\beta' = \beta(\nu)/c$ to be -2.2 fs cm. This is in

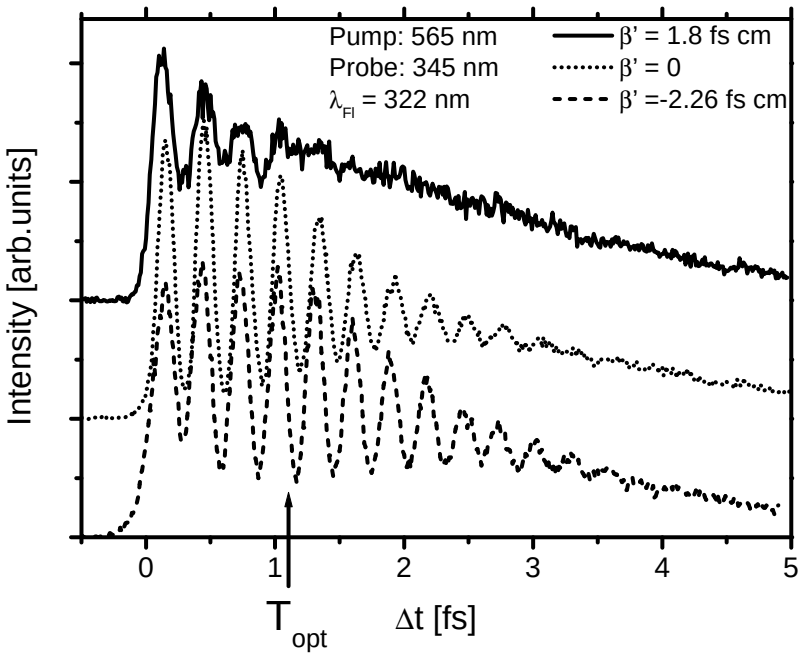

Figure 7.14: Pump-probe spectra excited with differently chirped pulses. All spectra were probed with unchirped laser pulses centered at 345 nm, and pump with zero chirp (dotted), negative chirped (dashed) and positive chirped (solid line) pulses centered at 560 nm.

agreement with the FROG evaluation within 0.06 fs cm. Obviously, a measurement of the pulse duration (*e.g.* in an autocorrelator) and spectral width is sufficient to determine the chirp, if the sign of the chirp is known.

Fig. 7.14 shows a series of three pump-probe spectra of the Br_2:Ar B state. The wave packet dynamics was excited with pump pulses centered at 560 nm, differing only in chirp. The dynamics was interrogated by unchirped 345 nm UV laser pulses. The modulation contrast of the oscillations clearly depends on the excitation pulse chirp. The modulation contrast of all three spectra shown in Fig. 7.14 decays as a function of time. In the very first picosecond, the spectrum excited by negatively chirped pulses (dashed line) has a weaker modulation contrast than the spectrum excited by an unchirped pulse. However, after about the fourth oscillation, the modulation contrast is better reaching an absolute maximum for the negatively chirped spectrum in that case.

The time of that maximal modulation contrast (focus time) can be compared with the theoretical focusing time $T_{\rm opt} = -(\beta'\nu^2)/(4\pi\omega_e x_e)$ (Eq. (2.15)). For the B state of Br_2, $\omega_e x_e$ = 1.6361 cm^{-1} [53]. With an oscillation time of about 300 fs at 560 nm excitation corresponding to ν = 100 cm^{-1} and a negative chirped pulse with β' = -2.2 fs cm, the $T_{\rm opt}$ according to Eq. (2.15) is 1.1 ps. This corresponds exactly to the experimental focus in the dashed spectrum in Fig. 7.14.

Exciting with a positively chirped pulse of β' = 1.8 fs cm (solid line in Fig. 7.14) leads to a reduced modulation contrast compared to the two other cases for all delay times Δt. However, positively chirped excitation provides a tool for the observation of fractional revivals, which will be presented in section 8.2.2.

The same experiments were carried out with a systematic variation of negative chirp parameters at an excitation wavelength centered around 567 nm. The chirp parameter β was deter-

mined in a cross-correlation with another visible laser pulse (that deserves as a probe pulse in the experiment). The cross-correlation was used once more with $\Delta\tau_{\mathrm{p}} = \sqrt{\Delta\tau_{\mathrm{cc}}^2 - \Delta\tau_{\mathrm{gate}}^2}$ and a gate pulse duration of 28 fs. The chirp parameter β' was determined using Eq. (4.10). The equivalence to a full FROG analysis was shown above.

The full collection of pump-probe spectra excited with six different negative chirps is shown in Fig. 7.15. The charge-transfer fluorescence was detected at 300 nm, thus only the electronic B state contributes to the pump-probe signal. The best modulation contrast (wave packet focus) appears at larger delays with increasing absolute value of the negative chirp as predicted in section 2.2. In addition, wave packet oscillations extend up to 3.5 to 4 ps in the spectra excited by larger absolute chirp, whereas this range is unstructured when exciting with no chirp. The focusing at T_{opt} does not lead to a modulation with zero background. The background will be used in section 8.2.1 to determine the vibrational dephasing.

7.2 Coherent host dynamics

Besides the intramolecular vibrational dynamics, another modulation is observed in pump-probe spectra of Br_2 in solid argon and also for I_2 in solid krypton. Those modulations, will be attributed to *coherent host dynamics* and have been neglected until now in the presentation of the ultrafast dynamics results. They contribute to a large extent to spectra in Fig. 7.4. The first part of this section deals with the spectra of Br_2:Ar, whereas in the second, spectra for I_2:Kr are shown.

7.2.1 Br_2 in solid argon

A distinct modulation observed in spectra appearing after a view picoseconds in Fig. 7.4 cannot be interpreted in terms of intramolecular dynamics. The spectrum in Fig. 7.4 with λ_{pump} = 520 nm, λ_{probe} = 348 nm is reproduced in Fig. 7.16a as an example.

The first peak in the experimental transient (solid line in Fig. 7.16a) shows a vibrational splitting. Afterwards, the splitting has vanished and one can follow the vibrational wave packet dynamics on the B state with a typical oscillation period of 340 fs. However after about 3 ps, a new oscillatory pattern with a period of 500 fs can be observed. This oscillation pattern will be attributed to *coherent host dynamics* in the discussion. The modulation is very weak and hardly visible on the transient. In order to increase the modulation contrast, the spectrum is normalized on the 70 data point average, shown as the dashed line in Fig. 7.16a. The oscillatory pattern is absent in this average. Dividing the spectrum by this average increases the oscillatory contrast at late delay times (Fig. 7.16b). Indeed, the pattern after 3 ps becomes more pronounced. The normalization preserves the phase of the oscillation as indicated by the solid vertical lines. The modulation of 500 fs is very stable in frequency and phase. However, the noise on the 500 fs modulation at delay times close to 5 ps increases due to the signal decay in the original data.

This 500 fs modulation can be observed for many pump and probe wavelength combinations. As an example, Fig. 7.17 shows Br_2:Ar transient spectra at λ_{probe} = 348 nm with λ_{pump} varied between 500 and 530 nm.

The exact time zero (the temporal overlap between pump and probe pulse) is not measured in this experiment. Therefore, the experimental spectra are shifted such, that the first rise of all spectra overlap. The intramolecular vibrational wave packet dynamics is visible for small delay times with its characteristic variation of the splitting. The vertical arrows in Fig. 7.17 indicate the inset of the 500 fs modulation. For the transient pumped at λ_{pump} = 500 nm, the inset is approximately at 2 ps. The inset is delayed as the excitation energy is shifted to lower vibrational levels. At λ_{pump} = 530 nm, the 500 fs oscillation period starts at about 3 ps.

The host induced modulation on the pump-probe spectra of Br_2:Ar is not only observed

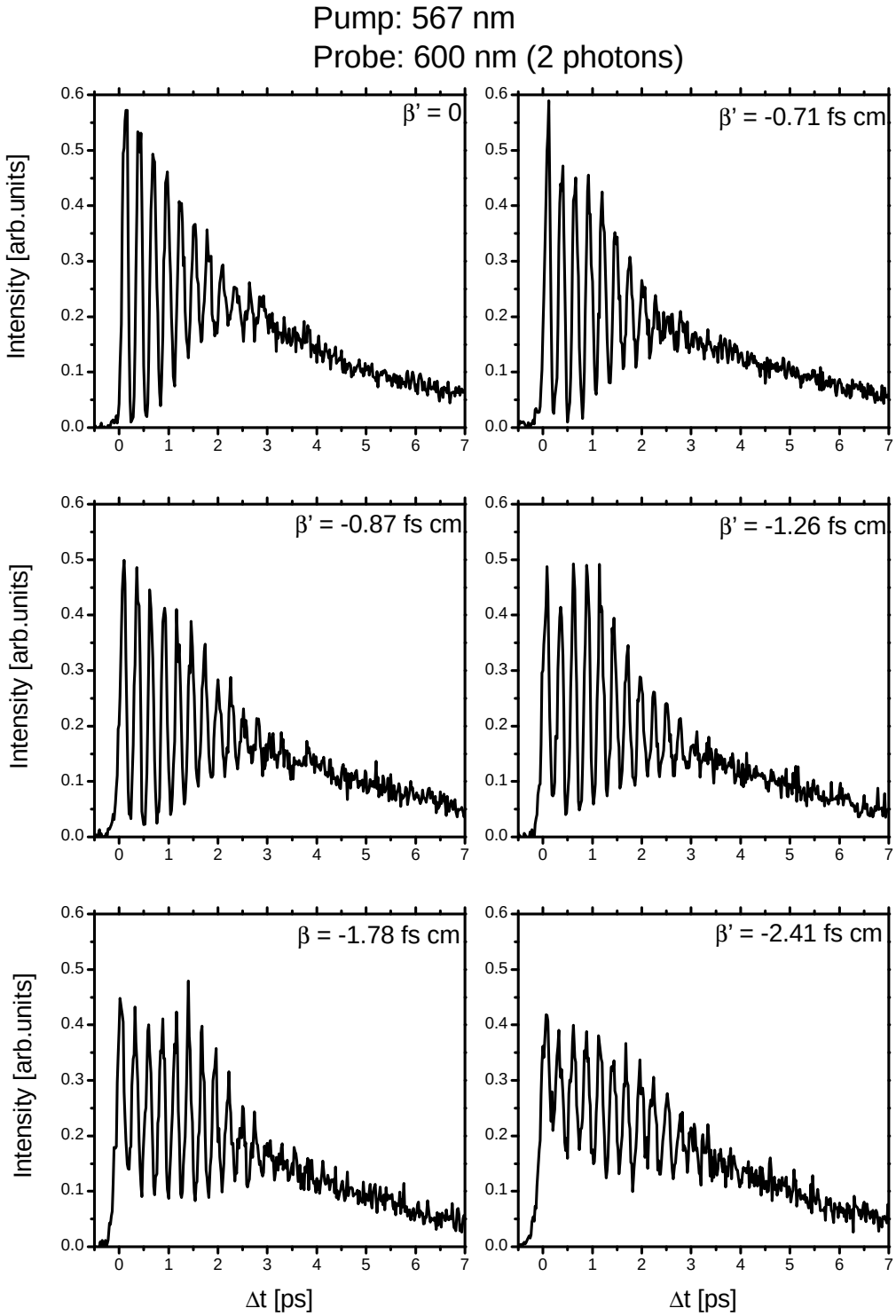

Figure 7.15: Pump-probe spectra of Br_2:Ar B state for different excitation chirps. The probe process proceeded via a two-photon transition using 600 nm pulses. The fluorescence of the charge-transfer states was collected at λ_{Fl} = 300 nm in order to be sensitive on B state dynamics only.

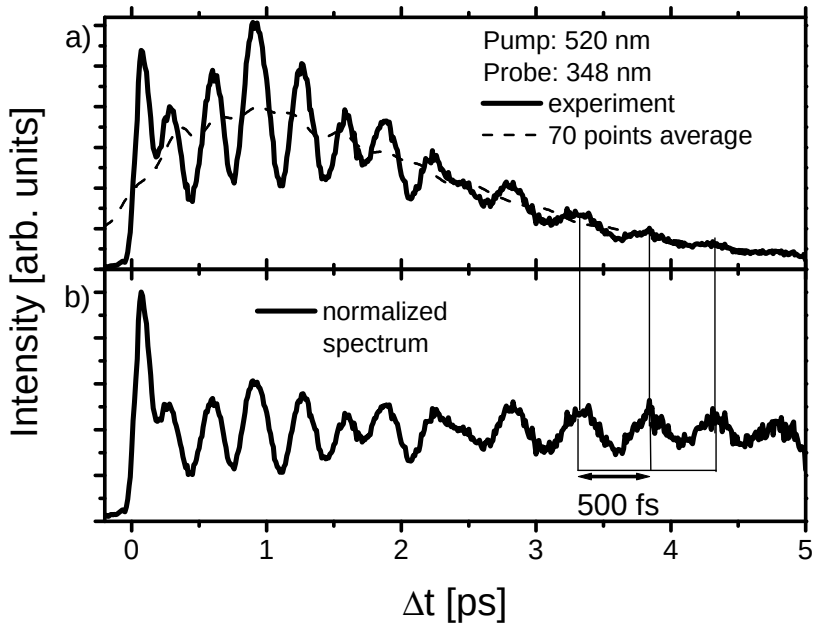

Figure 7.16: Pump-probe spectrum of Br_2:Ar with λ_{pump} = 520 nm and λ_{probe} = 348 nm. The solid line in a) gives the experimental transient, while the dashed line was calculated by a 70 points average of the experiment. b) shows the experimental spectrum normalized by the average from a).

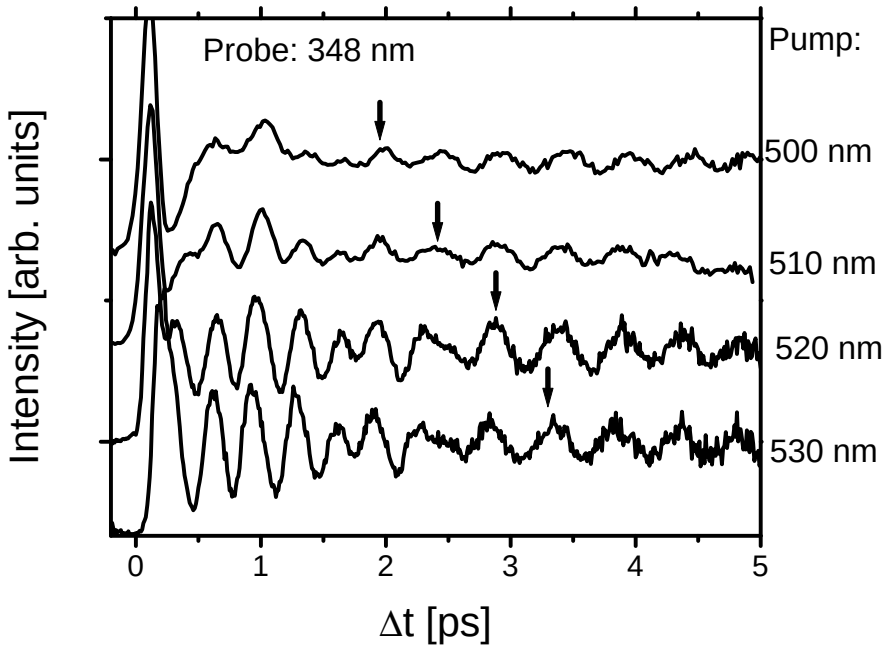

Figure 7.17: Pump-probe spectra of Br_2:Ar with λ_{probe} = 348 nm and λ_{pump} varied from 500 to 530 nm. The arrows mark the approximate inset of the 500 fs oscillation frequency.

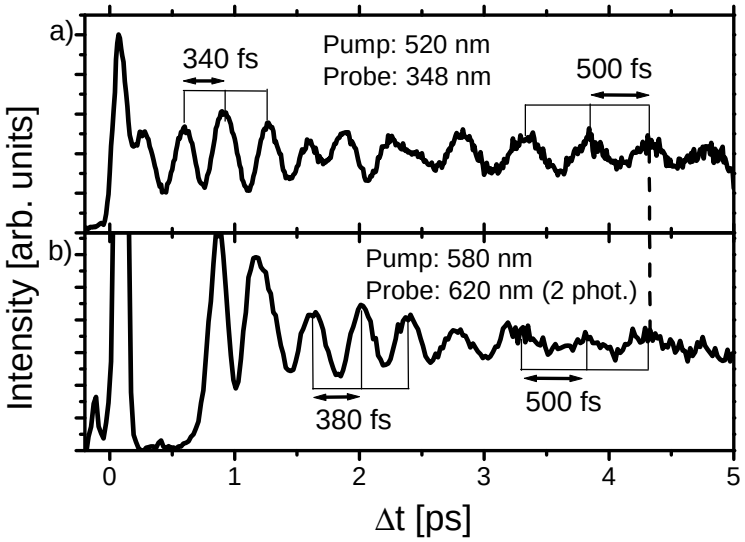

Figure 7.18: Normalized pump-probe spectra of Br_2:Ar probing the B state a) or the A state b). The intramolecular vibrational dynamics is very different. After 3 ps, the 500 fs (host induced) dynamics shows up on both spectra.

when probing the B state of Br_2, but also when probing the A state. Fig. 7.18a repeats the normalized spectrum of Fig. 7.16b. It is compared to a spectrum, where only the A state is probed by a two-photon transition (Fig. 7.18b). As expected, the intramolecular vibrational wave packet dynamics at small delay times is different. The A state is excited above the gas phase dissociation limit, resulting in a long first period. The relaxed A state vibrational wave packet has a period of 380 fs. However, after 3 ps, the 500 fs oscillation starts. The dashed line shows no phase offset in the 500 fs oscillation of the A and B state spectra.

Fig. 7.19 shows the Fourier transformation of the spectrum with λ_{pump} = 520 nm and λ_{probe} = 348 nm from Fig. 7.17b. Besides a peak centered at 3 THz with a width of 0.5 THz, a rather narrow band at about 2 THz is visible. The broad peak is well known from the Br_2 B state vibrational wave packet motion. The narrow maximum is the spectral analogue of the 500 fs modulation that will be attributed to host dynamics.

7.2.2 I_2 in solid krypton

Besides the spectra for Br_2:Ar, also transients for I_2 in solid krypton were measured by the author. In this case, one observes features very similar to the Br_2:Ar case.

Fig. 7.20a shows a pump-probe spectrum of the I_2 :Kr B state wave packet when pumping at λ_{pump} = 530 nm and probing at λ_{probe} = 508 nm (one-photon probe transition to the first charge-transfer manifold of I_2:Kr). As in the case of Br_2 in an argon crystal, two different oscillatory patterns occur: The dynamics from 0 to 4 ps shows an oscillation period around 420 fs. It is damped and hence vanishes at 4 ps. This period can be consistently interpreted as the trace of the B state intramolecular vibrational wave packet in I_2:Kr. At 4 ps, a new pattern with 650 fs period starts. To improve the modulation contrast, the spectrum is once more normalized to an average. The normalized spectrum is shown in Fig. 7.20b. The 650 fs period behaves in a similar way as the 500 fs period in the Br_2:Ar case. It does not decay and its phase is stable. This is illustrated by fitting the 650 fs modulation by a single sinusoidal function (dashed curve in Fig. 7.20b). As in the case of Br_2 :Ar, the apparent noise level at long delays rises due to the normalization procedure.

The A state of I_2 in solid Kr can be excited at λ_{pump} = 654 nm without any B excitation. Fig. 7.20c shows an A state spectrum probed at λ_{probe} = 387.5 nm. Since the A state is again excited above its gas phase dissociation limit, it shows a typical long excursion of the vibrational

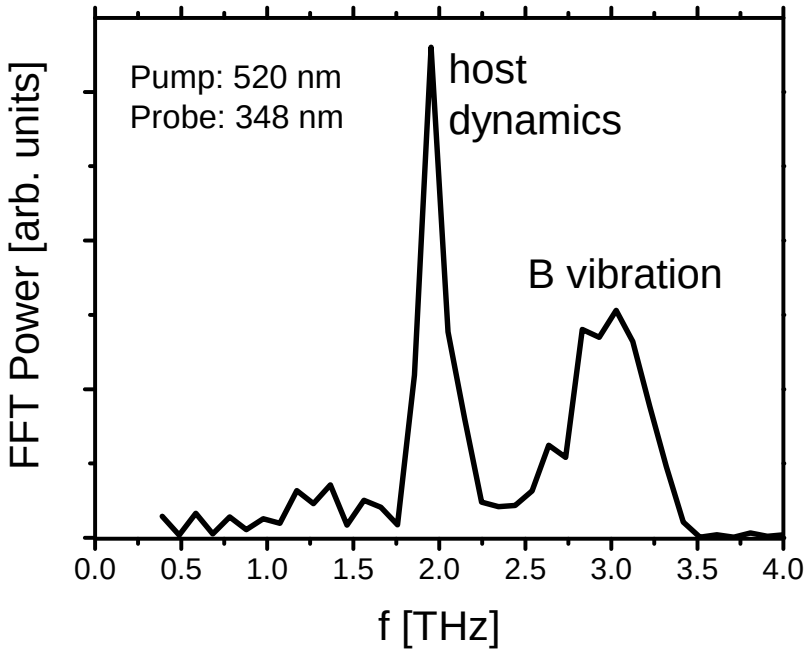

Figure 7.19: Power spectrum for the Fourier transform of the λ_{pump} = 520 nm, λ_{probe} = 348 nm transient of Br_2:Ar in Fig. 7.17b. Besides a broad peak at 3 THz attributed to the intramolecular vibrational wave packet, a narrow spectral maximum at about 2 THz corresponding to the 500 fs modulation appears.

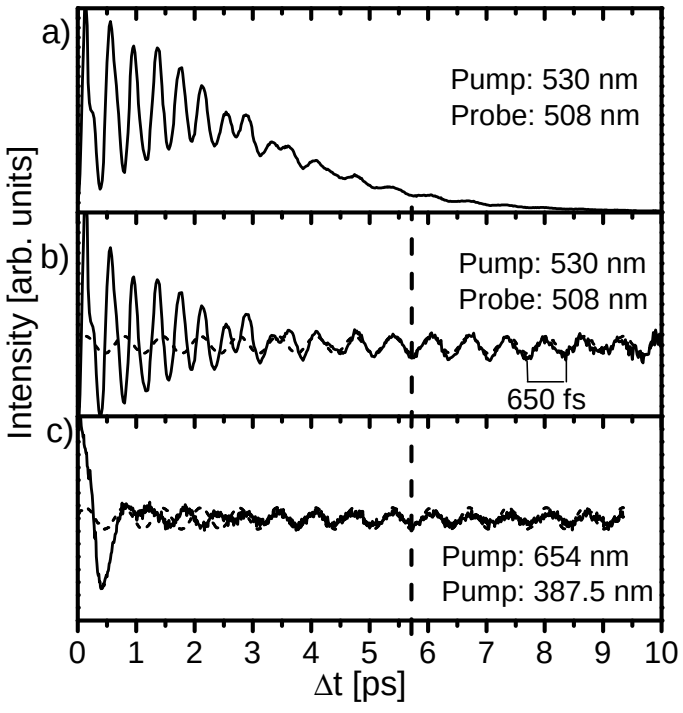

Figure 7.20: Pump-probe spectra of I_2:Kr . a) The original experimental spectrum, when exciting (λ_{pump} = 530 nm) and probing (λ_{probe} = 508 nm) the B state is shown. b) The spectrum normalized to a 70 data point average. Besides the vibrational dynamics of the B state with periods around 420 fs, a stable modulation with 650 fs period becomes visible after 4 ps. The solid line in (c) shows the normalized A state pump-probe spectrum with λ_{pump} = 654 nm and λ_{probe} = 387.5 nm. After the initial A state wave packet dynamics, again a 650 fs modulation sets in at 3 ps. The phase of the late dynamics is the same in b) and c) (dashed line). A cosine curve (dashed) is plotted in b) and c).

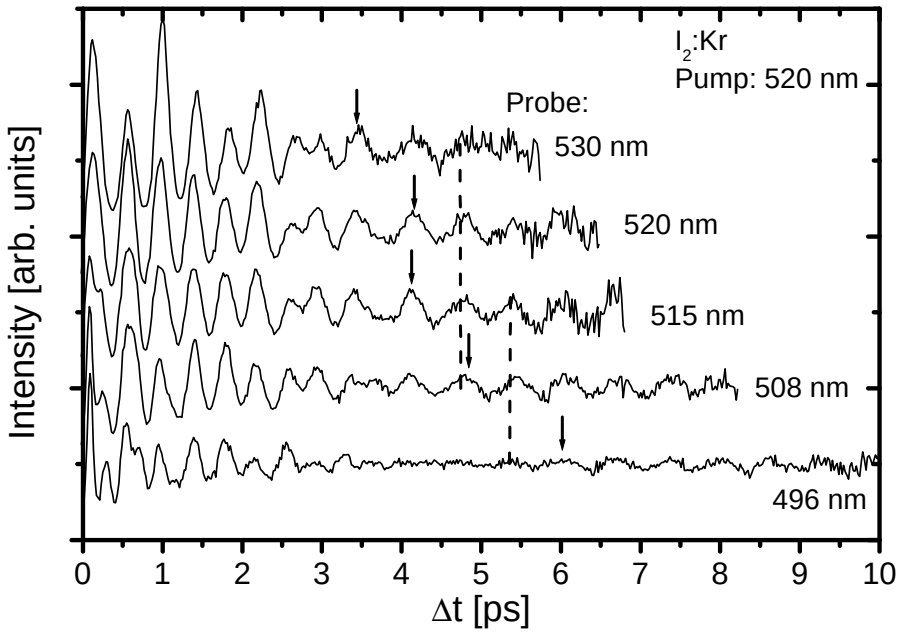

Figure 7.21: Pump-probe spectra of I_2:Kr with λ_{pump} =520 nm and λ_{probe} varied from 496 to 530 nm. The vertical arrows mark the inset of the 650 fs modulation. The relative phase of this modulation is the same in the series, as indicated by the dashed lines.

wave packet in the first picosecond. After 3 ps, this vibrational dynamics has decayed and again, a stable 650 fs modulation dominates the dynamics. As in the case of Br_2:Ar, the modulations shown in (b) and (c) have the same phase. The time zero for the B and A state transients in the case of I_2:Kr can be seen directly in different pump-probe spectra because the signals appear directly on positive and negative time delays. The negative time delays correspond to an exchange in the role of pump and probe pulse. The minimum between the first peaks of the respective spectra to positive and negative time delays corresponds to the time zero. The time zero of spectrum c) in Fig. 7.20 was determined by measuring simultaneously B and A state with λ_{probe} = 387.5 nm and polarization selective techniques.

Figure 7.21 shows a series of pump-probe spectra, all pumped by 520 nm pulses. The characteristic splitting of the first peaks appears analogous to the Br_2:Ar spectra. At high probe photon energies the splitting is large and becomes smaller at lower ones. The splitting has vanished at λ_{probe} = 520 nm. Thus in analogy to Br_2 in solid argon, one identifies a resonance for the $\lambda_{\mathrm{pump}} = \lambda_{\mathrm{probe}}$ = 520 nm case. The initial B state wave packet decays and the 650 fs host induced modulation becomes visible. The inset of the dynamics is marked by the vertical arrows. At low probe quantum energies, for example at 530 nm probe wavelength, the host dynamics begins at 3 ps. The inset is shifted to larger delay times as the probe quantum energy increases. In the extreme case of λ_{probe} = 496 nm, it is located at about 6 ps. The frequency and phase of the host modulation is the same throughout the series.

A similar systematic study was carried out keeping λ_{probe} fixed and varying λ_{pump}. Fig. 7.22 shows different pump-probe transients. The host induced 650 fs period starts at delays marked

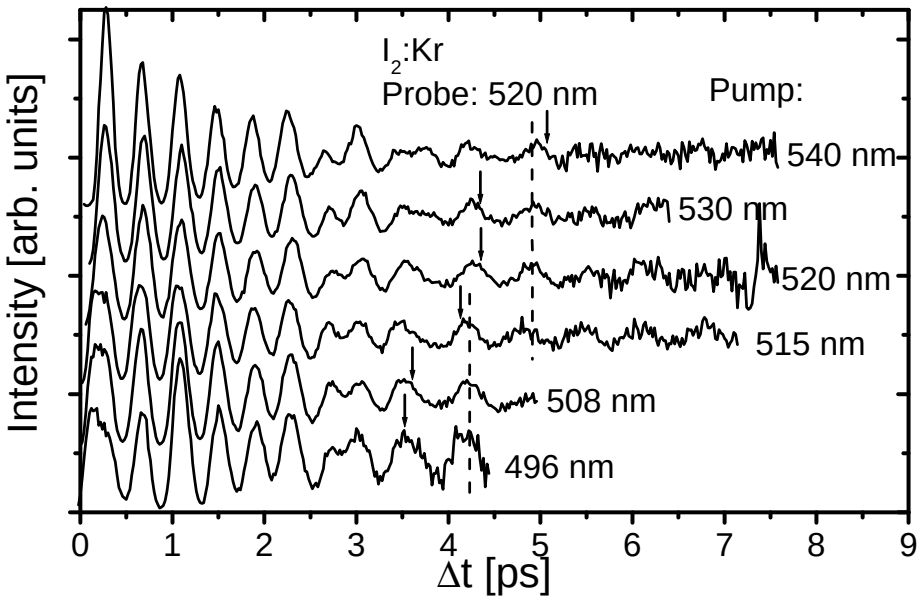

Figure 7.22: Pump-probe spectra of I_2:Kr for fixed λ_{probe} = 520 nm and λ_{pump} varied from 530 to 496 nm. The inset of the 650 fs modulation is marked by the vertical arrows. Its phase stability is indicated by the dashed lines.

by the arrows. The inset of the host modulation at λ_{pump} = 530 nm occurs at 4 ps. With increasing excitation energy, the appearance of the 650 fs modulation shifts to earlier times. At 496 nm pump wavelength, it appears at 3.5 ps. The frequency and phase among the spectra is the same as indicated by the dashed lines.

Fig. 7.23 shows the Fourier transformation of the normalized transient in Fig. 7.20b. The intramolecular vibrational wave packet dynamics shows up as a relatively broad peak at 2.5 THz corresponding to a period around 400 fs. The host induced dynamics with its 650 fs period is also contained in Fig. 7.23 as a narrow peak centered at 1.5 THz. The line width of that peak is essentially given by the observation window length in Fig. 7.20b of 10 ps. Thus, the peak at 1.5 THz reflects the surprising frequency stability of the host induced modulation.

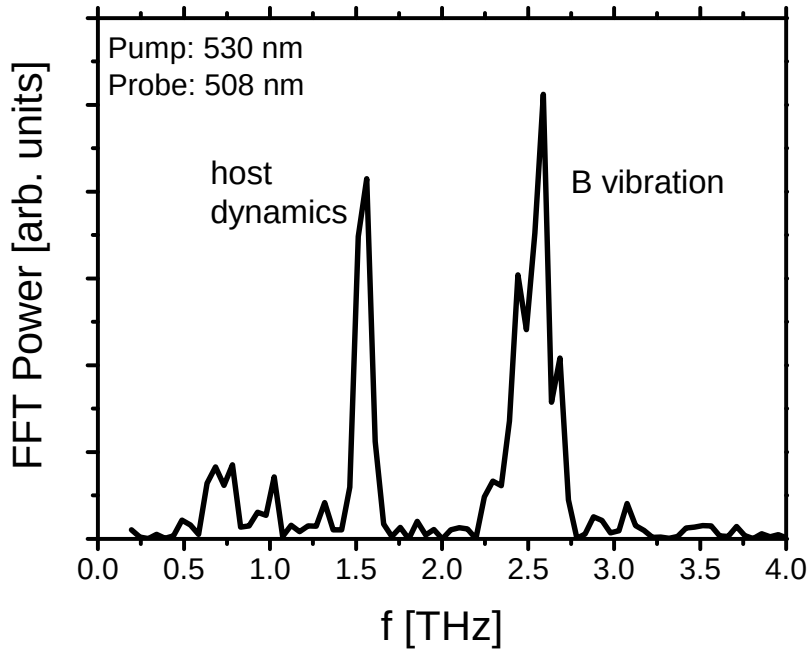

Figure 7.23: Power spectrum of a Fourier transformation of spectrum in Fig. 7.20b). The B vibrational wave packet dynamics shows up as a broad peak centered at 2.5 THz, the 650 fs host modulation corresponds to the narrow maximum at 1.5 THz.

Chapter 8

Discussion of ultrafast dynamics

The construction of the electronic B state potential in solid Ar, the vibrational energy relaxation and molecular trajectory will be deduced for Br_2 in argon crystals (section 8.1). The methods to determine dephasing and the connected wave packet control schemes are successfully applied as demonstrated in section 8.2. The different time constants and their abbreviations used in this thesis are collected in Tab. 8.4. Finally, excitation and probing of the coherent host dynamics is clarified and compared to alternative models (section 8.3).

8.1 Intramolecular dynamics

8.1.1 Vibrational periods in the B state

One of the aims in this chapter is to construct a B state potential energy surface of the Br_2:Ar from the vibrational periods T, according to the RKR procedure. Clearly, the B state potential curve is anharmonic. The effect of the anharmonicity can be observed for example in Fig. 7.2. The oscillatory periods become longer as the vibrational energy of the wave packet is increased (by decreasing the pump wavelength). Another sign of the anharmonicity is the dispersion, which will be discussed in section 8.2.1. In anharmonic oscillators, special care is required when determining the oscillation periods as a function of excitation energy, because the choice of the probe window changes the apparent period. This has been called "window effect" in the well documented case of I_2 in solid Kr [13, 25].

Probe window effects on the molecular period

Experimental data indicating the window effect are shown in Fig. 8.1. The spectra in this graph are all recorded for the same λ_{pump} = 560 nm, whereas the probe wavelength was varied. The vibrational periods are marked by the vertical lines. One realizes a tilt in the second and third line with respect to the dashed reference line which corresponds to a shortening of the vibrational period when taking the spectra with shorter λ_{probe}. For example one reads from the graph a double vibrational period of $2T = (660 \pm 20)$ fs for the transient with λ_{probe} = 354 nm. The spectrum recorded with λ_{probe} = 342 nm shows a double period of $2T = (600 \pm 20)$ fs. The overall shift in the time interval of two periods is $2\Delta T = (60 \pm 40)$ fs. The dependence of T on the probe quantum energy is explained in Fig. 8.2. The pump pulse with central quantum energy hν_{pump} (grey arrow) populates several B state vibrational levels when acting on the electronic ground state $v = 0$ wave function. The wave packet energy distribution is shown as the grey curve to the left. The lower parts of the wave packet oscillate with a high frequency, corresponding to a short period T. The higher parts of the wave packet have a longer T, since the oscillator is anharmonic. This leads to dispersion (section 2.2). The probe pulse has a central quantum energy $h\nu_{\mathrm{probe}}$. The internuclear position R_{win} at which the wave packet is probed is given by the condition $\Delta V(R_{\mathrm{win}}) = h\nu_{\mathrm{probe}}$ (Eq. (2.26)).

Figure 8.2 shows two different probe pulses with quantum energies $h\nu_{\mathrm{probe1}}$ (solid arrow)

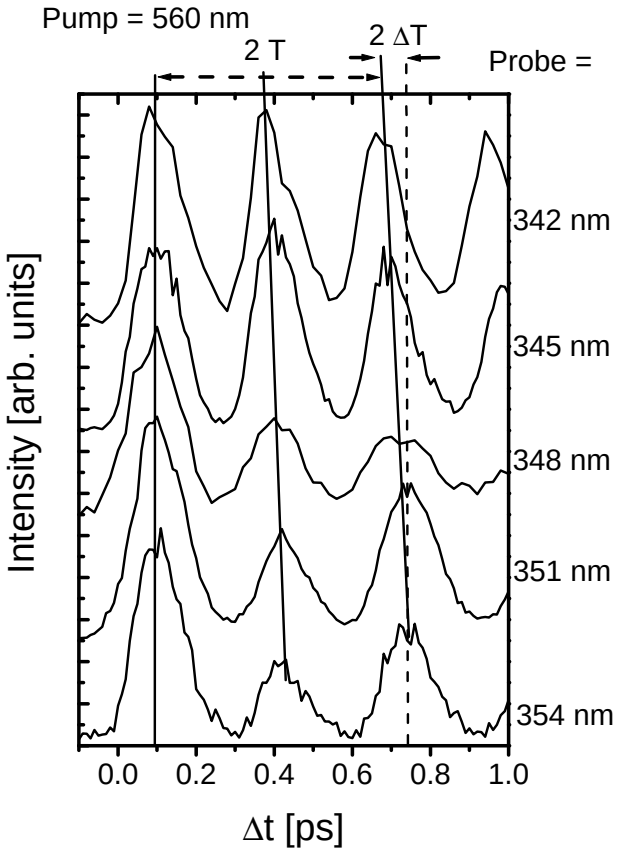

Figure 8.1: Br_2:Ar pump-probe spectra for λ_{pump} = 560 nm. The value of λ_{probe} is varied between 342 and 354 nm. The vertical lines connect the maxima and indicate the vibrational periods. For long λ_{probe} the periods are longer than for short ones, as can be seen by comparison with the dashed vertical reference line. After two periods $2T$, the mismatch in periods has accumulated to $2\Delta T$.

and $h\nu_{\mathrm{probe2}}$ (dashed arrow), leading to two different probe distances R_{win1} and R_{win2} and window energies E_{win1} and E_{win2} in the B state. The probe windows are governed by the dependence of ΔV on R. If the slope of $\Delta V(R)$ is negative in the range of interest (as it is in the case of the sketched B-E difference potential), then E_{win} and R_{win} shift to smaller values for larger $h\nu_{\mathrm{probe}}$. Probe 1, having a larger quantum energy, probes deeper in the B well than probe 2; therefore, probe 1 leads to a shorter apparent vibrational period T_1 than does probe 2 with T_2.

In the example of Fig. 8.1, probe 1 corresponds to λ_{probe} = 342 nm, whereas probe 2 would be the λ_{probe} = 354 nm pulse. The apparent experimental period T_1 = (300 $\pm$ 10) fs is indeed shorter than period T_2 = (330 $\pm$ 10) fs (T_1 and T_2 should *not* be mistaken for dissipation and dephasing times here).

An additional condition for λ_{probe} has to be imposed in order to find the correct vibrational period for a given wave packet excitation energy; the probe window energy should be located at the energetic center of the wave packet. The optimal probe pulse would lie between pulse 1 and 2 in Fig. 8.2. According to the probe resonance condition (section 2.3.1), the probe quantum energy has to be systematically decreased until the vibrational splitting just vanishes. The appropriate probe wavelength for an excitation of 560 nm is apparently at 345 nm, since at 342 nm probe, the splitting is still observed in the asymmetric shapes of the vibrational peaks. At 342 nm this has vanished.

Br_2:Ar oscillation periods

The oscillation periods are determined from the catalogue of spectra shown in Figs. 7.3 and 7.4 by applying the resonance criterion. The oscillation times for excitation wavelengths from 530 to 580 nm were constructed in that way. For excitation wavelengths 590 and 600 nm,

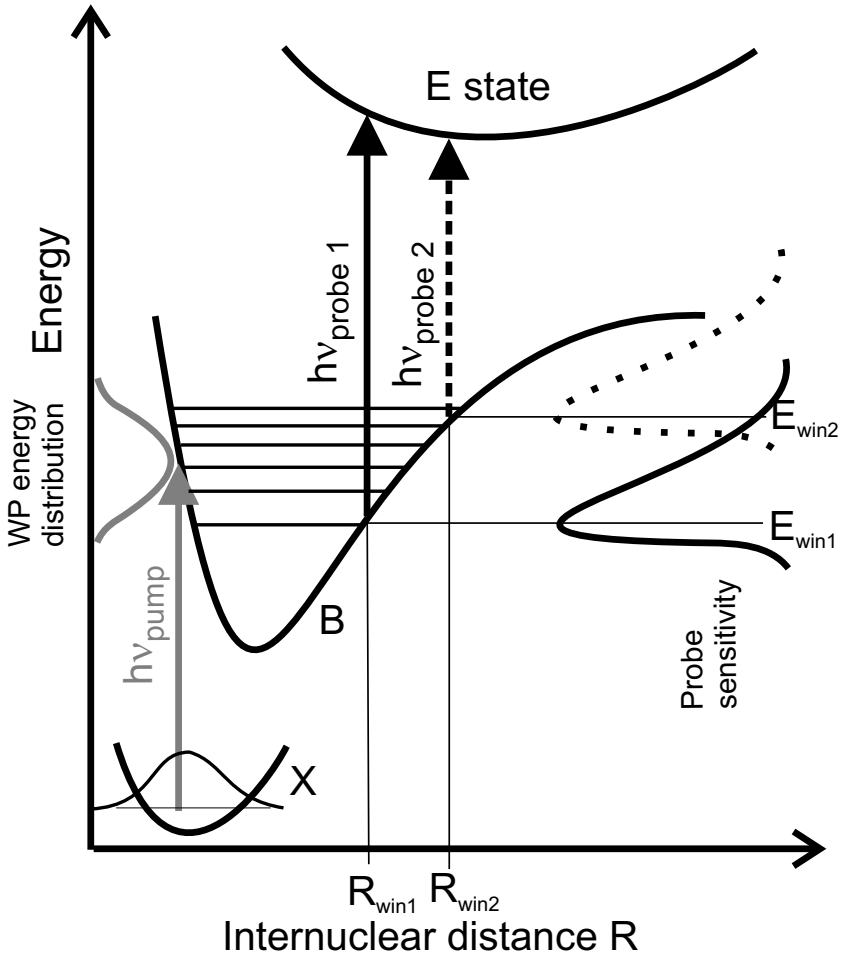

Figure 8.2: Illustration of the window effect. The wave packet is excited by a pump pulse (grey arrow) with mean quantum energy hν_{pump}, which acts on the ground state (X) vibrational level $v = 0$. Since the spectrum of the pump pulse has a finite width (solid grey curve to the left), several vibrational eigenstates in the B electronic potential are populated. The B oscillator is anharmonic, thus the lower parts of the wave packet have a smaller oscillation period T than the parts on higher vibrational levels. This corresponds to a decreasing vibrational level spacing with higher vibrational energy. Two different probe pulses are shown: one has the mean quantum energy hν_{probe1} (solid arrow) and the other one a smaller energy hν_{probe2}. The probe position R_{win} is determined by the difference potential between B and E state. Pulse 1 probes deep in the potential B well at (R_{win1}, E_{win1}), pulse 2 higher at (R_{win2}, E_{win2}). The probe sensitivity curves (solid for 1, dashed for 2) are sketched at the right side of the graph. Their shape has been described in Fig. 2.9. Pulse 1 probes the low vibrational levels of the B state wave packet, whereas pulse 2 probes the high levels. This leads to different vibrational periods due to the B anharmonicity.

Table 8.1: B state periods T versus energy. The pump wavelength is transformed to a pump quantum energy E_{pump}. Using the B state absorption spectrum, the mean energy of the wave packet E_{WP} is calculated. E_B is the vibrational energy of the wave packet in the B state. The oscillation period T is taken from pump-probe spectra using the probe resonance condition at λ_{probe}, where 2p indicates a two-photon probe process.

λ_{pump} [nm]	E_{pump} [cm^{-1}]	E_{WP} [cm^{-1}]	E_B [cm^{-1}]	T [fs]	λ_{probe} [nm]
490	20408	20410	4688	636 ± 20	345
500	20000	20039	4317	573 ± 20	345
510	19608	19667	3945	526 ± 20	345
520	19231	19281	3559	475 ± 20	345
530	18868	18944	3222	400 ± 10	345
540	18519	18626	2904	358 ± 10	351
550	18182	18319	2597	330 ± 10	348
560	17857	18025	2303	300 ± 10	345
570	17544	17746	2024	280 ± 10	342
580	17241	17480	1758	270 ± 10	339
590	16949	17230	1508	260 ± 10	590 (2p)
600	16667	16994	1272	250 ± 10	580 (2p)

spectra probed by two photons were used. For excitation wavelength of 520 nm and shorter, the situation is more complicated. As already shown in context with Fig. 7.5, an additional vibrational splitting appears for long probe wavelengths due to the host motion. For example, choosing λ_{pump} = 520 nm, the double splitting never vanishes and the resonance criterion does not work. An alternative way to estimate the first oscillation period at these excitation conditions is presented in section 8.1.2 with help of the RKR scheme.

When assigning the oscillation to a specific vibrational energy E_{B} in the B state, the absorption profile has to be taken into account. Thus, the excitation pulse profiles are folded with the absorption spectrum of the B state, based on the calculated Franck-Condon (FC) factors and the projection method (see Fig. 6.4). The rise in B state absorption with energy, up to values of about 20500 cm^{-1}, leads to a blueshift of the wave packet central energy with respect to the excitation pulse spectral center. The effect is strong in the red wing of the B absorption, since FC factors rise exponentially in that region. Table 8.1 shows a collection of vibrational periods in the B state, taking this effect into account.

8.1.2 Potential construction

The topic of this subsection is the construction of a potential from the systematic experimental periods T. It is very similar to a method well known in high resolution gas phase spectroscopy as the RKR (Rydberg-Klein-Rees) method [161–163]. Here the classical analog of the RKR method described in chapter 12 of Ref. [218] is used. The method has been applied in a seminal work by Zewail and coworkers to transform time resolved data of free iodine in a potential energy curve of the electronic B state [146].

Vibrational periods from pump-probe spectra

The periods T with the correct central energies E_{WP} are collected in Tab. 8.1. Subtracting the B state T_e of 15722 cm^{-1} according to Langen *et al.* [66] from E_{WP} leads to the central vibrational energy E_{B} of the excited wave packet in the B state. The resonant probing condition can be fulfilled for excitation energies of 1200 to 3200 cm^{-1} above the B state minimum.

Fig. 8.3 shows the squared vibrational frequency $\nu_{\mathrm{vib}}^2 = 1/T^2$ versus the energy E_{B} above

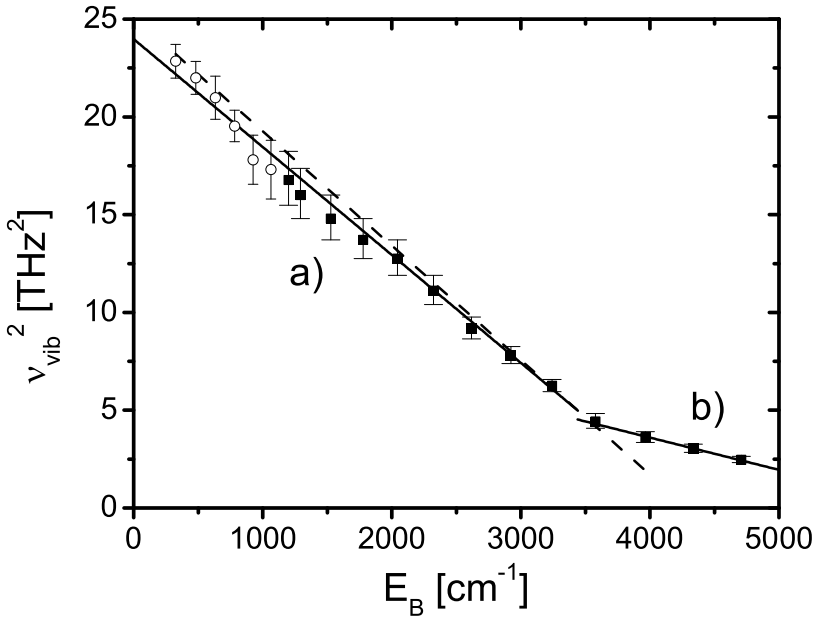

Figure 8.3: Squared vibrational frequencies ν_{vib}^2 of the Br_2:Ar B state. The open circles are taken from Bondybeys excitation spectrum [55], the solid squares are taken from Tab. 8.1. The solid lines represent linear fits (see text). The dashed solid line represents the free Br_2 values approximated by a Morse potential [53].

Table 8.2: Morse fits for Br_2:Ar vibrational frequencies: $\nu_{\text{vib}}^2 = b + mE_{\text{B}}$. Case a) refers to the values E_{B} from 0 to 3200 cm^{-1} in Fig. 8.3, whereas case b) refers to the values above 3200 cm^{-1}.

	b [THz^2]	m [THz^2/cm^{-1}]
a)	23.98 $\pm$ 0.46	(-5.52 $\pm$ 0.19) 10^{-3}
b)	10.2 $\pm$ 1.4	-1.65 $\pm$ 0.32

the B state minimum. The plot was chosen because a Morse oscillator obeys Eq. (2.13) ($\nu_{\text{vib}}(E) = \nu_e\sqrt{1 - E_{\text{B}}/D_e}$). The open circles are taken from an excitation spectrum of Br_2:Ar by Bondybey (see Fig. 1 in [55]). For that purpose, the energy differences of the ZPL maxima were determined with error bars reflecting the uncertainty. This range from 0 to about 1000 cm^{-1} was not covered by our pump-probe spectra yet, since the FC factors are too small in this range. The higher energy range indicated by squares are taken from Tab. 8.1 and extends beyond the gas phase dissociation at 3800 cm^{-1}. We first concentrate on the data in Fig. 8.3 from 0 to 3200 cm^{-1} which are taken with the resonance criterion. These points are fitted by a linear function of the form $\nu_{\text{vib}}^2 = b + mE_{\text{B}}$. The fitted values are given in row a) in Tab. 8.2 and the fitted graph is shown as the solid line denoted a) in Fig. 8.3. The potential $V(R)$ can now be constructed up to an energy E_{B} = 3200 cm^{-1}, using the RKR algorithm.

Calculation of the potential

From the oscillation periods as a function of energy in the B state $T(E_{\text{B}})$, one can calculate the inner and outer turning points of a classical trajectory. The velocity $v = dr/dt$ of a trajectory excited at an energy E_{B} is given by $v = \sqrt{2(E_{\text{B}} - V(R))/\mu}$. Thus the infinitesimal time step dt is given by: $dt = dr/\sqrt{2(E_{\text{B}} - V(R))/\mu}$ with the reduced mass μ. Integrating over one

vibrational period in the potential $V(R)$ leads to the path length $\Delta R(U)$ (according to Chapter 12 of Ref. [218]):

$$\Delta R(U) = \frac{1}{\pi\sqrt{2\mu}} \int_0^U \frac{T(E_\mathrm{B})}{\sqrt{U - E_\mathrm{B}}} dE_\mathrm{B}. \tag{8.1}$$

U is the maximal potential energy of the respective trajectory and $\Delta R(U)$ is the distance between outer $R_o(U)$ and inner turning point $R_i(U)$: $\Delta R(U) = R_o(U) - R_i(U)$. The analytic function for $T(E_\mathrm{B})$ is taken from the fit (see Tab. 8.2) of the squared vibrational periods. In a RKR fit for free molecules, one uses the rotational structure to calculate the values of $R_i(U)$ and $R_o(U)$. Since the Br_2 molecules are not rotating in the stiff Ar cage (see section 7.1.2), an assumption on the inner limb of the potential energy curve has to be made to deduce the outer limb from $\Delta R(U)$. The discussion of the absorption spectra in chapter 6.1 showed that the inner limb of the potential contributing to absorption is not changed compared to the free Br_2 molecule. The minimum potential energy is nevertheless shifted from T_e = 15900 cm^{-1} [53] in case of the free molecule to T_e = 15722 cm^{-1} according to Ref. [66]. Therefore, the inner part $R_i(U)$ of the potential is constructed as a Morse function:

$$R_i(U) = R_e - \frac{1}{\beta} \ln(1 + \sqrt{U/D_e}), \tag{8.2}$$

that coincides with the gas phase potential in regions around the absorption maximum of the B state and has its minimum energy at 15722 cm^{-1} above the electronic ground state $v = 0$ vibrational level. The Morse parameters of this inner limb for $R_i(U)$ are: R_e = 0.26775 nm, β = 20.3 1/nm and D_e = 3750 cm^{-1}. To construct the outer potential limb, the values of $\Delta R(U)$ calculated by numerical integration of Eq. (8.1) are added to the values of $R_i(U)$. Inverting the expression $R(U)$ leads to the potential $U(R)$ or $V(R)$, as it is usually called. The electronic potential of the Br_2:Ar B state is now constructed up to a value of E_B = 3200 cm^{-1}. For higher energies we have to replace the resonance condition. In this domain, the energy relaxation during the first collision with the matrix changes the central energy of the wave packet considerably, as will be described in context with Fig. 8.9. The vibrational wave packet ends up at an energy corresponding to an excitation with a pulse which has a central wavelength of 560-570 nm. This wave packet is resonantly probed by a UV pulse with 345 nm wavelength. The wave packet undergoes mild energy relaxation at its new vibrational energy. The situation is shown in Fig. 8.4b. The energy loss holds for all wavelengths from 530 to 490 nm.

We want to construct a first vibrational period of the wave packet from its inner turning point at the time of excitation until it reaches the inner turning point again. The vibrational wave packet is excited at a high vibrational energy close to the gas phase dissociation limit at time 0. It crosses the probe window at time 1 and travels for a long time on the outer potential bow, according to Fig. 8.4b. There, it loses a lot of vibrational energy and falls down to vibrational levels, that are resonantly probed by 345 nm pulses. It crosses R_win at time 2 and finishes a complete period until it changes direction and crosses the window again at time 3. From spectra like the one shown in Fig. 8.4a (λ_pump = 510 nm, λ_probe = 345 nm) the timing 1-2-3 can be quantified: The time interval from 1 to 2 is called Δt_{12}, the interval between 2 and 3 is called Δt_{23}. The Δt_{23} is one vibrational period of the wave packet at its relaxed vibrational energy. The initial oscillation period of the highly excited wave packet, however, has to be counted from time 0 until the next time, the wave packet reaches the inner turning point again. This time is called 2' and is reached exactly in the middle between 2 and 3. Thus, the initial period for the wave packet excited at 510 nm is T_{510}=Δt_{01}+Δt_{12}+$\Delta t_{22'}$. Taking the time T_false=Δt_{12}+Δt_{23}=Δt_{12}+$\Delta t_{22'}$+$\Delta t_{2'3}$ as the period, causes an error. The times T_{510} and T_false would be equal when $\Delta t_{2'3}$=Δt_{01}. This is however not the case in an anharmonic oscillator and

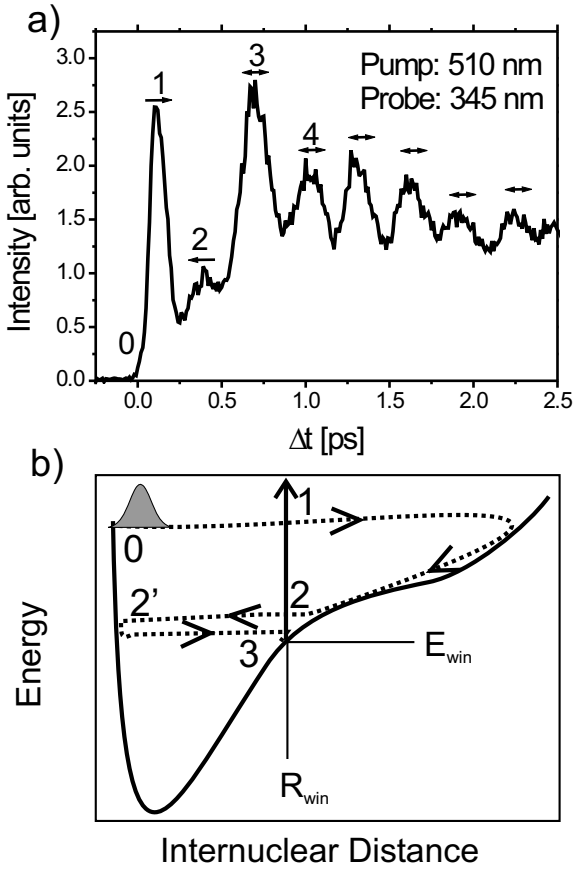

Figure 8.4: a) Pump-probe spectrum of Br_2:Ar excited at 510 nm. The wave packet is probed to the E state at (R_{win}, E_{win}) by a probe pulse entered at 345 nm. The arrows above the peaks display the direction of the movement. The first apparent oscillation period from 1 to 3 is very long (above 600 fs), the following are shorter than 300 fs. b) Sketch of the molecular trajectory. The first collision with the Ar cage atoms causes a large vibrational energy loss. The molecular potential bends up at the dissociation limit due to the cage (see Fig. 8.6).

Δt_{01} is shorter because of the steep inner limb and the higher kinetic energy. Unfortunately, the time 0 (the pump-probe temporal overlap) could not be measured at the position of the sample in the experiment. Therefore, we follow another strategy. The constructed potential up to 3200 cm^{-1} is used to *calculate* the time Δt_{01} as a function of excitation energy. The values for Δt_{01} are about 50 fs shorter than $\Delta t_{2'3}$. This correction is short compared to the values for the full periods. Those times are added to the times Δt_{12}+$\Delta t_{22'}$ that are directly determined from the pump-probe spectra using a probe wavelength of 345 nm. The actual times are then converted into squared vibrational frequencies and plotted versus E_{B} in Fig. 8.3. These additional values cover the energy range between 3600 and 4700 cm^{-1} in the B state. The values are fitted by a linear function and the fit parameters are shown in Tab. 8.2b. The analytical expression is converted into oscillation times and once more fed into the RKR numerical routine together with the values from fit a). When calculating the potential curve once more, the potential is unchanged up to E_{B} = 3200 cm^{-1} and is extended now to higher energies.

The resulting Br_2:Ar RKR potential is shown in Fig. 8.5 (solid curve) together with the gas phase potential from Ref. [43] (dashed curve). It is worth mentioning, that the RKR potential is an effective potential describing the interaction of a vibrational wave packet in the B state of Br_2 with the Ar host environment. At low excitation energies in the B state, the cage does not interact strongly with the Br_2 wave packet motion, and the energy relaxation is rather mild (see Fig. 8.9). But at excitation close to the dissociation limit, the energy relaxation in the first round trip has a strong effect. In this energetic range, the interaction with the cage must be strong, since host phonons are created during one collision. The potential indicates this effect, since oscillation periods are measured that contain the energy relaxation mechanism. The passage times for the wave packets excited at high vibrational energies are taken before and after the

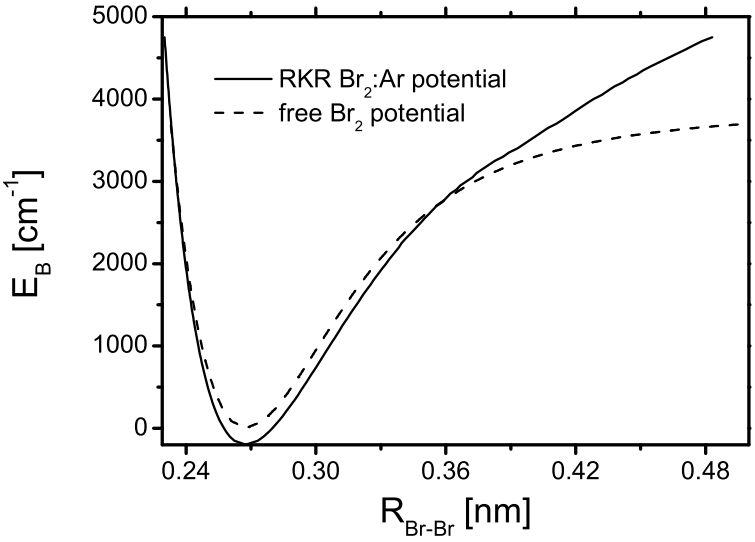

Figure 8.5: Solid curve: the RKR potential energy curve for the electronic B state of Br_2:Ar (see text). Dashed curve: B state potential for a free Br_2 molecule from Ref. [43].

strong first collision with the cage. Thus, one has to consider the constructed RKR surface as a projection of a very complicated multidimensional surface, including many degrees of freedom on the internuclear Br-Br axis.

The most prominent feature in the effective RKR potential is the lack of a dissociation limit in the Br_2:Ar potential curve. The cage effect (see section 3.2.1) does not allow for dissociation of the molecules. As a result, the outer electronic potential limb depicted over the internuclear distance bends up, as was clarified in similar studies for I_2 in solid rare gas environments [25, 111–113]. Here this effect is documented for Br_2 in solids. Apart from the repulsive interaction with the matrix, an attractive interaction between Br and Ar occurs, leading to a decrease of the effective B potential surface between 0.24 and 0.36 nm internuclear Br-Br distance. In this range, the cage seems to expand the molecular bond. This effect has also been observed in DIM calculations of Cl_2 molecules in solid argon [219]. A simple model of the cage environment explains the attractive and repulsive effect. The model geometry shown in Fig. 8.6a consists of a single Br_2 molecule placed between the so called "head-on" atoms, that are the nearest Ar atoms located along the elongated internuclear axis. The distance between the center of the Br_2 molecule and the Ar atoms is called R_{Ar}, whereas the internuclear distance in the bromine molecule is called $R_{\mathrm{Br-Br}}$. The free molecule B potential is given as the thin solid curve in Fig. 8.6b. The interaction is calculated via pair potentials in the DIM formalism, that will be explained in section 8.3.1. As will be described later on, the Br-Ar interaction has isotropic (V_0 see Eq. (8.4)) and anisotropic (V_1 see Eq. (8.5)) components. The superposition[1] leads to the dashed potentials shown in Fig. 8.6b. The model with 2 Ar atoms is indeed a crude approximation, since in reality the whole cage of 18 Ar atoms is interacting with the Br_2 molecule, however some effects can be discussed.

The minimum of the electronic B potential lowers by about 70 cm^{-1} compared to the gas phase value. This is the correct trend and the measured shift of the potentials T_e of 200 cm^{-1} is larger because it includes the full cage. The two model potentials (dashed curves in Fig. 8.6b) bend up near the dissociation limit, expressing the cage effect. As the bromine molecule ex-

[1]The potential of one Br atom in the molecular B state with head-on argon atom is given by: $V_{\mathrm{B}}(r) = \frac{1}{4}(3V_0 + V_1)$, where r is the distance between the Br and the Ar atom. This leads to a potential of V_{II} for the whole system. The potential parameters are given in Tab. 8.5 and the equations are documented in section 8.3.1.

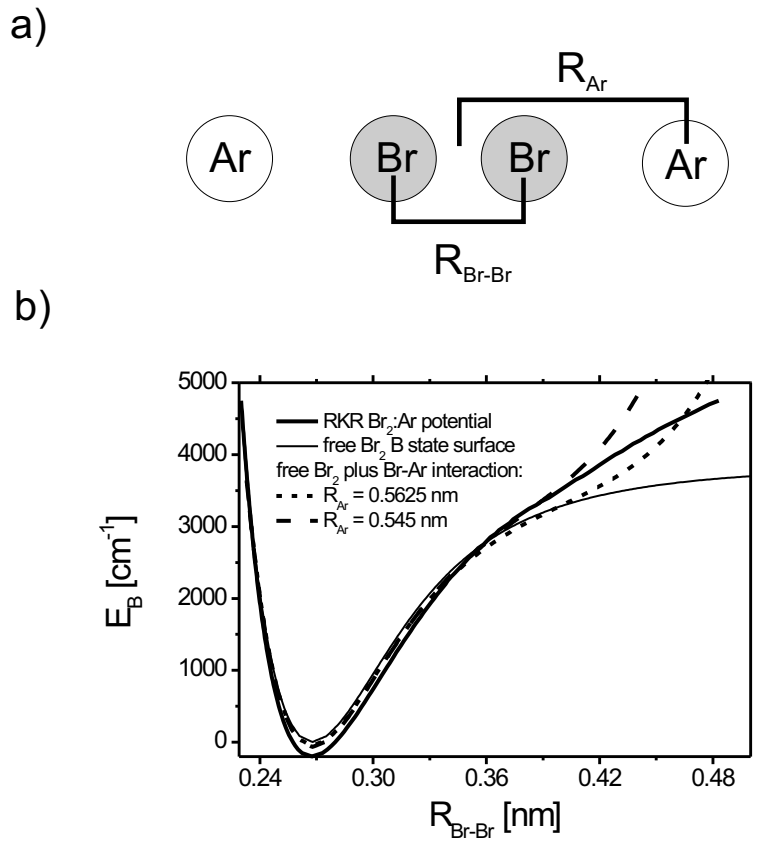

Figure 8.6: a) Scheme of the Br_2 molecule with the internuclear distance $R_{\mathrm{Br-Br}}$ and the two "head-on" Ar atoms sitting in distance R_{Ar} from the molecular center. b) Solid line: RKR surface of Br_2:Ar. Thin solid line: free Br_2 potential [43]. Short dashed line: free Br_2 plus Br-Ar interactions with head-on atoms sitting at R_{Ar} = 0.5625 nm distance from the molecular center (according to the nearest neighbor distance in a undisturbed Ar lattice). Dashed line: free Br_2 plus Br-Ar interactions with head-on atoms sitting at R_{Ar} = 0.545 nm distance from the molecular center.

pands in axial direction, the repulsive character of the Br-Ar interaction governs the potential. The numerical values depend on the distance of the Ar atoms from the molecular center R_{Ar}. For a distance of R_{Ar} = 0.5625 nm (given by 1.5 times the nearest neighbor distance in the Ar crystal of 0.375 nm), the model B potential is shown as the short dashed curve. In a range of $R_{\mathrm{Br-Br}}$ = 0.35 to 0.46 nm, the curve lies below the RKR potential. This is in contradiction to experiments. If a trajectory would run on such a potential, the round trip times would be longer than the observed round trip times. The single Ar atom seems to be too far away from the molecule. Thus, a smaller value of R_{Ar} = 0.545 nm is also chosen in the model calculation. The new model potential is shown as the dashed curve in Fig. 8.6b. It never lies below the experimental RKR curve. Close to the dissociation limit, it bends up too strongly compared to the RKR curve. The model is completely static. The experimental RKR curve however includes an outward motion of the Ar "head-on" atoms when the vibrational wave packet approaches its outer turning point. Furthermore, the inward motion of the wave packet after the collision with the matrix could be strongly slowed down by the so called belt atoms, as in the case of I_2:Kr [25] which is not included. This effect elongates the periods used to construct the RKR potential. It causes a wider RKR potential than the interaction of bromine with the two atom Ar cage would imply. A comparison of the R_{Ar} values used here with the equilibrium values R_{Ar} for the Br_2 B state seems to confirm the assumptions: Fig. 8.22d shows the equilibrium positions for the first shell Ar atoms. The "head-on" atom distance is too large and has to be diminished. Thus the trend observed for simple model potentials is confirmed.

8.1.3 Vibrational energy relaxation

When exciting a vibrational wave packet on Br_2:Ar near the gas phase dissociation limit of the electronic B state at 19740 cm^{-1} (507 nm), the molecule does not dissociate but recombines (section 3.2.1). This must be ascribed to the Ar cage repulsion, and the phenomenon has been quantified in terms of an effective Br_2:Ar potential in section 8.1.2. During the collision with the cage, energy is transferred to the host by the excitation of phonons. A description of the pump-probe spectra occurring in case of energy relaxation has already been given with help of Fig. 2.10.

The vibrational energy relaxation is now displayed in a real pump-probe spectrum shown in Fig. 8.4. The vibrational wave packet is excited with a laser pulse centered at 510 nm and probed with a UV pulse centered at 345 nm. It is created by the pump pulse at position 0 in Fig. 8.4. The first peak denoted by number 1 displays the outward motion of the vibrational wave packet from left to right in direction of longer internuclear elongations. The wave packet will spend a long time on the outer bow of the potential, hitting the cage and changing direction. It is again detected in its motion towards smaller internuclear distances, denoted by 2 in Fig. 8.4. The splitting of the vibrational motion into two peaks occurs, since the molecule was excited high above the energy E_{win} at which the B state is probed. After the first round trip, the splitting has vanished. The time interval between peaks 3 and 4 in the pump-probe spectrum corresponds to an oscillation period at energies much smaller than the initial excitation energy. At the new energy, the outer turning point of the wave packet coincides with the probe position R_{win} or is even smaller than that (see Fig. 8.4b). Thus, the molecule must have lost energy during the first elongation between peaks 1 and 2, which is due to the internuclear distance and the molecule-matrix interaction being maximal in this range.

The vibrational energy relaxation will be quantified in the following with a common probe wavelength of 345 nm. The full series of spectra is shown in Fig. 8.7. The molecular periods are determined for each excitation energy. The periods are called apparent periods, since window effects are neglected in their determination. Nevertheless, the apparent periods are indicative for the central vibrational energy of the wave packet. The first period is estimated by the time difference from peak 1 to 3 in Fig. 8.7. The loss in energy is displayed by the decay of T, since T is monotonically increasing with the vibrational energy in the case of an anharmonic oscillator. The most dramatic effect in the change of apparent periods occurs for excitation wavelength from 500 to 550 nm (Fig. 8.8). The step from the first to second period is rather large, indicating a high vibrational energy loss. Afterwards, the periods change only slightly. After the first round trip, the molecular wave packet has lost the ability to reach large internuclear elongations and couple effectively to the matrix. To determine an energy relaxation rate from Fig. 8.8, one has to determine the vibrational energy loss during the first round trip. This can be done by comparing the second apparent period with the first periods at different (lower) excitation energies.

One explicit example shall be given here: The second and following periods of the wave packet initially excited with 500 nm (20039 cm^{-1} including the absorption) have an apparent period of about 300 fs. This corresponds to the first period measured for an initial excitation of a 560 nm (18025 cm^{-1}) centered laser pulse. The energy difference from 500 to 560 nm corresponds to an energy loss of 2014 cm^{-1} within the first period. This period is 573 fs long (see Tab. 8.1). Therefore, the energy loss rate dE/dt is 2014 cm^{-1} per period or 2014/0.573 cm^{-1}/ps = 3514 cm^{-1}/ps.

The error of the energy relaxation rate is estimated in the following way: The energy loss cannot be determined better than the scan step of pump wavelengths used in the spectra (10 nm from spectrum to spectrum). The 10 nm step width corresponds to an energy uncertainty of $\pm$ 150 cm^{-1} in this range. The error in the oscillation period is already given in Tab. 8.1. The

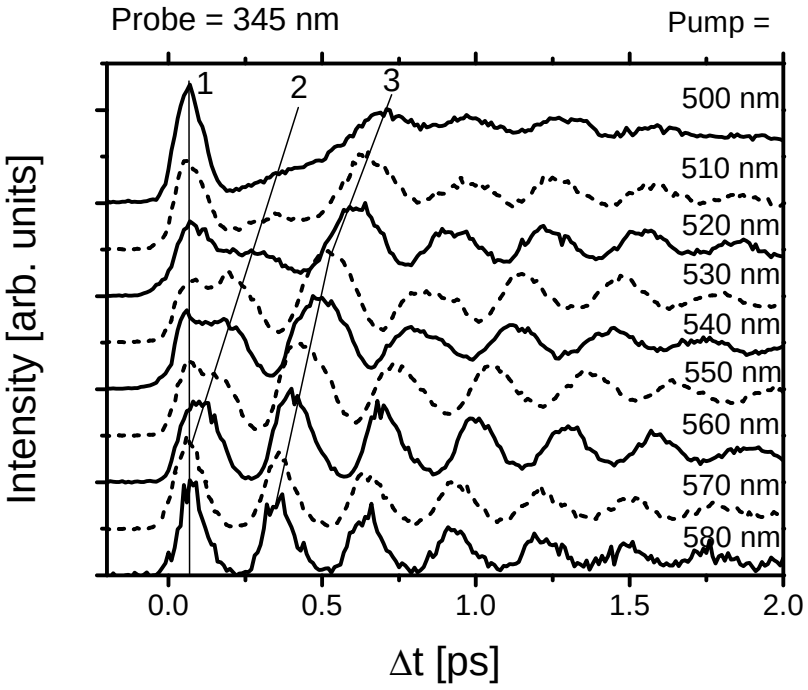

Figure 8.7: Br_2:Ar pump-probe spectra probed by 345 nm pulses, pumped from 500 to 580 nm. The first outward motion is marked with line 1. The following inward motion is visible from 500 to 550 nm and marked with line 2. The next wave packet recurrence is marked with line 3.

relative errors of energy uncertainty and period add up and lead to the resulting rate: (3500 $\pm$ 300) cm^{-1}/ps.

The vibrational energy relaxation rates for many different central energies of the wave packet E_B are shown as the solid squares in units of cm^{-1}/ps or as open circles for the unit cm^{-1}/period in Fig. 8.9. From E_B = 2600 cm^{-1} upwards, the energy relaxation occurs during the first round trip. Below, the rates were estimated by the decrease of the vibrational period T over several periods.

For the highest excitation energies, the energy loss in one vibrational period corresponds to almost 50 % of the total vibrational energy in the B state. For example, the wave packet excited at 500 nm has a central energy of 4320 cm^{-1} above the B state minimum and loses about 2000 cm^{-1} of vibrational energy during the first round trip, which is more than its width of 500 cm^{-1}. Two observations are very surprising: Vibrational levels, unpopulated before the strong energy loss, are instantaneously populated. Second, the population mechanism is coherent, since coherent wave packet oscillations are observed after the first round trip in all spectra (see Fig. 8.7). The lifetime of a vibrational level, or alternatively speaking its dissipation time T_1 (section 2.1), is short for vibrational eigenstates near the dissociation limit and gets longer with decreasing vibrational energy. At the free molecule dissociation limit, the dissipation time is essentially given by the molecule-cage collision time, which will be a subject of the next section. It is much shorter than half a vibrational period. At $E_B = 2300$ cm^{-1}, the dE/dt = 60 cm^{-1}/period. A vibrational period is 111 cm^{-1} (300 fs) in this range and therefore, the vibrational levels have a T_1 of about 2 periods or 600 fs.

First, concentrate on the observation of the large energy loss of about 50 % of the overall vibrational energy. The only way to lose vibrational energy to the matrix is the creation of

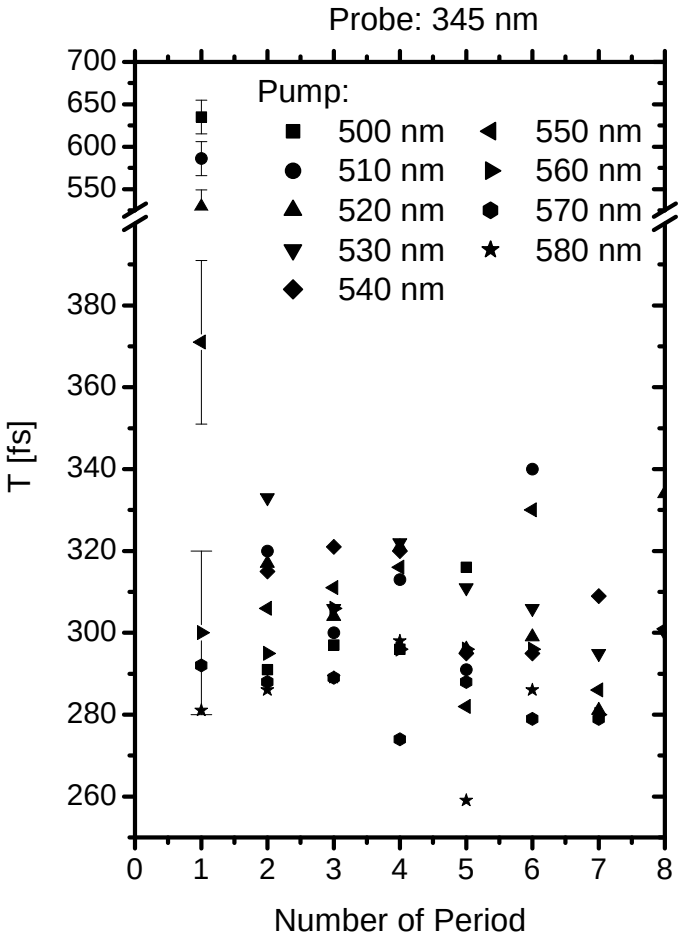

Figure 8.8: Apparent vibrational periods T of Br_2:Ar as a function of the period number after excitation. The wave packets were probed by pulses centered at 345 nm and pumped from 500 to 580 nm with a step width of 10 nm. The error bars for the apparent periods of $\pm$ 20 fs are valid for all data points, but for better visibility are only shown for the first period.

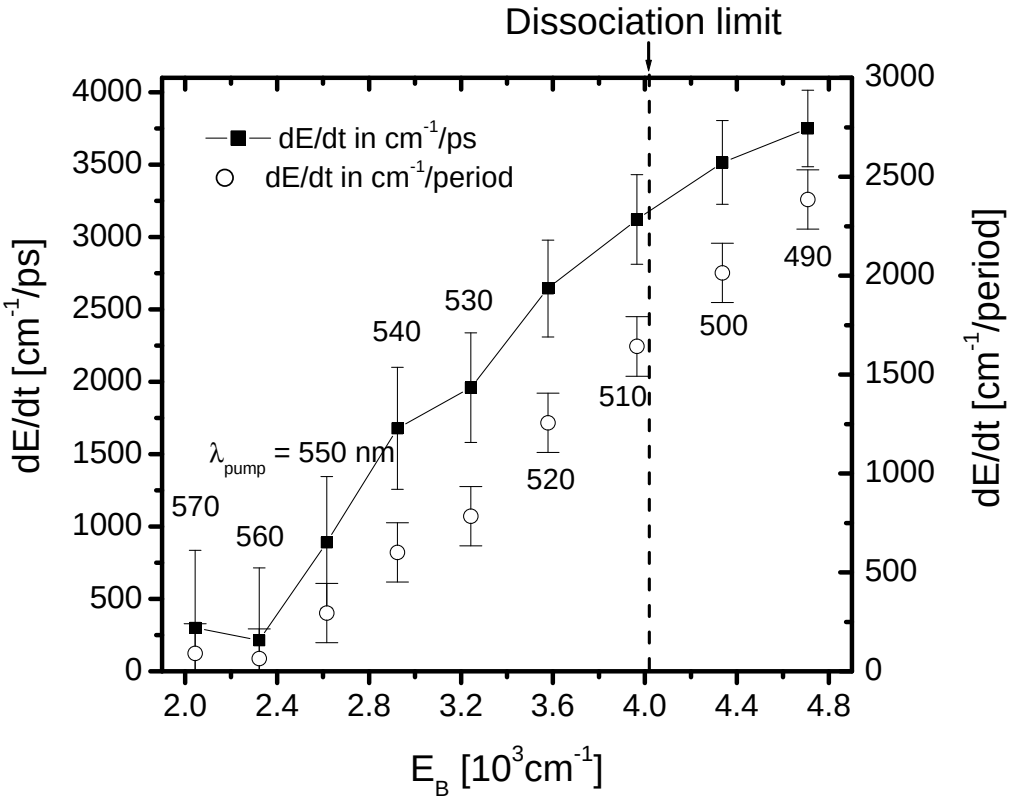

Figure 8.9: Vibrational energy relaxation rates for Br_2:Ar B state as a function of wave packet central energy E_{WP} in the B state. The gas phase dissociation limit at 4018 cm^{-1} is marked by the dashed line. The solid squares give the energy relaxation rate in unit cm^{-1}/ps (left axis), whereas the open circles refer to the right axis with unit cm^{-1}/period. The pump wavelength is given in nm next to the data points.

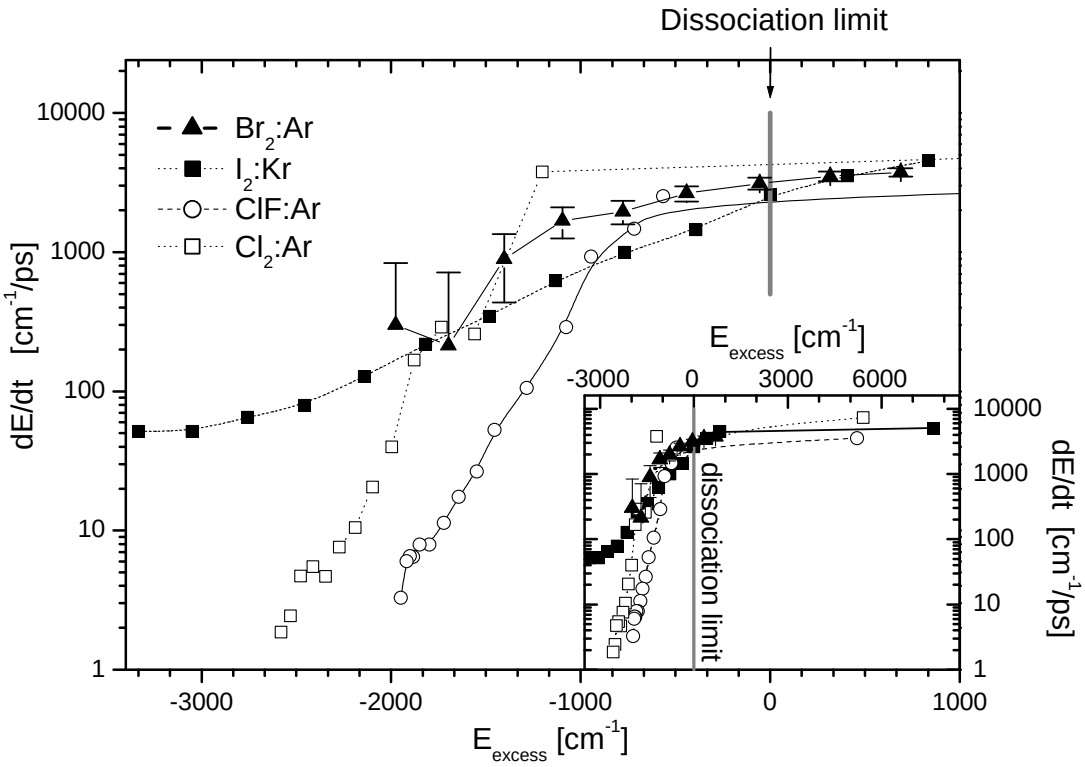

Figure 8.10: Comparison of the energy relaxation for Br_2:Ar (solid triangles), I_2:Kr (solid squares), Cl_2:Ar (open squares) and ClF:Ar (open circles). The energy loss dE/dt in cm^{-1}/ps is plotted versus the excess energy above the dissociation limit. In the bound part of the molecular potential, it is negative. In the case of Br_2 and I_2, the energy relaxation was determined from the periods in the pump-probe spectrum, as presented in section 8.1.3. For ClF and Cl_2, a method using the picosecond envelope function as described in Ref. [13] was applied to determine the molecular energy relaxation. The data for Br_2:Ar are reproduced from Fig. 8.9, the data for the other molecules are taken from Ref. [13]. The inset shows an enlarged range reaching far above the dissociation limit.

crystal phonons. For example, the zone boundary phonons in Ar have the largest possible frequency of 2 THz corresponding to 67 cm^{-1}. Thus, in one collision with the matrix more than 30 phonons can be created.

This is definitely far away from a regime, where the matrix is treated as a small perturbation to the molecule. A perturbative approach based on the energy gap picture [220], is based on molecular vibrational spacing much larger than the matrix phonon energy. In this case, the vibrational population decays step by step, going from one vibrational level v to the next one $v-1$. The scheme is inappropriate in the situation described here.

Figure 8.10 shows the experimental energy relaxation data of Br_2:Ar reproduced from Fig. 8.9 as solid triangles, compared to data of I_2:Kr (solid squares), Cl_2:Ar (open squares) and ClF:Ar (open circles) taken from [13]. The data are plotted versus the excess energy, that is the energy above the dissociation limit of the corresponding free molecule. In the bound part of the potential well, the excess energy is negative. In the case of Br_2 and I_2, the energy relaxation was determined from the periods in the pump-probe spectrum, as presented in section 8.1.3. This is not achieved for the other two molecules ClF and Cl_2, and a method using the picosecond envelope function as (see Ref. [13]) was applied to determine the energy relaxation.

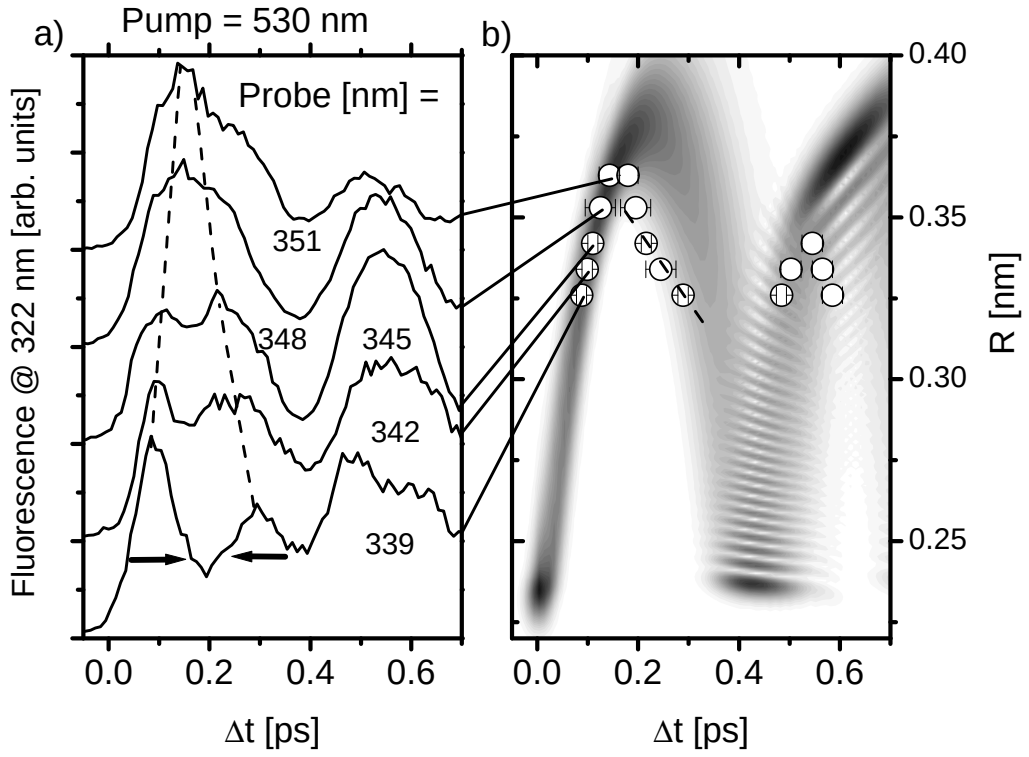

Figure 8.11: Trajectory for a wave packet with λ_{pump} = 530 nm for Br_2:Ar. a) The pump-probe spectra for different λ_{probe} show the in- and outward motion of the vibrational wave packet indicated for the first two maxima by the dashed lines (arrows indicate the direction). Each λ_{probe} corresponds to a distinct R_{win} (Tab. 8.3). b) The $R_{\mathrm{win}}(\lambda_{\mathrm{probe}})$ are plotted versus delay times Δt of the maxima (open circles). A numerical propagation on the potential of Fig. 8.5 of a free molecule wave packet with the same excitation conditions is given as the grey scale plot. The velocity of the returning wave packet is fitted to the value v shown in b).

The trend is the same for all molecules; the energy relaxation rates grow exponentially with increasing energy above the potential minimum, resulting in a milder rise close to the dissociation limit at E_{excess} = 0. The energy loss close to the dissociation limit occurs stepwise per collision with the matrix as seen in Fig. 8.8. The energy loss per collision at the dissociation limit is 30 % of the total vibrational energy for I_2:Kr, close to 50 % for Br_2:Ar and close to 70 % for Cl_2:Ar.

The rates for I_2:Kr, Cl_2:Ar and Br_2:Ar cross at E_{excess} = -1800 cm^{-1}. There, the T_1 for I_2:Kr is about one vibrational period (corresponding to 370 fs). The Cl_2:Ar T_1 is two periods or 480 fs. Both values are in the same range as the 600 fs T_1 value for Br_2:Ar.

8.1.4 Trajectory for the first excursion of a wave packet

The first collision with the matrix contains specific information about the molecule-matrix interaction. A trajectory of the wave packet shall be constructed from experimental data. For this purpose, a set of pump-probe spectra with fixed λ_{pump} = 530 cm^{-1} varying λ_{probe} is examined. As explained in Fig. 8.4, one can construct the history of a wave packet from the signature in the pump-probe spectrum. At every time delay Δt, the wave packet crosses a probe window at

Table 8.3: $R_{\mathrm{win}}(\lambda_{\mathrm{probe}})$ for different λ_{probe}. The construction is done via the probe resonance condition. The values are from the experimental RKR potential from Fig. 8.5.

λ_{probe} [nm]	$R_{\mathrm{win}}(\lambda_{\mathrm{probe}})$ [nm]
339	0.326
342	0.334
345	0.342
348	0.353
351	0.363

a given probe position R_{win}. A maximum in the pump-probe spectrum indicates the arrival time of the wave packets center. Variation of λ_{probe} leads to a scanning of R_{win}. From the arrival time, a construction of the wave packet center trajectory $R(\Delta t)$ is possible. This was shown in Refs. [13,25] for the case of I_2:Kr and is repeated here for the case of Br_2:Ar. Table 8.1 gives the resonant probe wavelengths for distinct excitation energies. From the excitation energy being resonant with λ_{probe} used in Fig. 8.11a, the calculation of R_{win} is done using the constructed RKR potential curve shown in Fig. 8.5. The values for $R_{\mathrm{win}}(\lambda_{\mathrm{probe}})$ are given in Tab. 8.3.

In Fig. 8.11a, the vibrational wave packet passes the R_{win}= 0.326 nm corresponding to 339 nm probe wavelength first at 88 fs delay in the outward direction and returns at 289 fs in inward direction (indicated by the arrows). The values for R_{win} are plotted versus the delay time of the maxima in the pump probe spectra as open circles in Fig. 8.11b.[2] The connection between successive points represents the experimental trajectory of the wave packet excited with λ_{pump} = 530 nm. The first outward motion is accomplished in about 170 fs. The inward motion is however not symmetric to the outward motion, as one would expect for a free oscillator. The wave packet returns to the inner turning point in a similar fashion as it had moved out. However, the slope of the trajectory becomes flatter afterwards indicating a strong deceleration after 200 fs. This is a contradiction to an expected further acceleration of a free wave packet when returning on the outer potential limb. From the slope of the data points (dashed line in Fig. 8.11b), one can derive the velocity in the time range from 200 to 300 fs to be v = (0.22 $\pm$ 0.05) nm/ps. This corresponds to a kinetic energy of (80 $\pm$ 20) cm^{-1}. The velocity of the wave packet in the *first outward* motion is about a factor of four higher in the range of interest. The second excursion of the wave packet between 490 and 590 fs in Fig. 8.11b also indicates the energy loss, since the second excursion does not reach as high values of R as the first excursion.

What causes the asymmetry in the first excursion and especially the further deceleration in the inward motion after 200 fs? Clearly, the Br_2 molecule collides with the cage atoms at the outer turning point and loses vibrational energy, due to the creation of phonons. But the deceleration after 200 fs requires the interaction with other cage atoms, since the wave packet has already undergone the collision with the cage. Unfortunately, no theoretical trajectories for Br_2:Ar are available yet. The system Cl_2:Ar, that is very similar to our experiment (double-substitutional site in the matrix because of similar Van der Waals radii) is well understood theoretically. In Ref. [84], trajectories of Cl_2:Ar are excited near the free molecule dissociation limit. It is shown that, while the molecular bond expands in the first excursion, the so called belt-atoms (atoms numbered 5 in Fig. 3.6) move in between the chlorine atoms and hinder the reformation of the molecular bond. The molecule has to *repel* the belt atoms when returning to small elongations. The same mechanism was proposed for I_2:Kr in Refs. [13, 25, 28].[3] The

[2]The absolute time zero of a pump-probe spectra can not be determined. Thus, the spectra are adjusted until the first maximum lies on the ridge of the calculated wave packet distribution (density plot in Fig. 8.11b).

[3]The I_2 velocity after the collision is 0.24 nm/ps [28]. That is very close to the corresponding Br_2 velocity.

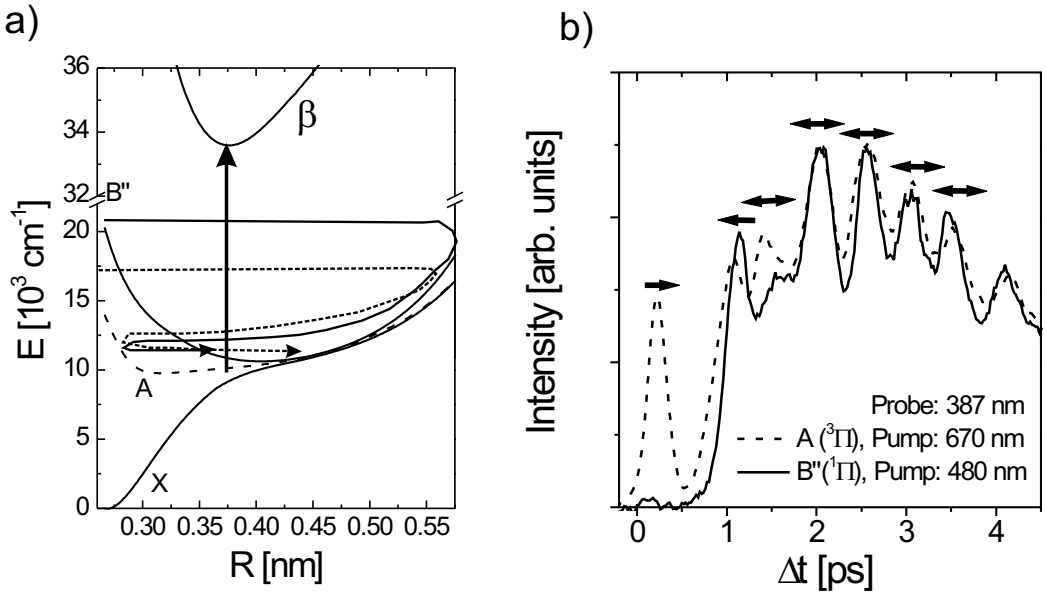

Figure 8.12: a) Electronic potential energy scheme of I_2:Kr. b) Pump-probe spectra of the A state upon A (dashed) and B" (solid) excitation. The B" wave packet undergoes an electronic transition and is probed in the A state.

interpretation for I_2:Kr is strongly supported by recent normal mode calculations in Refs. [31, 33]. To adapt the terminology for Br_2:Ar, the wave packet slides down the potential B state surface with minor kinetic energy (about 80 cm^{-1}) until it has pushed away the belt atoms and is released to move to the inner turning point.

The free molecule wave packet propagated numerically (see appendix) on the experimental RKR potential (Fig. 8.5) is compared to the experimental trajectory now. The population of the wave packet is shown as the density plot in Fig. 8.11b. The first excursion in the calculation was actually used to scale the delays of the different spectra. One immediately realizes the fact that the simulated wave packet seems to travel to larger bond elongations compared to the constructed trajectory (open circles). The origin for this behavior lies in the construction scheme of the RKR potential. The full experimental vibrational periods are used to generate the potential. The experimental periods included all the retarding effects like collision and belt repulsion. In the trajectory, the first excursion is asymmetric: the wave packet quickly collides with the matrix and needs a rather long time to return after it has reached is maximal elongation. The RKR algorithm assumes a symmetric excursion and thus shifts the potential barrier to larger internuclear distances in order to account for the longer second half of the period.

Energy relaxation and nonadiabatic transitions

The energy relaxation for I_2:Kr is very well documented [25, 27]. As mentioned above, the same belt modes play a role in the vibrational motion of the chromophore when excited at high vibrational levels. For this case we also studied combined nonadiabatic transitions to other states which were accompanied by strong vibrational energy relaxation. These were observed for I_2:Kr (also measured by the author), which shall be described now.

The I_2 dynamics were probed on the A state by a laser pulse centered at 387.5 nm, inducing a transition to the β CT state. The corresponding electronic potential energy scheme is given in Fig. 8.12a. When directly exciting the A state by pumping with 670 nm, the typical A state

wave packet dynamics of the iodine molecule are visible (dashed line in Fig. 8.12b). When exciting the B" ($^1\Pi_1$) state with a 480 nm centered pulse, no population should be detected in the A state, and this is true for the first picosecond. After the first round trip, the B" excited wave packet shows up in the A state (solid line in Fig. 8.12b) and its dynamics are identical to the A state excited wave packet. Therefore, the B" wave packet must have undergone an electronic transition to the A state within the first oscillation. Furthermore, it lost a lot of vibrational energy. It fell below the dissociation limit of the A state (as the initially on A excited wave packet). The B" state is repulsive for the free molecule and has the same dissociation limit of about 12000 cm^{-1} [176], thus the energy loss is circa 8000 cm^{-1} (1 eV!) during the first period. Since pronounced oscillations are visible afterwards, the molecular wave packet coherence has survived this strong energy loss and an electronic transition.

The electronic transition leads to a spin flip from a B" state with spin 0 ($^1\Pi$ state) to a triplet state A with spin 1 (A is a $^3\Pi$ state). The potential energies of the two states are parallel and close for large internuclear distances, as shown in Fig. 8.12. Therefore, the transition region is not obvious. A well defined crossing of two states defines a local transition with better coherence transfer properties [221]. Nevertheless, clear wave packet dynamics in the A state are observed afterwards, indicating a coherent wave packet transfer. The transition is triggered by the molecule-cage collision similar to the ultrafast spin flip on ClF in Ar [16, 17]. It shows the extraordinary coherence properties of small molecules in rare gas matrices, which shall be discussed in the next section.

Coherent energy relaxation

The Br_2 vibrational wave packet loses up to 50 % of its total vibrational energy in the first vibrational period. An intuitive picture of the relaxation process can be extracted from the experimental trajectory in Fig. 8.11b following the arguments for I_2:Kr published in Ref. [28]. The experimental data points of the trajectory covers the internuclear distance from 0.326 to 0.363 nm according to Tab. 8.3. The wave packet enters the region of interest at R = 0.326 nm with a kinetic energy of 1450 cm^{-1} (18944 cm^{-1} total energy from excitation at 530 nm minus 17500 cm^{-1} potential energy on the RKR B state). It leaves the region with roughly 100 cm^{-1} kinetic energy. Thus it has lost 1350 cm^{-1} of kinetic energy in the region of interest. The velocity v given in Fig. 8.11b is constant between R_{win}= 0.326 and 0.342 nm. Those internuclear distances correspond to a potential energy difference of 570 cm^{-1} corresponding to approximately 5 vibrational levels. Those levels are populated in the time interval of 220 to 290 fs *i.e.* within 70 fs. This time is much shorter than a vibrational period of 280 fs in this range. Therefore, those 5 levels are coupled coherently by this pulsed collision. The collision is well defined in time and internuclear distance. The coherent superposition of new vibrational levels initializes a well specified wave packet with coherent oscillations that produce the pronounced dynamical features. In this context, it is reasonable to state that "collisions transfer coherence" (the title of Ref. [28]) from initially populated levels to lower lying levels not populated before the collisions.

A well defined cage-molecule interaction has been found. Distortions for example from the thermal fluctuation of the crystal atoms are smaller than the molecular elongations. In addition, the cage distortions induced by the molecular motion seems to be sufficiently similar for all molecules in the ensemble.

Thus, small molecules in rare gas matrices provide a very unusual behavior considering the T_1 and T_2 times introduced in section 2.1; generally, the phase relaxation (T_2 process) is thought to be much faster than the energy relaxation (T_1 process). Eq. (2.8) states a connection of the two processes based on the model in Refs. [121, 122] that predicts the dephasing rate to be at

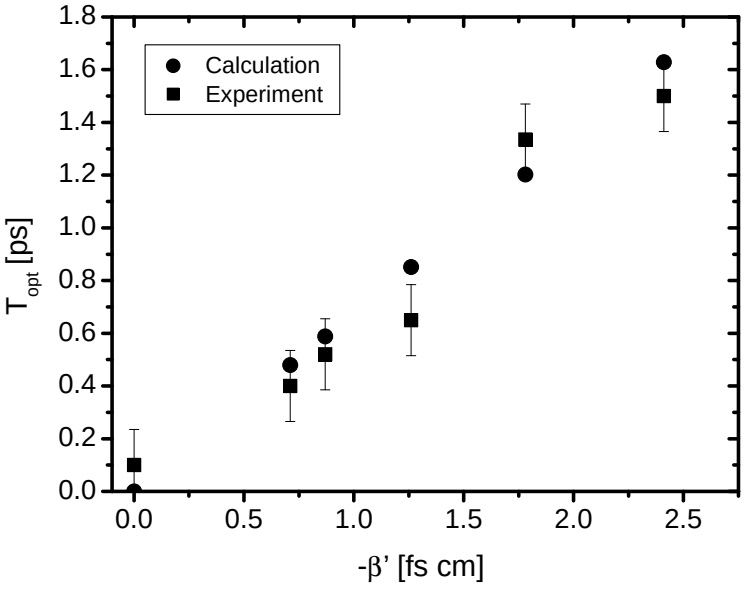

Figure 8.13: Focusing times $T_{\rm opt}$ versus negative chirp β'. The experimental values (solid squares) are compared to the ones calculated using $T_{\rm opt} = -\frac{\beta'\nu^2}{4\pi\omega_e x_e}$ (solid circles).

least half the dissipation rate (Eq. (2.8)). For an excitation in high vibrational levels of Br_2:Ar, T_1 is less than one period, however coherent wave packets can be observed afterwards, such that T_2 lasts for several oscillation periods. That is very different from the situation treated in Refs. [121, 122]. As stated before, the collision process is well defined, therefore statistical models are not appropriate in the description.

8.2 Methods to determine coherences

8.2.1 Wave packet focusing and vibrational coherence

The vibrational wave packet focusing scheme to deduce vibrational dephasing was introduced in section 2.3.3. The experimental results are presented in section 7.1.4. Pump-probe spectra for six different chirp parameters are collected in Fig. 7.14. The chirp parameter β' was determined from the measured pulse length according to Eq. (4.10) and one yields the focusing time $T_{\rm opt}$ using Eq. (2.15): $T_{\rm opt} = -\frac{\beta'\nu^2}{4\pi\omega_e x_e}$.

The oscillation period of the wave packet is determined in the pump-probe spectrum and has a value of T = 283 fs corresponding to a frequency of ν = 3.53 THz or 118 cm^{-1}. The anharmonicity of $\omega_e x_e$ = 1.54 cm^{-1} for the B state of Br_2 is taken from the value of m in Tab. 8.2a, converting it into the right units and expressing m as $4 \cdot \omega_e x_e$. The value has been calculated by the experimental RKR potential and is only 5 % smaller than the gas phase value of the $^{79}Br^{81}Br$ isotope. Therefore, the gas phase potentials will be used for the simulations throughout. The calculated $T_{\rm opt}$ are shown as solid circles in Fig. 8.13.

From Fig. 7.15 one can determine the approximate time of best modulation contrast (which is equivalent to $T_{\rm opt}$). These times are shown by solid squares in Fig. 8.13. The modulation contrast can be determined only within one molecular period. Fig. 8.13 shows an agreement of calculated and experimental values of $T_{\rm opt}$ as a function of the chirp parameter β'. Obviously, focusing according to the relation given by Eq. (2.15) has been achieved. Now, it can be applied according to the scheme presented in section 2.3.3. Fig. 2.11 presents the strategy; the pump-probe signal background at $T_{\rm opt}$ is used to determine the vibrational dephasing time $T_{\rm deph}^{\rm vib}$.

A typical pump-probe spectrum of Br_2 in solid argon is given by the solid line Fig. 8.14a.

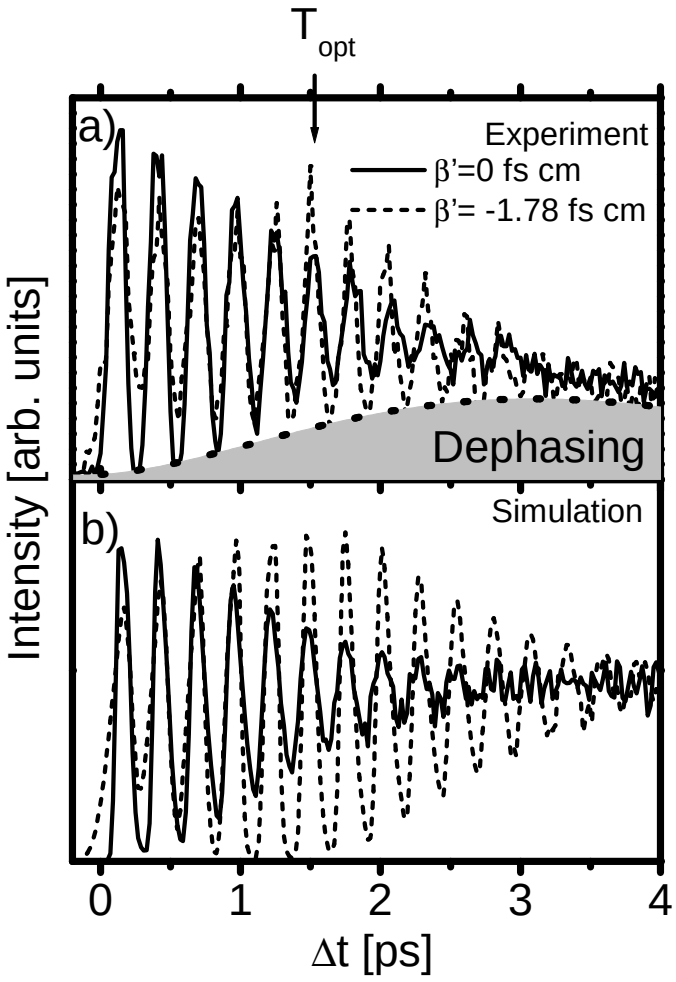

Figure 8.14: a) Pump-probe spectra of Br_2 in Ar for chirps $\beta' = 0$ (solid) and -1.78 fs cm (dashed) excited at λ_{pump} = 567 nm and probed at 600 nm. The dashed grey shaded line gives the experimentally determined vibrational dephasing background. b) Simulations using the same laser parameters for a free Br_2 molecule.

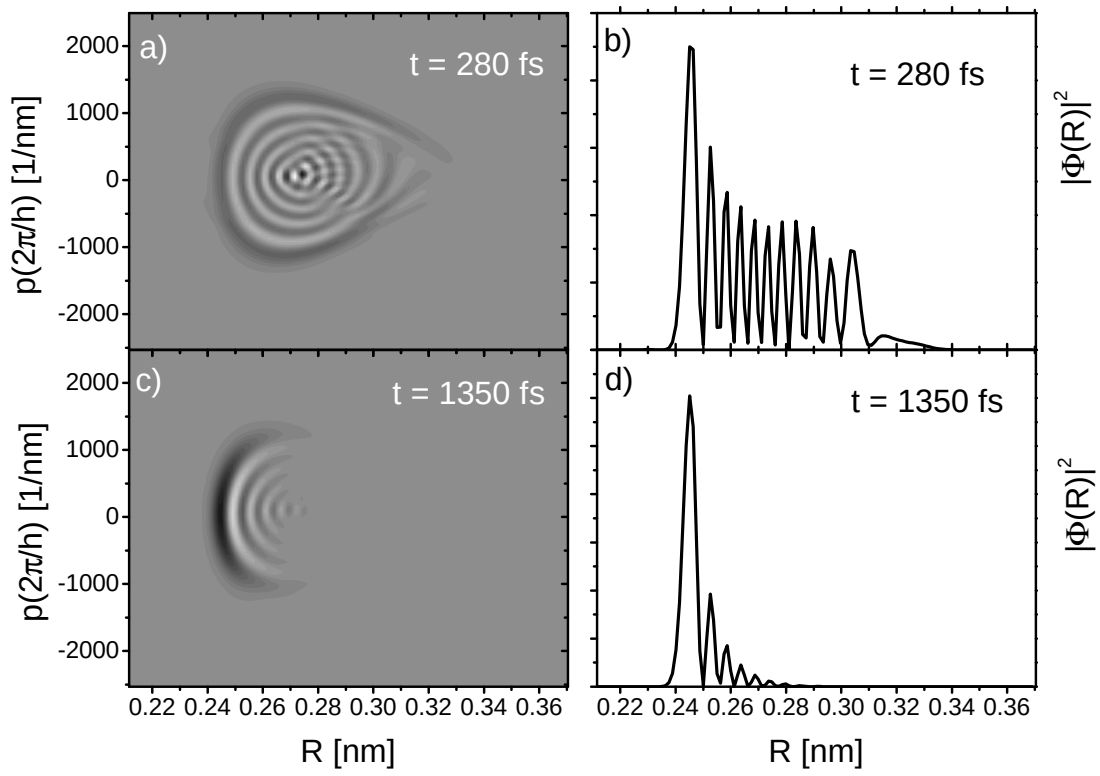

Figure 8.15: a) Simulated Wigner plot of free Br_2 with negatively chirped excitation of β' = -1.78 fs cm at the first minimum in pump-probe spectrum at 280 fs. b) The projection of a) onto the T axis. c) and d): Wigner distribution and projection onto R at t = 1350 fs (at pump-probe minimum close to T_{opt} form Fig. 8.14). Excitation center wavelength: 567 nm.

The overall average signal decay can be understood in terms of the energy relaxation funnelling the wave packet out of the probe window on the B state. In addition, the modulation depth of the oscillations decreases with time. The increasing background has to be decomposed into two contributions: The dispersion of the wave packet in the anharmonic potential energy surface and the irreversible dephasing of the vibrational wave packet due to its interaction with the rare gas environment. The dispersive broadening of the wave packet is already included in simulations dealing only with a free Br_2 molecule. Such a simulation is shown as the solid line in Fig. 8.14b. The average signal does not decay since no energy relaxation occurs. The modulation contrast however decays due to dispersion of the vibrational wave packet excited with similar pulses to those used in the real experiment.

The separation of dispersion and vibrational dephasing using the focusing scheme was presented in section 2.3.3. Fig. 8.14b shows a simulated pump-probe spectrum with a wave packet excited initially by a chirped pulse of β' = -1.78 fs cm (dashed curve). The modulation contrast in the beginning is not very pronounced compared to the solid line. The negatively chirped pulse was stretched from its Fourier limited duration of about $\Delta\tau_0$ = 30 fs to a duration of about $\Delta\tau$ = 160 fs, which broadens the initial spatial distribution of the wave packet over a large internuclear separation. This fact is reflected in the Wigner distribution in Fig. 8.15a. The wave packet spreads over the entire phase space. The projection onto the internuclear axis $|\Phi(R)|^2$ shows a rich interference pattern. At the outer turning point at about 0.32 nm some signal is

left, while the main part of the signal is localized at the inner turning point. However the wave packet contains the right phase information to reach its Fourier limited width at the focusing time T_{opt}. Indeed, the focus can be observed in the dashed spectra in Fig. 8.14b and at about 1.2 ps the modulation contrast reaches its maximum. No background on the minimum of the modulations is visible. Since in the simulation (and also in the experiment) the wave packet is probed at the outer turning point, the completely vanishing signal at the minima in the dynamics indicates a perfect localization at the inner turning point without any population reaching to the outer one. This is reflected in Fig. 8.15c and d). The wave packet is compact and shows no remaining amplitude at the outer turning point.

The dashed experimental spectrum is shown in Fig. 8.14a, however, it contains a background at T_{opt}. The spectrum was measured with a negatively chirped pump pulse of β' = -1.78 fs cm in accordance with the simulation. The initial wave packet dynamics are very similar to that in the simulation: The modulation contrast is the same and reduced with respect to the unchirped excited pump-probe spectrum. The modulation contrast is improving, until it reaches an optimal contrast at about 1.3 ps. The signal does not vanish in the minimum of the oscillatory dynamics. Higher order chirps and higher anharmonicity can be excluded. The background must be attributed to the *dephasing* of the vibrational wave packet in the course of its evolution on the electronic B surface. We have implemented the scheme to separate the dispersive and dephased contributions to the background: By focusing, the dispersion can be overcome at T_{opt}. However, the dephased parts cannot be focused and show up in the background at T_{opt}.

A systematic increasing of the negative chirp shifts the focusing times T_{opt} to longer delays in the pump-probe spectra according to Fig. 8.13. The T_{opt} was varied from 0 to 1.6 ps and for each T_{opt} the background was measured. The different pump-probe spectra are presented in Fig. 7.15. After about 2 ps all spectra and even those with a strong negative chirp in Fig. 7.15 show the same background. Therefore, this background originates from dephasing. The *dephased* background is shown in Fig. 8.14a as the grey shaded dashed line. By normalizing the background line to the average signal of any pump-probe spectrum (correction for energy relaxation), a monotonically increasing line with an exponential rise time of 3 ps is obtained. This rise time is the vibrational dephasing time of the molecular vibrational wave packet of $T_{\mathrm{deph}}^{\mathrm{vib}}$ = 3 ps. This corresponds to eleven molecular periods T of 280 fs each.

An important consequence is that all phenomena that require vibrational coherence (for example the fractional revivals) will have decayed after 3 ps. This is crucial for the next section.

8.2.2 Control of fractional revivals and electronic coherence

The fractional revivals were introduced in section 2.2.3. The full revival time T_{rev} of the Br_2 molecule is 21.08 ps. The higher the order of a fractional revival, the harder it is to observe it, mainly because of two reasons:

- In order to observe a $1/n$ revival, where n is 2,4,6,8,... , one has to couple $n/2 + 1$ vibrational levels coherently by an excitation pulse. Thus, a large pump pulse bandwidth is needed.

- The oscillation period associated with a $1/n$ revival is the fundamental oscillation period T of the anharmonic oscillator at the given excitation energy divided by $n/2$. The probe pulse has to be short enough to resolve the structure.

Figure 8.16a shows quite a broad pump pulse spectral shape achieved in the experiment. It is compared to the vibrational level structure of the free Br_2 molecule. The width (FWHM) of the almost Gaussian experimental pulse profile is 635 cm^{-1}, centered at 580 nm (17240 cm^{-1}).

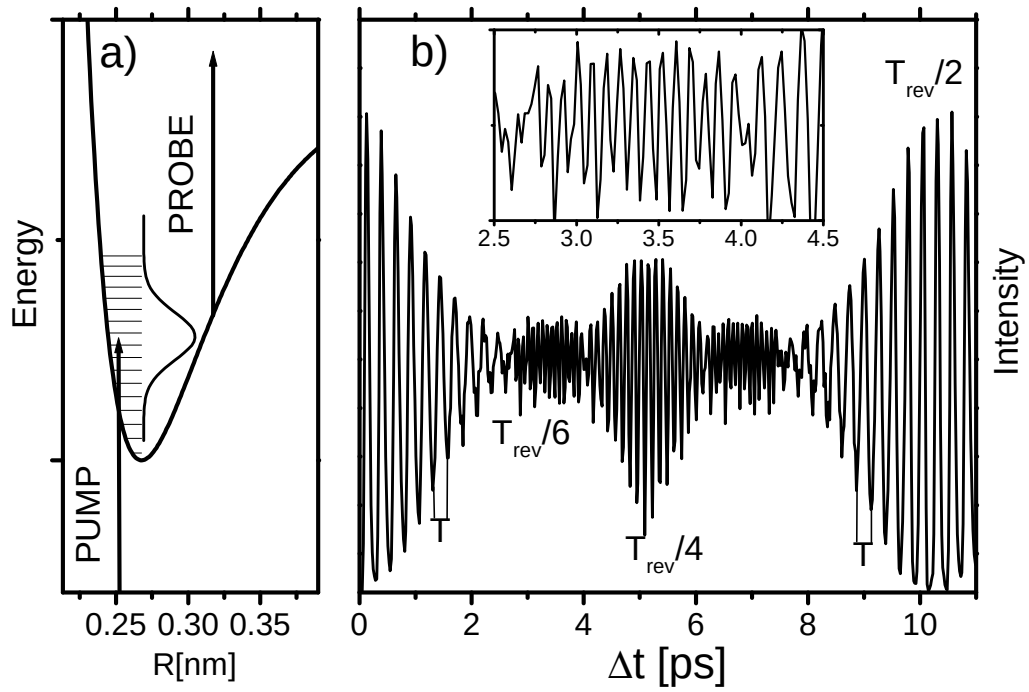

Figure 8.16: a) Pump pulse spectral profile of the excitation pulse used in the revival experiment. It contains four vibrational eigenstates of the Br_2 B state within the FWHM. The probe position for the simulated transient shown in b) was chosen to be R_{win} = 0.316 nm. The simulated pump-probe spectrum (see appendix) for the free molecule shows a revival structure. The oscillatory structure decays due to dispersion of the wave packet in the anharmonic potential. It has vanished at 3 ps. From 3 ps to 4 ps (see inset in b)), the threefold vibrational frequency shows up in the pump-probe spectrum. This corresponds to the 1/6 revival. After 10.5 ps, the fundamental period is visible again. This corresponds to a so called half revival $T_{\mathrm{rev}}/2$.

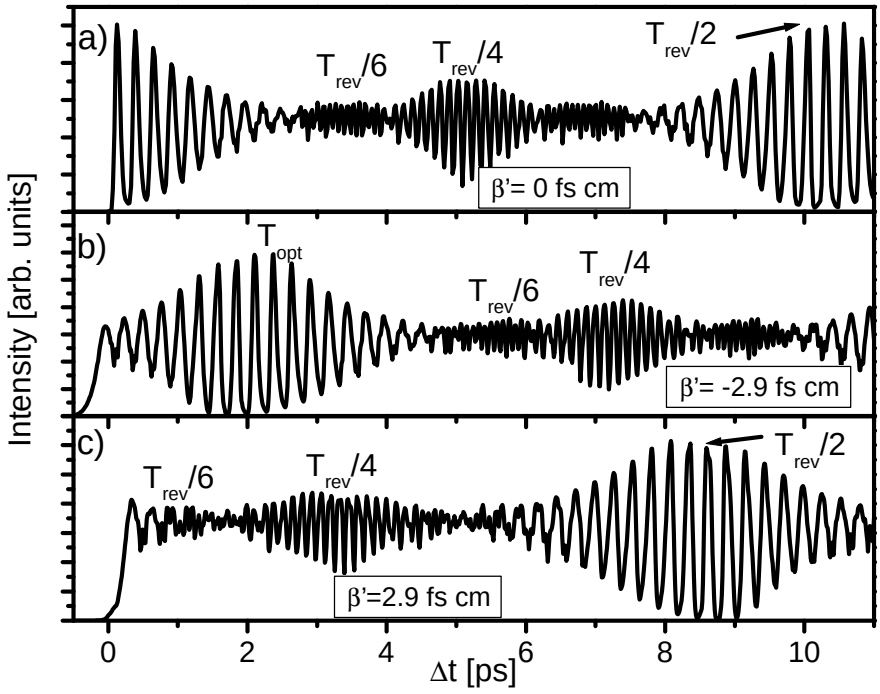

Figure 8.17: a) Unchirped excitation. Revival pattern for a pump pulse described in the text probed in the range of the outer turning point. b) Same conditions as in a) but with a *negative* excitation chirp of -2.9 fs cm. c) Same conditions as above but with a *positive* excitation chirp of +2.9 fs cm.

The vibrational levels v = 7,8,9 and 10 are covered by the pulses FWHM. A simulation of a pump-probe spectrum, based on the experimental pulse was done. The probe pulse was located at R_{win} = 0.316 nm close to the outer turning point of the vibrational wave packet. The result is shown in Fig. 8.16b. The wave packet oscillates with a vibrational period of T = 260 fs. The initial vibrational structure disperses until, at 3 ps, it has completely vanished. From 3 to 4 ps, dynamics exhibiting $T/3$ can be observed (see inset in Fig. 8.16b). This structure corresponds to a 1/6 revival as was explained in section 2.2.3. The signature of the 1/8 revival with T/4 seems to be missing. This is due to the fact that only four vibrational levels are contained within the FWHM of the pump pulse. Further levels in the wing are not sufficiently populated. In order to effectively observe the 1/8 revival, the pulse would have to be broader to cover five levels.

The earliest fractional revival observable in the experiment would be the 1/6 revival from 3 to 4 ps. The calculation of the exact revival time leads to an appearance at $T_{\mathrm{rev}}/6$ = 21.08 ps/6 = 3.5 ps in accordance with the simulation. The experiment was carried out according to the simulation and a 600 nm probe pulse with a time resolution of less than 30 fs was used. But no trace of a 1/6 revival could be observed. The reason is the vibrational dephasing time, which was determined to be $T_{\mathrm{deph}}^{\mathrm{vib}}$ = 3 ps in the spectral range pumped. The fractional revival relies on the vibrational coherence of all levels which are required to generate it. Since this coherence decays before the 1/6 revival has even started, it is not observable in this way. A method to advance the fractional revival features in time was presented in section 2.3.4 and will be quantified with realistic laser pulse chirps in the following.

Figure 8.17a shows the simulated pump-probe reference spectrum for excitation described in connection to Fig. 8.16b (no chirp). Fig. 8.17b corresponds to a negatively chirped pump pulse with $\beta' = -2.9$ fs cm. The pump pulse is stretched to a duration of 300 fs. The negative

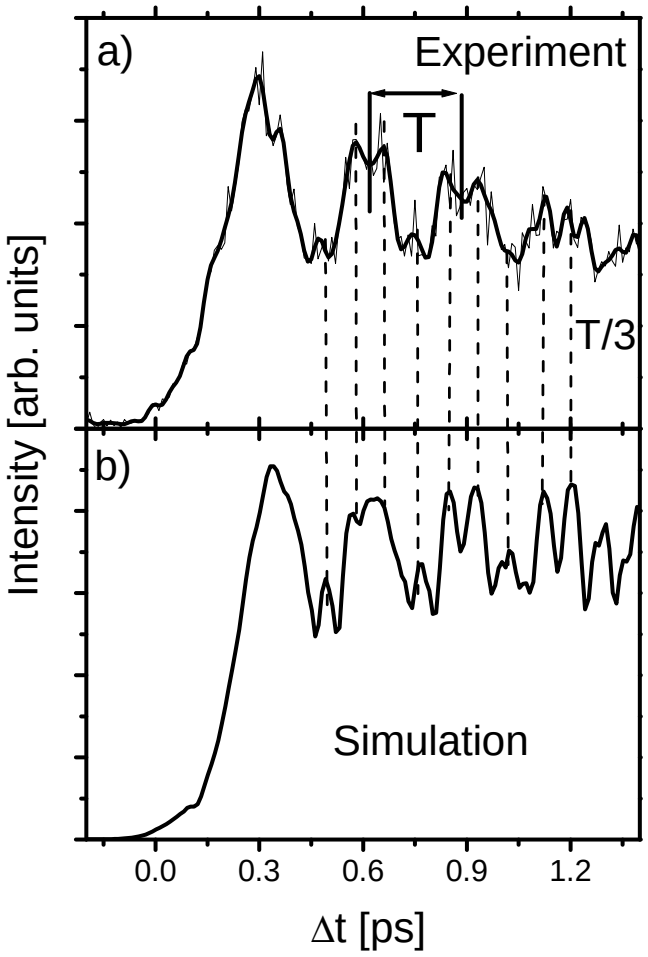

Figure 8.18: a) Experimental pump-probe spectrum of Br_2:Ar excited by a pump pulse centered at 580 nm of width 635 cm^{-1} (thin line) and smoothed by a bandpass filter (thick line). The excitation pulse had a chirp of 2.9 fs cm. The spectrum was probed at 600 nm via a two-photon transition. b) Simulation of the spectrum using the free Br_2 B state potential (R_{win} = 0.322 nm, ΔR_{win} = 0.011nm).

chirp produces a focus of the wave packet at T_{opt} =2.2 ps. The initial vibrational pattern and the revivals are shifted by 2.2 ps to later times. Obviously, the negative chirp induces a general shift forward in time in the propagation of the vibrational wave packet. The effect has never been recognized in this way before. The previous wave packet focusing literature [80, 82, 83, 127] concentrates on the effect of the dispersion compensation only. What happens in the positive chirped excitation? The pulse duration of 300 fs is much longer than the vibrational period of 265 fs. However, all revival structures that appear in the unchirped case also appear here, but at different times. The revival structures are shifted again by 2.2 ps but now to earlier delays in contrast to the negative chirped excitation. Indeed, Eq. (2.15) can be used universally, for a positively chirped excitation it gives a negative T_{opt} . Negative times do not appear in an experiment but if one shifts the time zero of the spectrum in Fig. 8.17a to -2.2 ps, indeed the spectrum in Fig. 8.17c is obtained. The 1/6 revival, that occurs around 3.5 ps with no chirp, is now shifted to (3.5 ps - 2.2 ps) = 1.3 ps for positive chirped excitation. The $T_{\mathrm{deph}}^{\mathrm{vib}}$ as a property of the molecule-matrix interaction is not influenced by the excitation conditions. Thus, for a positive chirp there is a chance to observe a fractional revival even in a solid environment with rather short $T_{\mathrm{deph}}^{\mathrm{vib}}$ of the molecular guest.

The result of an experiment performed with a positively chirped pulse is shown in Fig. 8.18a. The pulse duration was confirmed to be about $\Delta\tau$ = 300 fs in a cross-correlation experiment with the probe pulse at 600 nm. The Fourier transform limited duration of the 580 nm pump pulse is calculated to be $\Delta\tau_0$ = 23 fs. With Eq. (4.10), a positive chirp of β' = 2.9 fs cm is

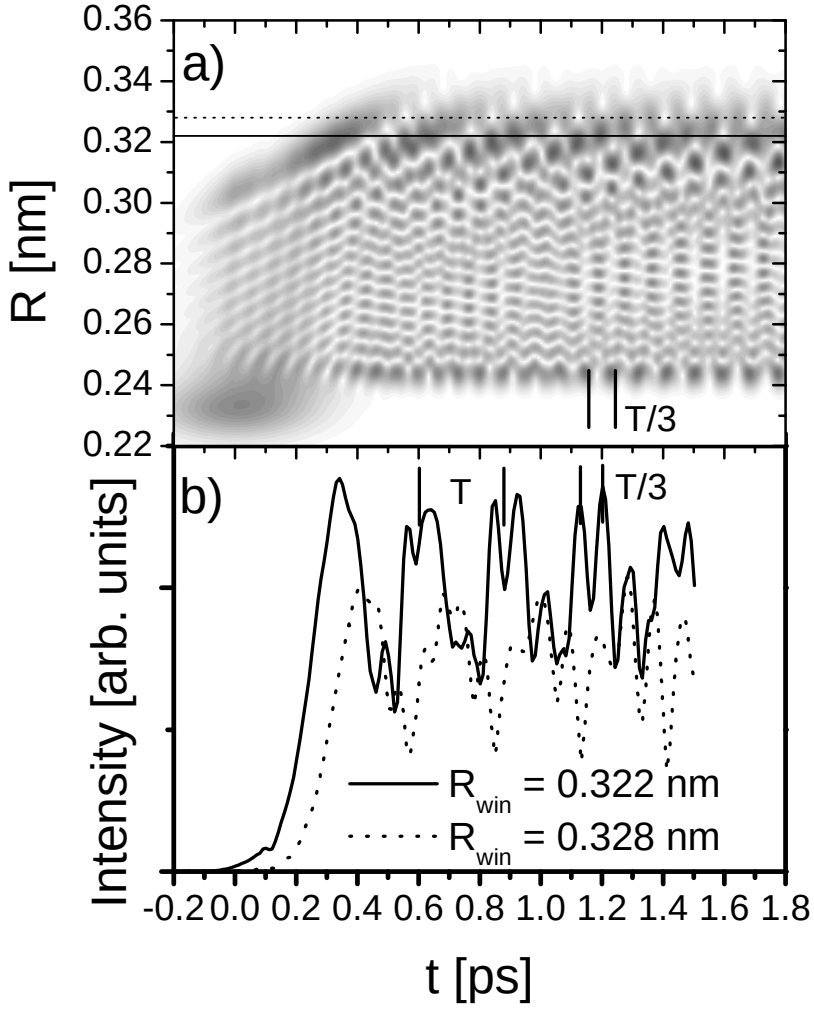

Figure 8.19: a) Wave packet population density as a function of internuclear distance and time. The wave packet was excited with a positively chirped pulse, used in the experiment described above. b) Pump-probe transients calculated by integrating the density along a window of constant R_{win} at 0.322 nm (solid) and 0.328 nm having a width ΔR_{win} of 0.011 nm.

derived. The positive chirp was accomplished by introducing plates of fused silica into the pump beam. The amount of chirp and the resulting pulse stretching given by the amount of material was calculated and compared to the experiment. A perfect agreement was found.

The spectrum in Fig. 8.18a shows modulations with $T/3$ of the fundamental period T. This tripled oscillation frequency is the clear signature of the 1/6 revival. The frequency is superimposed on the fundamental oscillation frequency. The T and $T/3$ contribution depend sensitively on the probe position, according to the simulations. For the simulation of the advanced 1/6 revival in Fig. 8.18a the probe window R_{win} was chosen to optimize reproduction of the experimental transient.

The background of the sensitivity on R_{win} is illustrated in Fig. 8.19a. It displays the time dependence of the vibrational wave packet under the experimental excitation conditions described above. The pulse duration of 300 fs is reflected in the unstructured wave packet passages close to zero time in Fig. 8.19a. Indeed, 300 fs exceed one vibrational period, which results in a rather complicated wave packet pattern already during the excitation. Fig. 2.7a shows as a contrast the

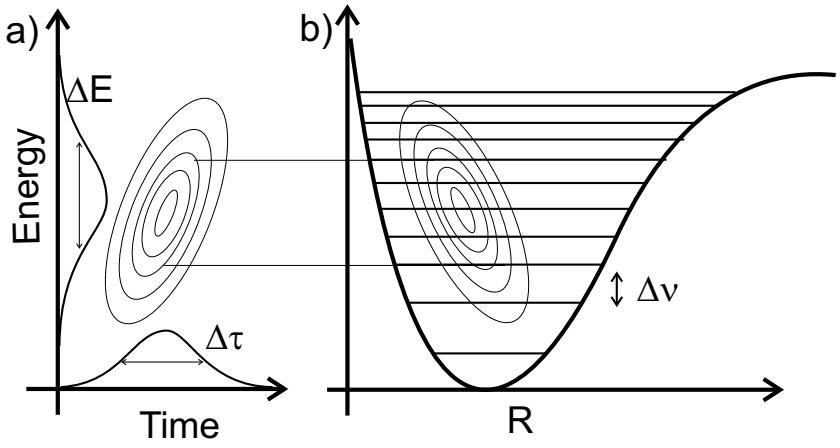

Figure 8.20: Population of vibrational levels by a positively chirped pulse. a): Wigner plot of a laser pulse with positive chirp. The different frequency components are separated in time. b): First the low vibrational levels are populated, afterwards the high levels are populated due to the laser pulse chirp (wave packet travels from left to right).

propagation of a Br_2 B state vibrational wave packet excited by an unchirped pulse of about 30 fs duration. The outgoing and ingoing wave packet traces are clearly distinguishable in this case.

To simulate an experimental pump-probe spectrum, the wave packet density form the grey plot in Fig. 8.19a is integrated in a Gaussian probe window with center R_{win} and ΔR_{win} for different times t. The spectra for two Gaussian windows in the internuclear coordinate R are reproduced in Fig. 8.19b. The width of the probe window ΔR_{win} was chosen as 0.011 nm, which is a realistic parameter when taking the bandwidth and difference potential curvature into account (Fig. 2.14). The temporal resolution of the probe pulse is neglected in the simulation, since the probe pulse duration is shorter than the expected features in the pump-probe spectra. The dashed line represents the pump-probe spectrum when the molecular population is probed at R_{win} = 0.328 nm, showing T and T/3. However, the relative positions of the peaks do not agree with those in the experiment. Probing at R_{win} = 0.322 nm, yields similar dynamics with T and T/3 components. The peak positions are now in good agreement with the experiment up to about 1.2 ps, as shown in Fig. 8.18b. In addition to the temporal position of the revival features, the relative intensities are also reproduced quite well. This indicates that the chosen probe window is in agreement with the experimental one.

A precondition to observe a 1/6 revival structure with a threefold oscillation frequency is a coherent coupling of four vibrational levels (section 2.2.3). Since the experimental spectrum is consistent with the theory for 1.2 ps, we can deduce that the dephasing time of this four vibrational levels T^4_{deph} will last about 1.2 ps and we define $T^4_{\mathrm{deph}} \approx 1.2$ ps.

8.2.3 Electronic dephasing

The question of electronic dephasing is addressed here. Fig. 8.19 shows the absolute square of the wave packet as a function of R and t. The positively chirped pulse is prolonged by a factor of ten to 300 fs and exceeds the molecular vibrational period of 265 fs. During the long pulse-molecule interaction, no fundamental molecular vibrational period is visible in Fig. 8.19. The time evolution generates the interference structure observable as the periods T and T/3, however, only if the imprinted phase of the vibrational levels follows the chirp .

Fig. 8.20a and b show the time sequence in which the different vibrational levels are populated during the course of a positively chirped pulse. The phase of each vibrational level is given by the chirp parameter of the pulse. The exact timing of the vibrational levels predetermines the evolution of the spatial and temporal interference structures of the wave packet. An electronic dephasing process shifts either the relative energy between electronic ground state

Table 8.4: Time constants used in this thesis.

Symbol	Description	Value
T	molecular period	e.g. 300 fs for $\lambda_{\mathrm{pump}} = 560$ nm on Br_2:Ar
T_{disp}	dispersion time	depends on $\omega_e x_e$ and ΔE
T_{rev}	revival time	21.08 ps for Br_2
T_{opt}	focusing time	depends on β' and $\omega_e x_e$
T_1	dissipation time	0.6 ps at $\lambda_{\mathrm{pump}} = 560$ nm on Br_2:Ar
$T^{\mathrm{vib}}_{\mathrm{deph}}$	vibrational dephasing time	3 ps at $\lambda_{\mathrm{pump}} = 570$ nm on Br_2:Ar
T^{4}_{deph}	vibr. deph. time of four vibr. levels	$\approx$ 1.2 ps $\lambda_{\mathrm{pump}} = 580$ nm on Br_2:Ar
$T^{\mathrm{el}}_{\mathrm{deph}}$	electronic deph. time in B $\longleftarrow$ X	$\geq$ 0.3 ps

and excited state (ΔE) or their relative internuclear position (ΔR) and in general both (section 2.1). If such an event would occur during the excitation of the levels, the phase sequence of the vibrational levels would be distorted. A change of ΔE and ΔR in a statistical way over the molecular ensemble probed (as usually meant by dephasing), would smear out the evolution of the interference structures.

Since we achieve the interference pattern of the full chirp in the experiment according to Fig. 8.18, it is clear that in our example $T^{\mathrm{el}}_{\mathrm{deph}}$ is longer than the pulse duration of 300 fs. Thus monitoring the evolution and persistence of the vibrational interference pattern versus increased chirp parameter β' (and thus pulse length) also provides a means to derive $T^{\mathrm{el}}_{\mathrm{deph}}$. Typically $T^{\mathrm{el}}_{\mathrm{deph}}$ is expected to be the shortest of the dephasing times with values on the order of 100 fs in multidimensional systems. In our case, it is longer than 300 fs while it still may be shorter than the vibrational dephasing times of some ps.

Before comparing the data to other methods, we summarize all times that have been used up to now in Tab. 8.4.

8.2.4 Comparison to other methods

The vibrational dephasing can be observed directly by pump-probe spectroscopy in weakly coupled cases. There, the revival times T_{rev} are much shorter than the dephasing times $T^{\mathrm{vib}}_{\mathrm{deph}}$, and the latter can be determined by the revival modulation contrast [76, 77, 148, 222]. For the very interesting and often appearing case of $T_{\mathrm{rev}} > T^{\mathrm{vib}}_{\mathrm{deph}} > T$ the novel focusing scheme presented here (section 8.2.1) has to be applied to separate dephasing from dispersion in order to determine $T^{\mathrm{vib}}_{\mathrm{deph}}$.

Besides pump-probe spectroscopy and its extension by the focusing method, nonlinear spectroscopic techniques allow for the determination of vibrational dephasing constants. Coherent Antistokes Raman Scattering (CARS) [158, 223–227] and Resonant Impulsive Stimulated Raman Scattering (RISRS) [228–238] were used to prepare ground state vibrational wave packets of molecules in condensed media.[4] CARS can also be used to measure the vibrational dephasing on an excited electronic state by interfering excited state and ground state wave packets. However a longer lived electronic coherence compared to the vibrational coherence is needed in this method, which is generally not the case. The same problems arise for Phase Locked Pulse Pair (PLPP) spectroscopy [159, 160, 239–245] and related techniques [246–250]: wave packets are interfered between ground and excited state, involving the electronic coherence of that transition. CARS and PLPP methods are thus ideally suited to determine the electronic dephasing constants and present an alternative to the positive chirp scheme (section 8.2.3).

[4] The focusing method invented here is not applicable to the electronic ground state of a molecule.

8.2.5 Comparison to other dephasing constants

Vibrational dephasing times

The vibrational dephasing time of free Br_2 molecules B state in a cooled gas jet extends into the range of several hundred picoseconds and is mainly induced by vibration-rotation coupling [35, 36]. Ultrafast data for vibrational dephasing times of Br_2 in condensed phase other than those presented in this thesis are not available. A variety of experimental and theoretical data exist for the I_2 molecule in different hosts.

The vibrational dephasing in the ground state of I_2 in solid argon [29,30,32,33] and krypton [31] has been studied by CARS in the Apkarian group. In the case of I_2 in solid argon, a vibrational dephasing time around 10 ps was reported in Ref. [29]. The dephasing rate increases linearly with v. The dephasing time decreases from about 10 ps at $v = 4$ to 2.5 ps at $v = 14$ (see Fig. 5 in Ref. [30]). The variation of the vibrational dephasing for I_2:Kr in the ground state with vibrational quantum number v and temperature has been tested in Ref. [31]. The rate increases with second and fourth power of v and and the corresponding time is 100 ps for $v = 1$ and 33 ps for $v = 6$ (see Fig. 8 in [31]). The authors discuss the different behavior in solid Ar and Kr and state that it reflects the interaction potential of the ground state I_2 with the cage. The cage is tight in the case of Ar, thus the molecule "feels" a very repulsive potential, whereas the cage is looser in Kr and the molecule samples a flat potential "locally quadratic and quartic" [31]. The fact of the tighter Ar cage in comparison with Kr does result in a faster dephasing. At comparable temperatures and vibrational eigenstates, the dephasing rates for Ar are approximately one order of magnitude larger than in the Kr solid.

Pump-probe spectroscopy conducted in rare gas solids delivered dephasing times of several picoseconds for wave packets on the B state of I_2 [20–28, 33, 81, 83]. However, the dispersion was not separated from vibrational dephasing (as applied in section 8.2.1) and therefore an exact determination of $T_{\mathrm{deph}}^{\mathrm{vib}}$ is not possible. Changing from ground state X to the electronically excited B state increases the molecule-host interaction: the molecular equilibrium distance grows roughly about 10 percent in the B $\longleftarrow$ X transition. Furthermore, the halogen rare gas interactions depend on the molecular state [86, 109] as will be demonstrated in Fig. 8.22. Thus the iodine atoms come closer to the nearest cage atoms. Keeping that in mind, the vibrational dephasing time in the B state of Br_2:Ar of 3 ps determined in this thesis is reasonable compared to the I_2:RGS ground state results.

Apart from a change in the molecular state of I_2, the host local density was varied in a series of experiments by the Zewail group [76, 77, 148, 187, 251–253] motivating theoretical studies by V. Engel, C. Meier and coworkers [78, 254–257]. The authors determine vibrational energy relaxation times T_1 and vibrational dephasing times T_2 as a function of rare gas pressure. The behavior of T_2 (corresponds to $T_{\mathrm{deph}}^{\mathrm{vib}}$ in the nomenclature used here) with rising pressure is nontrivial. Two processes induce a dephasing of the vibrational levels: collisions and vibration-rotation coupling. The free I_2 molecular rotation is not blocked in contrast to the model system described in this thesis. In the binary collision model, T_2 scales linearly with the collision time [258, 259], whereas the trend is reversed for the vibration-rotation dephasing [260]. The vibrational dephasing time scales from typically infinite values at 0 bar rare gas pressure to 1 ps at 2 kbar pressure (examples for He as buffer gas).

The results for Ar buffer gas [77] are now compared to those in the solid phase. The solid Ar environment used in our experiments has a number density of 27 nm^{-3}.[5] Extrapolating Zewails experiment linearly to the solid Ar density, yields a time constant shorter than 250 fs [77]. This

[5]The mass density of solid Ar at 4 K is 1.771 g/cm^3. Since Ar has a mass number of 40, 1.771/40 mol of Ar are inside one cm^3. This corresponds to 27 atoms/nm^3.

value is one order of magnitude shorter than $T_{\mathrm{deph}}^{\mathrm{vib}}$ = 3 ps for Br_2 :Ar. The wave packet excitation in the I_2:(gas Ar) case was accomplished near the potential minimum. In our experiment, the wave packet was excited half way between the minimum and the dissociation limit. Thus, the dephasing times of Br_2 in solid Ar near the minimum of the B state are expected to be even longer than 3 ps and the difference to the high pressure buffer gas is more dramatic.

The effect of a highly symmetric environment upon molecular processes has been proved before for the molecular predissociation. The predissociation rate of I_2 in buffer gases increases linearly with density [76, 148]. Even in liquid environments, this law is obeyed [23, 149, 150]. However, in the highly symmetric cages of a even denser rare gas matrices, predissociation is efficiently suppressed [26, 27]. The vibrational motion in the double-substitutional site is well guided by the environment and the molecules moves like a piston in a cylinder. At same number densities in high pressure gas phase or liquids, the environment shows less order and collisions with nearest neighbors will occur more frequently, leading to higher vibrational dephasing times.

Electronic dephasing times

The electronic dephasing time $T_{\mathrm{deph}}^{\mathrm{el}}$ > 300 fs (section 8.2.3) is compared to the times resulting from line widths in the excitation spectrum of Br_2:Ar (Fig. 3.8). The width of the Zero Phonon Line (ZPL) in the range around an excitation wavelength of 580 nm ($v' = 10$) is 15 cm^{-1}. Taking this as the FWHM of a Lorentz profile a time constant of 350 fs is derived. The line width for the $v' = 1$ level of 6 cm^{-1} corresponds to a time constant of 900 fs. Besides electronic dephasing, also vibrational dephasing and inhomogenous broadening can contribute to the observed line width and its broadening with increasing v'. Thus, the 350 fs are again a lower limit for the electronic dephasing time $T_{\mathrm{deph}}^{\mathrm{el}}$. This is consistent with our result in section 8.2.3.

Concerning ultrafast spectroscopic techniques, no experiments on the electronic dephasing of Br_2 in solvents are available. Recent unpublished PLPP experiments in the Schwentner group show that the electronic dephasing time in the B $\longleftarrow$ X transition of Cl_2:Ar is longer than 2 vibrational B state periods with T = 220 fs. The ZPL lines in the excitation spectrum of Cl_2:Ar [56] show widths similar to the Br_2:Ar ZPL.

CARS spectroscopy on I_2 in solid Ar and Kr do not show any coherences involving a propagation on the excited B state. Therefore, it was stated that the electronic coherence between the B and X state is shorter than one molecular period of 300 fs [29–32, 34]. An excitation spectrum for I_2 in rare gas solids has never been published to our knowledge.

In addition, to the experiments mentioned above, the electronic coherence of I_2 was also determined in photon echo experiments [224, 261]. They were carried out in gaseous rare gas environments by Dantus and coworkers [262]. Typical number densities in those experiments ranged up to 10^{-3} /nm^3, *i.e.* four orders of magnitude lower than for the solid Ar density of 27/nm^3. The electronic dephasing time at such densities in Ar was determined to be about 40 ps and the corresponding rate increases linearly with higher density. A linear extrapolation to the number density of solid Ar yields an electronic dephasing time of less than 2 fs. Compared to our result for bromine in solid Ar, this is more than two orders of magnitude too short. The authors use a collision based model to explain the trend in the low density experiments. The electronic phase in the transition is disturbed when an Ar atom passes at a certain distance changing the potential energy difference of the B $\longleftarrow$ X transition. The interaction time in the collision is estimated from the Ar velocity (at room temperature) and an interaction length which is 1.2 nm (much larger than the Van der Waals radii). This ballistic model seems to be completely inappropriate for the solid Ar case. Many atoms are included in the 1.2 nm shell around the chromophore (the lattice constant is 0.35 nm in an Ar crystal). However, the high

density of atoms in the low temperature crystal is spatially *fixed*. Only a change of their position induced for example by the phonons can results in a variation of the molecular transition energy, which leads to electronic dephasing.

8.3 Coherent phonon dynamics

The experimental data presented in section 7.2 strongly indicate a close similarity of the host induced phenomena for I_2 in solid krypton and Br_2 in solid argon. Therefore, the host induced dynamics of the two systems will be discussed simultaneously. First of all, the main observations from section 7.2 are collected. The 650 fs oscillation in I_2:Kr spectra and the 500 fs oscillation in Br_2:Ar spectra are attributed to host induced dynamics for the following reasons:

- The oscillation does not show any sign of dispersion expected from anharmonicity. The intramolecular states for I_2:Kr and Br_2:Ar are anharmonic oscillators; therefore, the dynamics cannot be assigned to any molecular state.

- The two frequencies for Br_2:Ar ($f_{\mathrm{P}} = 2$ THz) and I_2:Kr ($f_{\mathrm{P}} = 1.5$ THz) are quasi monochromatic and the line width is only limited by the observation time window (see Figs. 7.19, 7.23). For all intramolecular wave packets, energy relaxation occurs. Taking the anharmonicity of molecular electronic states into account, the vibrational relaxation will result in a shortening of the wave packet period in the course of the propagation. This once more excludes an intramolecular origin of the oscillations.

- The 650 fs (I_2:Kr) or 500 fs (Br_2:Ar) oscillation is observed when exciting at many different energies in the B state of the respective molecule (see Figs. 7.17 and 7.22) and also when exciting the electronic A state (see Figs. 7.18 and 7.20).

The 650 fs or 500 fs oscillation cannot be assigned to intramolecular vibrational wave packet dynamics when considering the evidence given above. If the dynamics are not molecular vibrations, the only origin can be a coherent vibration of the host that imprints its dynamics on the molecular pump-probe spectrum.

The facts collected in section 7.2 give clear evidence on what kind of host mode is responsible for the coherent dynamics, reflected in the 650 fs (I_2:Kr) or 500 fs (Br_2Ar) oscillation. Figs. 7.19 and 7.23 show Fourier transformations of pump-probe spectra measured for Br_2:Ar and I_2 :Kr respectively that are compared to the phonon dispersion relation of krypton and argon in Fig. 8.21.

Figure 8.21 shows the dispersion relation for solid ^{84}Kr (solid circles) and solid ^{36}Ar (solid squares) on the left side. The data were obtained using the technique of neutron scattering. The solid Ar data were published in Ref. [11]. The isotope used in those experiments was ^{36}Ar because of its high neutron scattering cross section.[6] However, in our experiments Ar in natural abundance, consisting mostly of ^{40}Ar, was used.[7] The phonon frequencies have to be shifted by $\sqrt{36/40}$ to account for the mass difference. The frequency of the Zone Boundary Phonon (ZBP) for ^{40}Ar is marked by an arrow on the left side of Fig. 8.21. The data for ^{86}Kr (which is the most abundant isotope) were published in Ref. [10]. All neutron scattering data were obtained in single crystals. The relevant data for all other rare gases are also published in Ref. [9]. Only the longitudinal parts of the <100> branch are shown. Comparing the phonon

[6] The coherent neutron cross section of ^{40}Ar is 0.4 barn, whereas the incoherent cross section of 0.25 barn produces a large background on the spectra [263]. The rare isotope ^{36}Ar has an unusually large coherent section of 74 barn, that allows for a better accuracy in the measurements.

[7] Argon consists of 99.6 % ^{40}Ar, 0.3 % ^{36}Ar and 0.1 % ^{38}Ar.

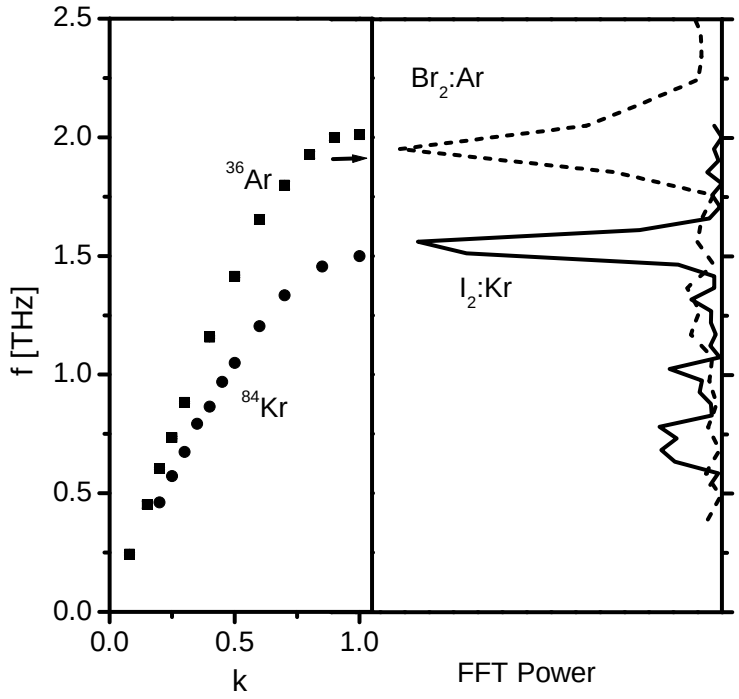

Figure 8.21: Left side: <100> branch of the phonon dispersion relation of argon (solid squares) and of krypton (solid circles). Only the frequencies of the longitudinal phonons are given. The arrow indicates the frequency of the zone boundary phonon of a ^{40}Ar host. Right side: The coherent host dynamics maxima of Br_2:^{40}Ar (dashed line) and I_2:Kr (solid line). The lines match exactly the frequency of the zone boundary phonon in the dispersion relation given on the right side.

dispersion relations with the Fourier transformations of the pump-probe spectra reveals the fact that the coherent host peaks match the frequency of the phonons with reduced wave vector $k = 1$, which are called *Zone Boundary Phonons (ZBP)*. Those have the shortest possible wavelength of all phonons. It is given by $2 \cdot a$, where a is the lattice constant. The ZBP are located at a frequency of 1.5 THz (50 cm^{-1}) in the case of solid krypton and at about 2 THz (67 cm^{-1}) for solid argon. Thus, the coherent dynamics observed in the pump-probe spectra can be attributed to *coherent zone boundary phonons* as was documented by us for I_2:Kr in Ref. [86] and in Ref. [97] for Br_2:Ar. The same type of coherent ZBP trace manifesting in a 2 THz or 500 fs oscillation for solid argon was observed on Cl_2:Ar pump-probe spectra obtained in our laboratory by M. Fushitani (unpublished results). In addition, coherent ZBP oscillations were also found on some pump-probe spectra for I_2 in solid Xe with a frequency of 1.25 THz corresponding to a period of 800 fs visible in the spectra [33]. It is worth noting here, that Apkarian and coworkers [30, 31, 33] propose a different interpretation with a local mode of the molecule-cage system instead of the ZBP (see section 8.3.3).

To summarize, we attributed the 1.5 THz oscillation on the I_2:Kr spectra and the 2 THz oscillation on the Br_2:Ar spectra to a coherent ZBP in the rare gas crystal. Questions to answer are: How are the coherent phonons excited (section 8.3.1) and why do they show up in the pump-probe spectrum of the molecule (section 8.3.2)? The ZBP have a vanishing group velocity $v_g = d\omega/dk$, since the slope in the phonon dispersion relation is zero near the edge of the first Brillouin Zone of the crystal. This fact will be quite crucial in clarifying the above mentioned questions.

8.3.1 Excitation scheme for coherent ZBP

To elaborate on an excitation scheme of the coherent ZBP, it is again useful to collect some of the experimental evidence given in section 7.2. First of all, one observes for the cases of iodine in solid krypton and bromine in solid argon only one host induced frequency. The experimental

observations also exclude phonon dynamics that are forced by the vibrational motion of the molecule. In such a *forced oscillation* scenario, the environment should show a mode being resonant with the exciting motion. The intramolecular vibrational oscillation period T was changed over a large range from T = 1 ps for excitations near the dissociation limits of I_2 and Br_2 down to 250 fs for Br_2 and about 350 fs for I_2 . Under all excitation conditions, a coherent ZBP motion of only one frequency could be observed. Thus, a forced oscillation cannot account for a phonon excitation.

The phase of the phonon oscillations also deserves attention. The relative phase is stable when changing the excitation energy of the B state as can be seen for I_2:Kr (Fig. 7.22) and Br_2:Ar (Fig. 7.17). The relative phase of the host induced oscillation is also the same when exciting the A state and comparing it to a B state excitation as can be followed in Fig. 7.20 for I_2:Kr and in Fig. 7.18 for Br_2:Ar. This overall phase stability implies a well defined phase with respect to $t = 0$, otherwise, the oscillation would be averaged out. The defined phase at $t = 0$ calls for an *impulsive* excitation of the environment correlated to the optical molecular excitation.

In principle, one can think about two different mechanisms of impulsive excitation. Considering the large internuclear elongations in the first wave packet oscillation near the gas phase dissociation limit, might lead to the following assumption: The molecule hits the matrix environment very hard during the first vibrational excursion and is afterwards essentially decoupled from the crystalline environment. This interpretation is rejected, since the experiment shows coherent host dynamics also for excitation energies significantly below the gas phase dissociation limit and it is essentially independent of the vibrational energy of the electronic state. For example, in the case of I_2 in solid krypton, the coherent phonon oscillation can be observed at $\lambda_{\mathrm{pump}} = 540$ nm, which is 1480 cm^{-1} below the B state dissociation limit. At $\lambda_{\mathrm{pump}} = 540$ nm, the energy relaxation is so low [25], that the molecule reaches its maximal elongation several times and is not decoupled after the first cage collision. This would again result in a forced oscillation scheme, which was excluded before.

An alternative impulsive excitation scheme will be proposed here, based on the Displacive Excitation of Coherent Phonons (DECP). The scheme was originally introduced for the excitation of zone center phonons in the case of semimetals and semiconductors [87–90]. If those materials are irradiated by an ultrafast laser pulse, an interband transition from bonding to antibonding orbitals occur. The electronically excited system reaches an equilibrium on timescales much faster than the nuclear response times. Due to the change of forces between the nuclei, the system begins to oscillate around the new equilibrium geometry. Only A_1 modes maintaining the crystal symmetry were excited. The coherent vibration of the lattice excited by DECP is detected by small reflectivity changes of an ultrafast (probe) pulse [91–94] or via diffraction of an ultrafast X ray pulse [95].

Such an impulsive excitation drives the system to a new equilibrium position, while initially at $t = 0$, the environment is still arranged in the electronic ground state equilibrium position. According to this, the oscillation starts with the extreme amplitude and the atoms will oscillate around their new equilibrium position finally. Therefore, the DECP excitation results in a $\pm\cos(2\pi f_{\mathrm{P}}\mathrm{t})$ characteristic of the coherently excited phonons. When extrapolating the phonon oscillation to the excitation time $t = 0$, the phonon amplitude has a maximum or minimum.

Now, the DECP scheme will be applied to doped solid rare gases. Instead of changing the electronic orbital configuration in the solid host, we change the electronic orbital of a chromophore embedded in the host similar to the mechanism proposed by Chergui for NO in different matrices [264–271]. The molecules I_2 or Br_2 are initially in the $v = 0$ level of the electronic ground state X $^1\Sigma_g$. The fs pump pulse excites the molecule to a $^3\Pi_{\Omega u}$ state, *e.g.* A ($\Omega = 1$) or

B ($\Omega = 1$). The internuclear distance of the molecule is not changed during the transition. Nevertheless, the electronic orbitals have changed, since the molecule ends up in another electronic potential. The environment however is still in its equilibrium around the electronic ground state. Considering typical phonon periods of several hundred fs, the excitation of a molecule by a 20-50 fs light pulse is indeed *impulsive*, because it is much faster than any phonon period. How does the solid state environment act on the change of the molecular orbital in an A $\longleftarrow$ X or B $\longleftarrow$ X transition?

To answer this question, the potential of a single rare gas atom in the vicinity of the halogen molecule is calculated. The potential minima give information about the equilibrium distance of the rare gas atom from the molecule. The framework of the calculation is the so called Diatomics In Molecules (DIM) formalism. It was originally designed to calculate the potential energy surfaces of triatomics [98–103] but finds a wide field of application in doped rare gas environments with dopants F_2 [104], HCl [105–108], Cl_2 [108], B [272, 273], Hg_2 [274], NO [275], and I_2 [111, 112, 114]. The DIM formalism is based on the pair potentials between all atoms.

The interaction potential between halogen and rare gas atoms are known from scattering experiments. For the calculations performed here, the scattering data from Ref. [276] for the I_2:Kr system and from Ref. [277] for the Br_2:Ar system were used. The interaction between the halogen atom and the rare gas atom is not isotropic, since the halogen has a hole in a p orbital (being equivalent to five electrons in the p orbital). The potentials contain two terms: One called V_Σ, the other one V_Π. The data are given by switching Morse potentials over a large range of internuclear distances. For the typical distances needed in the calculation a simple Morse potential is sufficient. Thus, a Morse fit to the potentials from Refs. [276, 277] was performed using:

$$V_\zeta = D_\zeta(1 - e^{-\beta_\zeta(R-R_\zeta)})^2 - D_\zeta, \tag{8.3}$$

with either Σ or Π for ζ. The parameters for I:Kr scattering and Br:Ar scattering are given in Tab. 8.5

Table 8.5: Morse parameters for I-Kr and Br-Ar

	I-Kr	Br-Ar
D_Σ [cm^{-1}]	287	124.14
D_Π [cm^{-1}]	126	80.3
β_Σ [nm^{-1}]	14.9	19.28
β_Π [nm^{-1}]	15.4	24.4
R_Σ [nm]	0.3733	0.3736
R_Π [nm]	0.43	0.392

With V_Σ and V_Π, the potentials of a rare gas atom and iodine or bromine molecules are calculated with the formalism presented in Refs. [111, 112]. One needs to define the potentials in polar coordinates. The center of the molecular axis represents the coordinate origin. The angle Θ is defined as the angle between intramolecular axis and the molecule to rare gas atom vector. V_0 describes the isotropic part of the interaction:

$$V_0(R) = \frac{2}{3}V_\Pi(R) + \frac{1}{3}V_\Sigma(R). \tag{8.4}$$

The potential V_1 accounts for the anisotropic part of the *halogen molecule*-rare gas interaction:

$$V_1(R, \Theta) = V_\Pi(R)\sin^2(\Theta) + V_\Sigma(R)\cos^2(\Theta). \tag{8.5}$$

For each molecular electronic state, an individual halogen molecule-rare gas atom interaction potential is built up from V_0 and V_1. For the molecular electronic ground state, the *halogen molecule*-rare gas atom potential V_X is given as:

$$V_X(R,\Theta)=\frac{1}{2}(V_0(R)+V_1(R,\Theta)). \tag{8.6}$$

The electronic excited B state has another potential form V_B which has a stronger isotropic character than the ground state potential V_X:

$$V_B(R,\Theta)=\frac{1}{4}(3V_0(R)+V_1(R,\Theta)). \tag{8.7}$$

The calculation was performed in spherical coordinates with the center of the molecular axis being placed at the origin. In this case, those positions of the rare gas atom with a vanishing gradient in radial direction were collected. In addition, the calculation was repeated in cartesian coordinates. In this case, the rare gas atom positions of vanishing gradient in Y direction were recorded (see Fig. 8.22c and d). It was found that both representations deliver the same results. Therefore, only the second case will be discussed. Fig. 8.22c shows the lines of vanishing force for the Kr atom in the vicinity of an I_2 molecule. The line of vanishing gradient for the B state lies at larger distances to the chromophore than for the ground state equilibrium line. Thus, when exciting the molecule from its electronic ground state to the B state, the molecule expands in the "eyes" of a rare gas atom. It can be seen for I_2:Kr (Fig. 8.22c) as well as for Br_2:Ar (Fig. 8.22d).

In addition, one has to search for atoms decoupled from the molecular vibrational motion. Fig. 8.22a and b show the (100) and (111) plane of the fcc Kr crystal respectively. The I_2 molecule on a double-substitutional site replaces two nearest neighbor atoms. The atoms are separated into four groups.

For example, the head-on atoms denoted as 3 are sitting on the elongation of the molecular axis. They are visible in the (100) and (111) plane. The head-on atoms are supposed to strongly couple to the molecular vibration as one can see in Fig. 8.22c. As the molecule vibrates in the B state, internuclear elongations of 0.45 nm are easily reached. However, at this elongation the Kr atom centered at approximately 0.59 nm will be repelled by the interaction with the molecule, since the equilibrium position is located at 0.67 nm. This "tightness" in the <110> direction gives rise to a strong vibrational energy relaxation as was confirmed in section 8.1.3, experiments on I_2 [25] and additional molecular dynamic simulations [22,24,81]. Furthermore, "shock waves" can be generated in this direction, travelling at ultrasonic speeds [278]. Thus, one can conclude, that the head-on atoms are strongly coupled to the intramolecular dynamics and thus not relevant for the DECP process.

Another group denoted by 5 in Fig. 8.22 is called belt atoms, since four of them are sitting in the plane which cuts the molecular axis perpendicularly, forming a "belt" around the molecular "waist". As can be seen in Fig. 8.22c and also in d, those atoms are repelled from the molecule in the electronic transition B $\longleftarrow$ X. However, when the molecule is vibrating in the B state, the belt atoms are strongly coupled to that motion. As the molecular internuclear distance elongates, the belt atoms are "sucked" in close to the molecular axis. As the internuclear distance shrinks in the next half cycle of a vibration, the belt atoms are repelled from the axis. In terms of volume conservation, the head-on atoms (3) increase their distance from the chromophore center and the belt atoms in turn are pushed inwards close to the molecule. The mechanism has been observed in molecular dynamic simulations [24,84,278]. The long outward excursion followed by a slow inward motion of the chromophore atoms were attributed to the belt motion of the molecule in

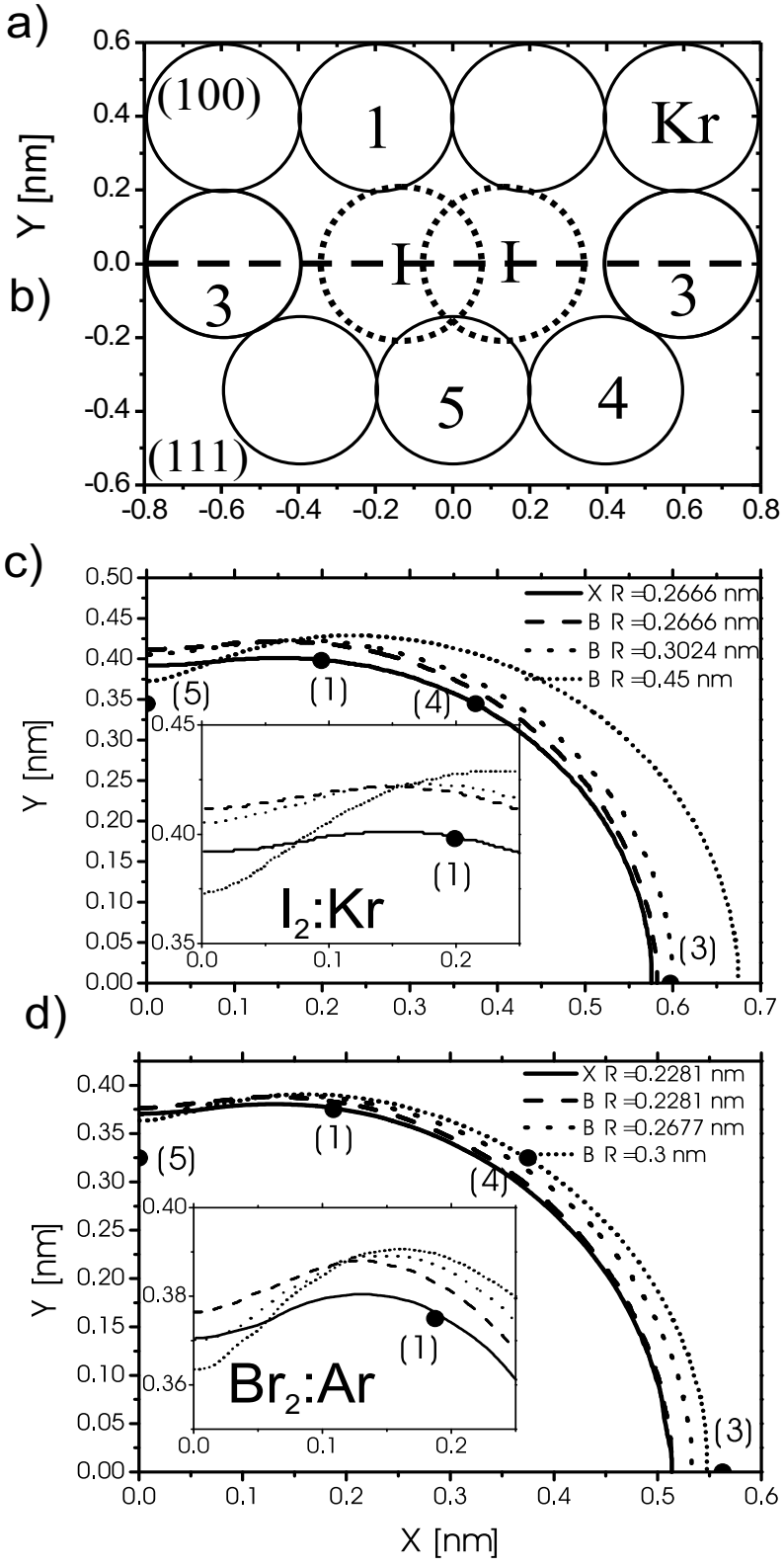

Figure 8.22: a) (100) plane of the I_2:Kr system. b) (111) plane of the I_2:Kr system. Rare gas atoms are separated into groups: 1 coherent phonon atoms, 3 head-on atoms, 4 window atoms, 5 belt atoms. c) Equilibrium lines (local potential minima) of a Kr atom around the I_2 molecule for different electronic states and internuclear distances. Only one quadrant is shown for symmetry reasons. Solid line: electronic ground state X with $R_{e,X}$ = 0.2666 nm, dashed line: excited state B with $R_{e,X}$ = 0.2666 nm, dotted line: excited state B with $R_{e,B}$ = 0.3024 nm, short dotted line: B state with large internuclear distance R = 0.45 nm. d) Same as c) but for Br_2:Ar system.

section 8.1.4. Thus, we conclude that the belt atoms are strongly coupled to molecular vibration and therefore are not involved in the coherent phonon we observe.

A third group of atoms is denoted by number 4. These are often called window atoms, since four of them are forming a rectangular window on each side of the molecule. During the elongation of the molecular axis the halogen atoms pass the window through its center. The coupling to the molecular vibration is strong and comparable to the head-on atoms (3).

Finally, there is one group of atoms that is essentially decoupled from the molecular vibrational motion. This group is sitting in the (100) plane of the fcc lattice symmetrical to the molecular center and is denoted by (1). As the molecule undergoes the B $\longleftarrow$ X transition, this group of atoms experiences a force in the Y direction. The inset in Fig. 8.22c for I_2 in Kr and panel d) for Br_2 in solid Ar magnifies the region of interest. The Ar atoms (1) are repelled to a position further away from the molecular axis in the Y direction (Fig. 8.22). This new position is very close to a point where all B state equilibrium lines for different internuclear distances of the chromophore intersect. The Kr or Ar atom of group (1) is essentially free of any force induced by the I_2 or Br_2 oscillation. Thus, the coherent phonon oscillation has to be attributed essentially to the group of atoms (1). The Ar atom (1) and its equivalents in the (100) plane seem to be further away from the zero-force line crossings than in the case of I_2:Kr. Therefore, one expects a stronger influence of the intermolecular Br_2 vibration on the coherent Ar crystal phonon than in the case of I_2:Kr. This might result in a faster dephasing of the Ar crystal coherent phonons compared to the Kr phonons.

The problem of the cage reaction on the molecular electronic transition was reduced to one type of cage atom. This is an approximation, since the influence of all other Ar atoms in the vicinity is neglected. Nevertheless, the calculation gives the right trend concerning the force imposed on a rare gas atom by molecular electronic excitation or vibration. Real positions of rare gas atoms are not needed in the argumentation. Since the phenomena we observe are strongly connected to the molecular excitation, one might think in such simple terms.

A detailed calculation on how the environment atoms move in the course of time is not yet available. The only information attainable right now is the assignment of the coherent phonon to group (1).

In summary the impulsive excitation of rare gas phonons was attributed to the expansion of the molecules electronic cloud during the transition from the electronic ground state to an excited covalent state. Furthermore, we can find a group of rare gas atoms in the (100) plane being decoupled from the intramolecular vibration. Since the electronic excitation is accomplished by a 20-50 fs light pulse, the phonons are excited impulsively. Most probably, many different phonon modes are excited in the vicinity of the molecule. In this context, it is very important to realize the symmetry of the phonon excitation. The molecule might be simplified as a cylinder. The electronic expansion changes the radius of the cylinder as can be seen in Fig. 8.22. Thus, phonons are excited symmetrically in one direction with wave vector $\mathbf{k}$ and in the other direction with a wave vector of $-\mathbf{k}$. The total wave vector of the phonons cancels. Therefore, *photons* of a very small wave vector $k = 2\pi/\lambda$ of typical values around $1 \cdot 10^7$ m^{-1} in the visible light range can excite zone boundary *phonons* of $k = 2\pi/a = 1.1 \cdot 10^{10}$ m^{-1}, with a being the Kr lattice constant of 0.565 nm. The momentum conservation is not violated due to the counter propagation of the phonons. The known examples for DECP processes usually lead to excitation of zone center phonons with small wave vector (see for example [91–95]). Two phonon processes can indeed be used to generate zone boundary phonons. This is documented in Ref. [279] for the case of Raman scattering in rare gas matrices. The ability to generate coherent zone boundary phonons makes the molecular excitation method quite unique.

After phonons have been excited in the impulsive process, given by the electronic expansion

of the molecule, the phonons travel away from the excitation source (molecule) according to their group velocity. The phonons form a kind of wave packet that propagates and disperses since its constituents propagate with different velocities. The part of the wave packet belonging to zone boundary type phonons stays at the excitation source since, as stated above, v_{g}= 0 at the boundary of the Brillouin zone. Thus, the dispersion relation of the crystal provides a sort of a filter mechanism. Zone center phonons propagate with the velocity of sound which is 1.64 nm/ps for longitudinal phonons in Ar and 1.375 nm/ps for longitudinal phonons in Kr (see for example Ref. [9] or [280]). Thus, after about 500 fs the zone center phonons have reached the second solvation shell and leave the vicinity of the chromophore. If the phonons are probed by the excitation source, only the zone boundary phonons remain and contribute to the coherent signal.

8.3.2 Detection scheme for coherent ZBP

So far the excitation and decoupling of the coherent ZBP have been explained. The mechanism of the phonon-molecule interaction that allows the phonon to show up in the pump-probe spectrum of the chromophore has to be answered now. The rare gas crystal is optically inactive in the range of visible and ultraviolet light used in this study. The first absorption band of Kr lies at 10 eV, in Ar at 12 eV. Therefore, the phonon has to influence the internuclear transitions to show up in the pump-probe spectrum. This aspect will be explained in this chapter via the solvation shift of the charge-transfer (CT) states. The observed pump-probe spectra consist of two spectral components. One being attributed to the intermolecular vibration, the other one to the coherent phonon contribution. Fig. 7.16 gives a good example for the case of Br_2:Ar, the pump-probe spectrum is dominated by the intramolecular vibrational motion up to 2 ps, afterwards being modulated by the coherent ZBP which shows up in the 500 fs period.

The intensity of the intramolecular contribution decays monotonically and simultaneously its modulation contrast is washed out more and more. Thus, the decaying intramolecular signal is modulated by the phonon contribution. If this statement holds then the measured signal intensity I_S at late times should be the product of the time averaged intramolecular contributions $< I_V >$ and the phonon modulation amplitude I_P

$$I_S =< I_V > I_P \tag{8.8}$$

To test this hypothesis we calculated the structureless mean value $< I_V >$ of Fig. 7.16a and divided the measured signal I_S in Fig. 7.16a by $< I_V >$ to obtain Fig. 7.16b. Indeed a very clear sinusoidal modulation is observed after 2 ps with well-defined frequency and essentially constant or weakly monotonically decaying amplitude. This result for I_P is a confirmation that the decomposition according to Eq. (8.8) catches the essence of the spectra at late times.

Furthermore it is now possible to work out this decomposition with respect to the region between 0 and 2 ps. In that domain, the structures in Fig. 7.16b are still dominated by the intramolecular dynamics. The key to distinguish the contributions is a variation of the probe photon energy.

The wavelength λ_{probe} = 348 nm in Fig. 7.16 was chosen to emphasize the intramolecular as well as the phonon contribution: A variation of λ_{probe} now allows for enhancement either of the intramolecular or the phonon contribution. This effect is used to identify the detection scheme for the phonon contribution. Probing deeper in the B state with a shorter probe wavelength (λ_{probe} = 345 nm) for the same λ_{pump} = 520 nm yields the spectrum $I_S^{345}/< I_S^{345} >$, which contains essentially only the intramolecular period of 310 fs and the modulation amplitude decays smoothly around 3 ps to the mean value (Fig. 8.23a). Probing higher with a probe wavelength λ_{probe} = 354 nm leads to $I_S^{354}/< I_S^{354} >$ with the phonon period of 500 fs between 2

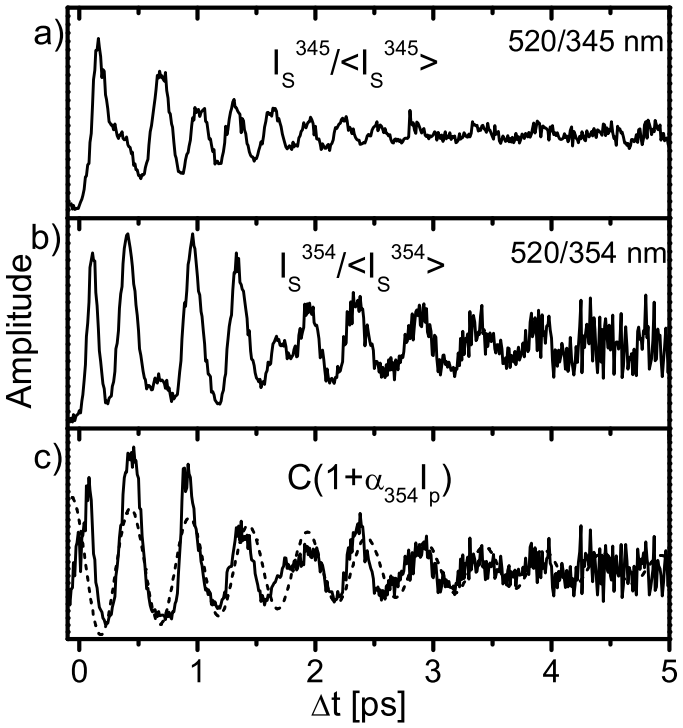

Figure 8.23: (a) and (b) Normalized pump-probe spectra of Br_2 in solid Ar with $\lambda_{\rm pump}$ = 520 nm and $\lambda_{\rm probe}$ = 345 and 354 nm, respectively. (c) Solid line: Spectrum calculated by dividing spectrum (b) by (a)(see text). Dashed line: 2 THz oscillation with exponential decay.

and 4 ps, and at shorter times, the oscillations are rather complex (see Fig. 8.23b). The reasons for the complex behavior are beatings between the intramolecular and the phonon periods. Thus the more general decomposition scheme for all times is given by:

$$I_S = I_V(1 + \alpha I_P). \tag{8.9}$$

The weight factor α for the strength of the phonon modulation varies with $\lambda_{\rm probe}$ and can be exploited to separate out I_V as well as I_P. Fig. 8.23a shows that $\alpha = 0$ for $\lambda_{\rm probe}$ = 345 nm, and this spectrum is close to the intramolecular dynamics I_V. Obviously α is large for $\lambda_{\rm probe}$ = 354 nm (Fig. 8.23b). Thus dividing the spectrum of Fig. 8.23b ($I_S^{354}/ < I_S^{354} >= I_S$) by the spectrum of Fig. 8.23a ($I_S^{345}/ < I_S^{345} >= I_V$) should yield:

$$\frac{I_S^{354}}{I_S^{345}} \frac{< I_S^{345} >}{< I_S^{354} >} = C(1 + \alpha_{354} I_P), \tag{8.10}$$

with a structureless $C =< I_S^{345} > / < I_S^{354} >$. The ratios are given in Fig. 8.23c and its modulation is expected to originate from the phonon contribution I_P. Indeed we obtain now a single sinusoidal modulation with the phonon period of 500 fs and smoothly decaying amplitude (as soon as both intensities are above noise, *i.e.* from 100 fs on). The possibility to exclusively extract the phonon part, especially in the regions dominated by the intramolecular dynamics, clearly demonstrates the validity of the decomposition scheme. The scheme clarifies that optimization of the phonon contribution has to compromise between an I_V signal significantly above noise and a large α. The $\lambda_{\rm probe}$ = 354 nm favors a large α, however, I_V decays rather fast. This is due to probe window lying rather high with respect to the relaxing B population. Therefore, the signal in Fig. 8.23b is lost in the noise beyond 3.5 ps. $\lambda_{\rm probe}$ = 348 nm provides a moderate α with a pronounced intramolecular region, however, the population in the phonon modulated region remains longer close to the probe window, and the phonon contribution is visible up to 5 ps in Fig 7.16b.

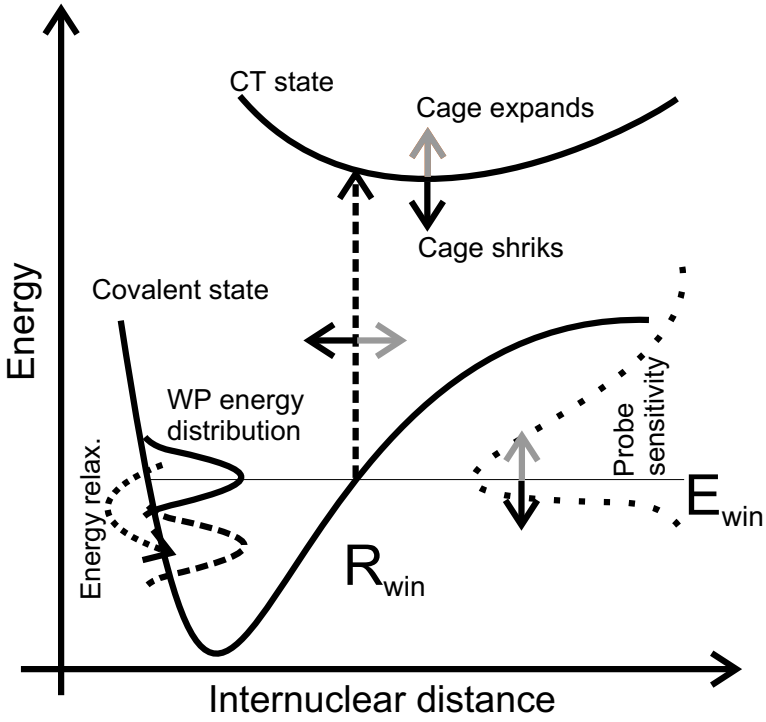

Figure 8.24: Phonon detection mechanism. The phonon modulates the charge-transfer (CT) state solvation energy. Thus, the probe resonance (R_{win}, E_{win}) and the schematic sensitivity curve (dashed, right hand side) shift accordingly, leading to a changing overlap of the probe sensitivity with the relaxing vibrational wave packet (WP) in the covalent state.

The phonon contribution in Fig. 7.16a is proved to appear as a modulation of the mean B state signal intensity according to Eq. (8.8), and it becomes visible at long delay times. At those times, the intramolecular modulation vanishes due to dispersion and dephasing in combination with energy relaxation. A smoothly decaying spectrum develops, and in addition the wave packet's center of gravity relaxes below the energy at which it is probed in the B state (E_{win}). Thus only the high-energy wing remains visible. The probe distance R_{win} was defined as the internuclear distance, at which the wave packet on the B state is resonantly probed to the charge-transfer state. Suppose, some process periodically shifts the energy of the CT states up and down, as indicated by the arrows from the CT state in Fig. 8.24. As a consequence, R_{win} would shift right- and leftwards. Thus, the probe window energy E_{win} would shift up and down. What are the consequences of the probe window shift on the pump-probe spectrum? To answer this question, one must take a closer look at the probe process. The wave packet is not only probed at energies corresponding to E_{win}, but also above and below as indicated by the sensitivity curve in Fig. 8.24. This is due to the broad Frank-Condon overlap of B and CT state and the finite energetic width of the probe pulse, as explained in Fig. 2.9. Above E_{win}, the sensitivity can be expressed classically and is proportional to $1/\sqrt{\Delta E}$, where ΔE is the energy difference to E_{win} [164]. Below E_{win}, the sensitivity decays rather quickly. Classical energy conservation would give a cut off which is reflected in a steeply decaying Franck-Condon factor.

The pump-probe signal is proportional to the overlap of the probe sensitivity curve with the vibrational wave packet. If the CT state shifts a bit, E_{win} and the whole sensitivity curve shift by a small amount. The overlap does not change much for a wave packet located on the maximum of the sensitivity curve, since the probe sensitivity versus energy is flat. In contrast, when the wave packet is located below E_{win} near the edge of the sensitivity curve, the overlap changes quite dramatically with a variation of energy, due to the steep decay in this range. The wave packet can be prepared in this range (compare Fig. 8.23b) or its energy can relax to this region with time (Fig. 8.23a). If the wave packet is prepared significantly above E_{win}, a periodic shift of the sensitivity curve causes a weak modulation of the pump-probe spectrum, since the $1/\sqrt{\Delta E}$ decay is quite smooth. Only after energy relaxation has transferred it below E_{win}, the

modulation can be observed with high sensitivity on the pump-probe spectrum. The effect was demonstrated for the B state of Br_2. Nevertheless, the explanation for the A state has to be completely the same, since the experimental features are similar to those in the B state (see. Fig. 7.18).

Now the source for the shift of the probe window is discussed. The solvation energy of the charge-transfer state with 3300 cm^{-1} amounts to 10 % of the transition energy and is huge compared to that of the B state. A local compression of the lattice around Br_2 is going to increase this solvation energy of the charge-transfer state by the shrinking of cavity diameter d in the Onsager model (see Eq. 3.3) [96, 193]. Stronger solvation pushes the E state downwards in energy, the probe position R_{win} shifts inwards and E_{win} down in energy to accommodate for the fixed probe photon energy. Coherent oscillation of matrix atoms in the Br_2 vicinity generate such density modulations that can be decoded from the B state pump-probe signal.

With this scenario in mind one can also interpret the behavior at early times in Fig. 8.23 when the B state dynamics causes strong fluctuations in the signal. The signal intensity I_S scales with the fraction of population of the wave packet which just passes the probe window, *i.e.* I_V in Eq. (8.9). In addition, it can be enhanced by a fraction αI_P due to a local compression if this increases the sensitivity. This explains why α in Eq. (8.9) is probe wavelength dependent and in general even time dependent. In Fig. 8.23a the probe energy is located deep in the potential well due to a short probe wavelength. Therefore a major part of the B state wave packet is accessible all the time and an increased sensitivity by compression has a marginal effect on the sensitivity α = 0. The wave packet is barely touched at its high-energy wing in Fig. 8.23b with the steep part of the sensitivity curve from the very beginning due to the long λ_{probe}. Thus, α is very high and a shift of the probe window by compression strongly enhances the signal and the phonon modulation becomes visible. However, soon the wave packet will be lost for detection, due to the additional energy relaxation, and the B state signal disappears in the noise. For the mean λ_{probe} of Fig. 7.16a a major part of the wave packet is caught at early times leading to a small α while after significant energy relaxation, α starts to rise and a long-standing coherent phonon signal can be deduced from the surviving B state signal.

So far, the argumentation was carried out for the case of Br_2 molecules in solid argon. The explanation for I_2 in solid krypton follows from the data given in section 7.2.1 and is completely similar. Fig. 7.20 presents pump-probe spectra of the A and B state. As in the case of Br_2, the intramolecular vibrational motion shows up first followed by a phonon modulated background. The phonon modulation is stable in frequency and amplitude, thus favoring a decomposition given in Eq. (8.9). As in the case of Fig. 8.23 for Br_2:Ar, the I_2 probe wavelength was changed while keeping the pump wavelength fixed. The result is shown in Fig. 7.21. The B state of I_2 is pumped in all spectra with the same pump wavelength λ_{pump} = 520 nm, and the probe wavelength is varied systematically from λ_{probe} = 496 nm to 530 nm. The phonon contribution beyond 3 ps has the same frequency and phase in all spectra, and the contrast shows the systematic behavior as described in connection with Eq. (8.10). With 496 nm, we probe deep in the B state well and catch the full vibrational wave packet. Therefore a shift of the probe window energy is not relevant for the sensitivity, α is close to zero, and the phonon contrast is negligible for a long time. Only after 6 ps, when the wave packet has relaxed below the probe energy, the contrast starts rising. Probing higher in the B state with longer wavelengths (508 nm and 515 nm) shifts the inset of good phonon modulation contrast to earlier times. If we catch only the high-energy wing by λ_{probe} = 530 nm then the signal is quickly lost in the noise due to relaxation out of the probe window and the connected signal reduction. However, the sensitivity modulation already appears in an intensity alternation of the B state dynamics in analogy to Fig. 8.23. The second peak in the pump-probe spectrum with 530 nm probe wavelength in

Fig. 7.21 is considerably reduced compared to the first and second one. Furthermore, the fourth maximum in reduced due to the same reason of phonon modulation at early times.

In the case of I_2:Kr, the model of the oscillating cage and the periodically shifting charge-transfer states can be even quantified [86]. The energy relaxation of the iodine B state in solid Kr can be determined to a high accuracy, as was demonstrated in Refs. [25, 28] and reproduced in Fig. 8.10. When looking at Fig. 7.20a, a history of the wave packet energy as a function of time can be generated by simulating the energy loss from the initial energy at $t = 0$ and the energy relaxation rates dE/dt. The oscillation around the decaying integrated signal can be reproduced in the simulation when setting the phonon induced shift of the charge-transfer states to 40 cm^{-1}. This is indeed very small compared to the overall matrix shift of about 3100 cm^{-1}.

When attributing the effect purely to the change of the cage diameter in the Onsager model (Eq. (3.3)), a diameter change of 0.002 nm will occur. This is a very small amplitude of the ZBP located at the chromophore. It is only 0.5% of the whole cage diameter d of the two nearest neighbor distances. Thus, one can conclude that the coherent ZBP amplitude is very small. Perhaps this is one of the preconditions for it to stay coherent on a time scale of several picoseconds.

Concerning the coherence lifetime, no experimental data are available. The spectral resolution in neutron scattering did not allow for a prediction of the lifetime [10, 11].

8.3.3 Comparison to alternative models

Comparison to previous I_2:Kr and Cl_2:Ar experiments and simulations

The observation of coherent host motions in molecular pump-probe spectroscopy is an interesting feature. Furthermore, it is very important for the problem of electronic state coupling. A prominent example is the predissociation of the I_2 electronic B state, that is very much reduced in rare gas matrices [22, 27] compared to high pressure gas environments [76, 148, 251] and liquids [23, 149, 150, 253]. The reason lies in the symmetry dependence of the coupling matrix elements [23, 111, 112]. Due to the high symmetry of the rare gas crystal, many contributions of the coupling cancel. When exciting host motions, some cancellation might be reduced and the coupling might be strengthened.

The group of Apkarian invested a lot of effort to clarify the motion of the cage atoms in the vicinity of the I_2 chromophore in different environments. The first experimental evidence for what we identified now as a coherent ZBP [86, 97] was published for I_2:Kr by Apkarian in Ref. [24]. The experimental data shown there were produced by one-color pump-probe spectroscopy of I_2 molecules in solid Kr. It was stated, that the observed 650 fs oscillation must be attributed to a modulation of the B state population in the probe transition to the charge-transfer states, in accordance with the interpretation given above. The modulation of the charge-transfer states was attributed to a local mode of the host. Despite the similarity in the detection process, the excitation of the host and the character of the host motion is in contradiction to the explanation given here in section 8.3.1. It was stated, that the host motion should be resonantly driven by the vibrational motion of the molecule. At the specific pump wavelengths used in Ref. [24], a 2:1 resonance of the I_2 intramolecular vibration period and the 650 fs coherent host vibration period was found. An impulsive creation (either electronic or vibronic in the first excursion of the intramolecular wave packet) was excluded, stating that "it would be difficult to imagine that such a collective coherence could last for ca. 8 ps if it were impulsively created".[8] The host motion was assigned to the belt atoms, denoted as number 5 in our nomenclature (see Fig. 8.22b). Those belt atoms are supposed to be strongly coupled to the intramolecular vibration. The simulation of the local belt mode resonantly driven by the molecule did however

[8] page 265 of Ref. [24]

not show any coherence (see Fig. 8 in [24]). The contradiction of coherence in the experiment and its lack in the simulation could not be resolved.

In a following study on Cl_2:Ar [84], the role of the host motions in pump-probe spectra was further examined. Normal modes of the cage-molecule system were calculated. The change of the Cl_2-Ar interaction potential when undergoing the B $\longleftarrow$ X transition was completely neglected. Thus, the possibility of impulsive excitation of phonons proposed here in section 8.3.1 was not contained in the simulation.

With the first results of CARS on the electronic ground state of I_2, a new tool to monitor host motion was at hand [29,30,32,85]. Long lasting coherent vibrations of the host-molecule system could be found. As an example, a coherent mode at 41.5 cm^{-1} was observed for 100 ps. For this mode, an impulsive excitation mechanism similar to the one presented here was proposed.[9] In CARS, it has to occur between the pump and Stokes pulse. In a normal mode analysis of the I_2(X):Ar system, such a mode with energy 41.5 cm^{-1} did not show up.

We presented clear evidence for an impulsive excitation of the 650 fs host motion [86]. The excitation quantum energy and thus the vibrational period was varied over a large range. For instance, the I_2 molecule was not only excited to its electronic B state but furthermore to the A state close to the free molecule dissociation limit (see Fig. 7.20). In that case, the vibrational frequency is about 500 fs, thus a 2:1 resonance of the pure molecular vibration and the host vibration of 650 fs was clearly ruled out.

However, the impulsive excitation mechanism was not accepted by Apkarian and coworkers. In a recent paper [33], they suggested an alternative to the impulsive excitation mechanism, that shall be briefly explained here: The molecule is initially excited to the B state that is assumed to predissociate after a while. This predissociation has to occur well-defined 700 fs after the wave packet excitation. The dissociative states in which some population ends up after the predissociation are bound by the cage for steric reasons. Thus, they are very sensitive to motions of the cage atoms. Their equilibrium distance is much larger than the covalent equilibrium distances. The normal mode of the molecule-cage system with the molecule sitting in cage-bound states modulates the probe transition by changing the shape and absolute energy of the cage-bound state. The cage-bound states have to be probed by a two-photon transition to the charge-transfer states, used in the LIF detection. A pump-probe spectrum consists of the cage-bound state spectrum *added* on the B state pump-probe spectrum in this picture.

In our latest article [97] on this topic and in the previous chapter of this thesis, we show clear evidence to refuse the mechanism explained above. We summarize the arguments briefly.

First, the coherent host motion contribution (coherent ZBP in our interpretation) is proportional to the B or A state decaying signal (see Fig. 7.20 for I_2:Kr and Fig. 7.18 for Br_2:Ar). It would be a non-plausible coincidence if the amplitude of cage-bound state dynamics would scale with the amount of B or A population that is left in the probe window.

Second, we have shown that our signals (even at short delays) have to be explained by a multiplicative connection of phonon and intramolecular dynamics (Eq. (8.9)), that clearly contradicts the additive mechanism proposed in Ref. [33]. Coming back to Fig. 8.23, one can clearly observe the increase or suppression of single vibrational peaks in 8.23a due to the phonon influence presented in b). The shoulder of the first vibrational peak in a) is strongly enhanced due to the higher density of the cage induced by the ZBP, whereas the second vibrational peak from a) is suppressed due to less cage density induced by the ZBP. This behavior cannot be explained by adding two signals, but is clearly a sign of the ZBP modulation on a vibrational spectrum. The argument was also given for the case of I_2:Kr, whose data are collected in Fig. 7.21.

Third, the coupled molecule-cage normal mode proposed by Apkarian *et al.* depends on

[9] This mechanism was proposed before by us in Ref. [86].

the properties of the rare gas *and* the molecule. In contrast, we observed for I_2:Kr, Br_2:Ar, and recently also Cl_2:Ar [10], that the period of the coherent host dynamics exclusively depends on the rare gas crystal. This is supported by pump-probe spectra of I_2 in solid Xe (by Apkarian), where a coherent host oscillation period of 800 fs (the ZBP period) was found (see Fig. 14 in [33]). Thus, the assignment to cage-bound state signals has to be neglected and indeed all coherent host oscillations show the ZBP period of the rare gas crystal used.

The coherent ZBP frequency seems to be exclusively connected to the detection of the CT state LIF in pump-probe experiments. If one monitors the LIF of I*I* states (in the IR range [23,281,282]), another type of coherent host dynamics can be observed [33]. Probably, the I*I* states are more sensitive to other types of cage motion than the charge-transfer states.

Finally, the spatial extension of the coherent zone boundary phonon has to be addressed. The excitation mechanism proposed in section 8.3.1 is highly local. The phonon is most likely confined to the vicinity of the chromophore. It forms a wave packet with certain width Δk near the zone boundary. The flat dispersion curve allows for its high spectral purity and its very slow dispersion. Nevertheless, the ZBP is the most local of all phonons. It has the shortest possible wavelength. Thus, a few atoms are sufficient to carry the zone boundary information of the phonon.

Problems in calculations of coherent ZBP

Longitudinal zone center phonons propagate with a group velocity v_g of 1.64 nm/ps in Ar and 1.38 nm/ps in Kr. In addition, molecular excitation in the matrix can result in supersonic sound waves or shock waves travelling with up to 3 nm/ps in solid Ar [266, 278]. This velocity corresponds to 5.5 lattice constants a ($a = 0.53$ nm) propagation in one picosecond. Furthermore, the shock waves waves travel along favored directions in the rare gas crystal [278].

In numerical simulations, a fcc cell of side length $M \cdot a$ contains $4 * M^3$ atoms. For $M = 5$, the cell includes 500 atoms. In trajectory simulations, the chromophore is embedded in the middle of a rare gas cell. Shock waves excited by the chromophore at $t = 0$ (for example by the expansion of the electron cloud) are reflected at the cell walls and travel back to the excitation source. Taking the velocity given above into account, the fastest supersonic waves reach the molecule again after passing $5 \cdot a$, which corresponds to about 1 ps in solid Ar. They destroy the small coherent amplitudes of cage atoms in the vicinity of the chromophore in the simulation.

The trajectories of I_2 in rare gas matrices have been calculated so far in cells of 108 atoms ($M = 3$) [111, 112] and 500 atoms ($M = 5$) [113] with the DIM approach and periodic boundary conditions. Periodic boundary conditions [283] lead to the same problem as in the single cell, since the excitation of one cell travels to the next. Increasing the cage size is hard with up to date computing power. Even for 500 atoms, only 16 trajectories could be calculated in a reasonable time in Ref. [113]. No signs of coherent ZBP were found in theory so far, which is comprehensible with the underlying cell sizes.

The only realistic solution for simulations would be the application of absorbing boundary conditions to effectively remove the high velocity matrix excitations from the simulation cell. The strategy is currently followed by the group of R. B. Gerber to gain insight into the detailed cage motion observed in the experiments presented in this thesis.

[10] M. Fushitani working in Prof. Schwentner's group found a host mode of 500 fs period in Cl_2:Ar, being the ZBP period in the Ar crystal.

Chapter 9

Summary

The thesis presents coherent dynamics of Br_2 molecules embedded in solid Ar. The dynamics is investigated via the femtosecond pump-probe method, which is newly established in Br_2:Ar by absorption and emission spectroscopy. The dephasing and dissipation rates observed are in the femto- to picosecond range. The halogen doped rare gas crystal can be idealized as a basic model for multi dimensional systems like biomolecules in solvents. The molecule presents a one dimensional quantum system, which allows for a quantum calculation of the vibrational wave packet. The multidimensional crystal induces decoherence in the molecule. Apart from vibrational coherences on the molecule, a coherent *host* mode is observed here on a surprisingly long timescale. To support the attribution of this mode to coherent Zone Boundary Phonons (ZBP), results on I_2 doped krypton crystals are presented.

Coherent intramolecular dynamics of Br_2 in solid Ar

Polarization dependent pump-probe spectra proved the suppression of the molecular rotation in the rare gas crystal. Exploiting the connection between the $\Delta\Omega$ selection rules and polarization dependent pump-probe spectra, the decomposition of wave packet dynamics from different states is achieved in the spectra.

The femtosecond pump-pulse excites an intramolecular vibrational wave packet on a covalent molecular electronic state. From the experimental periods T, an effective potential for the B state of Br_2:Ar is constructed using the RKR method. When the intramolecular wave packet is excited at the free molecule dissociation limit, the collision with the cage leads to vibrational energy losses of about 50 % during the first oscillation period. The vibrational relaxation decreases while lowering the vibrational energy of the wave packet.

A molecular trajectory constructed from the pump-probe spectra deserves to further examine the molecule-host interaction. The collision of the molecular fragments with the rare gas cage populates lower lying vibrational levels in about 70 fs, indicating the well defined nature of the interaction. A wave packet motion on those collision-excited levels can be observed afterwards. The observation gave rise to the phrase of *collision induced coherences*. The vibrational coherence also survives a nonadiabatic electronic transition, as exemplified in a $^1\Pi$ to $^3\Pi$ transition of the I_2 molecule in solid Kr.

The loss of vibrational coherence was further investigated with a novel scheme for Br_2:Ar. Negatively chirped excitation pulses allowed for a separation of dispersion (wave packet broadening on anharmonic potentials) and dephasing (irreversible loss of coherence) in pump-probe spectra. For a free molecule, the negatively chirped excitation results in a spatial focusing of the vibrational wave packet at time T_{opt} indicated by a background-free modulation in pump-probe spectra. Due to the effect of vibrational dephasing, a background on the modulation remains even at T_{opt}. A systematic change of T_{opt} by different chirp parameters allows for the determination of the vibrational dephasing time from the increasing background. A vibrational

dephasing time $T_{\mathrm{deph}}^{\mathrm{vib}}$ of 3 ps (or 11 vibrational periods, each of 280 fs) is measured in the B state of Br_2:Ar. This constant limits the time range in which vibrational level interferences ("fractional revivals") can be observed.

The fractional revivals contain detailed information about coherences among distinct groups of vibrational levels. The 1/6 revival, manifested by the threefold vibrational frequency in the pump-probe spectrum, requires the coherent coupling of four vibrational levels. However, it appears at times around 3.5 ps for Br_2, which is beyond the $T_{\mathrm{deph}}^{\mathrm{vib}}$ of the molecule in the Ar matrix. A wave packet dynamics control scheme based on linearly chirped pulses is developed with the help of a numerical wave packet propagation. By exciting the vibrational wave packet with positively chirped pulses in the experiment, a shift in the revival structures to earlier times was achieved in accordance with simulations. The 1/6 revival structure was measured up to 1.2 ps indicating a vibrational dephasing time for the four levels $T_{\mathrm{deph}}^{4} \approx 1.2$ ps. The measured interference pattern can only be achieved if the excitation pulse "imprints" the right phases on the vibrational levels of the B state during the molecule-laser pulse interaction. Due to the positive chirp, the laser pulse is stretched to a duration of $\Delta\tau$ = 300 fs, exceeding the intramolecular vibrational period of about 270 fs. The electronic coherence between ground and excited state has to live longer than $\Delta\tau$. Thus a lower limit for the electronic dephasing time $T_{\mathrm{deph}}^{\mathrm{el}}$ of 300 fs is obtained in the B $\longleftarrow$ X transition.

Coherent phonon dynamics

The pump-probe spectra contain oscillations that cannot be attributed to intramolecular vibrational dynamics. Almost monochromatic and phase stable modulations with periods of 500 fs for Br_2:Ar and 650 fs for I_2:Kr are observed when exciting a molecular wave packet with different photon energies in the electronic B and A state. The modulation frequencies of 2 THz (Br_2:Ar) and 1.5 THz (I_2:Kr) correspond to the Zone Boundary Phonon (ZBP) frequencies of the respective rare gas crystals. The excitation and probe scheme for the coherent host dynamics is established and compared to mechanisms in the literature.

The vicinity of the molecule is impulsively excited by an expansion of the molecular electronic could during the B $\longleftarrow$ X or A $\longleftarrow$ X transition induced by the fs pump pulse. The process corresponds to the Displacive Excitation of Coherent Phonons (DECP) scheme developed for coherent phonons in other materials.

All phonons having finite group velocity leave the vicinity of the excited molecule. The ZBP group velocity approaches zero and therefore its amplitude stays at the molecule. The coherent ZBP is decoupled from the intramolecular vibrational motion. A model calculation using the diatomics in molecules formalism identifies a group of atoms in the first solvation shell being impulsively excited in the electronic transition but decoupled from the molecular vibration afterwards.

The host motion is probed by the molecular impurity. The rare gas density in the vicinity of the molecule is periodically changed with the ZBP frequency. The molecular charge-transfer states react very sensitively even on small density changes by a shift of their solvation energy. The probe window parameters R_{win} and E_{win} depend on the potential energy difference of the charge-transfer states with the covalent states. A periodic change of the charge-transfer energy leads to a periodic shift of the probe window and thus to a modulation of the probed molecular population.

Future prospects

Vibrational and electronic dephasing

The focusing scheme to determine $T_{\mathrm{deph}}^{\mathrm{vib}}$, as well as the revival control method used to find $T_{\mathrm{deph}}^{\mathrm{el}}$ were only applied for one excitation energy in the B state. Changing the excitation energy of the wave packet will allow for a systematic study of electronic and vibrational dephasing through the whole Franck-Condon region. Furthermore, the schemes should be applied for different temperatures and co-doped crystals (inducing an asymmetric cage) to gain a complete picture of the dephasing processes. The revival control by positively chirped pulses was applied for the case of a 1/6 revival, deducing T_{deph}^{4} here. Apart, it can be generally applied for arbitrary fractional revivals, however limited by the time resolution of the probe pulse. The higher revivals will exhibit the dephasing times of larger groups consisting of n vibrational eigenstates. The dependence of T_{deph}^{n} on n can be determined by a series of experiments.

Extension of the wave packet control

Apart from applying the here invented schemes under different conditions, one can think about extensions of the existing ideas in different directions.

First, the focusing method to extract vibrational dephasing can be generalized to more complicated potentials. A *negative* linear chirp compensates the linear anharmonicity of a molecular Morse potential. Controlled higher order chirps can compensate even higher anharmonicities. To achieve laser pulses with well defined higher order chirps, computer controlled pulse shapers have to be used. The revival control by higher order *positive* chirps will allow to advance fractional revivals on potentials being more complicated than a Morse.

Second, the spatial interferences presented here in calculations provide information on the shape of the molecular electronic potential surface. The systematic determination of interference structures will give valuable information on the dynamic deformation of the potential induced by the cage motion.

Third, the revivals could be controlled in an alternative way: Instead of printing the right phase relation on a single pulse in order to shift the fractional revivals, one could use multi-pulse excitation schemes. A 1/4 revival consisting of two wave packets with half an oscillation period time delay can be created by a phase locked pair of two pulses. If the phase relation of the successively excited wave packets is disturbed by electronic dephasing, the 1/4 revival will be destroyed. This exhibits an alternative possibility for determination of $T_{\mathrm{deph}}^{\mathrm{el}}$. For a creation of 1/n revivals ($n > 2$), more than two pulses are needed and once more, a pulse shaper provides an ideal tool for experimental realization.

From wave packet control to reaction control

A phase-locked multiple pulse excitation scheme leads to sharp spectral features in the frequency domain. Those can be used to selectively excite a coherent superposition of Zero Phonon Lines (ZPL) or Phonon Sidebands (PS) of the chromophore. In an exclusive excitation of ZPL, no host phonons are excited and the molecular vibrational wave packet is practically free of energy relaxation. In contrast, an exclusive excitation of PS will result in a strong energy relaxation and cage asymmetry due to phonon creation. The symmetry plays a crucial role in the strength of nonadiabatic transitions. Thus, those transitions leading to reactions could be controlled by the multiple pulse excitation of a wave packet.

Bibliography

[1] J. Manz and L. Wöste. *Femtosecond Chemistry Vol. I + II*. VCH Verlagsgesellschaft, Weinheim, 1995.

[2] A. H. Zewail. *Femtochemistry, Ultrafast Dynamics of the Chemical Bond Vol. I + II*. World Scientific, Singapore, 1994.

[3] E. Schreiber. *Femtosecond Real-Time Spectroscopy of Small Molecules and Clusters*. Springer Verlag, Berlin, Heidelberg, 1998.

[4] S. A. Rice and M. Zhao. *Optical Control of Molecular Dynamics*. John Wiley and Sons, New York, 2000.

[5] J. A. Yeazell and T. Uzer. *The Physics and Chemistry of Wave Packets*. John Wiley and Sons, New York, 2000.

[6] W. P. Schleich. *Quantum Optics in Phase Space*. Wiley VCH, Berlin, 2001.

[7] D. J. Tannor and S. A. Rice. Control of selectivity of chemical reaction via control of wavepacket evolution. *J. Chem. Phys.*, 83:5013, 1985.

[8] D. J. Tannor, R. Kosloff, and S. A. Rice. Coherent pulse sequence induced control selectivity of reactions: Exact quantum mechanical calculations. *J. Chem. Phys.*, 85:5805, 1986.

[9] M. L. Klein and J. A. Venables. *Rare Gas Solids Vol. I + II*. Academic Press, London, 1976.

[10] J. Skalyo, Y. Edoh, and G. Shirane. Inelastic neutron scattering from solid krypton at 10 °K. *Phys. Rev. B*, 9:1797–1803, 1974.

[11] Y. Fujii, N. A. Lurie, R. Pynn, and G. Shirane. Inelastic neutron scattering from solid ^{36}Ar. *Phys. Rev. B*, 10:3647–3659, 1974.

[12] A. C. Sinnock and B. L. Smith. Refractive indices of the condensed rare gases. *Physical Review*, 181:1297–1307, 1969.

[13] M. Bargheer. *Ultrafast Photodynamics in Condensed Phase: ClF, Cl_2 and I_2 in Solid Rare Gases*. PhD thesis, Fachbereich Physik, Freie Universität Berlin, 2002.

[14] M. Bargheer, P. Dietrich, and N. Schwentner. Spectroscopy and photodissociation of ClF in rare gas solids. *J. Chem. Phys.*, 115:149–157, 2001.

[15] M. Bargheer, J. Pietzner, P. Dietrich, and N. Schwentner. Ultrafast laser control of iononic-bond formation: ClF in Ar solids. *J. Chem. Phys.*, 115:9827–9833, 2001.

[16] M. Bargheer, R. B. Gerber, M. V. Korolkov, O. Kühn, J. Manz, M. Schröder, and N. Schwentner. Subpicosecond spin-flip induced by the photodissociation dynamics of ClF in an Ar matrix. *Phys. Chem. Chem. Phys.*, 4:5554–5562, 2002.

[17] M. Bargheer, M. Y. Niv, R. B. Gerber, and N. Schwentner. Ultrafast solvent-induced spin-flip and nonadiabatic coupling: ClF in argon solids. *Phys. Rev. Lett.*, 89:108301, 2002.

[18] T. Kiljunen, M. Bargheer, M. Gühr, and N. Schwentner. A potential energy surface and a trajectory study of photodynamics and strong field alignment of ClF molecule in rare gas (Ar,Kr) solids. *Phys. Chem. Chem. Phys.*, 6:2185–2197, 2004.

[19] T. Kiljunen, M. Bargheer, M. Gühr, N. Schwentner, and B. Schmidt. Photodynamics and ground state librational states of ClF molecule in solid Ar. Comparison of experiment and theory. *Phys. Chem. Chem. Phys.*, 6:2932–2939, 2004.

[20] M. Bargheer, M. Gühr, and N. Schwentner. Depolarization as a probe for ultrafast reorientation of diatomics in condensed phase: ClF vs I_2 in rare gas solids. *J. Chem. Phys.*, 117:5–8, 2002.

[21] R. Zadoyan, P. Ashjian, C. C. Martens, and V. A. Apkarian. Femtosecond dynamics of coherent photodissociation-recombination of I_2 isolated in matrix Ar. *Chem. Phys. Lett.*, 218:504–514, 1994.

[22] R. Zadoyan, M. Sterling, and V. A. Apkarian. Dynamical spectroscopy of many body interactions, coherent vibrations and predissociation of I_2(B) in solid Kr. *J. Chem. Soc., Faraday. Trans.*, 92:1821–1829, 1996.

[23] R. Zadoyan, M. Sterling, M. Ovchinnikov, and V. A. Apkarian. Predissociation dynamics of I_2 in liquid CCl_4 observed through femtosecond pump-probe measurements: Electronic caging through solvent symmetry. *J. Chem. Phys.*, 107:8446–8460, 1997.

[24] R. Zadoyan, J. Almy, and V. A. Apkarian. Lattice dynamics from the 'eyes' of the chromophore, real-time studies of I_2 isolated in rare gas matrices. *Faraday Discuss.*, 108:255–269, 1997.

[25] M. Bargheer, M. Gühr, P. Dietrich, and N. Schwentner. Femtosecond spectroscopy of fragment-cage dynamics: I_2 in Kr. *Phys. Chem. Chem. Phys.*, 4:78–81, 2002.

[26] M. Gühr. Schwingungsrelaxation und Prädissoziation von Jodmolekülen in Edelgasmatrizen. Master's thesis, Fachbereich Physik der Freien Universität Berlin, 2001.

[27] M. Gühr, M. Bargheer, P. Dietrich, and N. Schwentner. Predissociation and vibrational relaxation in the B state of I_2 in a Kr matrix. *J. Phys. Chem. A*, 106:12002–12011, 2002.

[28] M. Bargheer, M. Gühr, and N. Schwentner. Collisions transfer coherence. *Israel J. Chem.*, 44:9–17, 2004.

[29] M. Karavitis, R. Zadoyan, and V. A. Apkarian. Time resolved coherent anti-Stokes Raman scattering of I_2 isolated in matrix argon: Vibrational dynamics on the ground electronic state. *J. Chem. Phys.*, 114:4131–4140, 2001.

[30] M. Karavitis, D. Segale, Z. Bihary, M. Pettersson, and V. A. Apkarian. Time-resolved CARS measurements of the vibrational decoherence of I_2 isolated in an Ar matrix. *Low Temp. Phys.*, 29:814–821, 2003.

[31] M. Karavitis and V. A. Apkarian. Vibrational coherence of I_2 in solid Kr. *J. Chem. Phys.*, 120:292–299, 2004.

[32] Z. Bihary, M. Karavitis, and V. A. Apkarian. Onset of decoherence: Six-wave mixing measurements of vibrational decoherence on the excited state of I_2 in solid argon. *J. Chem. Phys.*, 120:8144–8156, 2004.

[33] Z. Bihary, R. Zadoyan, M. Karavitis, and V. A. Apkarian. Dynamics and the breaking of a driven cage: I_2 in solid Ar. *J. Chem. Phys.*, 120:7576–7589, 2004.

[34] D. Segale, M. Karavitis, E. Fredji, and V. A. Apkarian. Quantum coherent dissipation: A glimpse of the "cat". *preprint*.

[35] M. J. J. Vrakking, D. M. Villeneuve, and A. Stolow. Observation of fractional revivals of a molecular wave packet. *Phys. Rev. A*, 54:R37–R40, 1996.

[36] I. Sh. Averbukh, M. J. J. Vrakking, D. M. Villeneuve, and A. Stolow. Wave packet isotope separation. *Phys. Rev. Lett.*, 77:3518–3521, 1996.

[37] G. Ribaud. Absorption of light by gas. *Ann. Phys.*, 12:107–226, 1919.

[38] D. J. Seery and D. Britton. The continuous absoption spectra of chlorine, bromine, bromine chloride, and iodine bromide. *J. Phys. Chem.*, 68:2263–2266, 1964.

[39] A. A. Passchier, J. D. Christian, and N. W. Gregory. The ultraviolet-visible absorption spectrum of bromine between room temperature and 440°C. *J. Phys. Chem.*, 71:937–942, 1967.

[40] G. Capelle, K. Sakurai, and H. P. Broida. Lifetime and self-quenching cross sections of vibrational levels in the B state of bromine excited by a tunable dye laser. *J. Chem. Phys.*, 54:1728–1730, 1971.

[41] J. A. Coxon. $B^3\Pi 0_u^+ - X^1\Sigma_g^+$ system of $^{79}Br^{79}Br$. *J. Mol. Spectr.*, 37:39, 1971.

[42] J. A. Coxon. The Extreme Red Absorption Spectrum of Br_2, $A^3\Pi(1_u) \leftarrow X^1\Sigma_u^+$. *J. Mol. Spectrosc.*, 41:548–565, 1972.

[43] R. F. Barrow, T. C. Clark, J. A. Coxon, and K. K. Yee. The $B^3\Pi 0_u^+ - X^1\Sigma_g^+$ system of Br_2: Rotational analysis, Franck-Condon factors, and long range potential in the $B^3\Pi 0_u^+$ state. *J. Mol. Spectrosc.*, 51:428–449, 1974.

[44] R. M. Lum and R. S. Hozack. Identification of selectively excited transitions in Br_2 isotopes at 5145 Å. *J. Mol. Spectr.*, 58:325–327, 1975.

[45] K. B. McAfee, R. M. Lum, and R. S. Hozack. Excited state bromine atom and molecule reactions. *J. Chem. Phys.*, 64:5073–5076, 1976.

[46] K. B. McAfee and R. S. Hozack. Lifetimes and energy transfer near the dissociation limit in bromine. *J. Chem. Phys.*, 64:2491–2495, 1976.

[47] R. J. Le Roy, R. G. Macdonald, and G. Burns. Diatom potential curves and transition moment functions from continuum absorption coefficients: Br_2^*. *J. Chem. Phys.*, 65:1485–1500, 1976.

[48] R. S. Hozack, A. P. Kennedy, and K. B. McAfee. Krypton ion laser-excited fluorescence in bromine. *J. Mol. Spectr.*, 80:239–243, 1980.

[49] A. Sur and J. Tellinghuisen. The D'→A' Transition in Br_2. *J. Mol. Spectrosc.*, 88:323–346, 1981.

[50] P. Berwanger, K. S. Viswanathan, and J. Tellinghuisen. The E→B transition (3000–3140 Å) in Br_2. *J. Mol. Spectrosc.*, 91:275–285, 1982.

[51] M. A. A. Clyne and Michael C. Heaven. Theoretical treatment of the spontaneous predissociation of Br_2, $B^3\Pi(0_u^+)$. *J. Chem. Phys.*, 76:5341–5349, 1982.

[52] E. Hwang, P. J. Dagdigan, and J. Tellinghuisen. Spectroscopy of metastable species in a free-jet expansion: The $\beta \leftarrow A$ transition in Br_2. *J. Mol. Spectrosc.*, 181:297–306, 1997.

[53] K. P. Huber and G. Herzberg. *Molecular Spectra and Molecular Structure IV. Constants of Diatomic Molecules*. Van Nostrand Reinhold Company Inc., New York, 1979.

[54] B. S. Ault, W. F. Howard, and L. Andrews. Laser-induced fluorescence and raman spectra of chlorine and bromine molecules isolated in inert matrices. *J. Mol. Spectrosc.*, 55:217–228, 1975.

[55] V. E. Bondybey, S. S. Bearder, and C. Fletcher. Br_2 $B^3\Pi(0_u^+)$ excitation spectra and radiative lifetimes in rare gas solids. *J. Chem. Phys.*, 64:5243–5246, 1976.

[56] J. M. Friedman, D. L. Rousseau, and V. E. Bondybey. Origin of resonant Raman excitation profiles red-shifted from optical absorption profiles. *Phys. Rev. Lett.*, 37:1610–1613, 1976.

[57] L. Andrews. Optical spectra of the dibromide and diiodide ions in the matrix-isolated $M^+Br_2^-$ and $M^+I_2^-$. *J. Am. Chem. Soc.*, 98:2152–2156, 1976.

[58] C. A. Wight, B. S. Ault, and L. Andrews. Laser-Raman and emission spectra of the dibromide molecular anion in the $M^+Br_2^-$ species. *Inorg. Chem.*, 15:2147–2150, 1976.

[59] J. M. Friedeman, V. E. Bondybey, and D. L. Rousseau. Br_2 in an Ar matrix: an example of complete damping of the resonance Raman scattering amplitude in the discrete resonance limit. *Chem. Phys. Lett.*, 70:499–503, 1980.

[60] M. Mandich, P. Beeken, and G. Flynn. Emission spectra and relaxation dynamics of excited $^{79}Br_2$ in Ar and Kr matrices. *J. Chem. Phys.*, 77:702–713, 1982.

[61] P. Beeken, M. Mandich, and G. Flynn. Photochemical dynamics of $^{79}Br_2$ in Xe matrices. *J. Chem. Phys.*, 76:5995–6001, 1982.

[62] B. Raffel and J. Wolfrum. Time resolved visible and UV absorption spectroscopy of bromine clusters in argon matrices. *Ber. Bunsenges. Phys. Chem.*, 87:643–648, 1983.

[63] J.-P. Nicolai, L. J. Van De Burgt, and M. C. Heaven. The A' $^3\Pi(2_u)$-$X^1\Sigma_g^+$ emission spectrum of Br_2 in argon matrix. *Chem. Phys. Lett.*, 115:496–500, 1985.

[64] J.-P. Nicolai and M. C. Heaven. Photoselection study of the Br_2 $A \rightarrow X$ emission system in an argon matrix. *J. Chem. Phys.*, 83:6538–6539, 1985.

[65] D. Thirumalai, E. J. Bruskin, and B. J. Berne. On the use of semiclassical dynamics in determining electronic spectra of Br in an Ar matrix. *J. Chem. Phys.*, 83:230–238, 1985.

[66] J. Langen, K.-P. Lodemann, and U. Schurath. Effect of guest-host interaction on spectra and relaxation dynamics of matrix isolated Br_2 $B^3\Pi_{0_u^+}$, $A^3\Pi_{1_u}$, and $A'^3\Pi_{2_u}$. *Chem. Phys.*, 112:393–408, 1987.

[67] I. Sh. Averbukh and N.F. Perelman. Fractional revivials: Iniversality in the long-term evolution of quantum wave packets beyond the correspondence principle dynamics. *Phys. Lett. A*, 139:449–453, 1989.

[68] I. Sh. Averbukh and N. F. Perel'man. Fractional regenerations of wave packets in the course of long term evolution of highly excited quantum systems. *Sov. Phys. JETP*, 69:464–469, 1989.

[69] I. Sh. Averbukh and N. F. Perel'man. The dynamics of wave packets of highly-excited states of atoms and molecules. *Sov. Phys. Usp.*, 34:572–591, 1991.

[70] S. I. Vetchinkin, A. S. Vetchinkin, and V. V. Eryomin. Gaussian wavepacket dynamics in an anharmonic system. *Chem. Phys. Lett.*, 215:11–16, 1993.

[71] S. I. Vetchinkin and V. V. Eryomin. The structure of wavepacket fractional revivals in a morse-like anharmonic system. *Chem. Phys. Lett.*, 222:394–398, 1994.

[72] C. Leichtle, I. Sh. Averbukh, and W. P. Schleich. Multilevel quantum beats: An analytical approach. *Phys. Rev. A*, 54:5299–5312, 1996.

[73] D. J. Tannor. *Introduction to Quantum Mechanics, A Time-Dependent Perspective*. University Science Books, Sausalito, 2003.

[74] T. Lohmuller, V. Engel, J. A. Beswick, and C. Meier. Fractional revivals in the rovibrational motion of I_2. *J. Chem. Phys.*, 120:10442–10449, 2004.

[75] R. W. Robinett. Quantum wave packet revivals. *Phys. Lett.*, 392:1–119, 2004.

[76] A. Materny, Ch. Lienau, and A. H. Zewail. Solvation ultrafast dynamics of reactions. 12. Probing along the reaction coordinate and dynamics in supercritical argon. *J. Phys. Chem.*, 100:18650–18665, 1996.

[77] Q. Liu, C. Wan, and A. H. Zewail. Solvation ultrafast dynamics of reactions. 13. Theoretical and experimental studies of wave packet reaction coherence and its density dependence. *J. Phys. Chem.*, 100:18666–18682, 1996.

[78] C. Meier and J. A. Beswick. Femtosecond pump-probe spectroscopy of I_2 in a dense rare gas environment: A mixed quantum/classical study of vibrational decoherence. *J. Chem. Phys.*, 121:4550–4558, 2004.

[79] M. Gühr, H. Ibrahim, and N. Schwentner. Controlling vibrational wave packet revivals in condensed phase: Dispersion and coherence for Br_2:Ar. *Phys. Chem. Chem. Phys.*, 6:5353–5361, 2004.

[80] B. Kohler, V. V. Yakovlev, J. Che, J. L. Krause, M. Messina, K. Wilson, N. Schwentner, R. M. Whitnell, and Y. Yan. Quantum control of wave packet evolution with tailored femtosecond pulses. *Phys. Rev. Lett.*, 74:3360–3363, 1995.

[81] M. Sterling, R. Zadoyan, and V. A. Apkarian. Interrogation and control of condensed phase chemical dynamics with linearly chirped pulses: I_2 in solid Kr. *J. Chem. Phys.*, 104:6497–6506, 1996.

[82] J. Cao and K. R. Wilson. A simple physical picture for quantum control of wave packet localization. *J. Chem. Phys.*, 107:1441–1450, 1997.

[83] M. Bargheer, P. Dietrich, K. Donovang, and N. Schwentner. Extraction of potentials and dynamics from condensed phase pump-probe spectra: Application to I_2 in Kr matrices. *J. Chem. Phys.*, 111:8556–8564, 1999.

[84] M. Ovchinnikov and V. A. Apkarian. Mixed-order smiclassical dynamics in coherent state representation: The connection between phonon sidebands and guest-host dynamics. *J. chem. Phys.*, 108:2277–2284, 1998.

[85] R. Zadoyan, D. Kohen, D. A. Lidar, and V. A. Apkarian. The manipulation of massive rovibronic superpositions using Time-Frequency-Resolved Coherent Anti-Stokes Raman Scattering (TFRCARS): From quantum control to quantum computing. *Chem. Phys.*, 266:323–351, 2001.

[86] M. Gühr, M. Bargheer, and N. Schwentner. Generation of coherent zone boundary phonons by impulsive excitation of molecules. *Phys. Rev. Lett.*, 91:085504, 2003.

[87] H. J. Zeiger, J. Vidal, T. K. Cheng, E. P. Ippen, G. Dresselhaus, and M. S. Dresselhaus. Theory for displacive excitation of coherent phonons. *Phys. Rev. B*, 45:768–778, 1992.

[88] T. K. Cheng, S. D. Brorson, A. S. Kazretoonian, J. S. Moodera, G. Dresselhaus, M. S. Dresselhaus, and E. P. Ippen. Impulsive excitation of coherent phonons observed in reflection in bismuth and antimony. *Appl. Phys. Lett.*, 57:1004–1006, 1990.

[89] T. K. Cheng, J. Vidal, H. J. Zeiger, G. Dresselhaus, M. S. Dresselhaus, and E. P. Ippen. Mechanism for displacive excitation of coherent phonons in Sb, Bi, Te, and Ti_2O_3. *Appl. Phys. Lett.*, 59:1923–1925, 1991.

[90] A. V. Kutsnetsov and C. J. Stanton. Theory of coherent phonon oscillations in semiconductors. *Phys. Rev. Lett.*, 73:3243–3246, 1994.

[91] K. Mizoguchi M. Hase, H. Harima, S. Nakashima, M. Tanbi, K. Sakai, and M. Hangyo. Optical control of coherent optical phonons in bismuth films. *Appl. Phys. Lett.*, 69:2474–2476, 1996.

[92] M. Hase, I. Ishioka, M. Kitajima, S. Hishita, and K. Ushida. Dephasing of coherent THz phonons in bismuth studied by femtosecond pump-probe technique. *Appl. Surf. Science*, 197-198:710–714, 2002.

[93] M. Hase, M. Kitajima, S. Nakashima, and K. Mizoguchi. Dynamics of coherent anharmonic phonons in bismuth using high density photoexcitation. *Phys. Rev. Lett.*, 88:067401, 2002.

[94] G. A. Garrett, T. F. Albrecht, J. F. Whitaker, and R. Merlin. Coherent THz phonons driven by light pulses and the sb problem: What is the mechanism? *Phys. Rev. Lett.*, 77:3661–3664, 1996.

[95] K. Sokolowski-Tinten, C. Blome, J. Blums, A. Cavalleri, C. Dietrich, A. Tarasevitch, I. Uschmann, E. Förster, M. Kammler, M. Horn-von-Hoegen, and D. von der Linde. Femtosecond X-ray measurement of coherent lattice vibrations near the Lindemann stability limit. *Nature*, 422:287–289, 2003.

[96] J. Helbing and M. Chergui. Solvation of ion-pair states in nonpolar media: I_2 in solid neon, argon and krypton. *J. Chem. Phys.*, 115:6158–6172, 2001.

[97] M. Gühr and N. Schwentner. Coherent phonon dynamics: Br_2 in solid Ar. *Phys. Chem. Chem. Phys.*, in print, 2005.

[98] F. O. Ellison. A method of diatomics in molecules .1. General theory and application to H_2O. *J. Am. Chem. Soc.*, 85:3540–3544, 1963.

[99] F. O. Ellison, J. C. Patel, and N. T. Huff. A method of diatomics in molecules .2. H_3 and H_{3+1}. *J. Am. Chem. Soc.*, 85:3544, 1963.

[100] J. C. Tully. Diatomics in molecules potential-energy surfaces .2. Nonadiabatic and spin-orbit interactions. *J. Chem. Phys.*, 59:5122–5134, 1973.

[101] J. C. Tully. Diatomics-in-molecules potential-energy surfaces .1. First-row triatomic hydrides. *J. Chem. Phys.*, 58:1396–1410, 1973.

[102] J. C. Tully and C. M. Truesdale. Diatomics-in-molecules potential-energy surfaces .3. Non hermitian formulation. *J. Chem. Phys.*, 65:1002–1007, 1976.

[103] J. C. Tully. Calculation of one-electron and two-electron molecular-properties by method of diatomics in molecules. *J. Chem. Phys.*, 64:3182–3184, 1976.

[104] M. Y. Niv, M. Bargheer, and R. B. Gerber. Photodissociation and recombination of F_2 molecule in Ar-54 cluster: Nonadiabatic molecular dynamics simulations. *J. Chem. Phys.*, 113:6660–6672, 2000.

[105] M. Y. Niv, A. I. Krylov, R. B. Gerber, and U. Buck. Photodissociation of HCl adsorbed on the surface of an Ar-12 cluster: Nonadiabatic molecular dynamics simulations. *J. Chem. Phys.*, 110:11047–11053, 1999.

[106] M. Y. Niv, A. I. Krylov, and R. B. Gerber. Photodissociation, electronic relaxation and recombination of HCl in Ar-n(HCl) clusters - Non-adiabatic molecular dynamics simulations. *Farad. Diss.*, 108:243–254, 1997.

[107] A. I. Krylov and R. B. Gerber. Photodissociation dynamics of HCl in solid Ar: Cage exit, nonadiabatic transitions, and recombination. *J. Chem. Phys.*, 106:6574–6587, 1997.

[108] I. H. Gersonde and H. Gabriel. Molecular-dynamics of photodissociation in matrices including nonadiabatic processes. *J. Chem. Phys.*, 98:2094–2106, 1993.

[109] M. Ovchinnikov and V. A. Apkarian. Condensed phase spectroscopy from mixed-order semiclassical molecular dynamics: Absorption, emission, and resonant raman spectra of I_2 isolated in solid Kr. *J. Chem. Phys.*, 105:10312–10331, 1996.

[110] M. Ovchinnikov and V. A. Apkarian. Quantum interference inresonant raman spectra of I_2 in condensed media. *J. Chem. Phys.*, 106:5775–5778, 1997.

[111] V. S. Batista and D. F. Coker. Nonadiabatic molecular dynamics simulation of photodissociation and geminate recombination of I_2 in liquid xenon. *J. Chem. Phys.*, 105:4033–4054, 1996.

[112] V. S. Batista and D. F. Coker. Nonadiabatic molecular dynamics simulation of ultrafast pump-probe experiments on I_2 in solid rare gases. *J. Chem. Phys.*, 106:6923–6941, 1997.

[113] N. Yu, C. J. Margulis, and D. F. Coker. Influence of solvation environment on excited state avoided crossings and photodissociation dynamics. *J. Phys. Chem. B*, 105:6728–6737, 2001.

[114] N. Yu and D. F. Coker. Ion pair state emission from I_2 in rare gas matrices: effects of solvent induced symmetry breaking. *Mol. Phys.*, 102:1031–1044, 2004.

[115] Z. Bihary, M. Karavitis, R. B. Gerber, and V. A. Apkarian. Spectral inhomogeneity induced by vacancies and thermal phonons and associated pbservables in time- and in frequency-domain nonlinear spectroscopy: I_2 isolated in matrix argon. *J. Chem. Phys.*, 115:8006–8013, 2001.

[116] Z. Bihary, R. B. Gerber, and V. A. Aparian. Vibrational self-consistent field approach to anharmonic spectroscopy of molecules in solids: Application to iodine in argon matrix. *J. Chem. Phys.*, 115:2695–2701, 2001.

[117] A. G. Redfield. On the theory of relaxation processes. *IBM J. Res. Dev.*, 1:19–31, 1957.

[118] A. G. Redfield. *Adv. Magn. Reson.*, 1:1, 1965.

[119] G. Lindblad. Generators of quantum dynamical semigroups. *Commun. Math. Phys.*, 48:119–130, 1976.

[120] G. Lindblad. Brownian motion of a quantum harmonic oscillator. *Rep. Math. Phys.*, 10:393, 1976.

[121] D. Kohen, C. C. Marston, and D. J. Tannor. Phase space approach to theories of quantum dissipation. *J. Chem. Phys.*, 107:5236–5253, 1997.

[122] D. Kohen and D. J. Tannor. Classical-quantum correspondence in the Redfield equation and its solutions. *J. Chem. Phys.*, 107:5141–5153, 1997.

[123] F. Bloch. Nuclear induction. *Phys. Rev.*, 70:460–474, 1946.

[124] L. I. Schiff. *Quantum Mechanics*. McGraw-Hill Book Co, Singapore, 1955.

[125] C. L. Cohen-Tannoudji, B. Diu, and F. Laloe. *Quantum Mechanics*, volume I. John Wiley and Sons, New York, 1977.

[126] G. Herzberg. *Molecular Spectra and Molecular Structure I. Spectra of Diatomic Molecules*. Van Nostrand Reinhold Company Inc., New York, 1950.

[127] J. Krause, R. M. Whitnell, K. R. Wilson, Y. Yan, and S. Mukamel. Optical control of molecular dynamics: Molecular cannons, reflectrons, and wave-packet focusers. *J. Chem. Phys.*, 99:6562–6579, 1993.

[128] S. Rutz, S. Greschik, E. Schreiber, and L. Wöste. Femtosecond wave packet propagation in spin-orbit coupled electronic states of the Na_2 molecule. *Chem. Phys. Lett.*, 257:365–373, 1996.

[129] J. Heufelder, H. Ruppe, S. Rutz, E. Schreiber, and L. Wöste. Fractional revivals of vibrational wave packets in the NaK $A^1\Sigma_+$ state. *Chem. Phys. Lett.*, 269:1–8, 1997.

[130] N. Mankoc-Borstnik, L. Fonda, and B. Borstnik. Coherent rotational states and their creation and time evolution in molecular and nuclear systems. *Phys. Rev. A*, 35:4132–4146, 1987.

[131] F. Rosca-Pruna and M. J. J. Vrakking. Revival structures in picosecond laser-induced alignment of I_2 molecules. I. Experimental results. *J. Chem. Phys.*, 116:6567–6578, 2002.

[132] M. Leibscher, I. Sh. Averbukh, P. Rozmej, and R. Arvieu. Semiclassical catastrophes and cumulative angular squeezing of a kicked quantum rotor. *Phys. Rev. A*, 69:032102, 2004.

[133] M. D. Poulsen, E. Peronne, H. Stapelfeldt, C. Z. Bisgaard, S. S. Viftrup, E. Hamilton, and T. Seideman. Nonadiabatic alignment of asymmetric top molecules: Rotational revivals. *J. Chem. Phys.*, 121:783–791, 2004.

[134] J. Parker and C. R. Stroud. Coherence and decay of Rydberg wave packets. *Phys. Rev. Lett.*, 56:716–719, 1986.

[135] E. J. Heller. The semiclassical way to molecular spectroscopy. *Acc. Chem. Res.*, 14:368, 1981.

[136] M. J. Davis and E. J. Heller. Multidimensional wave functions from classical trajectories. *J. Chem. Phys.*, 75:794–799, 1981.

[137] N. DeLeon, M. J. Davis, and E. J. Heller. Quantum manifestations of classical resonance zones. *J. Chem. Phys.*, 80:5036–5048, 1984.

[138] E. J. Heller and S. Tomsovic. Postmodern quantum mechanics. *Physics Today*, 46:38, 1993.

[139] M. Dantus, M. J. Rosker, and A. H. Zewail. Real-time femtosecond probing of "transition states" in chemical reactions. *J. Chem. Phys.*, 87:2395–2397, 1987.

[140] M. J. Rosker, M. dantus, and A. H. Zewail. Femtosecond real-time probing of reactions. I. The technique. *J. Chem. Phys.*, 89:6113–6127, 1988.

[141] M. Dantus, M. J. Rosker, and A. H. Zewail. Femtosecond real-time probing of reactions. II. The dissociation reaction of ICN. *J. Chem. Phys.*, 89:6128–6140, 1988.

[142] R. B. Bernstein and A. H. Zewail. Femtosecond real-time probing of reactions. III. Inversion to the potential from femtosecond transition-state spectroscopy experiments. *J. Chem. Phys.*, 90:829–842, 1989.

[143] T. S. Rose, M. J. Rosker, and A. H. Zewail. Femtosecond real-time probing of reactions. IV. The reactions of alkali halides. *J. Chem. Phys.*, 91:7415–7436, 1989.

[144] P. Cong, A. Mokhtari, and A. H. Zewail. Femtosecond probing of persistent wave packet motion in dissociative reactions: up to 40 ps. *Chem. Phys. Lett.*, 172:109–113, 1990.

[145] A. Mokhtari, P. Cong, J. L. Herek, and A. H. Zewail. Direct femtosecond mapping of trajectories in a chemical reaction. *Nature*, 348:225–227, 1990.

[146] M. Gruebele, G. Roberts, M. Dantus, R. M. Bowman, and A. H. Zewail. Femtosecond temporal spectroscopy and direct inversion to the potential: Application to iodine. *Chem. Phys. Lett.*, 166:459–469, 1990.

[147] Q. Liu, J.-K. Wang, and A. H. Zewail. Femtosecond dynamics of dissociation and recombination in solvent cages. *Nature*, 364:427–430, 1993.

[148] Ch. Lienau and A. H. Zewail. Solvation ultrafast dynamics of reactions. 11. Dissociation and caging dynamics in the gas-to-liquid transtion region. *J. Phys. Chem.*, 100:1829–1849, 1996.

[149] N. F. Scherer, L. D. Ziegler, and G. R. Flemming. Heterodyne-detected time-domain measurement of I_2 predissociation and vibrational dynamics in solution. *J. Chem. Phys.*, 96:5544–5547, 1992.

[150] N. F. Scherer, D. M. Jonas, and G. R. Flemming. Femtosecond wave packet and chemical reaction dynamics in iodine in solution: Tunable probe study of motion along the reaction coordinate. *J. Chem. Phys.*, 99:153–168, 1993.

[151] G. Flachenecker, P. Behrens, G. Knopp, M. Schmitt, T. Siebert, A. Vierheilig, B. Wirnsberger, and A. Materny. Femtosecond time-resolved dynamics of geminate and nongeminate recombination: Iodine enclosed in the nanocavities of a microporous SiO_2 modification. *J. Phys. Chem. A*, 103:3854–3863, 1999.

[152] V. A. Ermoshin, G. Flachenecker, A. Materny, and V. Engel. Caging of I_2 in decadodecasil 3R: Pump-probe experiments and molecular dynamics modeling. *J. Chem. Phys.*, 114:8132–5138, 2001.

[153] G. Flachenecker, V. A. Ermoshin, V. Engel, R. Neder, G. Wirnsberger, and A. Materny. Photodissociation and recombination dynamics of I_2 in DDR (decadodecasil 3R): Dependence on the geometry of the host matrix monitored by femtosecond time-resolved pump probe experiments. *Phys. Chem. Chem. Phys.*, 5:865–876, 2003.

[154] G. Flachenecker and A. Materny. The elementary steps of the photodissociation and recombination reactions of iodine molecules enclosed in cages and channels of zeolite crystals: A femtosecond time-resolved study of the geometry effect. *J. Chem. Phys.*, 120:5674–5690, 2004.

[155] A. L. Dobryakov, S. A. Kovalenko, and N. P. Ernsting. Electronic and vibrational coherence effects in broadband transient absorption spectroscopy with chirped supercontinuum probing. *J. Chem. Phys.*, 119:988–1002, 2003.

[156] S. Lochbrunner, K. Stock, and E. Riedle. Direct observation of the nuclear motion during ultrafast intramolecular proton transfer. *J. Mol. Struct.*, 700:13–18, 2004.

[157] C. Lupulescu, S. Vajda, A. Lindinger, A. Merli, and L. Wöste. Femtosecond pump-probe experiments on non-stoichiometric sodium-fluoride clusters - I. First direct observation of periodical structural changes in Na_2F. *Europ. Phys. J. D*, 24:173–176, 2003.

[158] M. Schmitt, G. Knopp, A. Materny, and W. Kiefer. Femtosecond time-resolved four-wave mixing spectroscopy in iodine vapour. *Chem. Phys. Lett.*, 280:339–347, 1997.

[159] N. F. Scherer, R. J. Carlson, A. Matro, M. Du, A. J. Ruggiero, V. Romero-Rochin, J. A. Cina, and G. R. Flemming. Fluorescence-detected wave packet interferometry: Time resolved molecular spectroscopy with sequences of femtosecond phase locked pulses. *J. Chem. Phys.*, 95:1487–1511, 1991.

[160] N. F. Scherer, A. Matro, L. D. Ziegler, M. Du, R. J. Carlson, J. A. Cina, and G. R. Flemming. Fluorescence-detected wave packet interferometry. II. Role of rotations and determination of the susceptibility. *J. Chem. Phys.*, 96:4180–4194, 1992.

[161] R. Rydberg. Graphische Darstellung einiger bandenspektroskopischer Ergebnisse. *Z. Phys.*, 73:376–385, 1931.

[162] O. Klein. Zur Berechnung von Potentialkurven für zweiatomige Moleküle mit Hilfe von Spektraltermen. *Z. Physik*, 76:226–235, 1932.

[163] A. Rees. The calculation of potential-energy curves from band-spectroscopic data. *Proc. Phys. Soc. London A*, 59:998–1008, 1947.

[164] R. Zadoyan, N. Schwentner, and V. A. Apkarian. Wavepacket diagnosis with chirped probe pulses. *Chem. Phys.*, 233:353–363, 1998.

[165] Merck AG. Sicherheitsdatenblatt Br_2. *www.chemdat.de*.

[166] Merck AG. Sicherheitsdatenblatt I_2. *www.chemdat.de*.

[167] L'Air liquide. *Gas encyclopedia*. Elsevier/North Holland Inc., New York, 1976.

[168] R. S. Mulliken. Iodine revisited. *J. Chem. Phys.*, 55:288–309, 1971.

[169] T. Ishiwata, K. Obi, and I. Tanaka. Optical-optical double-resonance spectroscopy of the $1_g(^3P_1)$ state of Br_2. *J. Mol. Spec.*, 127:353–361, 1988.

[170] M. S. Child. Repulsive potential curves from predissociation data. *J. Mol. Spectr.*, 22:487–493, 1970.

[171] A. C. Albrecht. Polarization and assignments of transitions: The method of photoselection. *J. Mol. Spectrosc.*, 6:84–108, 1961.

[172] J. Michl and E. Thulstrup. *Spectroscopy with polarized light*. VCH Publishers, New York, 1986.

[173] Y. Asano and S. Yabushita. Theoretical study of nonadiabatic transitions in the photodissociation of Cl_2 and Br_2. *Chem. Phys. Lett.*, 372:348–354, 2003.

[174] P. Sulzer and K. Wieland. Intensitätsverteilung eines kontinuierlichen Absorptions-Spektrums in Abhängigkeit von Temperatur und Wellenzahl. *Helv. Phys. Acta*, 25:653–676, 1952.

[175] J. Tellinghuisen. Resolution of the visible-infrared absorption spectrum of I_2 into three contributing transitions. *J. Chem. Phys.*, 58:2821–2834, 1973.

[176] J. Tellinghuisen. Potentials for weakly bound states in I_2 from diffuse spectra and predissociation data. *J. Chem. Phys.*, 82:4012–4016, 1985.

[177] K. K. Rebane. *Impurity Spectra of Solids*. Plenum Press, New York, 1970.

[178] S. H. Lin. *Radiationless Transitions*. Academic Press, New York, 1980.

[179] L. Khriachtchev, M. Pettersson, N. Runeberg, J. Lundell, and M. Räsänen. A stable argon compound. *Nature*, 406:874–876, 2000.

[180] R. B. Gerber. Formation of novel rare-gas molecules in low-temperature matrices. *Ann. Rev. Phys. Chem.*, 55:55–78, 2004.

[181] V. F. Lotrich and K. Szalewicz. Three-body contribution to binding energy of solid argon and analysis of crystal structure. *Phys. Rev. Lett.*, 79:1301–1304, 1997.

[182] C. Bechinger and H.-H. von Grünberg. Wenn drei Körper mehr Sind als drei Paare. *Physik Journal*, 3:33–38, 2004.

[183] V. A. Apkarian and N. Schwentner. Moleular photodynamics in rare gas solids. *Chem. Rev.*, 99:1481–1514, 1999.

[184] J. Franck and E. Rabinowitch. Some remarks about free radicals and the photochemistry of solutions. *Trans. Faraday Soc.*, 30:120–131, 1934.

[185] E. Rabinowitch and W. C. Wood. Properties of illuminated iodine solutions. I. Photochemical dissociation of iodine molecules in solution. *Trans. Faraday Soc.*, 32:547–556, 1936.

[186] E. Rabinowitch and W. C. Wood. Collision mechanism and the primary photochemical process in solutions. *Trans. Faraday Soc.*, 32:1381–1387, 1936.

[187] C. Wan, M. Gupta, J. S. Baskin, Z. H. Kim, and A. H. Zewail. Caging phenomena in reactions: Femtosecond observation of coherent, collisional confinement. *J. Chem. Phys.*, 106:4353–4356, 1997.

[188] A. L. Harris, J. K. Brown, and C. B. Harris. The nature of simple photodissociation reactions in liquids on ultrafast time scales. *Ann. Rev. Phys. Chem.*, 39:341–366, 1988.

[189] O. Roncero, N. Halberstadt, and J. A. Beswick. A wave-packet study of Ar...I_2(B) $\rightarrow$ Ar+I+I electronic predissociation. *Chem. Phys. Lett.*, 226:82–87, 1994.

[190] M. P. Demiranda, J. A. Beswick, and N. Halberstadt. One-atom cage effect in I_2-Ar complexes - can it be explained by linear ground-state isomers. *Chem. Phys.*, 187:185–194, 1994.

[191] O. Roncero, B. Lepetit, J. A. Beswick, N. Halberstadt, and A. A. Buchachenko. Ar I_2(X) $\rightarrow$ Ar I_2(B) photodissociation: Comparison between linear and T-shaped isomers dynamics. *J. Chem. Phys.*, 115:6961–6973, 2001.

[192] A. Buchachenko, N. Halberstadt, B. Lepetit, and O. Roncero. Ar ...I_2: A model system for complex dynamics. *Intern. Rev. Phys. Chem.*, 22:153–202, 2003.

[193] L. Onsager. Electric moments of molecules in liquids. *J. Am. Chem. Soc.*, 58:1486–1493, 1936.

[194] M. Macler and M. C. Heaven. Spectroscopy and relaxation dynamics of metastable electronically excited states of iodine in rare gas matrices. *Chem. Phys.*, 151:219–232, 1991.

[195] K. Huang and A. Rhys. Theory of light absorption and non-radiative transitions in F-centres. *Proc. Roy. Soc. London A*, 204:406–423, 1950.

[196] R. H. Silesbee and D. B. Fitchen. Optical analogs of the Mössbauer effect in solids. *Rev. Mod. Phys.*, 36:432–436, 1964.

[197] R. Englman. *Non-Radiative Decay of Ions and Molecules in Solids*. North-Holland Publishing Company, Amsterdam, 1979.

[198] C. Zener. Non-adiabatic crossing of energy levels. *Proc. R. Soc.*, 137:696–702, 1932.

[199] C. Rullière. *Femtosecond Laser Pulses*. Springer Verlag, Berlin, Heidelberg, 1998.

[200] J.-C. Diels and W. Rudolph. *Ultrashort Laser Pulse Phenomena*. Academic Press, San Diego, California, 1996.

[201] B. Schmidt, M. Hacker, G. Stobrawa, and T. Feurer. LAB2-a virtual femtosecond laser lab, http://www.lab2.de, 2002.

[202] Peter Dietrich. Refract, 1999.

[203] E.B. Treacy. Optical pulse compression with diffraction gratings. *IEEE J. Quantum Eletron.*, QE-5:454–460, 1969.

[204] R.L. Fork, O. E. Martinez, and J. P. Gordon. Negative dispersion using pairs of prisms. *Opt. Lett.*, 9:150–152, 1984.

[205] J. P. Gordon and R. L. Fork. Optical resonator with negative dispersion. *Opt. Lett.*, 9:153–155, 1984.

[206] F. J. Duarte. Generalized multiple-prism dispersion theory for pulse compression in ultrafast dye lasers. *Opt. and Quant. Electr.*, 19:223–229, 1987.

[207] K.W. DeLong, D.N. Fittinghoff, R. Trebino, B.K. Kohler, and K. Wilson. Phase retrieval in frequency-resolved optical gating based on the method of generalized projections. *Opt. Lett.*, 19:2152–2154, 1994.

[208] J.-P. Foing, J.-P. Likforman, M. Joffre, and A. Migus. Femtosecond pulse phase measurement by spectrally resolved up-conversion: Application to continuum compression. *IEEE J. of Quant. Electr.*, 28:2285–2290, 1992.

[209] P. M. W. French. The generation of ultrashort LASER pulses. *Rep. Prog. Phys.*, 58:171–262, 1995.

[210] H. A. Haus, K. Tamura, and E. P. Ippen. Pulse dynamics in stretched-pulse fiber lasers. *Appl. Phys. Lett.*, 67:158–160, 1995.

[211] T. Wilhelm, J. Piel, and E. Riedle. Sub-20-fs pulses tunable across the visible from a blue-pumped single-pass noncollinear parameteric converter. *Opt. Lett.*, 22:1494–1496, 1997.

[212] S. Lochbrunner, J. Piel, S. Schenkl, S. Spörlein, W. Zinth, E. Riedle, and M. Beuttner. Generation of 10 to 50 fs pulses tunable through all the visible and the NIR. *Appl. Phys. B*, 71:457, 2000.

[213] G. Cerullo, M. Nisoli, S. Stagira, and S. De Silvestri. Sub-8-fs pulses from an ultrabroadband optical parametric amplifier in the visible. *Opt. Lett.*, 23:1283–1285, 1998.

[214] A. Shirakawa and T. Kobayashi. Noncollinearly phase-matched femtosecond optical parameteric amplification with a 2000 cm^{-1} bandwidth. *Appl. Phys. Lett.*, 72:147–149, 1998.

[215] V. G. Dmitriev, G.G. Gurzadyan, and D. N. Nikogosyan. *Handbook of Nonlinear Optical Crystals*. Springer, Berlin, 1999.

[216] N. Schmitt. Phasen- und Amplitudenmessungen an Ultrakurzen Lichtpulsen. Master's thesis, Fachbereich Physik, FU Berlin, 1996.

[217] R. Schinke. *Photodissociation Dynamics*. Cambridge University Press, Cambridge / England, 1993.

[218] L. D. Landau and E. M. Lifschitz. *Lehrbuch der theoretischen Physik*, volume I: Mechanik. Akademie-Verlag, Berlin, 1979.

[219] M. Schröder. PhD thesis, Fachbereich Chemie, Freie Universität Berlin, 2004.

[220] A. Nitzan, S. Mukamel, and J. Jortner. Energy-gap law for vibrational-relaxation of a molecule in a dense medium. *J. Chem. Phys.*, 20063:200–207, 1975.

[221] M. Shapiro, M. J. J. Vrakking, and A. Stolow. Nonadiabatic wave packet dynamics: Experiment and theory in IBr. *J. Chem. Phys.*, 110:2465–2473, 1999.

[222] C. Meier. Private communication. 2004.

[223] N. Bloembergen. A quarter century of stimulated Raman scattering. *Pure Appl. Chem.*, 10:1229–1236, 1987.

[224] S. Mukamel. *Principles of Nonlinear Optical Spectroscopy*. Oxford University Press, New York, 1995.

[225] M. Schmitt, G. Knopp, A. Materny, and W. Kiefer. Femtosecond time-resolved coherent anti-Stokes Raman scattering for the simultaneous study of ultrafast ground and excited state dynamics: Iodine vapour. *Chem. Phys. Lett.*, 270:9–15, 1997.

[226] M. Schmitt, G. Knopp, A. Materny, and W. Kiefer. The application of femtosecond time-resolved coherent anti-Stokes Raman scattering for the investigation of ground and excited state molecular dynamics of molecules in the gas phase. *J. Phys. Chem. A*, 102:4059–4065, 1998.

[227] T. Siebert, M. Schmitt, A. Vierheilig, G. Flachenecker, V. Engel, A. Materny, and W. Kiefer. Separation of vibrational and rotational coherences with polarized femtosecond time-resolved four-wave mixing spectroscopy. *J. Raman Spectrosc.*, 31:25–31, 2000.

[228] F. Wise, M. J. Rosker, and C. L. Tang. Oscillatory femtosecond relaxation of photoexcited organic-molecules. *J. Chem. Phys.*, 86:2827–2832, 1987.

[229] J. Chesnoy and A. Mokhtari. Resonant impulsive-stimulated raman-scattering on malachite green. *Phys. Rev. A*, 38:3566–3576, 1988.

[230] S. Ruhman, A. Joly, and K. Nelson. Coherent molecular vibrational motion observed in the time domain trough impulsive stimulated raman scattering. *IEEE J. Quant. Electron.*, 34:460–468, 1988.

[231] B. Hartke, R. Kosloff, and S. Ruhman. Large-amplitude ground-state vibrational coherence induced by impulsive absorption in CsI - a computer-simulation. *Chem. Phys. Lett.*, 158:238–244, 1989.

[232] A. Weiner, D. Leaird, G. Wiederrecht, M. Banet, and K. Nelson. Spectroscopy with shaped femtosecond pulses: Styles for the 1990s. *SPIE Proc.*, 1209:185–195, 1990.

[233] S. L. Dexheimer, Q. Wang, L. A. Peteanu, W. T. Pollard, R. A. Mathies, and C. V. Shank. Femtosecond impulsive excitation of nonstationary vibrational-states in bacteriorhodopsin. *Chem. Phys. Lett.*, 188:61–66, 1992.

[234] W. T. Pollard and R. A. Mathies. Analysis of femtosecond dynamic absorption-spectra of nonstationary states. *Annu. Rev. Phys. Chem.*, 43:497–523, 1992.

[235] U. Banin, A. Bartana, S. Ruhman, and R. Kosloff. Impulsive excitation of coherent vibrational motion ground surface dynamics induced by intense short pulses. *J. Chem. Phys.*, 101:8461–8481, 1994.

[236] A. Bartana, U. Banin, S. Ruhman, and R. Kosloff. Intesity effects on impulsive excitation of ground surface coherent vibrational motion - a v-jump simulation. *Chem. Phys. Lett.*, 229:211–217, 1994.

[237] T. Baumert and G. Gerber. Molecules in intense femtosecond laser fields. *Phys. Scripta*, T72:53–68, 1997.

[238] E. Gershgoren, J. Vala, R. Kosloff, and S. Ruhman. Impulsive control of ground surface dynamics of I_3^- in solution. *J. Phys. Chem. A*, 105:5081–5095, 2001.

[239] V. Blanchet, M. A. Bouchene, O. Cabrol, and B. Girard. One-color coherent control in Cs_2: Observation of 2.7 fs beats in the ionization signal. *Chem. Phys. Lett.*, 233:491–499, 1995.

[240] V. Blanchet, M. A. Bouchene, and B. Girard. Temporal coherent control in the photoionization of Cs_2: Theory and experiment. *J. Chem. Phys.*, 108:4862–4876, 1998.

[241] K.Ohmori, Y. Sato, E. E. Nikitin, and S.A. Rice. High-precision molecular wave-packet interferometry with HgAr dimers. *Phys. Rev. Lett.*, 91:243003, 2003.

[242] J. Degert, C. Meier, B. Chatel, and B. Girard. Coherent control of matter-wave interference in molecular predissociation. *Phys. Rev. A*, 67:041402, 2003.

[243] F. Milota, J. Sperling, V Szöcs, A. Tortschanoff, and H. F. Kauffmann. Correlation of femtosecond wave packets and fluorescence interference in a conjugated polymer: Towards the measurement of site homogeneous dephasing. *J. Chem. Phys.*, 120:9870–9885, 2004.

[244] L. D. Noordam, D. I. Duncan, and T. F. Gallagher. Ramsey fringes in atomic rydberg wave pakets. *Phys. Rev. A*, 45:4734–4737, 1992.

[245] M. W. Noel and C. R. Stroud. Young's double-slit interferometry within an atom. *Phys. Rev. Lett.*, 75:1252–1255, 1995.

[246] O. Kinrot, I. Sh. Averbukh, and Y. Prior. Measuring coherence while observing noise. *Phys. Rev. Lett.*, 75:3822–3825, 1995.

[247] C. Leichtle, W. P. Schleich, I. Sh. Averbukh, and M. Shapiro. Wave packet interferometry without phase-locking. *J. Chem. Phys.*, 108:6057–6067, 1998.

[248] Ch. Warmuth, A. Tortschanoff, F. Milota, M. Shapiro, Y. Prior, I. Sh. Averbukh, W. Schleich, W. Jakubetz, and H. F. Kauffmann. Studying vibrational wavepacket dynamics by measuring fluorescence interference fluctuations. *J. Chem. Phys.*, 112:5060–5069, 2000.

[249] V. Szöcs and H. F. Kauffmann. Fluorescence interference noise in a two-site system: Excitation transfer dynamics from intensity fluctuations. *J. Chem. Phys.*, 109:7431–7442, 1998.

[250] A. Tortschanoff, K. Brinner, Ch. Warmuth, and H. F. Kauffmann. Coherence from fluorescence correlations: Oscillatory femtosecond fluorescence in pentacence/p-terphenyl. *J. Chem. Phys.*, 110:4493–4504, 1999.

[251] J. S. Baskin, M. Gupta, M. Chachisvilis, and A. H. Zewail. Femtosecond dynamics of microscopic friction: nature of coherent versus diffusive motion from gas to liquid density. *Chem. Phys. Lett.*, 275:437–444, 1997.

[252] J. S. Baskin, M. Chachisvilis, M. Gupta, and A. H. Zewail. Femtosecond dynamics of solvation: Microscopic friction and coherent motion in dense fluids. *J. Phys. Chem. A*, 102:4158–4171, 1998.

[253] M. Chachisvilis, I. Garcia-Ochoa, A. Douhal, and A. H. Zewail. Femtochemistry in nanocavities: dissociation, recombination and vibrational cooling of iodine in cyclodextrin. *Chem. Phys. Lett.*, 293:153–159, 1998.

[254] V. A. Ermoshin, A. K. Kazansky, and V. Engel. Quantum-classical molecular dynamis simulation of femtosecond spectroscopy on I_2 in inert gases: Mechanisms for the decay of pump-probe signals. *J. Chem. Phys.*, 111:7807–7817, 1999.

[255] A. K. Kazansky, V. A. Ermoshin, and V. Engel. Phase-energy approach to collision-induced vibrational relaxation. *J.Chem. Phys.*, 113:8865–8868, 2000.

[256] V.A. Ermoshin, V. Engel, and C. Meier. Collision-induced bound state motion in I_2. A classical molecular dynamics study. *J. Chem. Phys.*, 113:6585–6591, 2000.

[257] V. A. Ermoshin, V. Engel, and A. K. Kazanky. Phase and energy relaxation of vibrational motion and its manifestation in femtosecond pump-probe experiments on I_2 in rare gas enironment. *J. Phys. Chem. A*, 105:7501–7507, 2001.

[258] D. W. Oxtoby, D. Levesque, and J. J. Weis. Molecular-dynamics simulation of dephasing in liquid-nitrogen. *J. Chem. Phys.*, 68:5528–5533, 1978.

[259] D. W. Oxtoby. Hydrodynamic theory for vibrational dephasing in liquids. *J. Chem. Phys.*, 70:2605–2610, 1979.

[260] K. S. Schweizer and D. Chandler. Vibrational dephasing and frequency-shifts of polyatomic-molecules in solution. *J. Chem. Phys.*, 76:2296–2314, 1982.

[261] B. I. Grimberg, V. V. Lozovoy, M. Dantus, and S. Mukamel. Ultrafast nonlinear spectroscopic techniques in the gas phase and their density matrix representation. *J. Chem. Phys. A*, 106:697–718, 2002.

[262] M. Comstock, V. V. Lozovoy, and M. Dantus. Femtosecond photon echo measurements of electronic coherence relaxation between the $X^1\Sigma_{g+}$ and $B^3\Pi_{0u+}$ states of I_2 in the presence of He, Ar, O_2, C_3H_8. *J. Chem. Phys.*, 119:6546–6553, 2003.

[263] H. Egger, M. Gsänger, E. Lüscher, and B. Dorner. Phonon dispersion measurements in an argon single crystal at 4.2 degrees. *Phys. Lett. A*, 28:433, 1968.

[264] S. Jimenez, A. Paquarello, R. Car, and M. Chergui. Dynamics of structural relaxation upon Rydberg excitation of an impurity in an Ar crystal. *Chem. Phys.*, 233:343–352, 1997.

[265] C. Jeannin, M. T. Porella-Oberli, S. Jimenez, F. Vigliotti, B. Lang, and M. Chergui. Femtosecond dynamics of electronic 'bubbles' in solid argon: Viewing the inertial response and the bath coherences. *Chem. Phys. Lett.*, 316:51–59, 2000.

[266] S. Jimenez, M. Chergui, G. Rojas-Lorenzo, and J. Rubayo-Soneira. The medium response to an impulsive redistribution of charge in solid argon: Molecular dynamics simulations and normal mode analysis. *J. Chem. Phys.*, 114:5264–5272, 2001.

[267] M. Chergui. *Structural Dynamics in Quantum Solids*, chapter Trends in femtosecond lasers and spectroscopy, pages 1453–1467. Academie des sciences Paris, 2001.

[268] F. Vigliotti, L. Bonacina, M. Chergui, G. Rojas-Lorenzo, and J. Rubajo-Soneira. Ultrafast expansion and vibrational coherences of electronic 'bubbles' in solid neon. *Chem. Phys. Lett.*, 362:31–38, 2002.

[269] F. Vigliotti, L. Bonacina, and M. Chergui. Structural dynamics in quatum solids. II. Real-time probing of the electronic bubble formation in solid hydrogens. *J. Chem. Phys.*, 116:4553–4562, 2002.

[270] F. Vigliotti, L. Bonacina, and M. Chergui. Ultrafast structural dynamics in alectronically excited solid neon. I. Real-time probing of the electronic bubble formation. *Phys. Rev. B*, 67:115118, 2003.

[271] G. Rojas-Lorenzo, J. Rubayo-Soneira, F. Vigliotti, and M. Chergui. Ultrafast structural dynamics in electronically excited solid neon. II. Molecular-dynamics simulations of the electronic bubble formation. *Phys. Rev. B*, 67:115119, 2003.

[272] T. Kiljunen, J. Eloranta, J. Ahokas, and H. Kunttu. Magnetic properties of atomic boron in rare gas matrices: An electron paramagnetic resonance study with ab initio and diatomics-in-molecules molecular dynamics analysis. *J. Chem. Phys.*, 114:7144–7156, 2001.

[273] T. Kiljunen, J. Eloranta, J. Ahokas, and H. Kunttu. Optical properties of atomic boron in rare gas matrices: An ultraviolet-absorption/laser induces fluorescence study with ab initio diatomics-in-molecules molecular dynamics analysis. *J. Chem. Phys.*, 114:7157–7165, 2001.

[274] C. R. Gonzales, S. Fernandez-Alberti, J. Echave, and M. Chergui. Simulations of the absorption band of the d state of Hg_2 in rare gas matrices. *Chem. Phys. Lett.*, 367:651–656, 2003.

[275] F. Y. Naumkin and D. J. Wales. Diatomics-in-moleules potentials incorporating ab initio data: Application to ionic, rydberg-excited, and molecule-doped rare gas clusters. *Comp. Phys. Comm.*, 145:141–155, 2002.

[276] P. Casavecchia, G. He, R. K. Sparks, and Y. T. Lee. Rare gas-halogen atom interaction potentials from crossed molecular beams experiments: I($^2P_{3/2}$)+Kr, Xe($^1S_0$). *J. Chem. Phys.*, 77:1878–1885, 1982.

[277] P. Casavecchia, G. He, R. K. Sparks, and Y. T. Lee. Interaction potentials for Br(^{2}P)+Ar, Kr, and Xe(^{1}S) by the crossed molecular beams method. *J. Chem. Phys.*, 75:710–721, 1981.

[278] A. Borrmann and C. C. Martens. Nanoscale shock wave generation by photodissociation of impurities in solids: A molecular dynamics study. *J. Chem. Phys.*, 102:1905–1916, 1995.

[279] J. G. Leese and G. K. Horton. 2-phonon Raman-scattering of light in rare-gas crystals. *J. Low. Temp. Phys.*, 35:205–220, 1979.

[280] I. Ya. Fugol. Excitons in rare-gas crystals. *Adv. Phys.*, 27:1–87, 1978.

[281] A. V. Benderskii, R. Zadoyan, and V. A. Apkarian. Caged spin-orbit excited I*^{2}P$_{1/2}$+I*^{2}P$_{1/2}$ atom pairs in liquids and in cryogenic matrices: Spectroscopy and dipolar quenching. *J. Chem. Phys.*, 107:8437–8445, 1997.

[282] M. Karavitis and V. A. Apkarian. The I*^{2}P$_{1/2}$-I*^{2}P$_{1/2}$ contact pair emission in condesed media: A molecular spring-gauge for cavity sizing. *J. Phys. Chem. B*, 106:8466–8470, 2002.

[283] M. P. Allen and D. J. Tildesley. *Computer Simulations of Liquids*. Oxford University Press, New York, 1987.

[284] D. Tannor. Homepage http://www.weizmann.ac.il/chemphys/tannor/home.html.

[285] M. D. Feit, J. A. Fleck, and A. Steiger. Solution of the Schrödinger-equation by a spectral method. *J. Comput. Phys.*, 47:412–432, 1982.

Appendix

Description of the wave packet calculations

Most part of the Matlab computer code described here was programmed by Prof. D. Tannor and coworkers, and can be downloaded on the home page of D. Tannor. The source code is currently provided on [284]. The program was modified in a sense to include chirped pulse excitation and adapted to the Br_2 case.

The numerical propagation of the wave packet on the internuclear coordinate is performed on a discrete grid with 2^n points, to allow for a fast Fourier transformation application. The electronic ground state and B state potentials are defined as Morse potentials on that grid. Only the vibrational wave packet on the electronic excited B state of Br_2 will be simulated, no rotational motion was taken into account. The rotational motion is frozen anyhow, when introducing the Br_2 in the matrix host (see section 7.1.2). The ground state vibrational level $v = 0$ is assumed to be populated exclusively before the propagation. This condition is strictly fulfilled for the bromine X state at 20 K, as was shown in Tab. 6.1.

The pump step

The vibrational wave packet on the B state will be excited by a pump laser pulse using time dependent perturbation theory. Let H_X be the molecular Hamiltonian in the X state, H_{B} be the molecular Hamiltonian in the B state and $\mu_{XB}E(t)$ the perturbation due to the pump laser electric field, where μ_{XB} is the transition dipole from the ground state X to the B state in the Condon approximation and $E(t)$ is the electric field.[1] The wave function ψ_0 is the unperturbed wave function and ψ_1 the wave function including the perturbation. Since the perturbation is considered as small, the ψ_0 is the X $v = 0$ wave function and ψ_1 the wave function (or better wave packet) on the B state. The excitation in the first order time dependent perturbation theory reads like:

$$\psi_1(R,t) = \frac{1}{i\hbar}\int_0^t \mathrm{e}^{-\frac{\mathrm{i}}{\hbar}\mathrm{H_B(t-t')}}(-\mu_{\mathrm{XB}}\mathrm{E(t')})\mathrm{e}^{-\frac{\mathrm{i}}{\hbar}\mathrm{H_X(t')}}\psi_0(\mathrm{R,t})\mathrm{dt'}. \quad (1)$$

The propagation of the wave packet on the B state

Besides the perturbation term, so called propagation terms on the ground state X $\mathrm{e}^{-\frac{\mathrm{i}}{\hbar}\mathrm{H_X(t')}}$ and on the excited state B $\mathrm{e}^{-\frac{\mathrm{i}}{\hbar}\mathrm{H_B(t-t')}}$ appear. The propagation terms also appear in case the electric field is not acting on the molecule any more. This would correspond to the normal propagation of the molecular wave packet on the B state after the pump process.

The propagation step in the time interval from t to t' on a potential can be written as:

$$\psi(t') = \mathrm{e}^{\frac{-\mathrm{i}}{\hbar}\mathrm{H(t'-t)}}\psi(\mathrm{t}) = [\prod_0^{\mathrm{N}} \mathrm{e}^{\frac{-\mathrm{i}}{\hbar}\mathrm{H}\Delta\mathrm{t}}]\psi(\mathrm{t}), \quad (2)$$

[1] The electric field is besides the probe process the only part, that was implemented completely new by myself in D. Tannors program.

where the time interval from t to t' is divided into N pieces of length Δt. The strategy called split operator technique will be followed [73, 285]. The aim is to disentangle the kinetic parts of the Hamiltonian from the potential parts. This is done by the following approximation:

$$\mathrm{e}^{\frac{-\mathrm{i}}{\hbar}\mathrm{H}\Delta\mathrm{t}} = \mathrm{e}^{\frac{-\mathrm{i}}{\hbar}(\frac{\mathrm{p}^2}{2\mathrm{m}}+\mathrm{V(R)})\Delta\mathrm{t}} = \mathrm{e}^{\frac{-\mathrm{i}}{2\hbar}\mathrm{V(R)}\Delta\mathrm{t}}\mathrm{e}^{\frac{-\mathrm{i}}{\hbar}(\frac{\mathrm{p}^2}{2\mathrm{m}})\Delta\mathrm{t}}\mathrm{e}^{\frac{-\mathrm{i}}{2\hbar}\mathrm{V(R)}\Delta\mathrm{t}} + \mathrm{O}(\Delta\mathrm{t}^3). \tag{3}$$

The representation would be exact, if the commutator of the potential and the kinetic part would vanish (which is in general not the case). However, for small values of Δt, the contribution of the $O(\Delta t^3)$ is negligible [73]. Constructing the full propagator in the time interval from t to t' leads to the following expression:

$$\psi(t') = \mathrm{e}^{\frac{-\mathrm{i}}{\hbar}\mathrm{H}(\mathrm{t}'-\mathrm{t})}\psi(\mathrm{t}) \approx \mathrm{e}^{\frac{-\mathrm{i}}{2\hbar}\mathrm{V(R)}\Delta\mathrm{t}}[\prod_{0}^{\mathrm{N}-1}\mathrm{e}^{\frac{-\mathrm{i}}{\hbar}(\frac{\mathrm{p}^2}{2\mathrm{m}})\Delta\mathrm{t}}\mathrm{e}^{\frac{-\mathrm{i}}{\hbar}\mathrm{V(R)}\Delta\mathrm{t}}]\mathrm{e}^{\frac{-\mathrm{i}}{2\hbar}\mathrm{V(R)}\Delta\mathrm{t}}\psi(\mathrm{t}). \tag{4}$$

The last consists of an alternating row of propagations with R terms and with p (momentum) terms only. To propagate in R space, the wave function will be represented as $\psi(R,t)$. To propagate with the kinetic energy term, the wave function will be Fourier transformed to the p space (or k space), propagated with $\mathrm{e}^{\frac{-\mathrm{i}}{\hbar}(\frac{\mathrm{p}^2}{2\mathrm{m}})\Delta\mathrm{t}}$ and Fourier transformed back to R space. The two Fourier transforms (performed by the FFT algorithm[2]) and the propagation in p space is done much faster than transforming the $\mathrm{e}^{\frac{-\mathrm{i}}{\hbar}(\frac{\mathrm{p}^2}{2\mathrm{m}})\Delta\mathrm{t}}$ into R space. This is the original reason to use the split operator technique here. The wave packet $\psi(R,t)$ on the B state can be transformed into phase space by a Wigner transformation (Eq. (2.7)). This is once more done by using the FFT algorithm. Apart from this, the absolute square of the B state vibrational wave packet $|\psi(R,t)|^2$ can be plotted as a function of R and t as a density plot as shown for example in Fig. 2.7.

The probe step

According to section 2.3.1, the probe window position R_{win} is chosen by evaluating 2.26 for a given probe wavelength. The width of the probe window in space was chosen with help of the pulse spectral width and the difference potential of the states involved in the probe transition. For a given time in the pump-probe spectrum, the absolute square of the wave packet in the probe window is summed up and saved as one point in the pump-probe spectrum. Thus, the duration of the real probe pulse is not taken into account.

[2]Therefore, the grid has 2^N points, where N is a positive integer value.

The First Order Delay Marginal in SFG FROGS

The FROG trace I_{FROG} is a function of the delay time τ and the angular frequency ω of the recorded spectrum. In the special case of a SFG FROG, it is given as:

$$I_{\mathrm{FROG}}(\tau,\omega) = |\int_{-\infty}^{+\infty} E_r(t)E_g(t-\tau)\exp(i\omega t)dt|^2, \tag{5}$$

where

$$E_r(t) = E_{0r}\exp(-\frac{t^2}{2\tau_r^2} - i\frac{\gamma}{2}t^2 - i\omega_r t),$$

is a chirped pulse, whose chirp shall be determined and

$$E_g(t-\tau) = E_{0g}\exp(-\frac{(t-\tau)^2}{2\tau_g^2} - i\omega_g t),$$

is the gate pulse that is unchirped.
First, the integral in 5 is evaluated:

$$\begin{aligned}\int_{-\infty}^{+\infty} E_r(t)E_g(t-\tau)\exp(i\omega t)dt &= E_{0r}E_{0g}\int_{-\infty}^{+\infty}\exp(-(\frac{1}{2\tau_r^2}+\frac{1}{2\tau_g^2}+i\frac{\gamma}{2})t^2)\\ &\quad \exp(-i(\omega_r+\omega_g-\omega-i\frac{\tau}{\tau_g^2})t)\exp(-\frac{\tau^2}{2\tau_g^2})dt\\ &= E_{0r}E_{0g}\exp(-\frac{\tau^2}{2\tau_g^2})\int_{-\infty}^{+\infty}\exp(-(at^2+bt))dt\end{aligned}$$

with

$$\begin{aligned}a &= \frac{1}{2\tau_r^2}+\frac{1}{2\tau_g^2}+i\frac{\gamma}{2} = \frac{\tau_{\mathrm{cc}}^2}{2\tau_r^2\tau_g^2}+i\frac{\gamma}{2},\\ b &= i(\omega_r+\omega_g-\omega-i\frac{\tau}{\tau_g^2})\\ &= i(\omega_s - i\frac{\tau}{\tau_g^2}).\end{aligned}$$

The solution of the integral is found via quadratic supplement:

$$\int_{-\infty}^{+\infty} E_r(t)E_g(t-\tau)\exp(i\omega t)dt = E_{0r}E_{0g}\exp(-\frac{\tau^2}{2\tau_g^2})\sqrt{\frac{\pi}{a}}\exp(\frac{b^2}{4a}).$$

Therefore, the FROG trace is given as:

$$I_{\mathrm{FROG}}(\tau,\omega) = |E_{0r}|^2|E_{0g}|^2\exp(-\frac{\tau^2}{\tau_g^2})\exp(\frac{a^*b^2+b^{*2}a}{4a^*a}).$$

The evaluation of $4a^*a$ yields:

$$\begin{aligned}4a^*a &= 4|\frac{\tau_{\mathrm{cc}}^2}{2\tau_r^2\tau_g^2}+i\frac{\gamma}{2}|^2 = \frac{\tau_{\mathrm{cc}}^4}{\tau_r^4\tau_g^4}+\gamma^2\\ &= \frac{\tau_{\mathrm{cc}}^4+\gamma^2\tau_r^4\tau_g^4}{\tau_r^4\tau_g^4}.\end{aligned}$$

The evaluation of $a^*b^2 + b^{*2}a$ results in:

$$\begin{aligned} & (\frac{\tau_{\rm cc}^2}{2\tau_r^2\tau_g^2} + i\frac{\gamma}{2})(\frac{\tau^2}{\tau_g^4} + 2i\omega_s\frac{\tau}{\tau_g^2} - \omega_s^2) + cc \\ = \quad & \frac{\tau_{\rm cc}^2\tau^2}{\tau_r^2\tau_g^6} + \frac{\tau_{\rm cc}^2\omega_s^2}{\tau_r^2\tau_g^2} - \frac{2\omega_s\gamma\tau}{\tau_g^2}. \end{aligned}$$

Thus , $I_{\rm FROG}$ is given as:

$$I_{\rm FROG}(\tau,\omega) = |E_{0r}|^2|E_{0g}|^2\exp(-\frac{\tau^2}{\tau_g^2})\exp(\frac{\tau_{\rm cc}^2\tau^2\tau_r^2 + \tau_{\rm cc}^2\omega_s^2\tau_r^2\tau_g^2 - 2\omega_s\gamma\tau\tau_r^4\tau_g^2}{\tau_{\rm cc}^4 + \gamma^2\tau_r^4\tau_g^4}).$$

One finds the FODM $N(\tau)$ by setting the frequency derivation of $I_{\rm FROG}$ to zero:

$$\begin{aligned} 0 \quad = \quad & \frac{d}{d\nu}I_{\rm FROG}(\tau,\nu) \\ = \quad & \frac{d}{d\nu}(\frac{\tau_{\rm cc}^2\tau^2\tau_r^2 + \tau_{\rm cc}^2 4\pi^2\nu_s^2\tau_r^2\tau_g^2 - 2\pi\nu_s 2\gamma\tau\tau_r^4\tau_g^2}{\tau_{\rm cc}^4 + \gamma^2\tau_r^4\tau_g^4}) \\ = \quad & \frac{2\pi 2\tau_r^2\tau_g^2}{\tau_{\rm cc}^4 + \gamma\tau_r^4\tau_g^4}(-\tau_{\rm cc}^2 2\pi\nu_s + \gamma\tau\tau_r^2). \end{aligned}$$

The last condition is fulfilled if,

$$\nu_s = N(\tau) = \frac{\gamma\tau\tau_r^2}{2\pi\tau_{\rm cc}^2}\ .$$

With $\gamma = \frac{\beta\eta^2}{\tau_r^2}$ this results in:

$$N(\tau) = \frac{\beta\eta^2}{2\pi\tau_{\rm cc}^2}\tau. \tag{6}$$

Dispersion time T_{disp}

A wave packet in a Morse potential centered at energy E has a spectral full width half maximum of $\Delta E = 2\delta E$. We introduce energies E_1 = $E + \delta E$ and $E_2 = E - \delta E$. The wave packet has dispersed, when the classical trajectory at E_2 has undergone one more oscillation than the trajectory at E_1. The oscillation periods at E_1 and E_2 shall be T_1 and T_2 respectively. The condition for the dispersion time T_{disp}reads as:

$$T_{\mathrm{disp}} = nT_2, \tag{7}$$
$$T_{\mathrm{disp}} = (n-1)T_1. \tag{8}$$

The number of oscillations n can be deduced from the equations above and together with the first equation, the criterion for T_{disp} reads as:

$$T_{\mathrm{disp}} = \frac{T_1 T_2}{T_1 - T_2}. \tag{9}$$

From Eq. (2.13) one deduces for a oscillation period $T(E)$ in a Morse oscillator:

$$T(E) = (\omega_e^2 - 4E\omega_e x_e)^{-1/2}. \tag{10}$$

Plugging that in Eq. (9) with the correct energy leads to:

$$T_{\mathrm{disp}} = ((\omega_e^2 - 4E_2\omega_e x_e)^{1/2} - (\omega_e^2 - 4E_1\omega_e x_e)^{1/2}). \tag{11}$$

Now, the two square root terms are approximated by a first order Taylor expansion around the central energy E. This shall be shown for the second term of the last equation:

$$(\omega_e^2 - 4(E+\delta E)\omega_e x_e)^{1/2} = (\omega_e^2 - 4E\omega_e x_e) + \frac{1}{2}(\omega_e^2 - 4E\omega_e x_e)^{-1/2} 4\delta E\omega_e x_e + ... \tag{12}$$

The higher orders are neglected. Application of the Taylor expansion leads to:

$$T_{\mathrm{disp}} = \frac{(\omega_e^2 - 4E\omega_e x_e)^{1/2}}{4\delta E\omega_e x_e}. \tag{13}$$

With Eq. (10) and $2\delta E = \Delta E$ this leads to:

$$T_{\mathrm{disp}} = \frac{\nu(E)}{2\Delta E\omega_e x_e}. \tag{14}$$

Focusing time T_{opt}

First, the Wigner function of a laser pulse is briefly reviewed. The result is needed to develop the focusing time T_{opt}.

Besides other frequency - time functions, the Wigner function $W(\nu,t)$ of a laser pulse provides further insight in chirped excitation experiments. The Wigner function of a laser field $E(t)$ is given as:

$$W(\nu.t) = \int_{-\infty}^{\infty} E(t \pm \frac{\tau}{2}) E^*(t \mp \frac{\tau}{2}) e^{-i2\pi\nu t} d\tau. \tag{15}$$

Its projection on the time or frequency axis displays the pulse intensity on the addressed coordinate. Wigner functions can become negative, in contrast to the FROG traces, that are very similar to $W(\nu,t)$ in all other properties.

The Wigner function of a gaussian pulse with linear chirp β according to Eq. (4.6) is given by:

$$W(\nu,t) = 2F_0 \exp[-(\frac{t-(\nu-\nu_0)\beta/2\pi}{\tau}))^2 - (\frac{\nu-\nu_0}{\eta})^2],$$

when β and η are given in standard frequency instead of angular frequency units. F_0 is the total fluence of the laser pulse. Calculating the first order marginal in the spectral domain $\tau(\nu)$ delivers:

$$\tau(\nu) = \frac{\int tW(\nu,t)dt}{\int W(\nu,t)dt} = \frac{\beta}{2\pi}(\nu-\nu_0). \tag{16}$$

The derivation for T_{opt} given here follows that of Ref. [83]. The first order Taylor expansion of the oscillation frequency $\nu(E)$ around energy E_0 (wave packet energetic center) in anharmonic oscillator is expressed as:

$$\nu(E) = \nu(E_0) + \frac{d\nu}{dE}(E-E_0). \tag{17}$$

The difference in vibrational periods T for different energies E of the wave packet shall be called $\Delta T(E)$. It is given by:

$$\Delta T(E) = \frac{dT}{dE}(E-E_0) = -\frac{1}{\nu^2}\frac{d\nu}{dE}(E-E_0). \tag{18}$$

In anharmonic oscillators (like Morse oscillators are), the value for $d\nu/dE$ is different from zero. Thus, the different parts of the wave packet oscillate at different frequencies and the wave packet disperses, as seen in the last section. This "mismatch" in vibrational frequencies has to be compensated. The solution is to apply a chirped laser pulse. In case of a Morse oscillator, the oscillation times get bigger with increasing vibrational energy. In that case, one would have to apply a negatively chirped laser pulse, in order to start the high energy components earlier in time. At the focusing time T_{opt}, the advance of the high energy parts is used up and wave packet focuses. We quantify that relation now.

From the Wigner representation of a laser pulse, one knows about the time - energy relation $\tau(E)$ of a chirped laser pulse (Eq. (16)):

$$\tau(E) = \frac{\beta'}{2\pi}(E-E_0). \tag{19}$$

The β' has been introduced before as β/c and is given in the unit fs cm when the energy is given in the unit cm^{-1}. The vibrational period mismatch is compensated by a chirped pulse with

time-energy relation $t(E)$ after N oscillations, where $N = \tau(E)/\Delta T(E)$. Thus, the focusing time is given by:

$$T_{\mathrm{opt}} = T(E)N \tag{20}$$

$$T_{\mathrm{opt}} = T(E)\frac{\tau(E)}{\Delta T(E)}. \tag{21}$$

Inserting Eqs. (19) and (18) in (21) leads to:

$$T_{\mathrm{opt}} = \frac{\nu\beta'}{2\pi\frac{d\nu}{dE}}. \tag{22}$$

The value of $d\nu/dE$ for a Morse oscillator can be calculated from Eq. (2.13) leading to $d\nu/dE = 2\omega_e x_e/\nu$. Inserting this in Eq. 22 leads to the desired term for the focusing time:

$$T_{\mathrm{opt}} = \frac{\nu^2\beta'}{4\pi\omega_e x_e}. \tag{23}$$

Publications

Articles:

- M. Bargheer, M. Gühr, P. Dietrich, and N. Schwentner, ”Femtosecond Spectroscopy of the Fragment-Cage Dynamics: I_2 in Kr”, *Phys. Chem. Chem. Phys.*,4: 75-81, 2002
- M. Gühr, M. Bargheer, P. Dietrich, and N. Schwentner, ”Predissociation and Vibrational Relaxation in the B state of I_2 in a Kr Matrix”, *J. Phys. Chem. A*,106:12002-12011, 2002
- M. Bargheer, M. Gühr, and N. Schwentner, ”Depolarization as a probe for ultrafast reorientation of diatomics in condensed phase: ClF vs. I_2 in rare gas solids”, *J. Chem. Phys.*,117:5-8, 2002
- M. Gühr, M. Bargheer, and N. Schwentner, ”Generation of coherent zone boundary phonons by impulsive excitation of molecules”, *Phys. Rev. Lett.*,91:085504, 2003
- T. Kiljunen, M. Bargheer, M. Gühr, and N. Schwentner, ”A potential energy surface and a trajectory study of photodynamics and strong-field alignment of ClF molecule in rare gas (Ar,Kr) solids”, *Phys. Chem. Chem. Phys.*,6:2185-2197, 2004
- T. Kiljunen, M. Bargheer, M. Gühr, N. Schwentner, and B. Schmidt, ”Photodynamics and ground state librational states of CIF molecule in solid Ar. Comparison of experiment and theory”, *Phys. Chem. Chem. Phys.*,6:2932-2939, 2004
- M. Bargheer, M. Gühr, and N. Schwentner, ”Collisions Transfer Coherence”, *Israel J. Chem.*,44:9-17, 2004
- M. Gühr, H. Ibrahim, and N. Schwentner, ”Controlling vibrational wave packets revivals in condensed phase: Dispersion and coherence for Br_2 in solid Ar”, *Phys. Chem. Chem. Phys.*,6:5353-5361, 2004
- M. Gühr, and N. Schwentner, ”Coherent Phonon Dynamics: Br_2 in solid Ar”, *Phys. Chem. Chem. Phys.*,*Phys. Chem. Chem. Phys.*,7:760-767, 2005

Conference Proceedings:

- M. Gühr, and N. Schwentner, ”Generation of Coherent Zone Boundary Phonons by Impulsive Excitation of Molecules”, in: Ultrafast Phenomena XIV edited by T. Kobayashi, T. Okada, T. Kobayashi, K. A. Nelson, S. De Silvestri, Springer, Berlin, 2005
- M. Bargheer, M. Gühr, M. Fushitani, and N. Schwentner, ”Wavepacket Interferometry and Wavepacket Dynamics in Condensed Phase”, in: Ultrafast Phenomena XIV edited by T. Kobayashi, T. Okada, T. Kobayashi, K. A. Nelson, S. De Silvestri, Springer, Berlin, 2005

Curriculum vitae

Markus Gühr
geboren am 30.04.1976 in Gießen

1982 - 1995	Schulausbildung in Rabenau, Allendorf und Gießen
Juni 1995	Abitur an der Liebigschule Gießen
Aug. 1995 - Aug. 1996	Zivildienst
Feb. 1997 - Juli 2001	Stipendium der Studienstiftung des deutschen Volkes
Okt. 1996 - Sept. 1998	Grundstudium der Physik an der Freien Universität Berlin
Sept. 1998	Vordiplom in Physik
Okt. 1998 - Apr. 1999	Physikstudium an der University of Cambridge, England
Apr. 1999 - Juni 2001	Hautpstudium Physik an der Freien Universität Berlin
Okt. 1999 - Juli 2001	Tutor im Physikalischen Praktikum für Naturwissenschaftler
Juli 2000 - Juni 2001	Diplomarbeit in der AG Schwentner ”Schwingungsrelaxation und Prädissoziation von Jodmolekülen in Edelgasmatrizen”
Juni 2001	Diplom in Physik ”mit Auszeichnung” und Preis der Wilhelm und Else Heraeus Stiftung
seit Okt. 2001	Wissenschaftlicher Mitarbeiter in der AG Schwentner

Danksagung

Prof. Dr. N. Schwenter gilt mein größter Dank für die freundliche Arbeitsatmosphäre und die intensive Betreuung dieser Arbeit. Von unseren zahlreichen Diskussionen habe ich in jeder Hinsicht profitiert. Sein Engagement und seine Kritik haben ganz wesentlich zum Gelingen der Arbeit beigetragen.

Herrn Prof. Dr. J. Manz danke ich für die Vorlesung "Einführung in die zeitabhängige Quantenmechanik", die mich zur Formulierung der hier vorgestellten Wellenpaketkontrolle angeregt hat. Weiterhin danke ich Prof. Dr. D. Tannor für die Erlaubnis zur Benutzung seines Wellenpaket-Programmcodes.

Die Zusammenarbeit mit Dr. Matias Bargheer in der ersten Hälfte meiner Doktorandenzeit war hervorragend. Auch nach seinem Weggang geniesse ich die Diskussionen mit ihm sehr. Ausserdem danke ich Matias für die erste Durchsicht dieser Arbeit.

Dr. Toni Kiljunen, Heide Ibrahim und David Ambrosek verdanke ich weitere wertvolle Korrekturen. Bei Toni bedanke ich mich ausserdem für die tolle Zusammenarbeit am ClF-Ausrichtungsprojekt und die gute Büronachbarschaft. Heide Ibrahim danke ich für die Unterstützung bei den letzten Experimenten am Brom. Bei der Weiterführung wünsche ich ihr viel Erfolg.

Weiterhin bedanke ich bei Dr. Mizuho Fushitani und Nina Ovchimikov für die tolle Zusammenarbeit am Laser und das angenehme Arbeitsklima. Den anderen Mitgliedern der Arbeitsgruppe Ingeborg Twesten, Dr. Verena Ney und Dr. Manfred Soltwisch danke ich für die freundliche Aufnahme in die Gruppe und die schönen Unterhaltungen.

Bei Prof. B. Gerber, PD Dr. O. Kühn, Dr. M. Korolkov, Herrn A. Borowski, Herrn A. Cohen und Dr. M. Schröder bedanke ich mich für die hilfreichen Diskussionen im Rahmen unserer Kooperation.

Dem Glasbläser des Instituts, Herrn Zimmermann bin ich zu grossem Dank für die Herstellung der Brom-Glasapparatur verpflichtet. Weiterhin danke ich Roswitha Brunn für die Hilfe beim Umgang mit dem (nicht ganz ungefährlichen) Brom.

Dem Sfb 450 der Deutschen Forschungsgemeinschaft danke ich für die Finanzierung des Projektes und die Rahmenbedingungen, unter denen diese Arbeit gelingen konnte.

Bei meinen Eltern, Geschwistern und Freunden bedanke ich mich für das Verständnis und die Unterstützung während meiner Promotionszeit.